

**Towards integrated control of tokamak plasmas:
physics-based control of neoclassical tearing modes
in the TCV tokamak**

Présentée le 27 février 2020

à la Faculté des sciences de base
SPC - Théorie
Programme doctoral en physique

pour l'obtention du grade de Docteur ès Sciences

par

Mengdi KONG

Acceptée sur proposition du jury

Prof. R. Houdré, président du jury
Dr. O. Sauter, directeur de thèse
Prof. H. Zohm, rapporteur
Dr T. Hender, rapporteur
Dr F. Felici, rapporteur

千里之行，始于足下。

A journey of a thousand miles begins with a single step.

— Laozi, ancient Chinese philosopher

To my family

Abstract

Neoclassical tearing modes (NTMs), magnetic islands located at rational q surfaces, are an important class of resistive magnetohydrodynamics (MHD) instabilities in tokamak plasmas, with q the safety factor. NTMs are one of the main constraints of the achievable plasma pressure by increasing the local radial transport and NTMs can lead to plasma disruptions. It is therefore crucial to understand the physics of NTMs and ensure their reliable control.

This thesis explores the physics and control of NTMs, by means of dedicated experiments in the TCV tokamak and interpretative simulations with the modified Rutherford equation (MRE), a model widely used in interpreting island width evolutions. Triggerless NTMs originating from unstable tearing modes (TMs, stability index $\Delta' > 0$) and saturating under the effects of the perturbed bootstrap current are the main focus of this thesis.

In TCV, triggerless NTMs are reproducibly observed in low-density discharges with strong near-axis electron cyclotron current drive (ECCD), providing an excellent opportunity of studying these modes. Instead of direct computations of Δ' , a model for Δ' is developed based on extensive experiments and interpretative simulations. This model facilitates the clarification of the complete evolution of triggerless NTMs, from onset as TMs to saturation as NTMs. Our Δ' model also explains an unexpected density dependence of the onset of NTMs, where NTMs only occur with a certain range of density that broadens with increasing near-axis ECCD power and with lower plasma current. The density range is found to result from the density and plasma current dependence of the stability of ohmic plasmas and the density dependence of ECCD efficiency.

Given its high localization and flexibility, off-axis ECH/ECCD will be used for NTM control in future tokamaks. Comprehensive experimental and numerical studies of the dynamics of NTMs are carried out in this thesis, concerning both the stabilization of existing NTMs and the prevention of NTMs by means of preemptive off-axis ECCD. It is shown and predicted that the prevention of NTMs is much more efficient than NTM stabilization in terms of EC power. Interpretative simulations of the complex set of experiments constrain well the coefficients in the MRE and quantify NTM evolutions. The prevention effects from off-axis ECCD are found to result from local ECH/ECCD instead of a change of Δ' .

A key element of a reliable real-time (RT) control of NTMs is the alignment of EC beams with the target mode location. A small sinusoidal sweeping of the deposition location of EC beams around the target location proves to be effective for both NTM stabilization and prevention, making it a promising technique. Integrated control of NTMs, plasma pressure and model-estimated q profiles is demonstrated on TCV, including advanced plasma state reconstruction,

monitoring, supervision and actuator management. A RT-capable MRE module, based on our validated MRE, is developed for the first time and tested by extensive offline simulations for TCV and AUG. It provides a more intelligent physics-based NTM controller, aware of the EC power it requires to stabilize or prevent a given NTM. The information from the RT-MRE is also valuable for RT actuator allocations and decision-making in view of the overall integrated control, in particular for future long-pulse tokamaks like ITER and DEMO.

Keywords: neoclassical tearing modes (NTMs), modified Rutherford equation (MRE), triggerless NTMs, NTM stabilization, NTM prevention, integrated control, ITER, DEMO

Résumé

Les “neoclassical tearing modes” (NTMs), des îlots magnétiques, sont une classe importante d’instabilités magnétohydrodynamiques (MHD) résistives dans les plasmas de tokamak. Les NTMs limitent la pression du plasma, augmentent le transport radial et peuvent conduire à une disruption du plasma. Il est donc crucial de comprendre la physique des NTMs et d’assurer leur contrôle fiable.

Cette thèse explore la physique et le contrôle des NTMs, au moyen d’expériences dédiées dans le tokamak TCV et de simulations interprétatives avec la “modified Rutherford equation” (MRE), permettant l’interprétation des évolutions temporelles de la largeur des îlots. Les NTMs sans déclencheur proviennent de “tearing modes” instables (TMs, modes de cisaillement, $\Delta' > 0$), et saturent sous les effets du courant de bootstrap perturbé. L’analyse physique et le contrôle de ces types d’NTMs sont le principal objectif de cette thèse.

Sur TCV, des NTMs sans déclencheur ont été observés de manière reproductible dans les décharges de faible densité avec un fort courant cyclotron électronique (ECCD) proche de l’axe magnétique, permettant d’étudier ces modes. Au lieu de calculs directs de Δ' , cette thèse développe un modèle basé sur des expériences approfondies et des simulations interprétatives. Ce modèle a facilité la clarification de l’évolution complète des NTMs, de leur apparition comme TMs à la saturation en tant qu’NTMs. Notre modèle peut également expliquer une dépendance inattendue de l’apparition des NTMs sur la densité, instable dans une plage de densité qui s’élargit avec l’augmentation de l’ECCD et la diminution du courant plasma. Cette plage résulte de la dépendance de la stabilité des plasmas ohmiques sur la densité et le courant plasma ainsi que de la dépendance inverse de l’efficacité ECCD sur la densité.

Compte tenu de sa localisation et de sa flexibilité élevées, l’ECH/ECCD hors axe sera utilisé pour le contrôle NTM dans les futurs tokamaks. Des études expérimentales et numériques complètes de la dynamique des NTMs sont menées dans cette thèse, concernant à la fois la stabilisation des modes existants et la prévention des NTMs au moyen de l’ECCD hors axe. Il est démontré et simulé que la prévention des NTMs est beaucoup plus efficace que leur stabilisation en termes de puissance requise. Les simulations interprétatives de l’ensemble d’expériences complexes bien contraignent les coefficients du modèle MRE et quantifient l’évolution des NTMs. Les effets de prévention du ECCD résultent principalement des effets locaux du chauffage et de l’entraînement de courant au lieu d’un changement de Δ' .

L’alignement des faisceaux EC avec le mode est un élément clé du contrôle en temps réel (RT) fiable des NTMs. Un petit balayage sinusoïdal du dépôt radial des faisceaux EC autour du mode est très efficace à la fois pour la stabilisation et la prévention des NTMs, ce qui en

fait une technique prometteuse. Le contrôle intégré des NTMs, de la pression et du profil de q est démontré expérimentalement sur TCV, y compris la reconstruction avancée de l'état du plasma, la surveillance, la supervision et la gestion des actionneurs. Pour avoir un contrôleur NTM plus intelligent, utilisant un modèle physique, un module MRE compatible en RT, basé sur notre MRE validé, est développé pour la première fois et testé par de nombreuses simulations pour TCV et AUG. Les informations du MRE sont également précieuses pour les attributions des actionneurs RT et la prise de décision en vue de la commande intégrée globale, en particulier pour les futurs tokamaks à longue impulsion comme ITER et DEMO.

Mots-clés : neoclassical tearing modes (NTMs), modified Rutherford equation (MRE), NTM sans déclencheur, mode de cisaillement, stabilisation des NTMs, prévention des NTMs, contrôle intégré, ITER, DEMO

Contents

Abstract (English/Français)	v
1 Introduction	1
1.1 Thermonuclear fusion and plasmas	1
1.1.1 Nuclear fusion reactions	1
1.1.2 Plasmas and magnetic confinement fusion	2
1.2 The tokamak device	3
1.2.1 Configuration of magnetic field and coil systems	3
1.2.2 Auxiliary heating and current drive systems	5
1.2.3 MHD instabilities in tokamak plasmas	7
1.3 Motivation of the thesis	7
1.4 Outline of the thesis	10
2 Present and future tokamak devices	13
2.1 Introduction	13
2.2 The TCV tokamak	13
2.2.1 Auxiliary heating and current drive systems	15
2.2.2 Main diagnostics	17
2.2.3 Real-time control systems	21
2.3 The ASDEX Upgrade tokamak	23
2.4 ITER and beyond	24
2.4.1 ITER	24
2.4.2 Beyond ITER	25
3 Neoclassical tearing modes (NTMs)	27
3.1 Introduction	27
3.2 Onset of NTMs	29
3.2.1 Small island effects on NTMs	30
3.2.2 Seeding of NTMs	31
3.3 Control of NTMs	31
3.3.1 Avoidance and prevention of NTMs	32
3.3.2 Stabilization of existing NTMs	32
3.3.3 Control of NTMs on ITER	34
3.4 The Modified Rutherford Equation (MRE)	35

3.5	Summary	40
4	Triggerless onset of 2/1 NTMs in TCV	43
4.1	Introduction	43
4.2	Experimental results	44
4.2.1	Plasma scenario and experimental setup	44
4.2.2	Experimental observations of the density range for the triggerless onset of NTMs in TCV	46
4.3	A simple model for Δ'_0	47
4.3.1	Ramp-up of EC power with constant medium density	49
4.3.2	Ramp-up of EC power with higher or lower density	59
4.3.3	Density-ramp experiments with constant EC power	66
4.4	Recovery of the observed density range	71
4.5	Discussions	76
4.5.1	Effects of rotation on the triggerless onsets of NTMs in TCV	76
4.5.2	Contribution of pure heating to the triggerless onset of NTMs	77
4.6	Summary	81
5	Stabilization and prevention of 2/1 NTMs with EC beams in TCV	85
5.1	Introduction	85
5.2	Plasma scenario and experimental setup	86
5.3	Self-stabilization: slow ramp-down of near-axis co-ECCD power	87
5.4	Stabilization of NTMs with varying co-ECCD depositions	91
5.5	NTM stabilization with co-ECCD, counter-ECCD or ECH	97
5.6	NTM stabilization versus prevention	104
5.7	Effects of EC misalignment on the stabilization and prevention of NTMs	107
5.7.1	A series of NTM stabilization experiments with different EC misalignment	107
5.7.2	Statistics of the effect of beam-mode misalignment on the stabilization and prevention of NTMs	111
5.8	Summary	116
6	Real-time NTM control and integrated multi-actuator plasma control in TCV	119
6.1	Introduction	119
6.2	Real-time control of NTMs in TCV	119
6.2.1	Main challenges of real-time NTM control	119
6.2.2	Feedback NTM control algorithms in TCV	121
6.2.3	A simple real-time NTM stabilization experiment in TCV	122
6.3	Integrated multi-actuator plasma control in TCV	123
6.3.1	A new generic plasma control system (PCS) framework	124
6.3.2	Integrated control experiment with preliminary plasma supervision and actuator allocations	126
6.3.3	Integrated control experiments with advanced plasma supervision and actuator allocations	128

6.4	Inclusion of Modified Rutherford Equation in the plasma control system	132
6.4.1	Real-time determination of the coefficients in the MRE	133
6.4.2	Real-time information about beam-mode alignment	138
6.4.3	Real-time estimation of the EC power required for NTM control	139
6.4.4	Prediction of island width evolution	146
6.4.5	Further tests of the RT-MRE based on an AUG discharge	148
6.4.6	Foreseen implementation of the RT-MRE in the PCS	151
6.5	Summary and outlook	153
7	Conclusions	155
7.1	On the triggerelss onset of NTMs	156
7.2	On the stabilization and prevention of NTMs	157
7.3	On the real-time NTM control and integrated plasma control	158
A	A sensitivity study of Δ'	159
A.1	Introduction	159
A.2	Scan of the radial location of localized perturbations	160
A.3	Scan of the amplitude and width of localized perturbations	164
A.3.1	Perturbation scan near the center or edge	164
A.3.2	Perturbation scan with $\rho_{\text{center}} = \rho_{21}$	167
A.4	Scan with global change of q profiles	174
A.4.1	Rigid shifts of the q profile	174
A.4.2	Scan of q_a with fixed q_0	176
A.5	Summary	178
B	Locking/Acceleration of NTMs with tangential neutral beam injection (NBI)	179
B.1	Introduction	179
B.2	Locking/Locked NTMs with co-current NBI	180
B.3	Acceleration of NTMs with counter-current NBI	185
B.4	Discussions and outlook	188
	Bibliography	212
	Acknowledgements	213
	Curriculum Vitae	215

1 Introduction

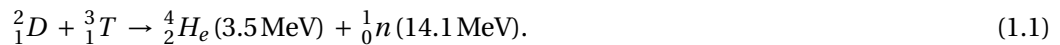
1.1 Thermonuclear fusion and plasmas

Nuclear fusion reactions power the Sun and the stars, ensuring the flourishing of life on the Earth. The dramatic advances in science and technology, especially in the 21st century, have greatly improved the living standards of human beings, and inevitably, caused an ever faster increase of energy demand. Apart from concerns about the shortage of fossil fuels such as coal and oil that still constitute a dominant portion of the world's energy sources, increased emissions of greenhouse gases such as carbon dioxide (CO₂) from the use of fossil fuels also exacerbate global warming. In particular, a statistic review of world energy [Dudley 2019] has disclosed that the primary energy consumption grew at a rate of 2.9% in 2018, almost double its 10-year average (1.5% per year); the carbon emissions grew by 2% in 2018, being the fastest growth for seven years. This once again highlights that breakthroughs, including those in science and technology, are needed to steer the world on a sustainable path.

1.1.1 Nuclear fusion reactions

Nuclear fusion is a promising candidate of sustainable energy production in the future, given its safety, abundant fuel reserves and minimal damage on the environment [Freidberg 2007]. Unlike nuclear fission, fusion does not involve chain reactions nor long-lived radioactive wastes, and is thus safer.

Among the possible options of nuclear fusion reactions, the reaction of deuterium (D) and tritium (T) nuclei listed in equation (1.1) has proven to be the easiest and been the central focus of fusion research worldwide [Freidberg 2007]. This is because the D-T reaction has the largest cross section among the possible fusion reactions, or in simple words, the highest probability of colliding and generating fusion energy.



Deuterium and tritium, fuels for the D-T reaction, are isotopes of hydrogen, among which deuterium is abundant in the seawater and can almost be regarded as inexhaustible. Tritium, on the other hand, has a relatively short radioactive half-life (12.3 years) and cannot be found in nature. However, it can be bred self-sustainably through reactions between neutrons (from fusion products) and widely-available lithium. In this sense, the fuels of the D-T reaction are nearly endless. The products of the D-T reaction, a helium nucleus (α particle) and a neutron, carry high kinetic energy resulting from the mass difference between the reactants and products. A total energy of 17.6 MeV is generated per reaction, meaning merely 1 kg of the fuel would fulfill the requirements of a 1 GW electrical power station for a day [Wesson 2004].

The energy of the high speed neutron can eventually be used to drive turbines and generate electricity, while that of the α particle can contribute to sustaining the high temperature required by D-T reaction. To achieve this, it is necessary to satisfy the *ignition condition* of D-T reactions [Wesson 2004]:

$$nT\tau_E > 3 \times 10^{21} \text{ m}^{-3} \text{ keVs}, \quad (1.2)$$

where n is the particle density, T here the temperature and τ_E the energy confinement time defined as the ratio between the total energy of the particles and the power losses. The ignition condition represents the requirement on $nT\tau_E$ (the so-called *triple product*) to reach burning fusion regime, where the fusion power from α particles is sufficient to maintain the high temperature required by D-T reactions (i.e. no external heating is needed any more).

The requirement on temperature stems from the mutual electromagnetic repulsion between the positively charged deuterium and tritium nuclei: high energy is needed to overcome the natural repulsion and increase the cross section (probability) of fusion. The necessary temperature is above 10 keV, corresponding to a stunning 116 million degrees centigrade. At this high temperature, the fuels exist at the fourth state of the matter: plasma.

1.1.2 Plasmas and magnetic confinement fusion

A plasma is an ionized gas that is quasi-neutral and exhibiting collective effects [Chen 2007]. Different from gas, liquid or solid, where the matter consists of neutral atoms with the electrons rotating around the central nuclei, plasmas are composed by electrons and ions that are detached from each other (through ionization) and move relatively freely. Plasmas exist in an extremely wide range of density and temperature, from 10^6 to 10^{34} m^{-3} and from 10^{-4} to 10^3 keV [Chen 2007], respectively. In fact, most of the matter in the observable universe is estimated to be in the plasma state, and plasmas can be found in the daily life as well, e.g. neon signs and the flash of a lightning bolt. Plasmas are also taking part in advanced scientific and technological domains, for example in medicine and electric space propulsion [von Woedtke et al. 2013; Rafalskyi and Aanesland 2016, and references therein].

In terms of thermonuclear fusion, where extremely hot plasmas are involved (with a tempera-

ture of the order of 10 keV as discussed), a suitable container is needed to accommodate the fusion reactions. Thanks to the charged nature of plasma particles, electromagnetic fields can be used to *confine* the hot plasma away from the wall of its physical container, a vacuum vessel, through Lorentz forces. This leads to the concept of *magnetic confinement fusion*, which has drawn much attention in the past decades. Different concepts have been proposed and various machines with different configurations have been built [Freidberg 2007], among which the tokamak, as will be introduced in the next section, has been the pioneering concept towards a commercial fusion power plant.

1.2 The tokamak device

1.2.1 Configuration of magnetic field and coil systems

The tokamak concept [Artsimovich 1972] was first developed by Soviet researchers in the late 1960s, with the name from a Russian acronym, meaning “toroidal chamber with magnetic coils”. As illustrated in figure 1.1, a tokamak is an axisymmetric toroidal device with a large toroidal (i.e. along the torus) magnetic field generated by external *toroidal field coils* (light blue) surrounding the vacuum vessel. The torus (doughnut) shape of the tokamak naturally circumvents the *end loss* problem of most linear devices, but the toroidal magnetic field itself is not sufficient to confine the plasmas. This is due to the existence of various types of particle drifts in tokamak plasmas, for example the vertical drifts caused by the curvature and gradient of the magnetic field, which meanwhile leads to charge separations (electric fields) and extra radial drifts. A poloidal magnetic field component is thus required to overcome these drifts and confine better the hot plasmas. In tokamaks, this poloidal magnetic field is self-generated by a *toroidal plasma current* (Ampere’s law).

The toroidal plasma current can be driven by an inner *transformer* circuit (also called ohmic transformer, ohmic coil or central solenoid, green in figure 1.1) through Faraday’s and Ohm’s law. Given the limit of the current passing through the transformer coils, the operation of tokamaks will be *pulsed* in this way and not completely compatible with the requirement of future power plant. To achieve the steady-state operation of tokamaks, alternatives need to be found to drive this plasma current non-inductively. This can be partly provided by the self-generated *bootstrap current* [Peeters 2000; Sauter et al. 1999, 2002a] inside the plasma and partly by auxiliary current drive systems that will be discussed in section 2.2.1. An additional set of poloidal coils (*outer poloidal field coils*, grey in figure 1.1) are also needed to maintain the position of the plasma inside the vacuum vessel and to shape the plasma into desired configurations. The toroidal and poloidal magnetic fields altogether produce the helical magnetic fields required to confine fusion plasmas.

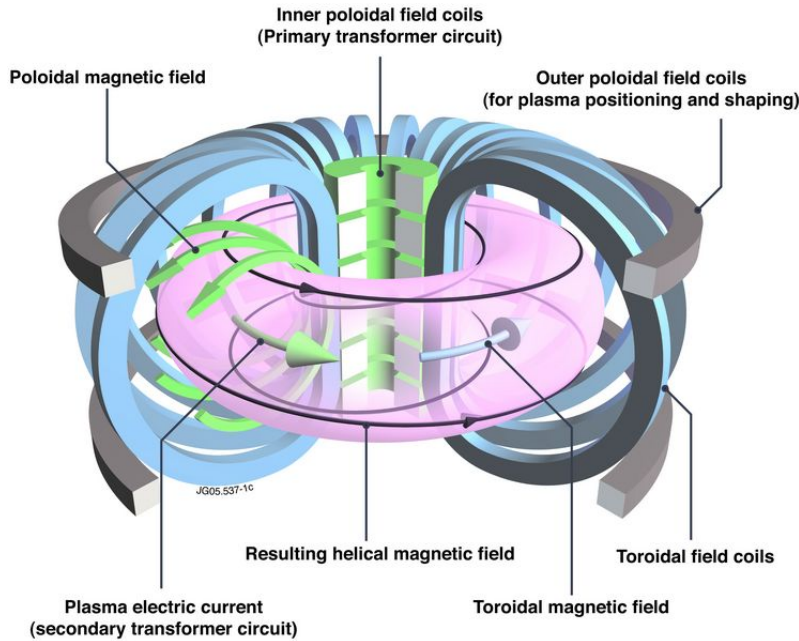


Figure 1.1. Illustration of the magnetic field and coil configurations of tokamaks: light blue - external toroidal field coils that generate toroidal magnetic fields along the torus; green - primary transformer circuit that drives a toroidal current in the plasma and eventually generates poloidal magnetic fields (green arrows); grey - additional poloidal field coils used for plasma positioning and shaping. Image from www.euro-fusion.org.

Inside the vacuum vessel (not shown in figure 1.1), the magnetic topology consists of nested flux surfaces (*closed magnetic surfaces*) and open ones, as illustrated in figure 1.2 (a poloidal cross section of the tokamak). Magnetic fields lie on these surfaces and wind helically around the plasma volume (figure 1.1). In a well-confined tokamak plasma, there is a radial distribution of the flux-surface-averaged plasma temperature and density across the flux surfaces, typically being warmer/denser towards the magnetic axis (marked in figure 1.2). The outer flux surfaces intersect the vacuum vessel, leading to localized heat loads on the vessel wall due to the free streaming of hot plasmas along the magnetic field lines.

To better control the heat and particle flows to the wall, a diverted plasma configuration has been proposed and applied in many present-day tokamaks. As shown in figure 1.2 (a), in this configuration, the magnetic field lines in the peripheral region of the plasma are controlled (by external coils) such that the magnetic field lines outside the *last closed flux surface* (LCFS) (or separatrix) are directed towards a target divertor region. The LCFS crosses an *X point*, representing a null of the poloidal magnetic field. Compared to the limited plasma configuration shown in figure 1.2 (b), where the LCFS is defined by the intersection of magnetic field lines with physical objects (limiters), the diverted configuration is more suitable for high performance plasma scenarios: it avoids the direct contacts between the plasma-facing components and the main confined plasma, and facilitates the pump-out of helium ash generated in D-T reactions and possible impurities in the plasma.

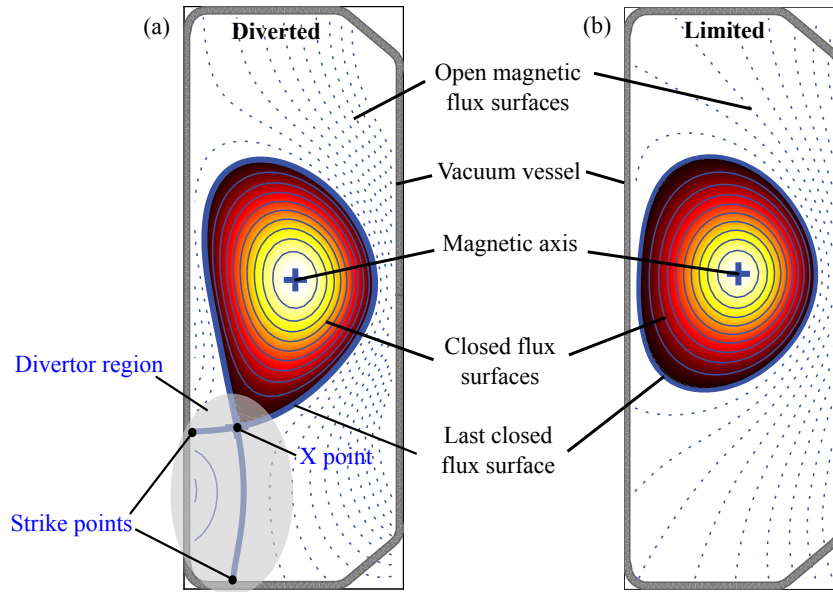


Figure 1.2. Illustration of the magnetic configurations inside the tokamak vacuum vessel: (a) diverted configuration and (b) limited configuration, with different components/regions marked in the plot. The examples are taken from the poloidal cross section of the TCV tokamak that will be introduced in chapter 2.

1.2.2 Auxiliary heating and current drive systems

Building a Sun on the Earth is not an easy task. As discussed along with the ignition condition, the temperature has to be high enough (~ 10 keV) to have self-sustainable fusion reactions. The ohmic heating from the plasma itself (through Coulomb collisions among the charged particles) can contribute to part of this energy; unfortunately, it becomes practically useless for temperatures above ~ 3 keV as the plasma resistivity decreases with increasing electron temperature - so does the ohmic heating power. Therefore, auxiliary heating systems have to be applied to heat the plasma beyond the a transition temperature ($5 \sim 7$ keV) when the α power from D-T reactions is high enough to sustain the reactions [Freidberg 2007]. Auxiliary current drive systems are also required to drive non-inductive currents that are essential for the steady-state operation of tokamaks, as discussed before. Since most of the methods used to heat a plasma can also drive current, the auxiliary heating and current drive systems will be discussed together.

Neutral beam injection (NBI)

The main candidate for heating up plasmas in large tokamaks is neutral beam injection (NBI). As indicated by its name, NBI injects high-energy beams of neutral deuterium or tritium atoms into the plasma. Being initially neutral, these beams are not affected by the electromagnetic fields and can penetrate deep into the plasma. Once ionized by collisions with the background plasma, the resulting high-speed charged particles are confined by the magnetic fields and

gradually transfer their energy to the background plasma through Coulomb collisions, i.e. heating up the plasma. The energy of the injected beam determines its penetration depth, therefore the requirement is higher for larger devices (to reach and heat the plasma core). In fact, to achieve the fusion goal in future larger tokamaks, the beam energy needs to be higher than 1 MeV. At this high energy, the conventional positive ion source that is used to generate the fast neutrals for NBI (through neutralization by electrons), is not effective any more. This is because the neutralization efficiency for positive ions drops dramatically with increasing ion energy and becomes negligible with energy above 100 keV. An innovative *negative ion source* concept has thus been proposed and is undergoing intensive research [Fantz et al. 2007; Toigo et al. 2017, and references therein]. Apart from heating, NBI can also drive current and injects momentum when injected tangentially to the torus. This momentum modifies the rotation of plasmas and affects their stability, for example as discussed in appendix B.

Heating and current drive by radio frequency (RF) waves

Another option for auxiliary heating and current drive is to use RF waves, where high-frequency electromagnetic waves from an external source are launched into the plasma. Strong absorption of wave energy happens when the applied wave frequency matches a resonant frequency of the plasma. Depending on its frequency, the applied wave can interact more effectively with the ions or electrons: ion cyclotron heating and current drive (ICH/ICCD) when the applied wave frequency matches the cyclotron frequency of ions (30 ~ 55 MHz in tokamaks); electron cyclotron heating and current drive (ECH/ECCD) when it matches the electron cyclotron frequency (100 ~ 170 GHz).

In terms of ICH/ICCD, the main advantage is that it directly interacts with the ions (e.g. deuterium and tritium nuclei), thus contributing more directly to fusion reactions; the main difficulty is that the low frequency wave cannot propagate in vacuum or low-density plasmas, so an antenna has to be placed very close to the plasma surface to ensure good coupling between the IC wave and the plasma [Koch 2006], which causes concerns about antenna arcing and plasma breakdown. For ECH/ECCD, the high frequency wave can propagate through vacuum, so its antenna can be placed further away from the plasma, unlike the other RF techniques; the beam is also well-focused, with higher power density than any other methods [Prater 2004]. Moreover, steering mirrors can be used to flexibly deposit EC beams at different locations inside the plasma; the interactions with electrons ensure that the power and current driven by EC beams are very localized. The narrow, localized and flexible feature of ECH/ECCD has enabled it to perform many unique tasks that are not addressable by other approaches, including the control of plasma instabilities that will be discussed in this thesis. It is worth mentioning that the application of ECH/ECCD was made possible by the development of its high-power and high-frequency power sources (*gyrotrons*). Active research is still ongoing in this respect to tackle more challenges in future long-pulse large devices [Prater 2004; Genoud et al. 2019, and references therein].

Another method that is mainly used for driving current is the lower hybrid current drive

(LHCD) system. It injects RF waves in the lower hybrid frequency range (about 5 GHz) and is suitable for driving a non-inductive current far off-axis [Liu et al. 2015]. LHCD has a higher current drive efficiency than other approaches and is a promising candidate for maintaining steady-state operation of tokamaks. Similar to ICH/ICCD, LHCD also requires an antenna placed close to the plasma, thus facing similar challenges.

1.2.3 MHD instabilities in tokamak plasmas

Apart from the desired magnetic coils and auxiliary heating and current drive systems, the stability of plasmas also needs to be ensured to obtain controllable fusion reactions. This is because small deviations of the plasma from a thermodynamic equilibrium state can provide a source of free energy that leads to instabilities under certain conditions. The strongest instabilities in tokamaks are those described by the magnetohydrodynamic (MHD) model of plasmas [Wesson 2004], i.e. the so-called MHD instabilities (modes).

The basic destabilizing mechanisms for MHD modes arise from the current and/or pressure gradients of plasmas. These macroscopic MHD modes can lead to large degradations of plasma confinement and performance, and under certain circumstances, lead to *disruptions*, where the plasma current drops to zero abruptly, causing large thermal and mechanical stresses on machine components. To achieve controllable fusion reactions in future fusion power plants, the underlying physics of the deleterious MHD modes needs to be well understood and the reliable real-time control of these modes needs to be ensured. In particular, the physics and control of neoclassical tearing modes (NTMs), one of the most dangerous modes encountered by high-performance tokamak plasmas, constitute the main subject of this thesis.

1.3 Motivation of the thesis

NTMs are magnetic islands located at rational $q = m/n$ surfaces, where m and n represent the poloidal and toroidal mode number, respectively, and q is the safety factor that indicates the degree the helicity of magnetic field lines. NTMs have been observed in many present-day tokamaks and proven to be the main constraint of the achievable β (ratio between plasma pressure and magnetic pressure) [Sauter et al. 1997; Maraschek 2012; Isayama et al. 2003; La Haye 2006, and references therein]. 2/1 NTMs, with a more outward location than other NTMs, are the most deleterious modes, causing more than 20% degradation of plasma confinement and capable of leading to disruptions [La Haye 2006; Sauter et al. 2010]. NTMs are predicted to occur in future high-performance tokamaks as well and the situation will be even more challenging: the higher β in future devices on one hand decreases the threshold of NTM onset and on the other hand increases its growth rate, i.e. plasmas will be more susceptible to NTMs and modes will grow more rapidly once they appear; the lower plasma rotation (e.g. due to larger inertia) in future large tokamaks, together with the faster mode growth, makes it easier to lock the mode and cause plasma disruptions. Therefore, it is crucial to understand the

physics of NTMs and ensure their reliable control.

As will be detailed in chapter 3, NTMs are metastable, i.e. they require the existence of a large enough seed island to grow. This provides the possibility of avoiding the occurrence of NTMs by controlling the occurrence/size of the seed island. Different mechanisms of seed island formation have been identified, for example from sawtooth crash, fishbone instabilities and edge-localized modes (ELMs) [La Haye and Sauter 1998; La Haye et al. 2000; Gude et al. 1999; Maraschek et al. 2005]. In particular, there is a special type where the seed island is provided by an unstable tearing mode (TM) that originates from unstable q profiles, i.e. with a positive stability index Δ' . This type of NTMs are typically summarized as “triggerless”, “seedless” or “spontaneous” NTMs [Reimerdes et al. 2002; Gerhardt et al. 2009; Ji et al. 2016; Fredrickson 2002]. Given their sensitivity to the current density and q profiles, triggerless NTMs have been observed in various plasma scenarios on different tokamaks [Reimerdes et al. 2002; Brennan et al. 2007; Gerhardt et al. 2009; Ji et al. 2016; Turco et al. 2018] and can occur in future devices as well. Despite the many observations of triggerless NTMs, physics studies are far from being adequate to quantify various contributions to the onset and growth of these modes. This is mainly hindered by the difficulty of obtaining reliable and consistent estimations of Δ' with realistic plasma equilibrium under a large variety of plasma conditions.

In the TCV tokamak (details in chapter 2), a highly reproducible plasma scenario with triggerless NTMs has been developed [Reimerdes et al. 2002; Felici 2011; Nowak et al. 2014; Kim 2015; Lazzaro et al. 2015], providing an excellent opportunity to study these modes. Instead of direct computations of Δ' (difficult to obtain reliably), a different approach, based on a combination of extensive experiments and interpretative simulations, has been utilized in this thesis (chapter 4) to study the underlying physics of triggerless NTMs systematically. This clarifies the complete evolution of a triggerless NTM, from its onset as a TM to its saturation as an NTM, explains several puzzling phenomena observed in TCV and leads to the development of a model for Δ' .

In terms of the control of NTMs, the well-localized and flexible EC system has proven effective in NTM stabilization and prevention on present-day tokamaks and will be used in future devices as well [Zohm et al. 1999, 2007; Nagasaki et al. 2005; La Haye et al. 2005; Prater et al. 2007; Felici et al. 2012; Kolen et al. 2014, and references therein]. These extensive theoretical, numerical and experimental studies worldwide have established the basics for the further study of NTMs, and especially, the modified Rutherford equation (MRE) [Rutherford 1973; Sauter et al. 1997; La Haye 2006] has proven to be a powerful tool in *interpreting* the evolution of NTM amplitude under varying plasma conditions. This background, together with the highly flexible EC system in TCV, provides a solid platform for a comprehensive experimental study of the dynamics of NTMs under varying EC conditions, e.g. different deposition locations, heating versus current drive, prevention versus stabilization, etc. More importantly, these experimental studies meanwhile provide valuable data sets to further validate the MRE and especially, to determine the range of free coefficients involved in the MRE, which is the main concern and a major step before applying the MRE in real-time *predictions*. These altogether

have motivated a detailed experimental and numerical study on the dynamics of NTMs under the effects of EC beams, as will be presented in chapter 5.

NTM control is not the only control task to be fulfilled: the normal operation of tokamaks requires the reliable control of many physics parameters, ranging from the control of plasma current, density and shape, to the control of MHD instabilities, q profiles and β . It is not rare that the same actuators are required to perform several control tasks simultaneously, leading to conflicting actuator requests. For example, the EC system can be required by both impurity accumulation control and q profile control during real-time operations. This is especially true for future long-pulse devices, where a large number of important control tasks need to be fulfilled simultaneously with only a limited set of actuators [Snipes et al. 2014; Humphreys et al. 2015]. Moreover, off-normal events such as NTMs and vertical displacements events, or faults such as power supply failures may occur [Eidietis et al. 2018; Blanken et al. 2019] and need to be properly handled in real-time. Therefore, an advanced plasma control system (PCS) is needed to be able to decide which plasma quantities to be controlled not only based on the pulse schedule, but also on real-time plasma and actuator states; it should also be able to take correct measures when unexpected events or faults happen. This has motivated the development of a new generic PCS framework in TCV with advanced monitoring, supervision and actuator allocation algorithms [Blanken et al. 2019; Vu et al. 2019], through a close teamwork. The new PCS has been successfully tested in real-time NTM control and/or integrated control experiments in TCV, as will be discussed in chapter 6.

Given the large number of real-time control tasks to be accomplished in future devices, it is advantageous to have more intelligent controllers that are aware of the resources they need to fulfill relevant control tasks, in *real-time*. In terms of the NTM controller, this means the EC power it requires to stabilize or prevent a given NTM. To the best of our knowledge, the requested EC power from present real-time NTM control algorithms is either pre-programmed (e.g. the maximum power of a given EC gyrotron), or based on the real-time responses of NTMs to EC beams (e.g. adding more power if the existing power is not sufficient to fully stabilize an NTM [Reich et al. 2014; Kong et al. 2017]). Although working well in present experiments, this inevitably causes delay in the control of NTMs, facing the risk of plasma disruptions, especially in future devices. Moreover, a better estimation of the required power contributes to a better allocation of the limited actuator resources in terms of integrated control. A faster and more accurate real-time (RT) estimation of the required EC power for NTM control is thus needed. The MRE, with well-defined coefficients determined by aforementioned interpretative simulations, is able to provide such information. A RT-capable MRE module has been developed for the first time, and tested by extensive offline simulations within the scope of this thesis. As will be discussed in chapter 6, the generic feature of the new PCS makes it convenient to include the new functionalities from the RT-MRE and experimental tests of the RT-MRE are foreseen.

1.4 Outline of the thesis

This chapter has introduced the basic concepts of fusion reactions, plasmas and magnetic confinement fusion, presented the configuration and various systems of tokamak devices, and discussed about the motivation of this thesis. The rest of the thesis is organized as follows:

- Chapter 2 will discuss about present and future tokamak devices worldwide, in particular, the TCV tokamak and ASDEX Upgrade (AUG) tokamak that are relevant to the studies in this thesis; ITER, a fusion test reactor under construction, and the tokamaks beyond it (e.g. demonstration power plants, *DEMO*) will also be introduced in view of future commercial fusion power plants
- Chapter 3 will introduce the fundamental physics of NTMs, discuss about their onset mechanisms and control strategies along with a brief review of the state-of-the-art of NTM studies, and present the MRE used in this thesis
- Chapter 4 will present the experimental and numerical studies of the triggerless onset of NTMs in TCV, especially the most dangerous 2/1 NTMs. An unexpected density dependence of mode onset observed in the experiments will be shown; the detailed development of a Δ' model, which proves to explain well the unexpected density dependence will be presented; interpretative simulations with the MRE that reproduce well the entire evolution of NTM island widths, along with the determination of several free coefficients of the MRE will be demonstrated
- Chapter 5 will focus on the dynamic evolution of NTM width under different EC settings, for example varying deposition location, power and different combinations of heating and current drive. The comparison between NTM stabilization and prevention, and the effects of the misalignment of EC beams with respect to the mode location on NTM evolution will be quantified. The good recovery of measured NTM island widths in a rather complex set of experiments by interpretative simulations, as well as the estimations of the range of coefficients in the MRE, especially those relevant to the heating and current drive effects from EC beams, will be presented
- Chapter 6 will discuss about recent progress on the RT control of NTMs and its integration with other control algorithms in TCV, along with presenting several examples of RT control experiments. The aforementioned new PCS structure and a generic NTM controller with standardized interfaces will be introduced. The detailed development of the versatile RT-capable MRE module will be presented; its various functionalities will be illustrated by examples of offline simulations based on both TCV and AUG discharges; the implementation of the RT-MRE in the PCS and its future application in the experiments will be discussed
- Chapter 7 summarizes the main results of the thesis and points out possible directions of further research

In addition to the main chapters, two appendices are included in the thesis. Appendix A presents a detailed sensitivity study of Δ' , through direct computations of Δ' (based on its definition, equation (A.1)) of various q profiles constructed by exerting different perturbations on an artificial parabolic q profile. This study highlights a dramatic change of Δ' with perturbations around the considered rational surface, and non-negligible global effects on Δ' . Appendix B represents an interesting direction of future research: it presents a set of dedicated NTM experiments with different amplitudes and directions of momentum injections from NBI, exhibiting evident “acceleration”, “deceleration” or “lock” of NTMs.

Part of the thesis has been presented in academic conferences and/or published in peer-reviewed journal papers. In particular, part of the results shown in chapter 4 and chapter 5 have been published in [Kong et al. 2020] and [Kong et al. 2019], respectively.

2 Present and future tokamak devices

2.1 Introduction

Tokamaks, currently regarded as the most promising candidate towards future fusion power plants, have been the main focus of fusion research for decades. Tokamaks of different sizes and specialties have been built or are being built worldwide, for example the Experimental Advanced Superconducting Tokamak (*EAST*) in China, Japan Torus-60 Super Advanced (*JT-60SA*) in Japan, Korea Superconducting Tokamak Advanced Research (*KSTAR*) in South Korea, *DIII-D* in the US, Joint European Torus (*JET*) in the UK, Axially Symmetric Divertor EXperiment Upgrade (*ASDEX Upgrade*) in Germany, Tokamak à Configuration Variable (*TCV*) in Switzerland and tungsten (with chemical symbol “W”) Environment in Steady-state Tokamak (*WEST*) in France.

Facing the ever-challenging scientific and technological problems to be solved, fusion research has been a joint international effort. One example of this is ITER (“the way” in Latin) [Shimada et al. 2007], the largest tokamak under construction in the world at the time of writing. China, the European Union, India, Japan, South Korea, Russia and the US, the seven ITER members, are now engaged in a 35-year collaboration to build and operate ITER.

In this chapter, the TCV tokamak, where most of the research in this thesis has been carried out, will be introduced in section 2.2. The ASDEX Upgrade (AUG) tokamak will be introduced in section 2.3, given the close collaborations with the AUG team [Meyer 2019] and studies on AUG within the scope of this thesis (e.g. chapter 6). In view of future fusion power plants, ITER and the tokamaks beyond it will be discussed in section 2.4.

2.2 The TCV tokamak

TCV [Hofmann et al. 1994], its first plasma shone in November 1992, is a medium-sized European tokamak located in Lausanne, Switzerland. As illustrated in figure 2.1, TCV is featured by its rectangular and highly elongated vacuum vessel and 16 independently-powered

Chapter 2. Present and future tokamak devices

poloidal magnetic field coils, rendering unique shaping capabilities. The vacuum vessel is made of stainless steel and 90% of the inner wall is covered by graphite tiles. The main heavy impurity in TCV is thus carbon, with respect to the main ion component (deuterium, hydrogen or helium). Some main parameters of TCV are summarized in table 2.1.

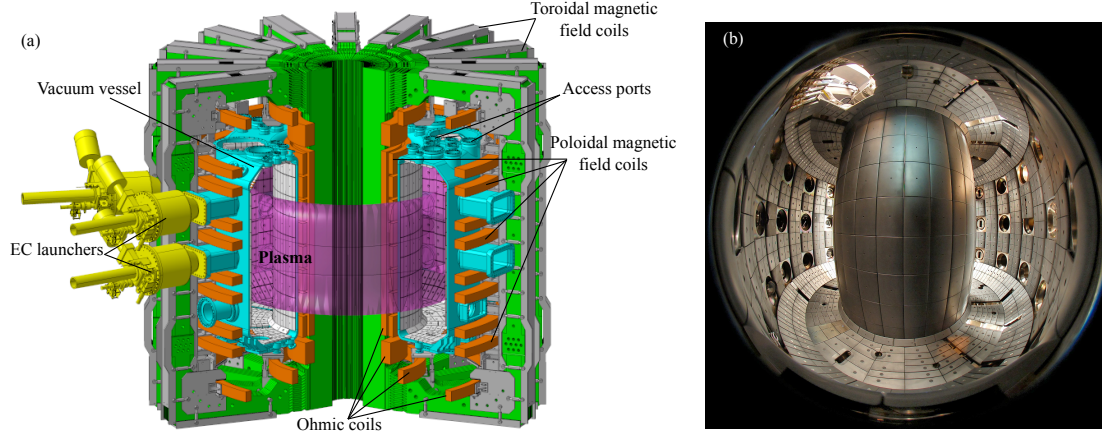


Figure 2.1. Illustration of the configurations of TCV. (a) A 3-D cutout view of TCV, showing the vacuum vessel, toroidal magnetic field coils, poloidal magnetic field coils and ohmic coils. The many access ports on the vessel enable flexible installation of various diagnostic systems and auxiliary heating and current drive systems (e.g. EC launchers). (b) The interior of TCV, covered by graphite tiles; the human access port for maintenance or upgrade is on the top left.

Table 2.1. Selected plasma and tokamak parameters of TCV

Major radius R	0.88 m
Minor radius a	0.25 m
Aspect ratio R/a	3.5
Plasma elongation κ	0.9 ~ 2.8
Plasma triangularity δ	-0.8 ~ +0.9
Maximum plasma current I_p	1.2 MA
Maximum toroidal magnetic field	1.54 T
Maximum discharge duration	2.6 s in ohmic, 4 s with ECCD
Core electron density n_e	$10^{19} \sim 20 \times 10^{19} \text{ m}^{-3}$
Core electron temperature T_e	$\leq 1 \text{ keV}$ (ohmic); $\leq 15 \text{ keV}$ (ECH);
Core ion temperature T_i	$\leq 2.5 \text{ keV}$ (NBI)
Height of vacuum vessel	1.54 m
Width of vacuum vessel	0.56 m

The direction of the toroidal magnetic field and plasma current in TCV (i.e. clockwise or counter-clockwise) can be chosen at will in any discharge [Coda et al. 2019]. Thanks to its highly flexible auxiliary heating and current drive systems, advanced real-time (RT) control systems and versatile diagnostic systems, a broad range of research is being carried out on TCV, for example disruption avoidance, runaway electrons, scenario development, control of MHD modes, negative triangularity plasmas, and so on [Coda et al. 2019]. The auxiliary

heating and current drive systems, diagnostics and RT control systems that are relevant to this thesis will be presented in the following sections.

2.2.1 Auxiliary heating and current drive systems

TCV is equipped with two different types of auxiliary heating and current drive systems at the time of writing: the electron cyclotron heating and current drive (ECH/ECCD) system since 1999 [Goodman 2008] and the neutral beam injection (NBI) system since 2015 [Karpushov et al. 2017; Vallar et al. 2019].

ECH/ECCD

The ECH/ECCD system consists of 6 second-harmonic X-mode (X2) gyrotrons (i.e. high-power microwave sources) and 3 third-harmonic (X3) gyrotrons, with the wave frequency of 82.7 GHz and 118 GHz, respectively. Each EC gyrotron has its own *transmission line* (wave guide) that transmits the microwave power to TCV; a *launcher* with steering mirrors is used at the end of the transmission line to deposit EC beams at the specified location of the plasma.

There are six X2 launchers in TCV, among which two launchers (labeled as $L1$ and $L4$) are located at the equatorial level of TCV while the other four launchers ($L2$, $L3$, $L5$ and $L6$) are at an upper level, as illustrated in figure 2.2. The injection direction of each EC ray is described in a spherical “launcher” coordinate shown in figure 2.3: θ_L is the angle of the EC ray leaving the last mirror (leftmost mirror in the figure, closest to the plasma) with respect to the axis of the launcher, while ϕ_L is on a plane that is perpendicular to the launcher axis, with $\phi_L = 0$ and $\theta_L > 0$ corresponding to a downward pointing EC ray. Each X2 launcher has 4 mirrors that can be rotated (in ϕ_L) before a discharge to provide different toroidal coverage ($-180^\circ \leq \phi_L \leq 180^\circ$); the last mirror directs the beam in an angle that provides poloidal coverage ($8^\circ \leq \theta_L \leq 50^\circ$). θ_L can be varied during a discharge to obtain varying EC deposition locations, making these X2 launchers suitable for controlling various MHD instabilities such as sawteeth and neoclassical tearing modes (NTMs).

The six X2 gyrotrons are grouped into two clusters of three gyrotrons each: cluster A (gyrotrons #1–3, corresponding to launchers #1–3) and cluster B (gyrotrons #4–6). Gyrotrons in the same cluster share a common power supply and have the same nominal output power: 0.75 MW each for cluster A and 0.5 MW each for cluster B. Individual gyrotrons that are not required by a given discharge can be deselected or fired into a dummy load. Most of the experiments presented in this thesis were carried out with 0.75 MW from cluster A ($L1$) and/or 1 MW from cluster B ($L4$ and $L6$, 0.5 MW each). At the time of writing, TCV is in the process of upgrading the gyrotrons: several gyrotrons that have reached the end of their technical life span have been removed while four additional gyrotrons will be installed, including two 0.75 MW units for X2 waves and two 0.75 MW dual-frequency units for either X2 or X3 [Alberti et al. 2017; Coda et al. 2019]. It is expected that up to 3.3 MW X2 and 3.1 MW X3 will be available in TCV

after the upgrade.

The 118 GHz X3 gyrotrons [Alberti et al. 2005] are used to heat plasmas with electron densities higher than the cutoff density of X2 waves ($4.2 \times 10^{19} \text{ m}^{-3}$), accessing densities up to $11.5 \times 10^{19} \text{ m}^{-3}$. X3 waves from different gyrotrons, transmitted through independent transmission lines, are injected into the plasma with a unique X3 launcher on the top of TCV (figure 2.2). It has a single mirror that injects X3 beams vertically into the plasma, increasing the path length through the plasma and thus the total absorbed power. The poloidal angle of the mirror, similar to X2 launchers, can be controlled in RT.

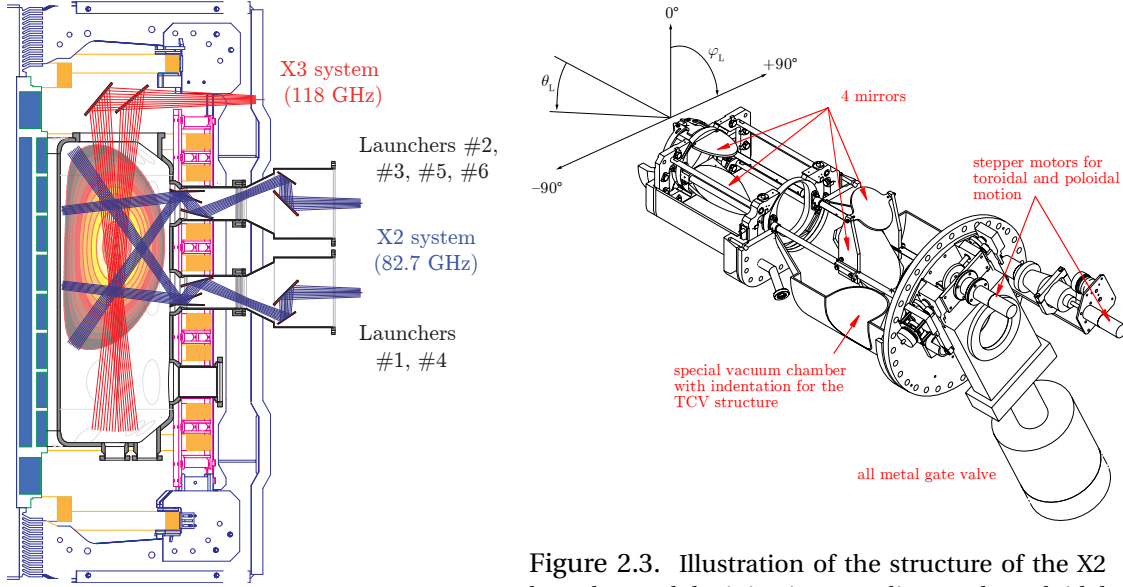


Figure 2.2. A poloidal view of TCV, showing the layout of X2 and X3 launchers.

Figure 2.3. Illustration of the structure of the X2 launcher and the injection coordinate. The poloidal angle (θ_L) of the last mirror (closest to the plasma, left-most) is steerable in RT.

NBI

A 15 ~ 25 keV NBI with maximum 1 MW power (at the highest energy) was installed in TCV at 2015 and has been under routine operations since early 2016. The NBI is placed in a tangential direction with respect to the torus axis, allowing a double pass through the plasma cross section [Karpushov et al. 2017; Vallar et al. 2019] and modifying plasma rotations. The NBI has expanded the attainable plasma regimes in TCV: higher plasma pressure, a wider range of T_i/T_e and significant fast ion populations. $T_i \approx 2 \text{ keV}$ and a toroidal rotation velocity of 160 km/s were promptly obtained in the first few *L*-mode discharges after its installation [Karpushov et al. 2017].

In 2017, the local control system of NBI was upgraded to allow the RT control of NBI power [Karpushov et al. 2017]. This has extended the RT capabilities of TCV, for example making NBI as one of the RT actuators for the RT control of plasma β and/or its integration with other control tasks [Karpushov et al. 2017; Vu et al. 2019]. Moreover, the large momentum injected

by NBI can strongly affect the dynamics of NTMs, causing a clear acceleration or deceleration of NTMs depending on the relative direction of NBI beams with respect to mode rotation, as discussed in appendix B. A second NBI system with 50 ~ 60 keV ion source and a maximum power of 1 MW is currently being planned for 2020, to extend the plasma regimes in TCV even further [Fasoli et al. 2020]. The new NBI will be directed in the opposite direction with respect to the existing NBI, enlarging the reachable range of rotation profiles in TCV.

2.2.2 Main diagnostics

Magnetic measurements

The extreme flexibility of plasma shapes in TCV requires magnetic sensors with high precision and good spatial coverage. The magnetic diagnostic system in TCV mainly consists of poloidal flux loops, magnetic probes and saddle flux loops [Moret et al. 1998; Piras et al. 2010], which gives information about the poloidal magnetic flux (and its derivatives), component of the poloidal magnetic field tangential to the vacuum vessel and radial magnetic field, respectively. These measurements are not only important for the RT control of plasmas, but also for the offline reconstructions of the magnetic topology.

Locations of the main magnetic sensors in TCV are illustrated in figure 2.4. 61 flux loops (red crosses) are placed either right outside the vacuum vessel (38 out of 61) or close to the coils. The magnetic probes (blue bars) are placed inside the vessel, located on 16 evenly distributed toroidal sectors, among which 4 sectors (separated by 90°) have a full poloidal array of 38 probes each [Moret et al. 1998, 2015]. The magnetic probes have an acquisition frequency up to 500 kHz, and the signals from two opposite toroidal sections are used for equilibrium reconstructions. Magnetic analyses of the acquired probe data can provide the mode number, amplitude and frequency of NTMs [Schittenhelm and Zohm 1997; Reimerdes 2001] that are useful for interpreting their dynamics, while RT singular value decomposition (SVD)-based analyses [Galperti et al. 2014, 2017] are able to obtain RT mode information that is essential for RT NTM control. The magnetic probes have thus been used as one of the main diagnostics in this thesis.

There are 24 saddle flux loops in TCV, consisting of 3 toroidal arrays (at the *top*, *middle* and *bottom*, respectively) of 8 saddle loops each. The vertical extension of each toroidal array is indicated by the magenta circles in figure 2.4. Each saddle loop covers a toroidal angle of 45°, so each toroidal array (with 8 saddle loops) covers the entire circumference of the vacuum vessel. Measuring the time-derivative of the radial magnetic flux, the saddle loops can be used to estimate the non-axisymmetric error fields in TCV [Piras et al. 2010] or detect a locked mode [Sheikh et al. 2018].

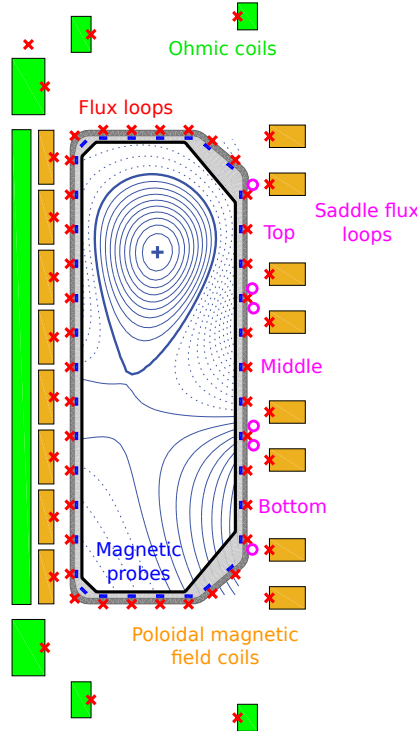


Figure 2.4. A poloidal cross section of TCV showing the location of the flux loops (red crosses) and magnetic probes (blue bars). The layout of the ohmic coils and poloidal field coils are also shown, in accordance with figure 2.1. The plasma shown is in a so-called *snowflake divertor* configuration [Labit et al. 2017], taken from TCV #48133 at $t = 0.8$ s.

Thomson scattering (TS)

TS is an essential diagnostic system in TCV, which measures incoherent scattering from electrons and gives information about the spatial profiles of n_e and T_e . The profiles are measured by a vertical laser beam passing through the plasma at $R = 0.9$ m. The scattered light from the observation volumes in the plasma are collected and focused onto sets of fiber bundles by wide-angle camera lenses installed on 3 horizontal ports of TCV, as illustrated in figure 2.5.

With its first version installed on TCV in 1991, the TCV TS system has been upgraded along the way. In particular, 40 compact 5-channel spectrometers with a new optical design were newly installed in 2017 [Hawke et al. 2017]. This upgrade substantially improved the spatial resolution of TS to approximately 1% of the minor radius of TCV, i.e. 2.5 mm; it also enhanced the spectral resolution at low T_e , e.g. at the plasma edge. A comparison of the view chords of the TS before and after this upgrade is depicted in figure 2.5 ((a) versus (b)).

More recently (in 2019), further upgrades of the TS system have been performed, among which additional 20 spectrometers have been installed to allow diagnosing the plasma in the relatively cold divertor region [Blanchard 2019], as shown in figure 2.5 (c). This is in line with

the recent upgrade of TCV divertor itself: in-vessel structures (*baffles*, cyan blocks in figure 2.5 (c)) have been installed to form a divertor chamber of variable closure [Reimerdes et al. 2017; Coda et al. 2019; Fasoli et al. 2020]. The new TS system allows measurements of T_e as low as 1.4 eV and n_e as low as $2 \times 10^{18} \text{ m}^{-3}$. Moreover, the connection of the TS system to the digital RT control system of TCV is ongoing, aiming at providing RT n_e and T_e profiles at a sampling rate up to 60 Hz [Arnichand et al. 2019]. This will complement the RT information obtained from a far infrared interferometer and soft X-ray diagnostics that will be introduced below.

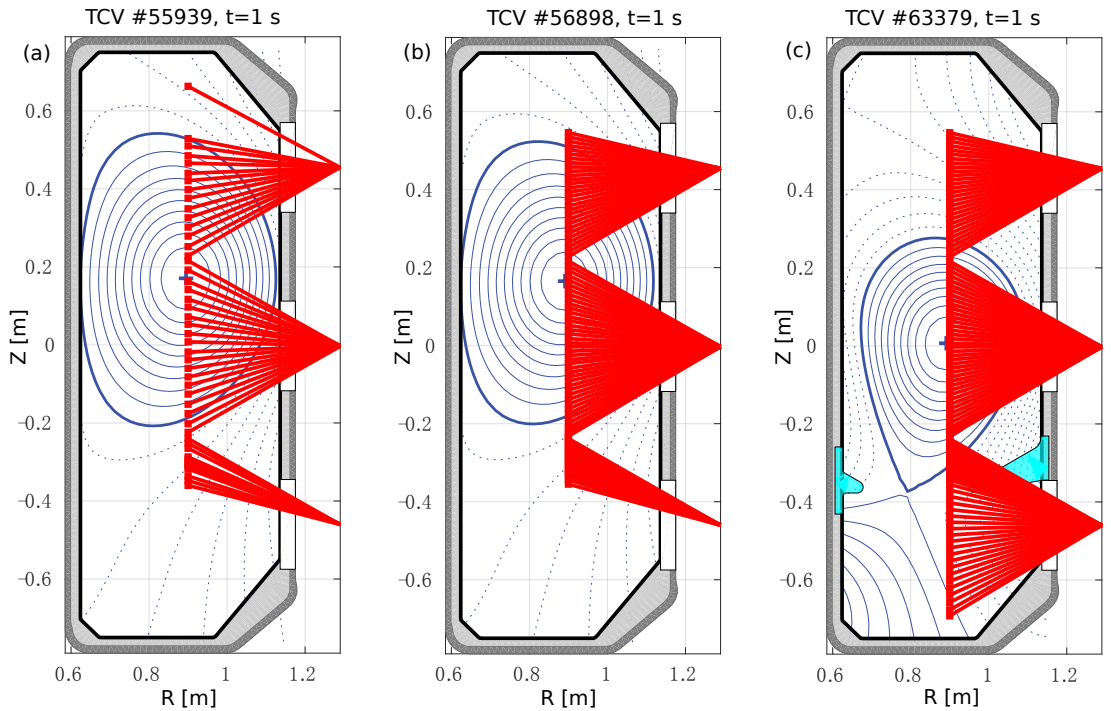


Figure 2.5. Comparison of the viewing chords of the TCV TS system (a) before the upgrade in 2017; (b) after the upgrade in 2017, with 40 compact 5-channel spectrometers installed; and (c) after the upgrade in 2019, with another 20 spectrometers installed near the divertor region of TCV (cyan: baffles).

Far infrared (FIR) interferometer

TCV is equipped with a 14-channel Mach-Zehnder type interferometer to measure the line-integrated density along 14 parallel vertical chords [Barry 1999]. The system consists of a continuous-wave FIR laser (wavelength $\lambda = 184.3 \mu\text{m}$) and a detector unit, with an acquisition frequency up to 20 kHz. FIR is fully automated and is a mandatory diagnostic essential for every TCV discharge. The measurement along the central chord passing through the plasma center is used for the RT control of plasma density, with gas valves as the actuators.

Soft X-ray (SXR) measurements

Measurements of the radiation emitted from the plasma provide information about n_e , T_e , the degree of impurities in the plasma as well as fluctuations of these quantities. Radiation emissions from a plasma mainly stem from Bremsstrahlung (from electron-ion Coulomb collisions), recombination radiation (free electrons captured by ions) and line radiation (transition of an electron from an excited bound state of energy to a bound state with lower energy). Emissions from the thermal range of electrons in typical TCV plasmas, i.e. in the keV photon energy range, fall into the SXR category. Several SXR diagnostics have been installed on TCV, as briefly introduced below.

A soft x-ray tomography (XTOMO) system, with 200 viewing chords from 10 cameras have been installed on TCV since its operation [Anton et al. 1996]. It mainly measures the Bremsstrahlung with energy higher than 1 keV and gives information about the line integrated radiation emission in the SXR energy spectrum. The XTOMO has an acquisition frequency up to 100 kHz, allowing detecting transient phenomena caused by MHD activities (e.g. sawteeth and NTMs). This diagnostic has been connected to the digital RT control system of TCV, as will be discussed in section 2.2.3.

As a complement to XTOMO, a duplex multiwire proportional x-ray (DMPX) detector has been installed on TCV [Sushkov et al. 2008]. It comprises 64 vertically viewing channels and has an acquisition frequency up to 200 kHz, improving the spatial and temporal resolution of SXR measurements in TCV. DMPX detects SXR emissions of 3 ~ 30 keV and has a radial resolution of about 5 mm. It is suitable to detect fast and localized phenomena such as MHD activities and can also be used as an improved measurement of the deposition profiles of EC beams. DMPX has been connected to the digital RT control system of TCV as well and applied to determine sawtooth period, infer T_e profiles, etc. [Felici 2011].

In addition, a multi-foil X-ray temperature diagnostic (XTe) based on the foil-absorption techniques [Donaldson 1978] has been installed on TCV, aiming at measuring central T_e (i.e. near the plasma center) with rather high temporal resolution (10 kHz). It is a single-chord measurement with 4 different detectors (absorbers), the ratio between which gives information about the central temperature. XTe has been included in the digital RT control system in TCV, estimating the central T_e in RT [Felici 2011].

Charge exchange recombination spectroscopy (CXRS)

The CXRS system in TCV provides local measurements of ion temperature, impurity (fully ionized carbon in TCV) density and rotation velocity, based on the active charge exchange (CX) reaction between the impurity ion (C^{6+}) and a high energy neutral hydrogen atom (H or D in TCV) from a diagnostic neutral beam injection (DNBI) system. The CX reaction transfers a bound electron from the neutral hydrogen atom to the target ion. The electron after the CX reaction has a finite probability of occupying an excited state in the target ion and de-

excites to the ground energy level through a cascade of radiative transitions before re-ionizing, given that the radiative de-excitation timescale (a few ns) is much faster than the ionization timescale (ms) for typical tokamak plasmas [Marini 2017]. The resulting line radiations range from visible light to X-ray, where the former is of particular interest for CXRS. Analyses of the spectral moments of a single emission line provide information about impurity density (from the zeroth moment, spectrum integral), rotation velocity (the first moment, spectrum centroid position) and impurity temperature (the second moment, spectrum width).

The CXRS diagnostic in TCV mainly consists of three optical observation systems: a low field side (LFS, i.e. on the outer ring of the tokamak torus) toroidal view system, a high field side (HFS) toroidal view system and a vertical view system. The unique DNBI used in TCV (with a total delivered power less than 80 kW), in contrast to the conventional practice of directly using the powerful NBI system (≥ 1 MW), dramatically decreases the perturbations to the plasma [Marini 2017]. This allows measuring kinetic ion parameters including the intrinsic rotation of the plasma, i.e. rotation that develops spontaneously without any external momentum injection [Bortolon et al. 2006]. The CXRS has an acquisition frequency of 10 ~ 500 Hz. It has been utilized to investigate the rotation profiles before NTM onset (chapter 4) and the influence of NBI on NTM dynamics (appendix B) in this thesis.

2.2.3 Real-time control systems

Currently, there are two RT control systems on TCV: a historical *hybrid control system* [Lister et al. 1997] built at the time of the first operations of TCV, and a new distributed digital control system (SCD, acronym of the *Système de Contrôle Distribué* in French) installed more recently [Paley et al. 2010; Le et al. 2014; Galperti et al. 2017].

The hybrid control system

The hybrid control system, as indicated by its name, is a combination of analogue and digital processes: it uses a set of analog matrix multipliers, whose coefficients are digitally programmable and can be switched during a TCV discharge at pre-specified time points. The hybrid control system has proven to be very reliable during almost 30 years of TCV operation and has been used to control plasma current, density, shape and position of TCV plasmas, using signals from the magnetic measurements and FIR interferometer as inputs. However, the hybrid control system is not compatible with the increasing requirement on the RT control system of tokamaks, given the limitations of its capabilities. For instance, more advanced control schemes such as the RT control of NTMs and the RT tailoring of magnetic and kinetic profiles require high-speed nonlinear computations, whereas the hybrid control system cannot perform any nonlinear operations; the inclusion of new control schemes meanwhile suggests an expansion of RT diagnostics and actuators (e.g. EC systems, NBI and gas valves) needed, which cannot be fulfilled by the hybrid control system given its limited number of input and output channels. Therefore, the SCD has been built on TCV and is expected to

entirely replace the hybrid control system in the future.

The SCD

Since its first development in 2008 [Paley et al. 2010], the SCD on TCV has been under continuous upgrades and is currently a fully functional RT control system capable of controlling almost all the plasma actuators, with the only exception of the fast power supplies of the internal coils at the time of writing. As indicated by its name, SCD is a distributed RT acquisition and processing system, consisting of seven modular computer nodes at present. The modular computer nodes are built on top of standard Linux PCs that may include local ADC and/or DAC cards, and they communicate with each other via a reflective memory (RFM) network, an industry-standard high-speed digital communication system that automatically synchronizes a shared memory [Galperti et al. 2017].

Different nodes can run with different cycle times, varying between $100\mu\text{s}$ and 100ms . More than 200 diagnostic channels (e.g. more than 100 magnetic measurements, 64 DMPX channels, 14 FIR channels, etc.) have been connected to SCD and it remains flexible to add more channels (e.g. RT TS in the near future). A large number of actuators of different types have been connected to the SCD as well: the 16 poloidal magnetic field coils for plasma shape and position control, the EC systems for controlling MHD instabilities (sawteeth, NTMs, etc.) and current density profiles, the NBI system for β control and the gas valves for RT density control, impurity seeding and disruption mitigation, etc. New actuators, when available, can be conveniently added.

The computer nodes with ADCs and/or DACs are interfaced with TCV's diagnostic and actuator systems [Galperti et al. 2017]. At the time of writing, *node 1* is interfaced with 64 DMPX, 4 XTe and 14 FIR channels, as well as 14 EC signals and 1 gas value command. *Node 2* acquires all magnetic data and is responsible for plasma shape and position control; it also acquires data from the central FIR channel for the RT control of plasma density. *Node 3* is a computational node that accommodates the RT version of the Grad-Shafranov equilibrium reconstruction code LIUQE (i.e. RT-LIUQE) [Moret et al. 2015]. *Node 4* is a backup node for node 2, while *node 5* is connected to the 200-channel XTOMO system in TCV. *Node 6* is a powerful multi-core computational node used to run complex control codes, e.g. a faster replica of RT-LIUQE, and advanced plasma performances controllers based on a rapid plasma transport simulator (RAPTOR) [Felici et al. 2011]. *Node 7* is devoted to RT analyses of fast magnetic perturbations [Galperti et al. 2017], providing RT information about the likelihood, amplitude and frequency of NTMs that is important for the RT control of NTMs. The advanced RT NTM and/or integrated control experiments presented in this thesis (chapter 6) have been carried out with this new SCD.

2.3 The ASDEX Upgrade tokamak

ASDEX Upgrade (AUG) is a medium-sized tokamak located in Garching, Germany. With its first plasma in 1991, AUG was built based on the original ASDEX tokamak that was in operation from 1980 to 1990. AUG has a D-shaped cross section and is featured by its full metal (mainly tungsten) wall, which is a key asset for extrapolating to future fusion devices as tungsten is currently regarded as the most viable material for the plasma facing component in a future fusion reactor [Neu et al. 2007; Meyer 2019]. A selected list of the main parameters of AUG is shown in table 2.2.

Table 2.2. Selected plasma and tokamak parameters of AUG

Major radius R	1.65 m
Minor radius a	0.5 m
Aspect ratio R/a	3.3
Plasma elongation κ	≤ 1.8
Plasma triangularity δ	≤ 0.5
Maximum plasma current I_p	1.4 MA
Maximum toroidal magnetic field	3.2 T
Maximum discharge duration	10 s
Plasma types	deuterium, hydrogen, helium

AUG has 16 toroidal magnetic field coils around the torus to generate the required toroidal magnetic field and 12 poloidal field coils that are controlled in RT for plasma shaping and positioning, similar to TCV. In addition, AUG has 16 in-vessel 3-D perturbation coils that can be used to control edge-localized modes (ELMs). The power supplies of these perturbation coils have been recently upgraded [Teschke et al. 2017], giving more flexibility to the system.

In terms of auxiliary heating and current drive, AUG is equipped with three different types of systems: NBI, ICH/ICCD and ECH/ECCD [Meyer 2019]. The NBI system on AUG consists of two injectors, with four ion sources each, injecting a total power of 20 MW [Den Harder et al. 2017; Hopf et al. 2017]; the ICH/ICCD system comprises four wave generators, a complex transmission and matching system and four antennas, delivering a power up to 7.2 MW [Faugel et al. 2005, 2014]; the ECH/ECCD system of AUG has been recently upgraded and currently conveys a total power of 6 MW at 140 GHz or 4.8 MW at 105 GHz [Wagner et al. 2017; Meyer 2019].

AUG is a well-diagnosed tokamak equipped with a large variety of diagnostic systems, e.g. magnetic measurements, Thomson scattering, soft X-ray measurements, charge exchange recombination spectroscopy, etc. In particular, AUG is equipped with a motional stark effect (MSE) diagnostic [Ford et al. 2015] that is able to measure the internal local poloidal magnetic field, contributing to the determination of the current density profiles inside the plasma. In view of the study on NTMs, a 60-channel electron cyclotron emission (ECE) diagnostic on AUG [Rathgeber et al. 2013; Denk et al. 2018] has been routinely used as a complement to the magnetic measurements, estimating the radial location and amplitude of NTMs [Reich et al.

2012; Rapson et al. 2017b]. The ECE diagnostic measures local T_e fluctuations caused by the rotating NTMs, the amplitude and phase profile of which reveal the width and location of NTMs [Meskat et al. 2001; Park and Welander 2006].

To perform the sophisticated experiments on AUG, a reliable discharge control system (DCS) has been built. DCS is an entirely digital control system, consisting of RT diagnostic integration, advanced feedback control schemes, actuator management, monitoring and pulse supervision [Treutterer et al. 2014]. Based on a modular software framework architecture, DCS supports distributed computing and allows multi-directional signal transfer and synchronization via a shared memory. Signals from more than twenty diagnostic systems with hundreds of channels have been connected to the DCS, for example the magnetic measurements and the ECE diagnostic. Various actuators have been connected to the DCS as well: 10 independently controllable magnetic coil circuits, 8 NBI boxes with different injection angles, 8 EC systems, 2 IC antennae, 5 gas valves, a pellet injector and a massive gas injection valve for disruption mitigation [Treutterer et al. 2014]. With the DCS, RT NTM control and integrated control experiments have been carried out on AUG [Rapson et al. 2014, 2017a,b].

2.4 ITER and beyond

2.4.1 ITER

ITER is a collaborative international effort towards the realization of controllable fusion energy on the Earth. It is currently under construction in Saint Paul-lez-Durance, southern France and is expected to obtain the first plasma at the end of 2025. ITER is an essential step on the path towards commercial fusion-based electricity, serving as an advanced integrated test of various material, technology and physics aspects. ITER is expected to produce 500 MW fusion power and reach $Q = 10$ for 300 ~ 500 s in the standard scenario [Shimada et al. 2007], where Q is the ratio of fusion power to the total external heating power. The world record of fusion power is currently held by JET: 16 MW fusion power was achieved with a total input heating power of 24 MW (i.e. $Q = 0.67$) in 1997 [Keilhacker et al. 1999].

ITER will also be a testbed for tritium breeding, i.e. to demonstrate the feasibility of generating tritium within a breeding blanket of the vacuum vessel. This is because the world supply of tritium, one of the main fuels for D-T reactions, is not sufficient for operating future fusion power plants [Kovari et al. 2018; Pearson et al. 2018].

ITER will be equipped with three different types of auxiliary heating and current drive systems to provide the 50 MW power required to bring the plasma to a temperature sufficient for abundant D-T reactions: NBI, ICH/ICCD and ECH/ECCD. The self-heating from fusion-generated α particles, as discussed in chapter 1, is then expected to sustain the plasma in the burning regime. Two NBI injectors with 1 MeV deuterium ion sources will be used, injecting a power of 16.5 MW each [Hemsworth et al. 2008]; the ICH/ICCD system, with a frequency of 40 ~ 55 MHz, is expected to deliver a total power of 40 MW into the plasma [Wilson and Bonoli

2015]; the ECH/ECCD system, with 24 gyrotrons and 12 high voltage power supplies, will convey a total power of 20 MW at 170 GHz into the plasma [Omori et al. 2015; Takahashi et al. 2015, and references therein], and can be used to control MHD instabilities such as NTMs.

2.4.2 Beyond ITER

ITER, an experimental reactor by design, is not the final step before commercial fusion-based power plants. With the knowledge and experience gained from building and operating ITER, demonstration power plants (DEMO) will be built independently, producing large amounts of fusion power in long-pulse or steady-state and working as the last step before commercial fusion power plants [Ward 2010].

The road map to fusion power plants after ITER differs worldwide. In Europe, DEMO is considered to be the nearest-term reactor design to follow ITER, whose objectives are expected to be realized by the middle of the 21st century [Federici et al. 2018]. Extensive research is being carried out concerning the design of various components of the EU-DEMO [Poli et al. 2012; Federici et al. 2018; Siccino et al. 2019, and references therein]. In China, the Chinese fusion engineering testing reactor (CFETR) is designed to bridge the gap between ITER and a DEMO, and eventually a fusion power plant [Wan et al. 2017; Zhuang et al. 2019]. CFETR will be operated in two phases: phase I focuses on steady-state operation and tritium self-sufficiency, with a fusion power up to 200 MW and Q up to 5; phase II emphasizes DEMO validation, aiming at 1 GW fusion power and $Q > 10$ [Wan et al. 2017].

Fusion energy, at the start of the exponential growth phase, may come late compared with the current development of wind power, solar photovoltaics, etc., however, its unparalleled advantages such as high energy density and low territory occupation make it a promising energy source in the long run [Lopes Cardozo et al. 2016]. It will be thrilling to see a Sun on the Earth.

3 Neoclassical tearing modes (NTMs)

3.1 Introduction

Neoclassical tearing modes (NTMs), located at rational $q = m/n$ surfaces, are one class of resistive magnetohydrodynamics (MHD) instabilities in tokamak plasmas. NTMs have been observed in various present-day tokamaks and typically lead to a lower achievable β (ratio between plasma pressure and magnetic pressure) than the predictions by ideal MHD [Sauter et al. 1997; La Haye 2006], which assumes perfectly conducting plasmas and predicts a maximum achievable $\beta = 4l_i I / aB_\phi$ [Troyon et al. 1984; Strait 1994, and references therein], where I is the plasma current in megamperes, a the minor radius of the plasma in meters, B_ϕ the toroidal magnetic field in tesla and l_i the internal inductance. This is because at rational q surfaces, ideal MHD breaks down and extra physics such as plasma resistivity needs to be considered, allowing local magnetic reconnection and the generation of resistive tearing modes. Compared to conventional tearing modes (TMs) that are linearly unstable, NTMs are linearly stable and their evolution is dominated by the effects of a helically perturbed bootstrap current (thus neoclassical), as illustrated in figure 3.1.

The equilibrium magnetic field \mathbf{B} near the $q = m/n$ rational surface is approximated by $\mathbf{B} = \mathbf{B}_s + \mathbf{B}^*$, where \mathbf{B}_s is the magnetic field at the $q = m/n$ surface and \mathbf{B}^* the helical component of \mathbf{B} in the direction of $\zeta = \theta - n\phi/m$ (perpendicular to \mathbf{B}_s), with θ and ϕ the poloidal and toroidal coordinate, respectively. The amplitude of \mathbf{B}^* has the form of

$$B^* = B_\theta \left(1 - \frac{q}{q_s}\right) \approx -\frac{q'_s}{q_s} (\rho - \rho_s) B_\theta, \quad (3.1)$$

where ρ here represents the radial coordinate related to the square root of the toroidal flux, i.e. $\rho = \sqrt{\Phi/\Phi_b}$, with Φ the toroidal flux contained by a given flux surface and Φ_b the value at the plasma boundary; ρ_s is the radial location of the $q = m/n$ surface and B_θ the poloidal magnetic field. q_s is the q value at $\rho = \rho_s$, i.e. $q_s = m/n$ and “ $'$ ” here refers to radial derivative with respect to ρ . With a small radial perturbation $\delta B_\rho(\rho) \sin \zeta$, the initially straight \mathbf{B}^* lines (denoted by the straight arrows in figure 3.1) are deformed and magnetic islands are generated,

Chapter 3. Neoclassical tearing modes (NTMs)

with O-points and X-points as marked. Given the large parallel (with respect to the magnetic field lines) thermal conductivity, the radial heat transport is locally enhanced, causing a flattening of the temperature and thus pressure profiles in the island region. The bootstrap current, which is proportional to the pressure gradients, thus locally decreases and generates a negatively perturbed bootstrap current δj_{bs} that is in the opposite direction to the equilibrium parallel current density j_{\parallel} , as shown in figure 3.1. In conventional tokamaks with $dq/d\rho > 0$, this δj_{bs} tends to reinforce the perturbed magnetic field and increase the width of the magnetic island (i.e. destabilizing for NTMs).

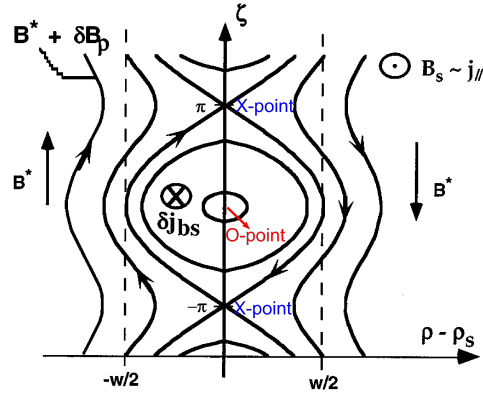


Figure 3.1. Adapted from [Sauter et al. 1997]. Illustration of the formation of magnetic island structure: a small radial perturbation δB_{ρ} added to the helical (ζ) component of the equilibrium magnetic field B^* deforms the magnetic field lines and leads to the formation of magnetic island. The fast radial transport in the island region causes a flattening of the temperature and pressure profiles across the island, resulting in a local perturbation to the bootstrap current δj_{bs} , which in turn reinforces the perturbed magnetic field and increases the size of the magnetic island.

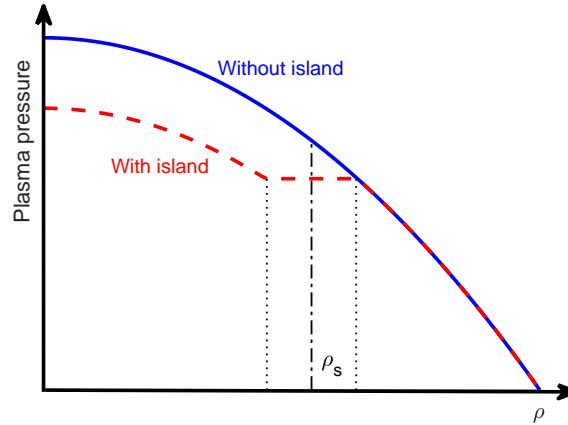


Figure 3.2. Illustration of the confinement degradation caused by NTMs: the existence of an NTM causes an local flattening of the pressure profile and a degradation of the achievable β , based on the belt model [Chang and Callen 1990].

The flattening of the pressure profile meanwhile degrades the stored energy, as illustrated in figure 3.2. This decreases the achievable β as well as the energy confinement time, and is more

detrimental when an NTM is located more towards the edge of the plasma. For example, the belt model [Chang and Callen 1990] estimates

$$\frac{\Delta\beta}{\beta} = \frac{\Delta\tau_E}{\tau_E} = 4 \frac{\bar{\rho}_s^3}{a^3} \frac{w_{\text{sat}}}{a}, \quad (3.2)$$

where τ_E is the energy confinement time, $\bar{\rho}_s = \rho_s a$ the radial location of the mode in meters and w_{sat} the saturated island width. With a $w_{\text{sat}}/a = 10\%$ that is easy to reach in tokamaks and a location near $\rho_s = 0.8$ (e.g. for 2/1 NTMs), the confinement degradation goes up to 20%. Moreover, rotating NTMs (in the laboratory frame) can interact with the resistive vessel wall as well as error fields and get locked eventually. The locked modes can further increase in size and lead to plasma disruptions, i.e. a violent loss of plasma confinement. Therefore, for the long-pulse and high- β operations of future tokamak devices like ITER, the reliable and efficient control of NTMs is crucial. This requires a better understanding of NTM physics as well as the development of robust NTM control algorithms, where much theoretical, numerical and experimental efforts from the community have been put.

This chapter aims to introduce more details about the physics and control of NTMs by reviewing the studies on several key aspects of NTMs in the literature. This meanwhile prepares the readers for further investigations of NTMs carried out within this thesis that will be detailed in the following chapters. In section 3.2, the onset of NTMs, involving both threshold and seeding physics will be discussed. Various methods used for NTM control in different tokamaks will be presented in section 3.3. In section 3.4, the modified Rutherford equation (MRE) [Rutherford 1973; Sauter et al. 1997; La Haye 2006] that has been widely used for simulating island width evolutions will be introduced; the detailed forms of the MRE that have been implemented and extensively tested in simulations of various TCV discharges in the following chapters will also be discussed. A summary of the chapter will be given in section 3.5.

3.2 Onset of NTMs

NTMs are metastable, i.e. they require a large enough seed island (w_{seed}) to be able to grow neoclassically [Sauter et al. 2002b]. This provides the possibility of preventing the occurrence of detrimental NTMs and highlights the importance of understanding their onset mechanisms. The metastable nature of NTMs is best illustrated by the dependence of the island width growth rate ($\frac{dw}{dt}$) on the island width (w) itself, as shown in figure 3.3. One can see that with relatively high β (thus high destabilizing effects from the perturbed bootstrap current discussed previously), there are two zeros of the $\frac{dw}{dt}(w)$ curve, denoted as w_{crit} and w_{sat} , respectively. w_{crit} refers to the critical island width beyond which an NTM can occur, since a $w_{\text{seed}} \leq w_{\text{crit}}$ leads to $\frac{dw}{dt} \leq 0$ and NTMs cannot grow. With $w_{\text{seed}} > w_{\text{crit}}$, $\frac{dw}{dt} > 0$ and w eventually grows up to w_{sat} , where $\frac{dw}{dt} = 0$ and w saturates (i.e. cannot grow or shrink under the given plasma condition). It is thus clear that there are two main aspects in the onset of NTMs: the generation of the threshold w_{crit} (threshold physics) and the formation of the seed island w_{seed} (seeding physics) [La Haye 2006]. With smaller β , i.e. less destabilizing

effects from the perturbed bootstrap current, $\frac{dw}{dt}(w)$ curve moves downwards, increasing w_{crit} as well as decreasing w_{sat} ; with $\beta = \beta_{\text{marg}}$, the maximum of the $\frac{dw}{dt}(w)$ curve reaches 0 at w_{marg} , where β_{marg} and w_{marg} are typically referred to as marginal β and marginal island width, respectively; with even smaller β , the entire $\frac{dw}{dt}(w)$ curve stays below 0 and the plasma is unconditionally stable to NTMs regardless of w_{seed} . Much work has been carried out on both the threshold and seeding physics of NTMs, as will be reviewed and discussed in the following sections.

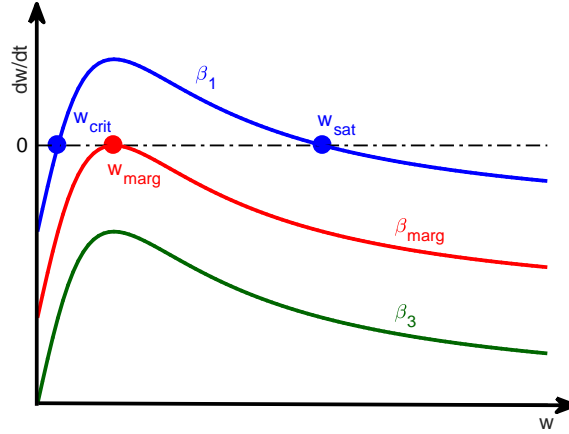


Figure 3.3. Illustration of several typical $\frac{dw}{dt}(w)$ traces of NTMs at different β levels, showing the existence of w_{crit} and w_{sat} at relatively high β (e.g. β_1), the marginal case when the maximum of $\frac{dw}{dt}(w)$ reaches 0 at w_{marg} under β_{marg} , and the case when the maximum of $\frac{dw}{dt}(w)$ stays below 0 and plasmas are unconditionally stable to NTMs at relatively low β (e.g. β_3).

3.2.1 Small island effects on NTMs

The stabilizing effects at small w contribute to the generation of w_{crit} , i.e. the threshold for the occurrence of NTMs. Two main models have been proposed to explain these stabilizing effects. The first one takes into account the incomplete flattening of the pressure profile at small w , resulting from a finite perpendicular transport at small w that can compete with the parallel transport [Fitzpatrick 1995]. This tends to decrease the amplitude of the perturbed bootstrap current caused by the flattening, thus a less destabilizing effect on $\frac{dw}{dt}$ at small w . The other model highlights the generation of a polarization current in the presence of a rotating island with frequency ω (in the frame of the plasma flow), due to different responses of electrons and ions to the time-varying electric field generated by island rotation [Connor et al. 2001; Waelbroeck et al. 2001; Imada et al. 2019]. Depending on the sign of ω , the polarization current can be stabilizing or destabilizing for NTMs, e.g., Waelbroeck et al. found that the polarization current is stabilizing for $0 < \omega < \omega_i^*$ [Waelbroeck et al. 2001], where ω_i^* is the ion diamagnetic drift frequency.

3.2.2 Seeding of NTMs

As discussed above, the growth of NTMs requires $w_{\text{seed}} > w_{\text{crit}}$, where w_{seed} has been experimentally observed to be provided by different mechanisms. For example, sawtooth crashes of long-period sawteeth have been found to be in good correlation with the occurrence of NTMs [La Haye and Sauter 1998; Gude et al. 1999; Sauter et al. 2002c; Maraschek et al. 2005; Chapman 2011; Canal et al. 2013]; fishbone instabilities (and/or their harmonics) have been observed to precede NTMs [Gude et al. 1999]; and edge localized modes (ELMs) can also excite NTMs [La Haye et al. 2000]. Apart from the typical triggers mentioned above, there is another special type where the seed island is provided by an unstable TM, i.e. the mode is linearly unstable (with a positive classical stability index Δ') and starts to grow from $w = 0$. Once the w of the TM goes above the w_{crit} , the mode will grow neoclassically, i.e. from a current-driven TM to a pressure-driven NTM [Reimerdes et al. 2002]. The NTMs thus generated are typically called “triggerless”, “seedless” or “spontaneous” NTMs [Reimerdes et al. 2002; Gerhardt et al. 2009; Ji et al. 2016; Fredrickson 2002], to be distinguished from NTMs triggered by other mechanisms.

These triggerless NTMs have been observed in different tokamaks and plasma scenarios [Reimerdes et al. 2002; Brennan et al. 2007; Gerhardt et al. 2009; Ji et al. 2016; Turco et al. 2018], depending on the details of the current density and q profiles. For instance, in DIII-D, 2/1 modes have been found to result from $\Delta' > 0$ instead of sawtooth crashes, ELMs or direct rotation effects in high- β experiments with ITER baseline scenarios [Turco et al. 2018, 2015]. Δ' has also been shown to increase sharply near the ideal stability boundary, leading to the onset of TMs and limiting the duration of operating at high β [Brennan et al. 2007; Turco et al. 2012]. In TCV, triggerless NTMs have been reproducibly observed in low-density discharges with strong near-axis electron cyclotron current drive (ECCD) [Reimerdes et al. 2002; Nowak et al. 2014; Lazzaro et al. 2015; Kim 2015]. Further studies about triggerless NTMs have been carried out in TCV with dedicated experiments and interpretative simulations, concerning both their onset and control [Kong et al. 2019, 2020], which will be the main topic of chapters 4 and 5, respectively.

3.3 Control of NTMs

Given their deleterious effects on confinement and the possibility of causing plasma disruptions, NTMs are required to be controlled reliably, especially for the long-pulse high- β operation of future tokamaks. Much progress has been made in this respect, either through the avoidance/prevention of the onset of NTMs, or by stabilizing already excited NTMs. This section discusses about the different methods applied in the control of NTMs in various machines as well as the future NTM control on ITER.

3.3.1 Avoidance and prevention of NTMs

The metastable nature of NTMs indicates that it is possible to avoid the onset of NTMs. In this respect, different strategies have been explored in present-day devices [La Haye 2006; Maraschek 2012; Kim 2015]. One approach is to move the target resonant surface to a region with smaller pressure gradient (thus smaller bootstrap current contribution), through tailoring the q profile as well as the pressure profile. For example, lower hybrid current drive (LHCD) and off-axis neutral beam injection (NBI) have been used in combination to tailor the profiles such that both the $q = 2/1$ and $3/2$ surfaces are radially located in a region where the pressure gradient is reduced [Isayama 2005]. Note that the change of q profiles in this case also affects the linear stability of the plasma (i.e. Δ') and the threshold for NTM onset.

Another method used to avoid the onset of NTMs is to control the formation of seed islands such that w_{seed} remains below w_{crit} . For instance, different strategies have been developed to control the frequency and amplitude of sawtooth crashes, one of the main perturbations that can trigger NTMs in standard tokamak scenarios. In JET, ion cyclotron heating (ICH) and current drive (ICCD) have been used to destabilize $q = 1$ sawteeth, resulting in more frequent but smaller crashes [Sauter et al. 2002c; Graves et al. 2009; Lennholm et al. 2011]. This kept the w_{seed} small and no NTMs were triggered even under high normalized β (denoted as β_N). In TCV, similar experiments have been performed with local electron cyclotron heating (ECH) and ECCD [Angioni et al. 2003]. Especially two new approaches, sawtooth pacing [Goodman et al. 2011] and sawtooth locking [Lauret et al. 2012], have been demonstrated experimentally with ECCD on TCV, where the occurrence of each sawtooth crash and the sawtooth cycle can be well controlled.

Apart from the avoidance of NTMs, a typical strategy used is the active prevention of NTMs by means of preemptive radio frequency (RF) depositions (e.g. ECCD) around the target mode location. Both $3/2$ and $2/1$ NTMs have been successfully prevented with preemptive ECCD [Nagasaki et al. 2003, 2005; La Haye et al. 2005; Prater et al. 2007]. Compared with the stabilization of existing NTMs, as will be discussed in the next section, preemptive ECCD typically requires less EC power and is more efficient than NTM stabilization in this sense [Nagasaki et al. 2005; Kolemen et al. 2014; Kong et al. 2019]. However, it is worth emphasizing that prevention of NTMs may require a much longer temporal duration of the EC power and thus a larger total input energy, which needs to be taken into consideration in the selection of NTM control strategies [Sauter et al. 2010].

3.3.2 Stabilization of existing NTMs

Another approach of controlling NTMs, in the case of their appearance, is to partially or fully suppress them. This can in general be obtained by decreasing the destabilizing effects (e.g. lowering the perturbed bootstrap current), or by increasing the stabilizing effects. It decreases the total $\frac{dw}{dt}$ that governs the evolution of w , i.e. effectively moves the $\frac{dw}{dt}(w)$ curve in figure 3.3 downward, leading to a smaller w_{sat} (partial stabilization) or a negative $\frac{dw}{dt}$ for all w (full

stabilization).

Since the dominating destabilizing effect for NTMs is from the perturbed bootstrap current that is proportional to β , the simplest NTM suppression strategy would be decreasing the operational β . However, this contradicts the requirement of burning plasma devices and may not be desirable. Instead, active methods can be taken to replace the missing bootstrap current at the mode location, e.g., by driving current in the same direction as the plasma current with RF waves. Given their highly localized depositions, EC waves have proven to be a promising candidate for the effective control of NTMs and will be used in ITER [La Haye 2006; Henderson et al. 2015]. In the case of tangential injection of EC beams, external current is driven both directly through ECCD and indirectly through heating effect [Hegna and Callen 1997]. As another main term counteracting the destabilizing effects from the perturbed bootstrap current (at relatively large w in the case of triggerless NTMs), Δ' is also expected to play a role in the stabilization of NTMs. For example, in addition to the direct current drive effect, EC waves modify the current density and q profiles, thus affecting Δ' and $\frac{dw}{dt}$ [Westerhof 1990; Westerhof et al. 2016]. In COMPASS-D, LHCD has also proven to be effective in the complete stabilization of 2/1 NTMs, through a reduction of Δ' [Warrick et al. 2000].

For the stabilization of NTMs with narrow ECCD, it is necessary to keep precise alignment of the peak ECCD density with respect to the target rational surface, since a misalignment as small as $\left| \left(\bar{\rho}_{mn} - \bar{\rho}_{dep} \right) \right| / \max(w, w_{dep}) \approx 0.7$ can negate any stabilizing effect [Prater et al. 2003; De Lazzari and Westerhof 2009], where $\bar{\rho}_{mn}$ is the radial location of the $q = m/n$ surface in meters, $\bar{\rho}_{dep}$ the radial deposition location of EC beams and w_{dep} the full e^{-1} deposition width. Four possible schemes can be applied to align ECCD with respect to the target mode location: varying the toroidal field which affects the deposition location of ECCD; varying the plasma major radius; changing the frequency of RF waves; or adjusting the angle of the launching mirror of EC beams. For instance, a slow toroidal field scan has been used in ASDEX Upgrade to align the ECCD with respect to the $q = 3/2$ surface for stabilizing 3/2 NTMs [Gantenbein et al. 2000]. In DIII-D, a real-time control of the plasma major radius has been utilized to align ECCD, through a so-called “search and suppress” scheme [La Haye et al. 2002]. The application of steerable launching mirrors to align ECCD with NTMs was firstly demonstrated in JT-60U [Isayama et al. 2000, 2003], where 3/2 NTMs were completely stabilized. This method has then been explored experimentally for controlling NTMs in various devices [Felici et al. 2012; Kolen et al. 2014; Rapson et al. 2017b] and will be used in ITER [Henderson et al. 2015].

Given the difficulty and uncertainties in the accurate determination of mode location, an alternative and robust control technique has been proposed, which adds a (sinusoidal) sweep-ing to the deposition location of EC waves. This relaxes the strict requirement on the precise alignment of EC beams with the target location, which is almost infeasible to reach and maintain accurately (within a half width of the occasionally small island) for various plasma scenarios and time-varying plasma conditions, and ensures that the EC power can reach the correct mode location for at least part of the time. First proposed and tested in TCV for both NTM stabilization and prevention cases [Kim 2015], this technique has also been applied

in NTM control on ASDEX Upgrade [Reich et al. 2014] and proves to be effective in the full stabilization of NTMs. Further studies in this thesis will show experimentally and be explained by simulations with the modified Rutherford equation (MRE) that sweeping around the target mode location is an efficient NTM prevention method (chapter 5).

The necessity of modulating the ECCD power in phase with the O-point of rotating NTMs has been emphasized, especially for relatively broad depositions with $w_{\text{dep}} > w_{\text{marg}}$ [Maraschek et al. 2007]. Note that the scattering of EC beams due to plasma turbulence increases the effective w_{dep} [Nikkola et al. 2003; Poli et al. 2015; Chellaï et al. 2019, and references therein], especially in large tokamaks. In ASDEX Upgrade, it has been shown that 3/2 NTMs cannot be fully suppressed with unmodulated ECCD in the experiments where broader w_{dep} was involved [Zohm et al. 1999; Maraschek et al. 2007]. In JT-60U, a dedicated scan of the relative phase of ECCD with respect to the O-point of NTMs showed favorable effects of modulated deposition at the O-point, whereas detrimental effects of modulated deposition at the X-point has also been shown [Isayama et al. 2009].

3.3.3 Control of NTMs on ITER

The understanding of NTM physics and control facilitates the design of NTM control schemes for future burning plasma experiments like ITER, which are predicted to be metastable for both 3/2 and 2/1 NTMs [Sauter et al. 2002b; La Haye 2006]. Given the slower plasma rotation and closer proximity to the resistive wall, it has been predicted that 2/1 NTMs, once triggered, can lock with a width of only 5 cm in ITER, leading to subsequent loss of H-mode and disruption [La Haye et al. 2006]. This highlights the importance of reliable control of NTMs in ITER.

In this respect, the upper launcher of the ITER EC system has been planned to be the primary actuator for NTM control in ITER [Hender et al. 2007], delivering up to 20 MW of power at 170 GHz. Assuming perfect alignment of peak ECCD on the target rational surface, evaluation of the required EC power indicates that the proposed 20 MW is adequate for 3/2 and 2/1 NTM control in ITER [La Haye et al. 2006]. However, the narrower ECCD resulting from an updated design using “front” steering [Henderson et al. 2015] makes the alignment of ECCD with the island more critical. It is expected that ECCD effectiveness drops to zero for misalignment as small as 1.7 cm, requiring an alignment resolution error of less than 1 cm and a realignment rate of at least 1 cm/s to avoid mode locking with a moderate continuous ECCD power [La Haye et al. 2009].

The fast growth rate of NTMs and the possibility of mode locking at small island width highlight the importance of early detection of NTMs in ITER, especially for the case of 2/1 NTMs [Van Den Brand et al. 2012]. Assuming a noise level of 2 ~ 4 cm for mode detection and that the requested stabilization power can be made available to the upper launcher within 3 s (based on the constraints of the switching mechanisms), the island would have reached 7 ~ 8 cm and locked by the time the EC power is made available on the 2/1 surface [Poli et al. 2018b]. It is thus critical to stabilize a mode within a few seconds from its onset, posing strict constraints

on the NTM control algorithms in ITER.

The necessity of using modulated ECCD for NTM control in ITER has also been explored. Though relatively narrower with the new design, the deposition width of ECCD for NTM stabilization is still expected to be broader than the w_{marg} (i.e. smallest island width before full stabilization) in ITER, especially when considering beam broadening by fluctuations [Nikkola et al. 2003; Poli et al. 2015, and references therein]. This favors the usage of ECCD power modulation in phase with the O-point of the island [Zohm et al. 2007]. However, power modulation requires a reliable detection of the phase of the island O-point and can be challenging at small island width. Instead, the use of continuous ECCD upon the detection of an NTM and turned off after complete stabilization may be good enough [La Haye et al. 2009]. Clearly, much remains to be considered to determine the best algorithm(s) for NTM control in ITER, which is still a subject of much interest.

3.4 The Modified Rutherford Equation (MRE)

Theoretical efforts have been made to explore the effects of various terms on the evolution of NTMs, by using the MHD model [Yu et al. 2004; Février et al. 2016, 2017, and references therein] or the MRE. In this thesis we focus on the MRE, which has been used widely in interpreting the w evolution of NTMs and takes the form of [Sauter et al. 1997, 2002b; La Haye 2006; De Lazzari and Westerhof 2009, 2010]

$$\frac{\tau_R}{\bar{\rho}_{mn}} \frac{dw}{dt} = \bar{\rho}_{mn} \Delta' + \bar{\rho}_{mn} \Delta'_{BS} + \bar{\rho}_{mn} \Delta'_{GGJ} + \bar{\rho}_{mn} \Delta'_{CD} + \bar{\rho}_{mn} \Delta'_H + \bar{\rho}_{mn} \Delta'_{POL}, \quad (3.3)$$

where $\tau_R = \frac{\mu_0 \bar{\rho}_{mn}^2}{1.22 \eta_{neo}}$ is the effective resistive time, with η_{neo} the neoclassical resistivity at the rational surface [Sauter et al. 1999, 2002a] and $\mu_0 = 4\pi \times 10^{-7}$ H/m the vacuum permeability; $\bar{\rho} = \sqrt{\frac{\Phi}{\Phi_b}} \cdot a$, with Φ the toroidal flux contained by a given flux surface, Φ_b the value at the plasma boundary and a the plasma minor radius based on plasma equilibrium (around 0.25 m for TCV); $\bar{\rho}_{mn}$ refers to the radial location of the $q = m/n$ surface in meters; Δ'_{BS} represents the destabilizing effects from the perturbed bootstrap current, as discussed in section 3.1; Δ'_{GGJ} considers the effects of favorable curvature on NTMs, which is stabilizing, though the amplitude is typically small in conventional tokamaks with relatively large aspect ratio; Δ'_{CD} and Δ'_H refer to the effects of external current drive and heating on NTMs, respectively, through for example off-axis ECCD and ECH beams; Δ'_{POL} represents the effect of the polarization current in the presence of a rotating island and can be stabilizing or destabilizing depending on the relative rotation of the NTM with respect to the diamagnetic frequencies. Detailed forms of each term in equation (3.3) are listed as follows.

$$\bar{\rho}_{mn} \Delta'_{BS} = a_2 \bar{\rho}_{mn} \widetilde{\Delta'_{BS}} \frac{w}{w^2 + w_{de}^2}, \quad (3.4)$$

Chapter 3. Neoclassical tearing modes (NTMs)

with

$$\bar{\rho}_{mn} \widetilde{\Delta'_{BS}} = \bar{\rho}_{mn} \beta_p |L_{bs}| \frac{L_q}{(-L_p)} \approx \bar{\rho}_{mn} \frac{2\mu_0 R_0 q_{mn}}{s_{mn} B_0} j_{bs,mn}, \quad (3.5)$$

where the subscript “mn” in the equations represents the value evaluated at the $q = m/n$ rational surface; w_{de} accounts for the finite ratio of perpendicular to parallel heat transport ($\chi_\perp / \chi_\parallel$) at small w and is given as

$$w_{de} = \left[5.1 \left(\frac{1}{\epsilon_{mn} s_{mn} n} \right)^{\frac{1}{2}} \right]^{\frac{4}{3}} \left(\frac{\chi_{\perp,mn}}{\chi_{\parallel,mn}} \right)^{\frac{1}{3}} \bar{\rho}_{mn}, \quad (3.6)$$

when introducing a convective form for the parallel transport [Fitzpatrick 1995; Sauter et al. 2002b], with $\epsilon = \bar{\rho} / R_0$ the local inverse aspect ratio, R_0 the major radius (0.88 m for TCV) and s the magnetic shear; $\beta_p \equiv 2\mu_0 p / B_p^2$ can be replaced by $\beta_p \approx 2\mu_0 p_{mn} R_0^2 q_{mn}^2 / (\bar{\rho}_{mn}^2 B_0^2)$ through the approximate relation between B_p and B_0 under the large aspect ratio assumption (or exact relation if the definition $B_p = \frac{1}{R_0} \frac{d\Psi}{d\rho}$ is used), with p the plasma pressure, B_p the poloidal magnetic field, B_0 the toroidal magnetic field at the magnetic axis and Ψ the poloidal magnetic flux; $L_q^{-1} = \frac{1}{q} \frac{dq}{d\rho} = s / \bar{\rho}$; $L_p^{-1} = \frac{1}{p} \frac{dp}{d\rho}$; j_{bs} refers to the perturbed bootstrap current density.

$$\bar{\rho}_{mn} \Delta'_{GGJ} = a_3 \bar{\rho}_{mn} \widetilde{\Delta'_{GGJ}} \frac{1}{\sqrt{w^2 + 0.2 w_{de}^2}}, \quad (3.7)$$

with

$$\bar{\rho}_{mn} \widetilde{\Delta'_{GGJ}} = -6 \bar{\rho}_{mn} D_R \approx -\frac{12\mu_0 R_0^2 \epsilon_{mn}^2 p_{mn}}{B_0^2 s_{mn}^2 (-L_p)} (q_{mn}^2 - 1), \quad (3.8)$$

where $D_R = \frac{\epsilon^2 \beta_p}{s} \frac{L_q}{-L_p} \left(1 - \frac{1}{q^2} \right)$.

$$\bar{\rho}_{mn} \Delta'_{CD} = -a_4 \frac{16\mu_0 R_0 q_{mn}}{\pi s_{mn} B_0} \sum_{j=1}^{n_l} \frac{I_{cd,j}}{w_{dep,j}^2} N_{cd,j} \left(\frac{w}{w_{dep,j}} \right) G_{cd,j} \left(\frac{w}{w_{dep,j}}, \bar{\rho}_{dep,j} \right) M_{cd,j} \left(\frac{w}{w_{dep,j}}, D_j \right), \quad (3.9)$$

and

$$\bar{\rho}_{mn} \Delta'_H = -a_5 \frac{16\mu_0 R_0 q_{mn}}{\pi s_{mn} B_0} \sum_{j=1}^{n_l} \frac{\eta_{H,j} P_{l,j}}{w_{dep,j}^2} N_{H,j} \left(\frac{w}{w_{dep,j}} \right) G_{H,j} \left(\frac{w}{w_{dep,j}}, \bar{\rho}_{dep,j} \right) M_{H,j} \left(\frac{w}{w_{dep,j}}, D_j \right), \quad (3.10)$$

where n_l refers to the total number of EC launchers involved; I_{cd} is the driven current from a given EC launcher, P_l the absorbed power, $\bar{\rho}_{dep}$ the location of the peak of the deposited power density and w_{dep} the full e^{-1} width; η_H estimates the efficiency with which the EC power is converted into a perturbative inductive current and is given by [De Lazzari and Westerhof

2009]

$$\eta_H = \frac{3w_{\text{dep}}^2}{8\pi R n_{e,mn} \chi_{\perp}} \frac{j_{\text{sep}}}{T_{\text{sep}}}, \quad (3.11)$$

with $n_{e,mn}$ the local electron density, j_{sep} the inductive part of the current density at the island separatrix and T_{sep} the corresponding electron temperature in electron volts; $M_{cd,H}$ and D terms in equations (3.9) and (3.10) represent the effect of EC power modulation and the power on-time fraction, respectively, and both equal 1 for continuous wave injections used here; $N_{cd,H}$ terms represent the dependence on w , with

$$N_{cd} = 0.25 \left(1 + \frac{2}{3} w^{*2} \right)^{-1} \quad (3.12)$$

when assuming local continuous wave deposition [Sauter 2004], $w^* \equiv w/w_{\text{dep}}$ and N_H taken from the equation (28) of [De Lazzari and Westerhof 2010], i.e.

$$N_H = \frac{0.077 w^{*2} + 0.088 w^*}{w^{*2} + 0.8 w^* + 2.17}; \quad (3.13)$$

$G_{cd,H}$ terms represent the effects of misalignment with respect to the $q = m/n$ surface, with G_H based on the equation (29) of [De Lazzari and Westerhof 2009] and taken as

$$G_H = \exp \left(- \left(\frac{x_{\text{norm}}}{g(w^*)} \right)^2 \right), \quad g(w^*) = 0.00035 w^{*4} - 0.008 w^{*3} + 0.07 w^{*2} + 0.02 w^* + 0.5, \quad (3.14)$$

and G_{cd} approximated by

$$G_{cd} = (1 + G_{\text{coeff}}) \frac{\left[1 - \tanh \left(\frac{0.75 x_{\text{norm}} - 0.3}{0.2} \right) \right]}{\left[1 - \tanh \left(\frac{-0.3}{0.2} \right) + 2 x_{\text{norm}}^3 \right]} - G_{\text{coeff}} \exp(-G_{\text{exp}} x_{\text{norm}}^2); \quad (3.15)$$

$G_{\text{coeff}} = 0.6$ and $G_{\text{exp}} = 1$ are used based on the figure 2 of [De Lazzari and Westerhof 2009] for $w^* = w/w_{\text{dep}} \approx 1$; the form of G_{cd} used in the simulations will be discussed in more details along with the experimental and simulation results in chapter 5 (section 5.4); x_{norm} quantifies the misalignment level of EC beams with respect to the rational surface and is defined by

$$x_{\text{norm}} = \frac{|\bar{\rho}_{\text{dep}} - \bar{\rho}_{mn}|}{\max(w, w_{\text{dep}})}. \quad (3.16)$$

$$\bar{\rho}_{mn} \Delta'_{POL} = a_6 \bar{\rho}_{mn} \widetilde{\Delta'_{POL}} \frac{w}{w^4 + w_{d,\text{pol}}^4}, \quad (3.17)$$

with

$$\widetilde{\bar{\rho}_{mn}\Delta'_{POL}} = \beta_p \left(\frac{L_q}{-L_p} \right)^2 w_p^2 g(\epsilon, \nu_{ii}^*) \approx \frac{2\mu_0 p_{mn} R_0^2 q_{mn}^2}{\bar{\rho}_{mn}^2 B_0^2} \left(\frac{L_q}{-L_p} \right)^2 w_p^2 g(\epsilon, \nu_{ii}^*), \quad (3.18)$$

and

$$g(\epsilon, \nu_{ii}^*) = \begin{cases} \epsilon^{3/2}, & \text{if } \nu_{ii}^* \leq 0.3, \\ 1, & \text{otherwise,} \end{cases} \quad (3.19)$$

where w_p is the poloidal ion Larmor radius; $w_{d,pol}$ refers to an empirical dependence of the polarization term at small w and is typically estimated by $w_{d,pol} = w_b$ [Reimerdes et al. 2002; Sauter et al. 2002b; Poli et al. 2005], with $w_b = \sqrt{\epsilon} w_p$ the ion banana width; $\nu_{ii}^* \equiv \nu_{ii} / (\epsilon \omega_e^*)$ represents a normalized ion collisionality with respect to the electron diamagnetic frequency ω_e^* .

a_2 to a_6 in the above equations are constant coefficients accounting for the assumptions in the model and the uncertainties in the data to fit the experimental results. a_2 is typically tuned based on the observed saturated island width w_{sat} since

$$w_{sat} = \frac{a_2 \bar{\rho}_{mn} \widetilde{\Delta'_{BS}} + a_3 \bar{\rho}_{mn} \widetilde{\Delta'_{GGJ}}}{-\bar{\rho}_{mn} \Delta'} \approx \frac{a_2 \widetilde{\Delta'_{BS}}}{-\Delta'} \quad (3.20)$$

at large w [Sauter et al. 2002b], and for example was taken as 2.6 when assuming $\bar{\rho}_{mn} \Delta' = -m$ [Sauter et al. 1997]; $\bar{\rho}_{mn} \Delta'_{GGJ}$ is typically small compared to the other terms in the MRE for conventional aspect ratio tokamaks considered here (e.g. TCV) and a_3 has been fixed to 1 or 0.25 in the simulations involved in this thesis - the effects of using different a_3 on the onset and evolution of NTMs will be discussed in detail in chapter 4; a_4 and a_5 can be determined through dedicated NTM stabilization experiments with co-ECCD (ECCD in the same direction as the plasma current I_p), counter-ECCD (ECCD in the opposite direction to I_p) and ECH beams as well as corresponding simulations, as will be detailed in chapter 5. Note that co-ECCD, counter-ECCD and ECH all have a stabilizing heating effect (i.e. $\bar{\rho}_{mn} \Delta'_H < 0$) despite different contributions from $\bar{\rho}_{mn} \Delta'_{CD}$.

For the polarization term $\bar{\rho}_{mn} \Delta'_{POL}$, the relative importance of its effect versus that from the incomplete flattening of the pressure profile at small w has been investigated in detail in [Sauter et al. 2002b], indicating a dominant effect of the polarization term only at very small w (typically below 1 cm) given its $1/w^3$ dependence (equation (3.17)). This is below the noise level of the measured w in the tested TCV discharges involved in this thesis (1.5 ~ 2.5 cm), so here we only retain the stabilizing effect from finite $\chi_\perp / \chi_\parallel$ at small w by including w_{de} in the bootstrap term (equation (3.4)) and neglect the effect of polarization current, i.e. $a_6 = 0$ will be used in the rest of the thesis. Note that there is no noticeable change of plasma rotation near the threshold of mode onset in the test discharges, as will be discussed in chapter 4.

The $\bar{\rho}_{mn} \Delta'$ term in the MRE (equation (3.3)) can in principle be calculated from the equilibrium

and effective q profiles, based on its definition

$$\Delta' = \lim_{\varepsilon \rightarrow 0} \frac{\frac{\partial \psi}{\partial \rho}|_{\rho_{mn}+\varepsilon} - \frac{\partial \psi}{\partial \rho}|_{\rho_{mn}-\varepsilon}}{\psi(\rho_{mn})}, \quad (3.21)$$

where $\varepsilon > 0$, $\rho \equiv \bar{\rho}/a$ and ψ refers to the perturbed helical flux computed by [Wesson 2004]

$$\frac{d^2 \psi}{d\rho^2} + \frac{d\psi}{\rho d\rho} - \left(\frac{m^2}{\rho^2} + \frac{\mu_0 \frac{\partial j}{\partial \rho}}{B_p (1 - \frac{n}{m} q)} \right) \psi = 0, \quad (3.22)$$

assuming cylindrical geometry. However, it is very difficult to get consistent results of $\bar{\rho}_{mn}\Delta'$ with this method, given the sensitivity of ψ and thus $\bar{\rho}_{mn}\Delta'$ to the derivatives of the reconstructed q and current density (j) profiles. A conventional approach applied in simulations with the MRE is to use a constant $\bar{\rho}_{mn}\Delta'$ when only relatively large w is involved [Sauter et al. 1997, 2002b, 2010; La Haye 2006, and references therein], which is a valid assumption considering the modification of the j and q profiles by the island itself. $\bar{\rho}_{mn}\Delta' = -m$ is typically used as the medium value inferred from PEST-III simulations [Sauter et al. 1997], which is between the marginal classical stability $\bar{\rho}_{mn}\Delta' = 0$ and the lower bound of large- m stability ($\bar{\rho}_{mn}\Delta' = -2m$). A different value of $\bar{\rho}_{mn}\Delta'$ would require a different coefficient a_2 to fit the experimental w_{sat} since $w_{\text{sat}} \propto a_2 \Delta'_{BS}/\Delta'$ (equation (3.20)). For triggerless NTMs originating from unstable q profiles (i.e. $\Delta' > 0$ at $w = 0$), as the ones involved in this thesis, the stabilizing effect from the modification of the j and q profiles by the island itself [Reimerdes et al. 2002; White et al. 1977] needs to be considered self-consistently to simulate the entire time evolution:

$$\bar{\rho}_{mn}\Delta' = \bar{\rho}_{mn}\Delta'_0 - \alpha \frac{w}{\bar{\rho}_{mn}}, \quad (3.23)$$

where $\bar{\rho}_{mn}\Delta'_0$ represents the stability at $w = 0$ as mentioned and is positive at the time of triggering.

In equation (3.23), α represents the rate of the variation of $\bar{\rho}_{mn}\Delta'$ with respect to varying w and its first approximation can be estimated by taking the lowest order terms from [White et al. 1977]:

$$\alpha \approx \frac{m^2 a^2}{\bar{\rho}_{mn}^2} \left(1 - \frac{s_{mn} \bar{\rho}_{mn}}{ma} \right), \quad (3.24)$$

while ensuring $\alpha > 0$ by taking the maximum between equation (3.24) and m for example. This gives $\alpha = 10 \sim 20$ for various test discharges (with different density and EC power levels) shown in this thesis. [Reimerdes et al. 2002] provides a method to indirectly “measure” α through delicate power-off experiments and for example gives $\alpha = \alpha_{\text{ref}} \cdot \bar{\rho}_{mn} \approx 33[\text{m}^{-1}] \cdot 0.12[\text{m}] \approx 4$ for similar plasma scenarios as used here. Applying the same method in a few test discharges where better measurements of w were obtained, α is estimated to be $5 \sim 10$ in our test discharges. Given these uncertainties, the effect of α on the time evolution of w and the possible range of α in the test discharges will be discussed in more detail along with dedicated

simulations in chapter 4 (section 4.3.1).

Quasilinear effects as the island develops have been found to be important as well [Pletzer and Perkins 1999], and we define an ad-hoc model both considering these quasilinear effects and representing a constant $\bar{\rho}_{mn}\Delta'$ for large w as used in previous simulations [Sauter et al. 1997, 2002b, 2010; La Haye and Sauter 1998; Buttery et al. 2002; La Haye 2006]:

$$\bar{\rho}_{mn}\Delta' = \bar{\rho}_{mn}\Delta'_0 - \frac{(\bar{\rho}_{mn}\Delta'_0 - \bar{\rho}_{mn}\Delta'_{\text{sat}})w}{\sqrt{w^2 + ((\bar{\rho}_{mn}\Delta'_0 - \bar{\rho}_{mn}\Delta'_{\text{sat}})\bar{\rho}_{mn}/\alpha)^2}}, \quad (3.25)$$

where $\bar{\rho}_{mn}\Delta'_{\text{sat}}$ represents the stability index at large w . In this case, equation (3.25) gives $\bar{\rho}_{mn}\Delta' = \bar{\rho}_{mn}\Delta'_{\text{sat}} = \text{const}$ (e.g. $\text{const} = -m$) for relatively large w and recovers equation (3.23) at small w . The $\bar{\rho}_{mn}\Delta'_0$ in equation (3.25) remains to be specified to simulate self-consistently the entire island width evolution, from the onset as a TM at $w = 0$ to the saturation as an NTM up to w_{sat} . In this thesis we have proposed a simple model for $\bar{\rho}_{mn}\Delta'_0$ (equation (4.2)) based on experimental observations and interpretative simulations with the MRE, as will be detailed in chapter 4.

3.5 Summary

This chapter introduced the fundamental physics of NTMs, discussed about their onset mechanisms and control strategies, and presented one of the theoretical models widely used in simulations of NTMs, i.e. the modified Rutherford equation (MRE). In section 3.1, the formation of magnetic islands through magnetic reconnection and the neoclassical nature of NTMs resulting from the destabilizing feedback of the perturbed bootstrap current have been illustrated. The metastable feature of NTMs has been discussed in detail in section 3.2, along with several characteristic $\frac{dw}{dt}(w)$ traces of NTMs. Small island effects contribute to the formation of a critical island width w_{crit} in the evolution of NTMs, making them metastable: NTMs can only grow with a large enough seed island ($w_{\text{seed}} > w_{\text{crit}}$). These stabilizing effects at small w have been explained by finite perpendicular transport or by the existence of a polarization current. In terms of seeding physics, various mechanisms have been identified in the literature and seed islands have been observed to be provided by large sawtooth crashes, ELMs, fishbones, etc. in present-day tokamaks. A special type of NTMs, originating from unstable TMs (i.e. with $\Delta' > 0$ at $w = 0$) and named as “triggerless”, “seedless” or “spontaneous” NTMs, have been discussed in section 3.2 as well. Given their Δ' -triggered nature, i.e. the strong dependence on the details of current density and q profiles, triggerless NTMs have been observed in various tokamaks and distinct scenarios and will be the main type of NTMs to be discussed in this thesis.

The detrimental effects of NTMs such as degrading confinement and causing disruptions make it crucial to secure their reliable control, especially for future long-pulse high- β devices like ITER. Extensive studies have been carried out in this respect, as have been briefly reviewed

and discussed in section 3.3. Given their flexibility and highly localized depositions, steerable EC launchers will be used as the main actuators for NTM control in ITER. Two main control strategies, namely the avoidance/prevention of the occurrence of NTMs and the stabilization of existing NTMs have been discussed. Prevention of NTMs by means of localized preemptive ECCD near the target mode location is generally shown to be more efficient than stabilization in terms of the EC power required for control, but its requirement of typically longer duration of the EC power may lead to a higher total input power that needs to be considered in the selection of the overall control strategy. The fast growth rate of NTMs, the proximity to mode locking and the strict requirement on EC beam alignment with the mode location highlight the importance and difficulty of reliable NTM control on ITER.

The modified Rutherford equation (MRE) has proven to be a powerful tool in interpreting the w evolution of NTMs and quantifying the contribution of various terms to the evolution. The main effects involved and the various terms included in the MRE used in the thesis have been presented in detail in section 3.4, with the key coefficients and parameters summarized in table 3.1. The MRE will be used to explore the underlying physics of both the onset (chapter 4) and the control (chapter 5) of triggerless NTMs observed in various TCV discharges. With a good knowledge of the coefficients and parameters involved in the MRE, as will be explored in chapters 4 and 5, the MRE can also be applied in predictive simulations, providing valuable information for NTM control as well as the overall integrated control strategy. For example, with relevant information from real-time (RT) measurements and transport simulations, the MRE can predict the EC power required to prevent or stabilize a given NTM in RT, as will be firstly illustrated in chapter 6.

Table 3.1. List of key MRE coefficients and parameters to be specified before a simulation

Item	Relevant equation(s)	Description
a_2	(3.4)	coefficient scaling $\bar{\rho}_{mn}\Delta'_{BS}$
a_3	(3.7)	coefficient scaling $\bar{\rho}_{mn}\Delta'_{GGJ}$
a_4	(3.9)	coefficient scaling $\bar{\rho}_{mn}\Delta'_{CD}$
a_5	(3.10)	coefficient scaling $\bar{\rho}_{mn}\Delta'_H$
a_6	(3.17)	coefficient scaling $\bar{\rho}_{mn}\Delta'_{POL}$ (set to 0 in this thesis)
Δ'_{sat}	(3.25)	Constant classical stability at large island width; a_2/Δ'_{sat} determines w_{sat} (equation (3.20))
Δ'_0	(3.25) and (4.2)	Classical stability at zero island width, to be specified in chapter 4
α	(3.24) and (3.25)	Rate at which Δ' varies with varying w at small w

4 Triggerless onset of 2/1 NTMs in TCV

4.1 Introduction

Triggerless NTMs refer to NTMs that originate from unstable TMs (i.e. with $\Delta' > 0$ at $w = 0$) and grow neoclassically when the size of the TM reaches beyond the critical island width (w_{crit}). In TCV, triggerless NTMs have been observed reproducibly in low-density discharges with strong near-axis co-ECCD [Reimerdes et al. 2002; Nowak et al. 2014; Lazzaro et al. 2015; Kim 2015]. Within the scope of this thesis, further studies about triggerless NTMs have been carried out, through more dedicated experiments in TCV and interpretative simulations with the MRE. This chapter focuses on the underlying mechanisms of the onset of these triggerless NTMs while the control of NTMs with off-axis ECCD or ECH will be the subject of chapter 5.

A key parameter in the study of triggerless NTMs is Δ' , which not only determines the onset of these NTMs (i.e. $\Delta' > 0$ at mode onset), but also being significant for the w evolution at finite w (i.e. an important term in equation (3.3)). A reliable evaluation of Δ' with varying w and plasma conditions (e.g. different density and EC power levels) would allow studying self-consistently the entire w evolution, from the onset of the TM at $w = 0$ to the saturation of the NTM at $w = w_{\text{sat}}$. By definition (equation (3.21)), Δ' at $q = m/n$ can be computed based on the logarithmic “jump” of the perturbed poloidal flux around the $q = m/n$ rational surface, which in turn depends on the equilibrium q and current density j profiles and their derivatives (equation (3.22)).

In TCV, efforts are made to calculate Δ' based on its definition and reconstructed equilibrium profiles by solving equations (3.21) and (3.22), with a cylindrical approximation. However, it is very difficult to obtain consistent results given the sensitivity of Δ' to the derivatives of q and j , especially when considering uncertainties in equilibrium reconstructions of experimental profiles. Therefore, a detailed sensitivity study of Δ' based on simple artificial q profiles and different types of perturbations is performed, as presented in appendix A. It is found that a small perturbation on the q or j profile, especially around the $q = m/n$ rational surface, can cause a dramatic change of the corresponding Δ' , similar to the observations in [Felici et al. 2009]. The sensitivity study also shows that increasing radial location of the $q = m/n$ surface

and/or increasing local magnetic shear tend to cause an increase of Δ' (i.e. more destabilizing). Moreover, more global effects, through a global change of the q and j profiles, are expected to play a role as well. Calculations with codes that consider more realistic toroidal geometries, for example as presented in [Glasser et al. 2016; Glasser and Kolemen 2018, and references therein], may provide a better estimate of Δ' . However, the uncertainties of equilibrium reconstructions and the sensitivity of Δ' to the details of q and j profiles (up to the second derivative) keep the task challenging.

Given these difficulties and with a focus on the trend (instead of the exact values) of Δ' with various w and plasma conditions, a simple model for the stability index at $w = 0$ (denoted as Δ'_0) is newly developed based on experimental observations in numerous TCV discharges and extensive simulations with the MRE, as will be detailed in this chapter. This Δ'_0 model (equation (4.2)), together with the w -dependence of Δ' (equation (3.25)), provides a complete model for Δ' that proves to capture self-consistently the (occasionally small) variations of Δ' in different plasma conditions. The model also works for interpreting NTM control experiments, including both NTM stabilization and prevention cases, as will be discussed in chapter 5.

An unexpected density dependence of the onset of triggerless NTMs is newly observed along with the NTM studies in TCV. It is found that lower plasma density does not always lead to easier mode onset - instead, there is a certain range of density within which triggerless NTMs can occur. This is counter-intuitive since lower plasma density leads to higher driven current by the central co-ECCD beams used to trigger NTMs and is expected to be more favorable for mode onset. The density range is found to broaden with increasing near-axis ECCD power and/or lower plasma current. These phenomena are explained well by the Δ'_0 model that is developed with a different set of experiments and simulations, as will be presented in this chapter.

The rest of the chapter is organized as follows. Section 4.2 presents the experimental setup and observations of the density range for triggerless onset of NTMs in TCV. In section 4.3, the detailed development of the Δ'_0 model through dedicated experiments and interpretative simulations with the MRE is presented. Section 4.4 explores the underlying physics of the observed density range with the Δ'_0 model. Section 4.5 discusses about the possible effects of plasma rotation and pure EC heating on the onsets of these NTMs. Key messages from this chapter will be summarized in section 4.6.

4.2 Experimental results

4.2.1 Plasma scenario and experimental setup

In the test discharges, limited L -mode plasmas with constant plasma current I_p and toroidal magnetic field ($B_0 \approx -1.44$ T) are used, similar to the scenarios used in [Reimerdes et al. 2002; Nowak et al. 2014; Lazzaro et al. 2015; Kim 2015]. Constant $I_p \approx -110$ kA or -90 kA are involved in different experiments, with $q_{95} \approx 7$ and 8, respectively, where q_{95} refers to the q value at the

95% poloidal flux surface. The negative values of B_0 and I_p represent a clockwise direction viewing from the top of the TCV tokamak. Similar plasma shapes with $\delta \approx 0.25$ (triangularity) and $\kappa \approx 1.3$ (elongation) at the plasma edge are used in various discharges. The line-averaged density along the chord passing through the plasma center (denoted as n_{el}), measured by the FIR interferometer introduced in chapter 2, ranges from 1×10^{19} to $4 \times 10^{19} \text{ m}^{-3}$ in different experiments.

Second harmonic X-mode (X2) EC beams are deposited near the plasma center through different EC launchers to trigger NTMs, mainly by a modification of the current density and q profile, i.e. a Δ' effect. There are no or only tiny sawtooth crashes in the test discharges given the low I_p ; and there is no sign of fishbones in these L -mode discharges either. The toroidal angles of the EC launchers can be set to allow ECH, co-ECCD or counter-ECCD; and the poloidal angles were fixed to deposit near the plasma center in the experiments shown in this chapter. The deposition location, power absorption rate and driven current of the EC beams are computed by the ray-tracing code TORAY-GA [Matsuda 1989].

The local n_e and T_e are measured by TCV's Thomson scattering system [Hawke et al. 2017; Blanchard 2019] introduced in chapter 2, while the Grad-Shafranov equilibrium solver LIUQE [Moret et al. 2015] is used to reconstruct the plasma equilibrium. The measured and reconstructed data are then used by the transport code ASTRA [Pereverzev and Yushmanov 2002] to solve the diffusion equation of the poloidal flux Ψ , i.e.

$$\sigma_{\parallel} \left(\frac{\partial \Psi}{\partial t} - \frac{\rho \dot{B}_0}{2B_0} \frac{\partial \Psi}{\partial \rho} \right) = \frac{F^2}{16\pi^4 \mu_0 B_0^2 \rho} \frac{\partial}{\partial \rho} \left[\frac{g_2 g_3}{\rho} \frac{\partial \Psi}{\partial \rho} \right] - \frac{V'}{2\pi \rho} j_{ni}, \quad (4.1)$$

based on the plasma boundary, the measured n_e and T_e profiles, and EC-relevant parameters, with I_p as the boundary condition. $\sigma_{\parallel}(\rho, t)$ in equation (4.1) refers to the neoclassical conductivity, $\rho \equiv \sqrt{\Phi/\Phi_b}$ the normalized radial location, where Φ_b is the toroidal flux at the plasma boundary; $F(\rho, t) = RB_{\phi}$, with B_{ϕ} the toroidal magnetic field; $g_2(\rho, t) = \langle (\nabla V)^2 / R^2 \rangle$, $g_3(\rho, t) = \langle 1/R^2 \rangle$, where $\langle \cdot \rangle$ represents flux-surface averaging and V the plasma volume; $V'(\rho, t) = \partial V / \partial \rho$; $j_{ni} = j_{bs} + j_{cd}$ refers to the total non-inductive current density, comprised of bootstrap (j_{bs}) and external driven current (j_{cd}) densities. ASTRA outputs such as q profiles and bootstrap current density profiles (using formulas from [Sauter et al. 1999, 2002a]) that are required for simulations with the MRE (equations (3.3) to (3.25)) are then used as MRE inputs to simulate w evolutions, as will be discussed in sections 4.3 and 4.5.

The occurrence, m/n number, frequency and amplitude of the rotating modes are determined by analyzing the signals from the magnetic probes (section 2.2.2 of chapter 2). The experimental island widths (w_{exp}) are estimated by fitting the helical flux perturbations to the measurements from the probes [Schittenhelm and Zohm 1997; Reimerdes 2001] and can have error bars up to 20%. The radial location (ρ) of an NTM can be determined by its m and n numbers from magnetic analyses and the $q(\rho)$ profile.

4.2.2 Experimental observations of the density range for the triggerless onset of NTMs in TCV

Studies on the triggerless onset of NTMs in TCV were motivated by the initial difficulty and inconsistency of triggering NTMs in the experiments: the same experimental settings (e.g. I_p , n_{el} , EC angle, EC power, etc.) do not always lead to the onset of NTMs. This hinders subsequent experimental studies on NTM control. Active scans of different plasma parameters such as I_p and n_{el} were thus performed in the experiments, from which the unexpected dependence of mode onset on n_{el} mentioned previously is observed. To further illustrate this, 91 stationary instances taken from 48 TCV discharges are summarized in figure 4.1. All the discharges have the same I_p (~ 110 kA) and very similar plasma shape, whereas different total co-ECCD power (distinguished by different symbols) has been applied. The minimum line-averaged density that can be reached after completely turning off the gas valve is about $1 \times 10^{19} \text{ m}^{-3}$ in these discharges, while $n_{el} > 3 \times 10^{19} \text{ m}^{-3}$ corresponds to a relatively high density near the plasma center (above $4 \times 10^{19} \text{ m}^{-3}$) that leads to the cut-off of X2 EC beams. These explain why most of the discharges have been carried out with $n_{el} \in [1, 3] \times 10^{19} \text{ m}^{-3}$. The density range involved here is still far from the Greenwald density limit of these TCV discharges ($5.1 \times 10^{19} \text{ m}^{-3}$) [Kirneva et al. 2015].

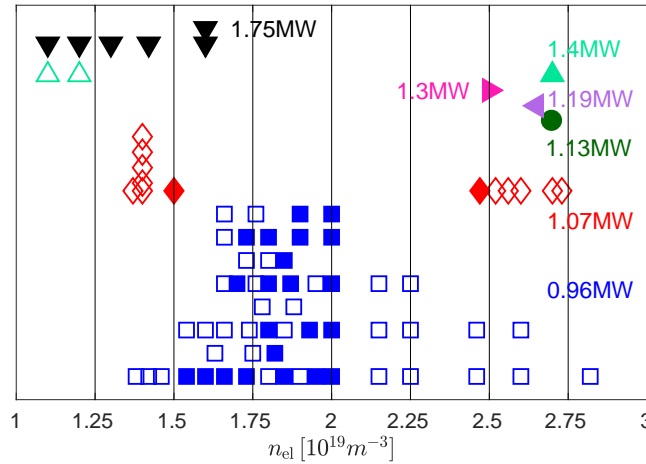


Figure 4.1. A collection of 91 stationary instances taken from 48 TCV discharges with different n_{el} and total co-ECCD power levels, showing the density ranges of the triggerless onset of NTMs in TCV. Solid symbols: onset of NTMs; open ones: no NTMs. Figure from [Kong et al. 2020].

The solid symbols in figure 4.1 represent the appearance of an NTM, and open symbols when no modes are observed. The instances with similar density levels are separated vertically to avoid overlapping. It can be seen that there is a density range for the onset of these modes and the range broadens with higher EC power. For instance, with 0.96MW co-ECCD power (blue squares), NTMs can only be triggered when $n_{el} \in [1.54, 2] \times 10^{19} \text{ m}^{-3}$. The fact that roughly half of the instances within this density range are without a mode (open blue squares) indicates it is marginal to trigger NTMs with 0.96MW in the tested discharges, corresponding to the

inconsistency of mode onset observed during these experiments. The n_{el} range for NTM onset seems to broaden with increasing total EC power. For example, the red diamonds give a range of $[1.5, 2.4] \times 10^{19} \text{ m}^{-3}$ with slightly higher power (1.07 MW), while onsets of NTMs are always observed with $n_{el} \geq 2.4 \times 10^{19} \text{ m}^{-3}$ at larger EC powers. The instances with the highest tested power (1.75 MW, black downward-pointing triangles) show a lower bound of n_{el} smaller than $1.1 \times 10^{19} \text{ m}^{-3}$, lower than the cases with less EC power.

Given the Δ' -triggered nature of the NTMs involved, the co-ECCD power and n_{el} dependence of NTM onset implies a dependence of Δ'_0 on the power of co-ECCD beams (the driven current I_{cd}) and n_{el} in the tested discharges. In similar experiments performed with $I_p \approx -90 \text{ kA}$, plasmas are found to be more unstable to NTMs (section 4.3.3), indicating the role of I_{cd}/I_p in the triggerless onset of NTMs in our discharges. This is also consistent with observations in similar plasmas with very different I_p discussed in [Kim 2015]: plasmas are more stable to NTMs with larger values of I_p . Instead of determining the accurate values of Δ' that is very difficult to obtain, it is more interesting to understand the formation of the observed density range for the triggerless onset of NTMs. This is achieved with a newly proposed simple model for Δ'_0 , which will be developed in detail in the next section through a different set of experiments and corresponding simulations with the MRE. Based on the Δ'_0 model, the underlying physics of the observed density range will be discussed in section 4.4.

4.3 A simple model for Δ'_0

As presented in appendix A, Δ' by definition is directly related to the details of q profiles such as the radial location of the given $q = m/n$ surface (ρ_{mn}), the local magnetic shear (s_{mn}), etc. Therefore, it is in principle possible to derive a model that directly links Δ' with these parameters, for example similar to the empirical formula given in appendix A (equation (A.5)), which is summarized based on a sensitivity study of Δ' with one type of q profiles (with fixed q_0 and q_{95}). However, as mentioned in appendix A, effects resulting from a more global change of the q profile (e.g. through varying q_0 and/or q_{95}) cannot be reproduced by the formula yet, indicating more parameters to be included. Theoretical derivations based on first principles and/or more comprehensive sensitivity studies covering a wider range of q profiles may provide a more general formula for Δ' , with respect to parameters such as ρ_{mn} and s_{mn} , but are out of the scope of this thesis.

A different approach based on extensive experimental observations and interpretative simulations with the MRE is applied in this thesis. Concentrating on the stability at zero island width (i.e. Δ'_0), relevant for the NTM onset studies in this chapter, we propose a simple model for Δ'_0 :

$$\bar{\rho}_{mn}\Delta'_0 = \bar{\rho}_{mn}\Delta'_{\text{ohmic0}} + k \frac{I_{cd,\text{tot}}}{I_p}, \quad (4.2)$$

where $\bar{\rho}_{mn}\Delta'_{\text{ohmic0}}$ represents the stability of the ohmic plasma to TMs at zero island width, $I_{cd,\text{tot}}$ stands for the total current driven by auxiliary current drive systems (ECCD in our

case), $kI_{\text{cd,tot}}/I_p$ refers to the modification of the stability by external driven current and k is a positive constant coefficient (hence co-CD is destabilizing). The first contribution of this model is to separate the contribution to Δ'_0 into the stability of ohmic plasmas and the modification caused by external driven current, which is generic to different plasma scenarios and tokamaks.

Interpretative simulations with ASTRA (i.e. solving equation (4.1)) show that the magnetic shear at the 2/1 surface increases with increasing $I_{\text{cd,tot}}$ (at constant I_p) in the discharges, which justifies equation (4.2) to some extent, since $\bar{\rho}_{mn}\Delta'_0$ increases with magnetic shear based on the sensitivity study with cylindrical approximation (appendix A). Determining the exact dependence of $\bar{\rho}_{mn}\Delta'_{\text{ohmic0}}$ and $kI_{\text{cd,tot}}/I_p$ on parameters such as ρ_{mn} , s_{mn} and the radial derivatives of s_{mn} would provide a more general analytical model for Δ'_0 in terms of these parameters, but as discussed previously, would require further theoretical investigations and/or more statistics with different plasma scenarios at different tokamaks. In this thesis, with the aim of understanding the observed density (represented by n_{el}) range for mode onset, we focus on obtaining the dependence of $\bar{\rho}_{mn}\Delta'_{\text{ohmic0}}$ and $kI_{\text{cd,tot}}/I_p$ on n_{el} , thus the n_{el} dependence of $\bar{\rho}_{mn}\Delta'_0$ eventually.

It is worth mentioning that the trend of the n_{el} dependence of $\bar{\rho}_{mn}\Delta'_{\text{ohmic0}}$ and $kI_{\text{cd,tot}}/I_p$ is generic: destabilization of 2/1 NTMs at high density is found to be the main mechanism causing the density limit of tokamak plasmas for the cases examined [Kirneva et al. 2015], while $I_{\text{cd,tot}}$ is expected to depend inversely on n_{el} [Cohen 1987; Lin-Liu et al. 2003, and references therein]. It should also be noted that $\bar{\rho}_{mn}\Delta'_0$, being the key parameter for the onset of triggerless NTMs, only has a higher-order effect on the evolution of w , given the w -dependence of $\bar{\rho}_{mn}\Delta'$ (equation (3.25)). The value of $\bar{\rho}_{mn}\Delta'_0$ can be estimated based on the measured occurrence of NTMs in offline interpretative simulations with the MRE, or adapted easily based on real-time w measurement in terms of real-time simulations, as will be discussed in this chapter and chapter 6, respectively.

Note that equation (4.2) accounts for the change of Δ' through a global change of q and j profiles by central current drive, given the relatively short resistive time scale on TCV (50 ~ 100 ms in the test discharges) and the strong co-ECCD involved here ($I_{\text{cd,tot}}/I_p = 35\% \sim 90\%$ depending on the density and EC power used). This is different from the effect of small off-axis EC depositions on Δ' discussed in [Westerhof 1990; Westerhof et al. 2016], where only local modifications of the j profile by off-axis EC beams are considered. Further improvements of equation (4.2) can be performed, for instance separating the effects of current drive and heating on Δ' , as will be discussed in section 4.5.2, and/or considering different time scales of varying $I_{\text{cd,tot}}$ and Δ'_0 by adding a term that includes the time dependence.

In the following sections, we focus on the evaluation of $\bar{\rho}_{mn}\Delta'_{\text{ohmic0}}$ and k in equation (4.2), through interpretative simulations of several dedicated power-ramp and density-ramp experiments with the MRE. Section 4.3.1 presents a power-ramp experiment with a constant medium density of the test discharges ($n_{el} \approx 1.7 \times 10^{19} \text{ m}^{-3}$), where a 2/1 NTM is observed

along with the ramp-up of the near-axis co-ECCD power. Interpretative simulations of this discharge with the MRE clarifies the range of parameters and coefficients involved in the simulations. To estimate the dependence of $\bar{\rho}_{mn}\Delta'_{\text{ohmic}0}$ on n_{el} , section 4.3.2 presents simulations of similar power-ramp experiments but with different n_{el} . As an overall test of the model, section 4.3.3 discusses the effects of I_p on $\bar{\rho}_{mn}\Delta'_{\text{ohmic}0}$ and details the simulations of a density-ramp experiment. The effects of using a different a_3 (coefficient of the Δ'_{GGJ} term in the MRE, equation (3.7)) on the onset and evolution of NTMs are discussed in sections 4.3.2 and 4.3.3, respectively.

4.3.1 Ramp-up of EC power with constant medium density

This section presents one example of the power-ramp experiments with medium density in TCV and its detailed interpretative simulations with the MRE. This contributes to the determination of corresponding $\bar{\rho}_{mn}\Delta'_{\text{ohmic}0}$ at this n_{el} level (with given I_p and plasma shapes), as well as the range of coefficients involved in the MRE such as k (equation (4.2)), α (equation (3.25)) and a_2 (equation (3.4)). In this discharge, as shown in figure 4.2, EC power is switched on at $t = 0.4$ s and drives co-ECCD near the plasma center through two independent launchers (L4 and L6). $I_p \approx -90$ kA and $n_{el} = 1.72 \times 10^{19} \text{ m}^{-3}$ are maintained, along with a ramp-up of the EC power (figure 4.2 (a)). A 2/1 NTM is detected at $t = 1.585$ s when the total EC power reaches about 0.78 MW (figure 4.2 (b)). The mode is sustained until turning off the EC power at $t = 2.25$ s. The measured w is depicted by the solid blue curve in figure 4.3, while the solid green curve represents the β_p trace that dominates $\bar{\rho}_{mn}\Delta'_{BS}$ term and is scaled based on a w_{ref} (typically w_{sat}) at a selected t_{ref} , i.e.

$$w_{\text{scaled}}(t) = \frac{\beta_p(t)}{\beta_p(t_{\text{ref}})} w_{\text{ref}}. \quad (4.3)$$

Given the noise level of the measurements and the Δ' -triggered nature of the NTMs involved (i.e. originating from $w = 0$), the two time instances “mode onset” and “mode appears” are distinguished: mode onset happens when $\frac{dw}{dt} > 0$ at $w = 0$, i.e. satisfying

$$\bar{\rho}_{mn}\Delta'_0 > -\bar{\rho}_{mn}\Delta'_{GGJ} \quad (4.4)$$

based on equation (3.3), as $\bar{\rho}_{mn}\Delta'_{BS} = 0$ at $w = 0$; the triggered mode then grows, eventually reaches beyond the noise level and is detected by the magnetic measurements (i.e. *appearing* on the spectrogram in this case), i.e. with a width of about 2.5 cm in #59151 (first blue triangle in figure 4.3). This is already higher than the marginal island width w_{marg} of the test discharges (around 2 cm as will be discussed in chapter 5), indicating that the measured w evolution is dominated by neoclassical effects (i.e. NTMs) whereas the onset of the mode as a TM at $w = 0$ and its initial growth up to 2.5 cm can only be reproduced in the simulations. This difficulty also explains why the detailed study presented here is needed to confirm the TM-triggered nature of the measured NTMs.

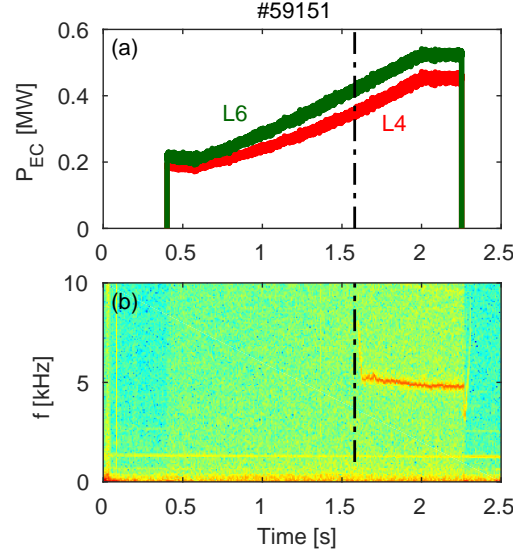


Figure 4.2. Experimental overview of a power ramp-up experiment with constant $n_{el} = 1.72 \times 10^{19} \text{ m}^{-3}$ and $I_p \approx -90 \text{ kA}$: (a) EC power traces; (b) 2/1 NTM spectrogram. Figure from [Kong et al. 2020].

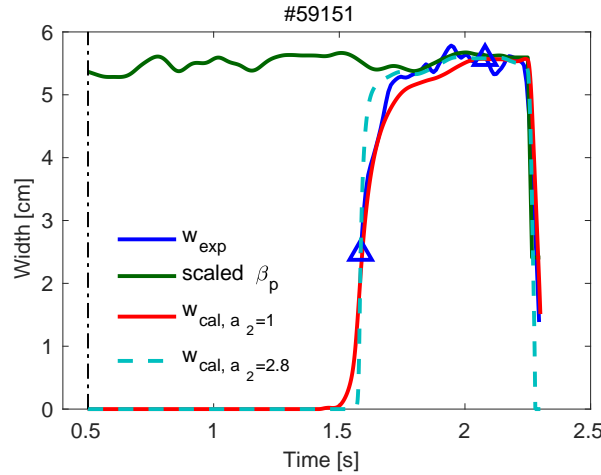


Figure 4.3. Island width evolution of #59151 (figure 4.2) with different a_z . Solid blue: from measurement; solid green: scaled β_p based on equation (4.3), with $t_{ref} = 1.9 \text{ s}$ and $\beta_p(t_{ref}) = 0.92$; solid red: simulation with $a_z = 1$; dashed cyan: simulation with $a_z = 2.8$. The two triangles represent the two constraints used in the simulations to determine $\bar{\rho}_{mn}\Delta'_{ohmic0}$ and $\bar{\rho}_{mn}\Delta'_{sat}$, as well as the time range within which χ (equation (4.5)) is evaluated. Figure from [Kong et al. 2020].

In addition to the time-varying equilibrium and profile information taken from LIUQE and ASTRA outputs, as discussed in section 4.2.1, the following key parameters and coefficients remain to be specified for interpretative simulations with the MRE: k , $\bar{\rho}_{mn}\Delta'_{ohmic0}$, α , $\bar{\rho}_{mn}\Delta'_{sat}$ and a_z . Based on the definition of $\bar{\rho}_{mn}\Delta'_0$ (equation (4.2)) and the condition of mode onset (equation (4.4)), k and $\bar{\rho}_{mn}\Delta'_{ohmic0}$ are expected to be the key parameters affecting the simulated onset of the mode. The evolution of the mode at w above the noise level is determined

by both $\bar{\rho}_{mn}\Delta'$ (equation (3.25)) and $\bar{\rho}_{mn}\Delta'_{BS}$ (equation (3.3)), thus can be affected by all five parameters. To better understand the main effects of each parameter on the evolution of w and to clarify the range of each parameter used in the simulations with the MRE, a detailed sensitivity study is performed based on #59151.

As indicated by the vertical dash-dotted black line in figure 4.3, the simulations start from $t = 0.5\text{ s}$ at $w = 0$. w_{de} in $\bar{\rho}_{mn}\Delta'_{BS}$ (equation (3.4)), representing the effect of incomplete flattening of pressure profiles at small w , can be estimated by equation (3.6). This gives $w_{\text{de}} \approx 2\text{ cm}$ with $\chi_{\parallel, mn} \approx 6 \times 10^7\text{ m}^2/\text{s}$ and $\chi_{\perp, mn} \approx 1\text{ m}^2/\text{s}$ in this discharge. Together with a power ramp-down experiment that will be discussed in the next chapter (section 5.3), where self-stabilization of NTMs along with decreasing β_p occurs at $w = 1.9\text{ cm}$, w_{de} is fixed to 1.9 cm in all the simulations of TCV discharges involved in this thesis. In each simulation, with each given set of (k, α, a_2) (i.e. scanning k , α and a_2), $\bar{\rho}_{mn}\Delta'_{\text{ohmic0}}$ and $\bar{\rho}_{mn}\Delta'_{\text{sat}}$ are fitted to make sure the calculated w (denoted as w_{cal}) crosses two specified measurement points (i.e. adding two constraints): one is the first measurement point when w just reaches above the noise level and the other when w_{sat} is reached, as marked by the two blue triangles in figure 4.3. The readers are reminded that k affects the contribution of EC beams to $\bar{\rho}_{mn}\Delta'_0$ (equation (4.2)), α represents the slope of the w -dependence of $\bar{\rho}_{mn}\Delta'$ (equation (3.25)) and a_2 is the coefficient of the main driving term $\bar{\rho}_{mn}\Delta'_{BS}$ (equation (3.4)). This method reduces the number of scanned parameters to three (i.e. k , α and a_2) and makes the sensitivity study easier.

A cost function χ is then evaluated for simulations with each set of parameters to quantify how well a simulation fits the measurements, and is defined as

$$\chi^2 = \frac{1}{N} \sum_{i=1}^N \left(\frac{w_{\text{cal}}(t_i) - w_{\text{exp}}(t_i)}{w_{\text{exp}}(t_i)} \right)^2, \quad (4.5)$$

where N refers to the total number of time points of the measurement within the selected two points (blue triangles in figure 4.3), $w_{\text{cal}}(t_i)$ is the simulated island width evaluated at the measurement time point t_i and $w_{\text{exp}}(t_i)$ the measured w at $t = t_i$. The $w_{\text{exp}}(t_i)$ in the denominator leads to an effective $1/w$ weighting in χ , which emphasizes more the evolution at small w and is consistent with the purpose of this study.

$\bar{\rho}_{mn}\Delta'_{\text{ohmic0}}$ and $\bar{\rho}_{mn}\Delta'_{\text{sat}}$ obtained by minimizing χ with randomly chosen sets of (k, α, a_2) have been compared to $\bar{\rho}_{mn}\Delta'_{\text{ohmic0}}$ and $\bar{\rho}_{mn}\Delta'_{\text{sat}}$ computed by fitting w_{exp} with the two constraints mentioned above. It is found that these two methods generate very similar results of $\bar{\rho}_{mn}\Delta'_{\text{ohmic0}}$, $\bar{\rho}_{mn}\Delta'_{\text{sat}}$ (both within 10%) and thus χ . More importantly, the trend of (the minimum) χ with respect to k , α and a_2 remains the same. This confirms that the parameter scan with the two constraints retain well the shape of χ in the five-dimensional parameter space.

The ranges involved in the entire sensitivity study are $k \in [2, 30]$, $\alpha \in [1, 100]$ and $a_2 \in [0.5, 3]$, with around 400 interpretative simulations in total. Simulations that both satisfy the two

constraints and fit reasonably the experimental width (i.e. with $\chi < 20\%$) have been collected, with around 200 instances in total. This rules out about half of the different combinations of parameters, though the ranges of parameters remain large: $k \in [2, 30]$, $\alpha \in [3, 100]$ and $a_2 \in [0.5, 3]$. These ranges, however, can be further shrunk when considering better fits (e.g. with $\chi \leq 5 \sim 10\%$) and taking into account observations in various experiments, as discussed below.

Effects of a_2

As a_2 (thus $\bar{\rho}_{mn}\Delta'_{BS}$ in equation (3.4)) is expected to affect more the evolution at relatively large w , where measurements are available, we start by discussing the range of a_2 and concentrating on the w evolution above the noise level. Based on the collection of 200 simulations, figure 4.4 illustrates the relative frequency of occurrence of staying below a certain χ at different a_2 values, defined as the ratio of the number of trials remaining below a certain χ (e.g. 10% or 5%) to the total number of trials at each a_2 . It can be seen that $a_2 = 1 \sim 2.5$ has a higher relative frequency of occurrence of obtaining $\chi \leq 10\%$ (within around 20% of the highest value) while the range shrinks to $1 \sim 1.5$ for $\chi \leq 5\%$. This is consistent with predictions based on the MRE: a_2 affects $\bar{\rho}_{mn}\Delta'_{BS}$, which is expected to be the dominant drive at relatively large w (e.g. larger than the noise level); the total $\frac{dw}{dt}$ at large w can thus be largely affected when different a_2 values are used. This happens beyond the noise level of the measurements and the range of a_2 can thus be better inferred. As an illustration, two simulations with $a_2 = 1$ and 2.8, respectively, are shown in figure 4.3, with the corresponding set of parameters listed in table 4.1. It can be seen that larger a_2 tends to cause a faster increase of w up to w_{sat} , due to a larger $\frac{dw}{dt}$ in the simulations, as expected.

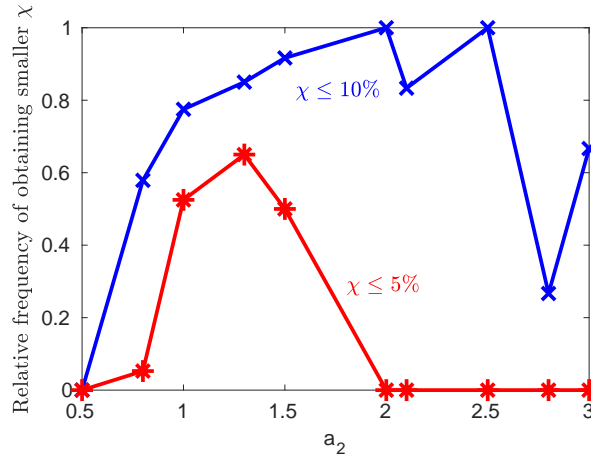


Figure 4.4. Relative frequency of occurrence of obtaining $\chi \leq 10\%$ and $\chi \leq 5\%$ at different a_2 . Figure from [Kong et al. 2020].

The effects of a_2 are more evident on $\frac{dw}{dt}(w)$ plots, as depicted in figure 4.5. $\frac{dw}{dt}(w)$ traces evaluated with the plasma information at various time slices (as indicated by the numbers in

the legend) are depicted by solid curves with corresponding colors, while w_{cal} at each time slice is denoted by a solid circle with the same color. The $\frac{dw_{\text{cal}}}{dt}(w_{\text{cal}})$ trace taken from the simulation (with $a_2 = 1$ and 2.8 respectively) is depicted by the dash-dotted black curve, which crosses the solid circles as expected. The $\frac{dw_{\text{exp}}}{dt}(w_{\text{exp}})$ trace taken from the measurement is shown by the dashed magenta curve, i.e. the same for figures 4.5 (a) and (b), though plotted on different scales. It can be seen that $\frac{dw_{\text{cal}}}{dt}(w_{\text{cal}})$ trace (dash-dotted black) fits better the measurement (dashed magenta) with $a_2 = 1$ (figure 4.5 (a)), whereas $a_2 = 2.8$ (figure 4.5 (b)) tends to overestimate the amplitude of $\frac{dw}{dt}(w)$, explaining the observed faster growth in figure 4.3. This also indicates that a_2 can be well determined by fitting experimental $\frac{dw}{dt}(w)$ trace.

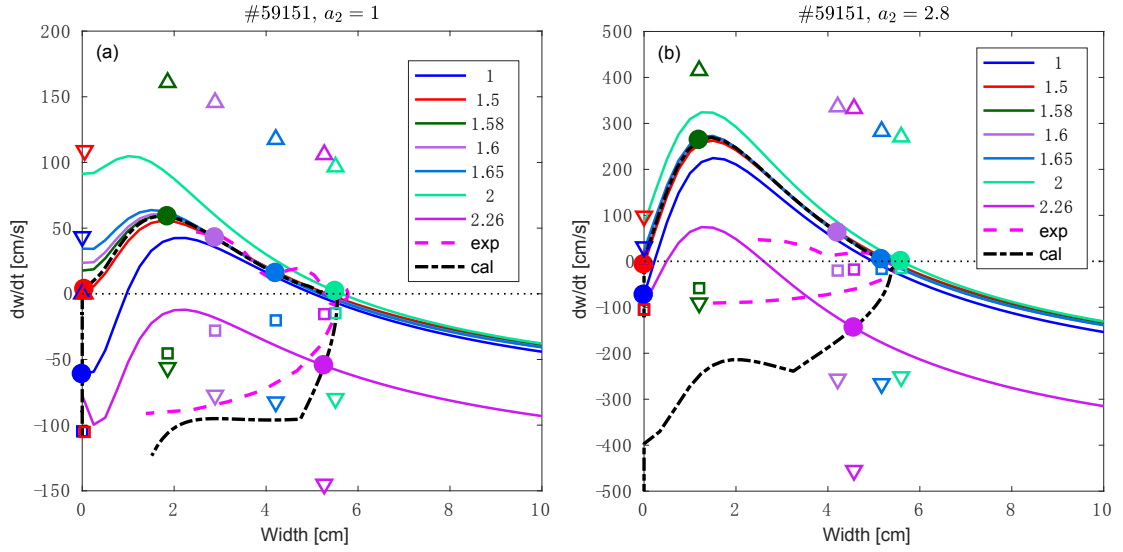


Figure 4.5. $\frac{dw}{dt}(w)$ traces of simulations with (a) $a_2 = 1$ and (b) $a_2 = 2.8$, respectively. Solid traces: $\frac{dw}{dt}$ evaluated at various time slices (as indicated by the numbers in the legend) and different w ; solid circles with corresponding colors: $\frac{dw}{dt}$ at the w_{cal} of each time slice. $\bar{\rho}_{mn}\Delta'$ (downward-pointing triangles), $\bar{\rho}_{mn}\Delta'_{BS}$ (upward-pointing triangles) and $\bar{\rho}_{mn}\Delta'_{GGJ}$ (squares) at the w_{cal} of each time slice, divided by $\tau_R/\bar{\rho}_{mn}$, are also listed. Dash-dotted black curves in (a) and (b): $\frac{dw_{\text{cal}}}{dt}(w_{\text{cal}})$ from simulations; dashed magenta: $\frac{dw_{\text{exp}}}{dt}(w_{\text{exp}})$ taken from the measurement (solid blue curve in figure 4.3, with extra smoothing to calculate $\frac{dw}{dt}$). Figure from [Kong et al. 2020].

Table 4.1. #59151, parameters for simulating with different a_2 at fixed k and α

k	α	a_2	$\bar{\rho}_{mn}\Delta'_{\text{ohmic0}}$	$\bar{\rho}_{mn}\Delta'_{\text{sat}}$	χ
4	10	1.0	-0.700	-0.460	4.92%
4	10	2.8	-0.756	-1.523	10.40%

To illustrate the amplitude of each term in the MRE (equation (3.3)), $\bar{\rho}_{mn}\Delta'$, $\bar{\rho}_{mn}\Delta'_{BS}$ and $\bar{\rho}_{mn}\Delta'_{GGJ}$ evaluated with the corresponding w_{cal} at each time slice, divided by $\tau_R/\bar{\rho}_{mn}$ (i.e. converted to [cm/s]), are indicated by the open downward-pointing triangles, upward-pointing triangles and squares in figure 4.5, respectively. It can be seen that $\bar{\rho}_{mn}\Delta'$ and $\bar{\rho}_{mn}\Delta'_{BS}$ are indeed the two dominant terms at finite w while $\bar{\rho}_{mn}\Delta'_{GGJ}$ is relatively small. The sum of these

terms recovers the total $\frac{dw}{dt}$ at each time slice, i.e. solid circles with corresponding colors.

Effects of k

Similarly, the range of k can be estimated through the statistics of simulations and observations in the experiments. As defined in equation (4.2), k represents the contribution of EC beams to the modification of Δ'_0 and is positive. The fact that no mode has been observed in similar plasmas with lower co-ECCD power or no EC power (i.e. ohmic discharges) indicates that k cannot be too small. For example, with $k = 1$, a perturbation of $\bar{\rho}_{mn}\Delta'_{\text{ohmic}0}$ of the order of $10^{-3} \sim 10^{-2}$ would have caused a fast growth of a mode that quickly reaches above the noise level of the measurements. More modes would have been observed, which is not the case in the experiments and we have thus chosen 2 as the lower bound of k in the simulations. Similar to figure 4.4, the relative frequencies of occurrence of obtaining smaller χ at various k have been compared, and it is found that $k = 2 \sim 10$ has higher relative frequency of occurrence of obtaining $\chi \leq 10\%$, while $k = 2 \sim 8$ satisfies more easily $\chi \leq 5\%$.

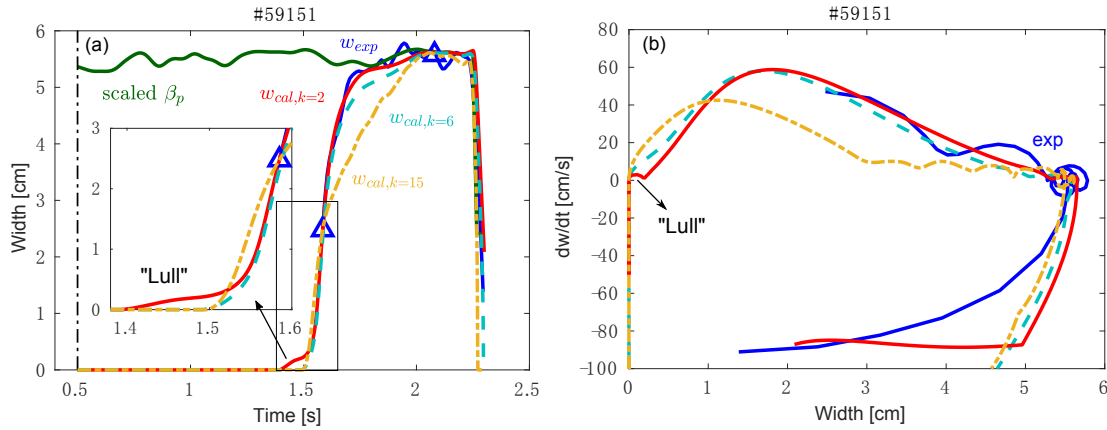


Figure 4.6. (a) Island width evolution of #59151 (figure 4.2) with different k . Solid blue: from measurement; solid green: scaled β_p based on equation (4.3), with $t_{\text{ref}} = 1.9$ s and $\beta_p(t_{\text{ref}}) = 0.92$; simulation with $k = 2$ (solid red), 6 (dashed cyan), 15 (dash-dotted orange), respectively. The two triangles represent the two constraints used in the simulations to determine $\bar{\rho}_{mn}\Delta'_{\text{ohmic}0}$ and $\bar{\rho}_{mn}\Delta'_{\text{sat}}$, as well as the time range within which χ (equation (4.5)) is evaluated. (b) With the same color and line type as in (a): $\frac{dw_{\text{cal}}}{dt}(w_{\text{cal}})$ traces of the simulations and that from measurement. Adapted from [Kong et al. 2020].

To better illustrate the effects of k on the evolution of w , simulations with $k = 2, 6$ and 15 are shown in figure 4.6. The set of parameters used and the corresponding χ are listed in table 4.2. $\frac{dw_{\text{cal}}}{dt}(w_{\text{cal}})$ traces of these simulations are depicted in figure 4.6 (b) with corresponding colors and line types, together with the experimental curve (solid blue). For the part up to w_{sat} thus $\frac{dw}{dt}(w, t) \geq 0$ discussed here, both cases with $\chi \leq 10\%$ ($k = 2$ and $k = 6$) follow well the whole $\frac{dw}{dt}(w, t)$ evolution, contrary to the case with $k = 15$. The timing of mode onset (at $w = 0$) and its evolution to 2.5 cm, i.e. below the noise level of the measurement, are also affected by the different parameters used.

A lower k value indicates that the q profile evolves more slowly towards an unstable profile as EC power (thus the amplitude of $I_{cd,tot}$) increases. This leads to a slower crossing of the marginal condition for mode onset as seen in figures 4.6 (a) (the red curves remain below $w = 0.5$ cm for about 0.1 s) and (b) (less positive $\frac{dw}{dt}$ for $k = 2$ and $w < 1$ cm), corresponding to a “lull” in the evolution of w . A similar lull region (reaching up to $w \approx 4$ cm) has been observed in DIII-D discharges near ideal stability boundaries and reproduced in simulations with a special handling of the $\bar{\rho}_{mn}\Delta'$ term (scaled based on plasma β) as well as the inclusion of a “cut-off” polarization model for small w [Brennan et al. 2003]. However, given the smaller size of NTMs involved in our test discharges and the noise level of the measurements, the existence or not of the lull in the present discharge cannot be concluded at this stage. More detailed studies can be performed when better measurements of w , especially at small w are available.

Table 4.2. #59151, parameters for simulating with different k at fixed α and a_2

k	α	a_2	$\bar{\rho}_{mn}\Delta'_{ohmic0}$	$\bar{\rho}_{mn}\Delta'_{sat}$	χ
2	10	1.0	-0.085	-0.435	2.36%
6	10	1.0	-1.330	-0.484	5.08%
15	10	1.0	-4.154	-0.767	15.52%

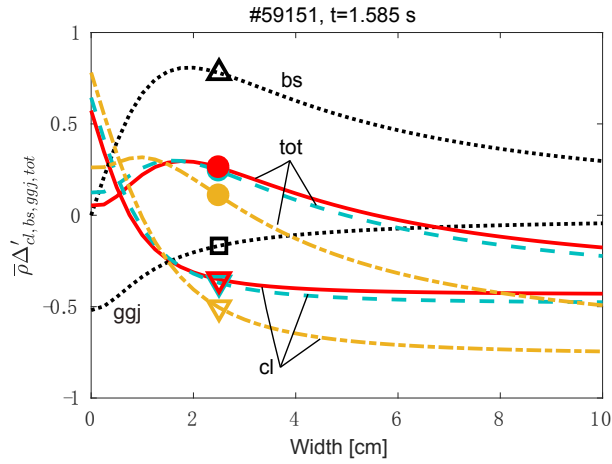


Figure 4.7. w dependence of different terms in the MRE (equation (3.3)) at $t = 1.585$ s. bs: $\bar{\rho}_{mn}\Delta'_{BS}$, overlapped for the three simulations; cl: $\bar{\rho}_{mn}\Delta'$ from the three simulations, with the same color and line type as in figure 4.6; ggj: $\bar{\rho}_{mn}\Delta'_{GGJ}$, overlapped for the three simulations; tot: the sum of all terms, with the same color and line type as in figure 4.6. Figure from [Kong et al. 2020].

Different values of k , together with the corresponding $\bar{\rho}_{mn}\Delta'_{ohmic0}$ and $\bar{\rho}_{mn}\Delta'_{sat}$ adjusted to satisfy the two constraints, also affect $w(t)$ and $\frac{dw}{dt}(w)$ traces at relatively large w , for example from 2.5 cm to w_{sat} as seen from figure 4.6. These differences mainly result from different shapes of $\bar{\rho}_{mn}\Delta'(w)$ traces with different k : a smaller k requires a less negative $\bar{\rho}_{mn}\Delta'_{sat}$ (at large w) to satisfy the defined constraint on w_{sat} , hence a larger total growth rate at large w and a faster growth to w_{sat} . As an example, the w dependence of different terms in the MRE (equation (3.3)) at $t = 1.585$ s are depicted in figure 4.7. This corresponds to the first

measurement point available for this discharge (with $w = 2.5$ cm), which has been chosen to be one of the constraints of the simulations, as discussed. With the same input profiles as well as the same a_2 and a_3 (equaling 1) for the three simulations, the $\bar{\rho}_{mn}\Delta'_{BS}$ and $\bar{\rho}_{mn}\Delta'_{GGJ}$ traces (dotted black) of the three simulations overlap, as expected. However, the $\bar{\rho}_{mn}\Delta'$ traces, thus the total $\frac{\tau_R}{\bar{\rho}_{mn}} \frac{dw}{dt}$ (denoted as “tot” in figure 4.7), are different. With a constant $\bar{\rho}_{mn}\Delta'_{ohmic0}$ in each simulation (corresponding values given in table 4.2), smaller k leads to a less increase of $kI_{cd,tot}/I_p$ along with the same ramp-up of co-ECCD power (i.e. ramp-up of $I_{cd,tot}/I_p$), leading to a smaller $\bar{\rho}_{mn}\Delta'_0$ (at $w = 0$), as seen from figure 4.7; $\bar{\rho}_{mn}\Delta'_{sat}$ is adjusted accordingly to satisfy the constraint of reaching w_{sat} with different k , typically with higher values (i.e. less negative) with smaller k ; these all together modify the w dependence of $\bar{\rho}_{mn}\Delta'$ and eventually the time evolution of w .

As another component of $\bar{\rho}_{mn}\Delta'_0$ defined in equation (4.2), $\bar{\rho}_{mn}\Delta'_{ohmic0}$ is in principle only affected by the choice of k : with $\bar{\rho}_{mn}\Delta'_0 \approx -\bar{\rho}_{mn}\Delta'_{GGJ}$ at mode onset (equation 4.4) and the same $I_{cd,tot}/I_p$ for each simulation, $\bar{\rho}_{mn}\Delta'_{ohmic0}$ is expected to have a linear dependence on k . However, the fact that no measurements are available for the exact timing of mode onset inevitably causes uncertainties of $\bar{\rho}_{mn}\Delta'_{ohmic0}$ even with the same k . To investigate the uncertainties, the projection of the collection of about 200 simulations (satisfying the two constraints and with $\chi < 20\%$) onto the $\bar{\rho}_{mn}\Delta'_{ohmic0}$ — k plane is illustrated in figure 4.8 and depicted by the blue plus symbols (some data points are overlapped). As indicated by the solid and dashed black lines, the linear dependence of $\bar{\rho}_{mn}\Delta'_{ohmic0}$ on k is well retained even with the large range of parameters involved in the simulations: $k = 2 \sim 30$, $\alpha = 3 \sim 100$ and $a_2 = 0.5 \sim 3$.

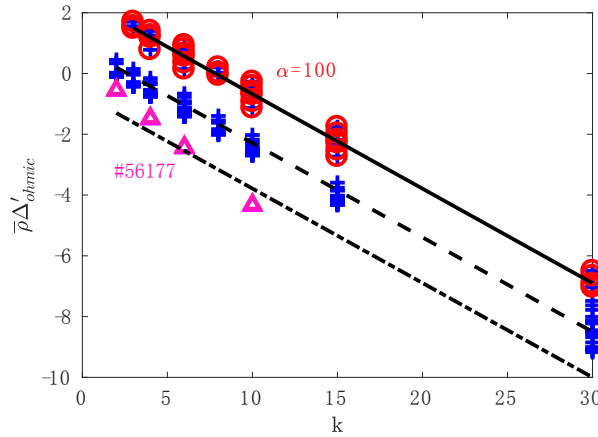


Figure 4.8. Dependence of $\bar{\rho}_{mn}\Delta'_{ohmic0}$ on k , taken from the projection of about 200 simulations of #59151, showing all instances (blue plus symbols), instances with $\alpha = 100$ (red circles), linear least square fit of the instances with $\alpha = 100$ (solid black curve), and linear least square fit of the instances with $\alpha < 100$ (dashed black, $\alpha = 3 \sim 30$ tested). Magenta triangles: instances taken from simulations of another discharge #56177 with lower n_{el} , as will be discussed in section 4.3.2. Dash-dotted black: a rigid shift of the dashed black curve by -1.5 . Figure from [Kong et al. 2020].

However, two different branches represented by the solid and dashed black lines are observed,

resulting from the distinct α values used: simulations with $\alpha = 100$, as highlighted by the red circles, lie on the upper branch with higher $\bar{\rho}_{mn}\Delta'_{\text{ohmic}0}$ while the ones with $\alpha = [3, 5, 10, 15, 30]$ lie on the other branch. This implies that in addition to k and $\bar{\rho}_{mn}\Delta'_{\text{ohmic}0}$, α plays a role in the evolution at small w (e.g. from $w = 0$ to 2.5 cm in this case). It is as expected from the $\bar{\rho}_{mn}\Delta'$ model used (equation (3.25)), where α affects the slope of the w dependence of $\bar{\rho}_{mn}\Delta'$, especially at small w (i.e. before reaching $\bar{\rho}_{mn}\Delta'_{\text{sat}}$ at relatively large w), as will be detailed below. The magenta triangles are taken from simulations of another power-ramp discharge (#56177) where lower n_{el} is maintained and will be detailed in section 4.3.2.

Effects of α

To better understand the effects of α , simulations with $\alpha = 5, 10$ and 100 (with fixed $k = 6$ and $a_2 = 1$, table 4.3) are shown in figure 4.9. It can be seen that $\alpha = 100$ predicts (below the noise level) a very different timing of mode onset and evolution at small w : there is a very long lull in the time evolution of w (i.e. staying below 1 cm for 1 s), corresponding to a very small $\frac{dw}{dt}$ at small w (figure 4.9 (b)). This was also observed to some extent with a small k (solid red curves in figure 4.6), as discussed, but with a shorter duration (about 0.1 s).

Table 4.3. #59151, parameters for simulations with different α at fixed k and a_2

k	α	a_2	$\bar{\rho}_{mn}\Delta'_{\text{ohmic}0}$	$\bar{\rho}_{mn}\Delta'_{\text{sat}}$	χ
6	5	1.0	-1.377	-0.776	7.15%
6	10	1.0	-1.330	-0.484	5.08%
6	100	1.0	0.803	-0.417	2.79%

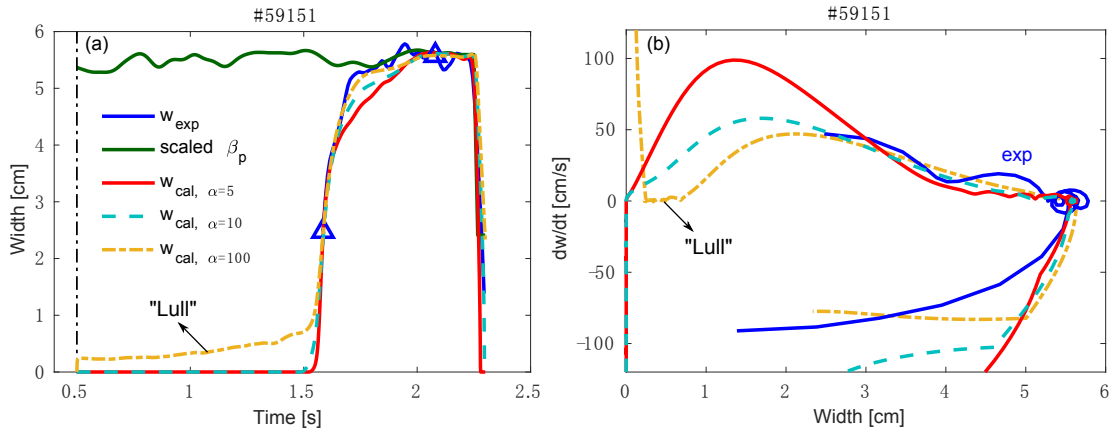


Figure 4.9. (a) Island width evolution of #59151 (figure 4.2) with different α . Solid blue: measurement; solid green: scaled β_p based on equation (4.3), with $t_{\text{ref}} = 1.9$ s and $\beta_p(t_{\text{ref}}) = 0.92$; simulation with $\alpha = 5$ (solid red), 10 (dashed cyan, the same as the dashed cyan curve in figure 4.6) and 100 (dash-dotted orange). The two triangles represent the two constraints used in the simulations to determine $\bar{\rho}_{mn}\Delta'_{\text{ohmic}0}$ and $\bar{\rho}_{mn}\Delta'_{\text{sat}}$, and the range within which χ (equation (4.5)) is evaluated. (b) With the same colors and line types as in (a): $\frac{dw_{\text{cal}}}{dt}(w_{\text{cal}})$ traces of the simulations and from measurement.

The lull with $\alpha = 100$ is generated by a “dip” of the $\frac{dw}{dt}(w)$ traces (figure 4.10 (b)), corresponding to a very small $\frac{dw}{dt}(w)$ at a range of w . This essentially comes from the competing effects of $\bar{\rho}_{mn}\Delta'_{BS}$ and $\bar{\rho}_{mn}\Delta'$ in the MRE (equation (3.3)). As an example, different MRE terms at $t = 1.585$ s are illustrated in figure 4.11. The higher $\bar{\rho}_{mn}\Delta'_{ohmic0}$ with $\alpha = 100$, as seen from figure 4.8 and table 4.3, leads to a higher $\bar{\rho}_{mn}\Delta'_0$ (equation (4.2)) at each time slice, whereas $\bar{\rho}_{mn}\Delta'_{GGJ}$ at mode onset ($w = 0$) remains the same; the onset condition of the mode (equation (4.4)) is thus fulfilled earlier along with the ramp-up of the co-ECCD power (i.e. $I_{cd,tot}/I_p$) with $\alpha = 100$, causing an earlier mode onset; the mode then starts to grow, which in turn modifies $\bar{\rho}_{mn}\Delta'_{BS}$ and $\bar{\rho}_{mn}\Delta'$ given their w dependence; the $\bar{\rho}_{mn}\Delta'_{BS}(w)$ curve features a peak near w_{marg} , as indicated by the contour of upper-pointing triangles in figure 4.10 as well as the dotted black curve in figure 4.11; the $\bar{\rho}_{mn}\Delta'$, on the other hand, drops from $\bar{\rho}_{mn}\Delta'_0$ with increasing w and eventually saturates at $\bar{\rho}_{mn}\Delta'_{\text{sat}}$ with large w , following the model defined in equation (3.25), where α affects the slope of the decrease; with larger α , the value of $\bar{\rho}_{mn}\Delta'$ drops more steeply from $\bar{\rho}_{mn}\Delta'_0$ to $\bar{\rho}_{mn}\Delta'_{\text{sat}}$ (then remains at $\bar{\rho}_{mn}\Delta'_{\text{sat}}$ with even larger w), as illustrated in figure 4.11; this competes with the w dependence of $\bar{\rho}_{mn}\Delta'_{BS}$ and affects the shape of total $\frac{dw}{dt}(w)$, e.g. leading to a “dip” with large α , as shown in figure 4.10.

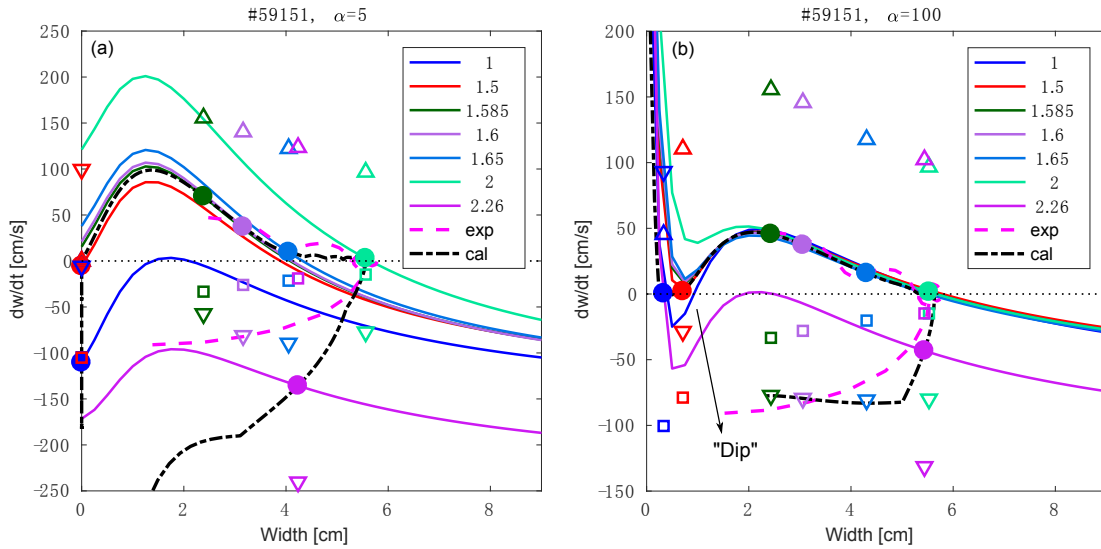


Figure 4.10. $\frac{dw}{dt}(w)$ traces of simulations with (a) $\alpha = 5$ and (b) $\alpha = 100$, respectively. Solid traces: $\frac{dw}{dt}$ evaluated at various time slices (as indicated by the numbers in the legend) and different w ; solid circles with corresponding colors: $\frac{dw}{dt}$ at the w_{cal} of each time slice. $\bar{\rho}_{mn}\Delta'$ (downward-pointing triangles), $\bar{\rho}_{mn}\Delta'_{BS}$ (upward-pointing triangles) and $\bar{\rho}_{mn}\Delta'_{GGJ}$ (squares) at the w_{cal} of each time slice, divided by $\tau_R/\bar{\rho}_{mn}$, are also listed. Dash-dotted black curves in (a) and (b): $\frac{dw_{\text{cal}}}{dt}(w_{\text{cal}})$ from simulations, corresponding to the solid red ($\alpha = 5$) and dash-dotted orange curve ($\alpha = 100$) in figure 4.9 (b), respectively; dashed magenta: $\frac{dw_{\text{exp}}}{dt}(w_{\text{exp}})$ taken from the measurement.

As discussed previously, the existence or not of the lull in our test discharges cannot be concluded yet given the smaller size of NTMs involved and the noise level of the measurements. In fact, experimental observations that no mode has been detected in ohmic discharges or

discharges with relatively low near-axis EC power (with similar plasma shape and density) seem to exclude the lull, especially the very long lull seen with $\alpha = 100$ in the test discharges, which could have seeded fast growing NTMs out of noise and been detected by the measurements. Detailed study on the lull region, the range of α in the model as well as the inclusion of a polarization term in the MRE are left for future work when measurements with lower noise levels are available.

On the other hand, however, the existence of the lull or not does not affect much the onset threshold of these NTMs ($\bar{\rho}_{mn}\Delta'_0$ defined in equation (4.2)), given the very small total $\frac{dw}{dt}$ involved in the lull region (figure 4.9 (b)). This can also be seen from figure 4.8, where the existence of the lull (e.g. with large α (100) or small k (figure 4.6) or both) only lead to a small rigid shift of the $\bar{\rho}_{mn}\Delta'_{\text{ohmic0}} - k$ mapping that determines $\bar{\rho}_{mn}\Delta'_0$ and thus the onset of the mode. Meanwhile, the timing of mode onset (figure 4.9 (a)) and the $\bar{\rho}_{mn}\Delta'_{\text{ohmic0}}$ values with the same k (figure 4.8) are very similar with $\alpha = 3 \sim 30$, which is also closer to the range of α estimated by equation (3.24) and dedicated power-off experiments ($\alpha = 5 \sim 20$). With an aim of understanding the triggerless onset of NTMs in various tested discharges in TCV, especially its density dependence as presented in section 4.2.2, the rest of this chapter will focus on the trend of the density dependence of $\bar{\rho}_{mn}\Delta'_0$, through interpretative simulations of various power-ramp and density-ramp experiments with a smaller range of k ($2 \sim 10$) and α ($3 \sim 15$). These simulations will in turn constrain better the range of parameters (such as k) in the MRE.

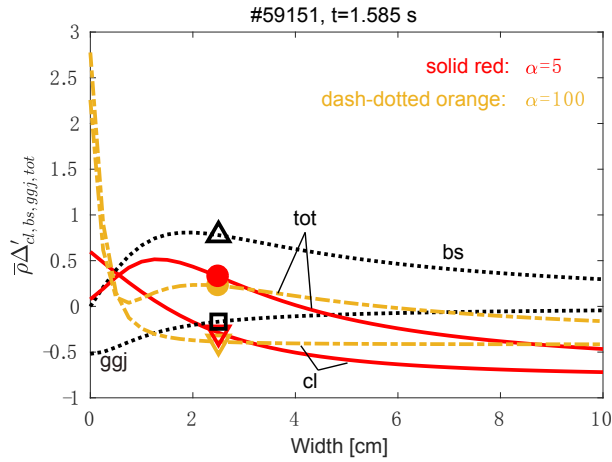


Figure 4.11. w dependence of different terms in the MRE (equation (3.3)) at $t = 1.585$ s, with $\alpha = 5$ and 100, respectively. bs: $\bar{\rho}_{mn}\Delta'_{BS}$, overlapped for both simulations; cl: $\bar{\rho}_{mn}\Delta'$ from the two simulations, with the same color and line type as in figure 4.9; ggj: $\bar{\rho}_{mn}\Delta'_{GGJ}$, overlapped for both simulations; tot: the sum of all MRE terms, with the same color and line type as in figure 4.9.

4.3.2 Ramp-up of EC power with higher or lower density

As discussed in section 4.3.1, the simulated onset of NTMs is mainly determined by $\bar{\rho}_{mn}\Delta'_{\text{ohmic0}}$ and $kI_{cd,tot}/I_p$, which are the two components of $\bar{\rho}_{mn}\Delta'_0$ defined in equation (4.2). To quantify the dependence of $\bar{\rho}_{mn}\Delta'_0$ on density, similar power ramp-up experiments have been per-

formed, with the same $I_p \approx -90$ kA as #59151, but different n_{el} levels in different discharges. Before going into the details, it is helpful to discuss and shrink further the range of parameters (especially k) to be used in the simulations. This is obtained by simulations of another power ramp-up experiment #56177 (figure 4.12), which is chosen given the larger range of EC power (thus $I_{cd,tot}/I_p$) covered in this discharge (with an extra EC launcher L1), though with a different I_p (-110 kA).

Power ramp-up with $I_p \approx -110$ kA

Constant $n_{el} = 1.45 \times 10^{19} \text{ m}^{-3}$ is kept in #56177. As shown in figure 4.12, a 2/1 NTM is triggered along with the ramp-up of the EC power and appears at $t = 0.985$ s when the total EC power reaches about 1.1 MW. Interestingly, a 3/2 NTM appears at around the same time as the 2/1 mode. The 3/2 mode disappears at $t = 1.16$ s along with the further ramp-up of the EC power, leading to a sudden increase of the amplitude of the 2/1 mode (as indicated by the spectrogram in figure 4.12 (b) or the measured w_{exp} in figure 4.13) and the appearance of its 2nd harmonic (4/2 mode).

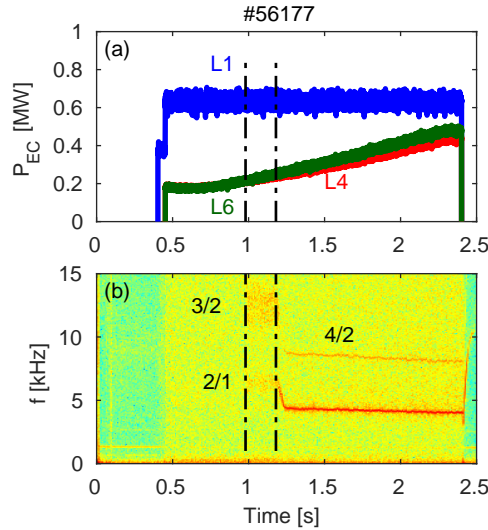


Figure 4.12. Experimental overview of a power ramp-up experiment with constant $n_{el} = 1.45 \times 10^{19} \text{ m}^{-3}$ and $I_p \approx -110$ kA: (a) EC power traces; (b) NTM spectrogram, showing the concurrence of 2/1 and 3/2 modes at $t = [0.985, 1.16]$ s and the increase of 2/1 mode amplitude once 3/2 mode disappears.

Similar to #59151 (figure 4.3), simulations of $w(t)$ of the 2/1 NTM are performed with the MRE, starting from $t = 0.5$ s with $w = 0$, as shown in figure 4.13. Following the discussions in section 4.3.1, a_2 has been fixed to 1.5 in these simulations to match the experimental $\frac{dw}{dt}$, as indicated by the dash-dotted black and the dashed magenta curves in figure 4.14. Different k and α are used in the simulations, as listed in table 4.4. In each simulation, $\bar{\rho}_{mn} \Delta'_{ohmic0}$ and $\bar{\rho}_{mn} \Delta'_{sat}$ are adjusted to cross two specified measurement points A and B (triangles in figure 4.13), corresponding to the earliest measurement point available and a time point shortly after

the disappearance of the 3/2 mode, respectively. Simulations have also been performed using A and C as the two constraints, which generate similar results as using A and B, as expected, but not detailed here for conciseness.

In figure 4.13, the simulated island widths (cyan, orange and purple traces) are much higher than the measurement during $t = [0.985, 1.16]$ s, i.e. with the coexistence of the 3/2 mode. Similar phenomena have been observed in simulations with other sets of parameters listed in table 4.4. Adding an ad-hoc extra term $\bar{\rho}_{mn}\Delta'_{32}$ during the presence of the 3/2 mode (i.e. $t = [0.985, 1.16]$ s) to the right hand side of the MRE (equation (3.3)) to take into account the possible effect of the 3/2 mode on the evolution of the 2/1 mode (a constant negative drag term), simulations can fit better w_{exp} , e.g. the dashed red curve in figure 4.13. This is similar to the observations in simulations of some JET discharges [Sauter et al. 2002b], where adding an extra term representing the “drag” from a concurrent 4/3 mode fits better the evolution of a dominant 3/2 mode. Note that in both cases the coupling between two modes always resulted in a stabilization effect on the most outside mode (with lower n). A possible explanation for this phenomenon is that the coexistent inner mode consumes part of the total energy available for mode growth that otherwise would have caused the outer mode more unstable.

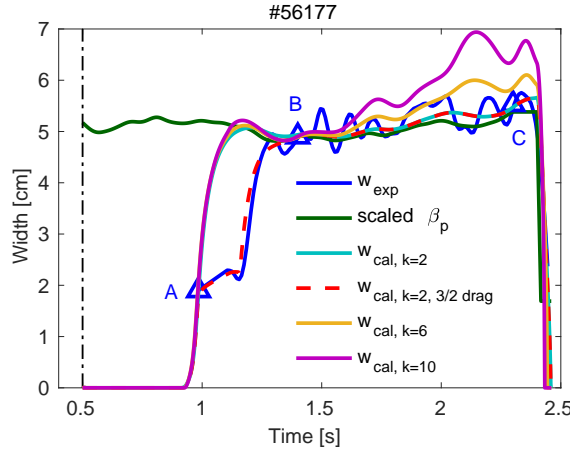


Figure 4.13. Island width evolution of the 2/1 mode in #56177 (figure 4.12). Solid blue: measurement; solid green: scaled β_p based on equation (4.3), with $t_{\text{ref}} = 1.4$ s and $\beta_p(t_{\text{ref}}) = 0.73$; solid cyan: simulation with $k = 2$ and $\alpha = 10$; solid orange: simulation with $k = 6$ and $\alpha = 10$; solid purple: with $k = 10$ and $\alpha = 10$; dashed red: with $k = 2$, $\alpha = 10$ and $\bar{\rho}_{mn}\Delta'_{32} = -0.36$ during the coexistence of 3/2 and 2/1 modes. Blue triangles labeled as A and B: the two constraints used to determine $\bar{\rho}_{mn}\Delta'_{\text{ohmic0}}$ and $\bar{\rho}_{mn}\Delta'_{\text{sat}}$; from B to C: the range within which χ (equation (4.5)) in table 4.4 is evaluated.

$\bar{\rho}_{mn}\Delta'_{32}$ used to better fit the evolution of the 2/1 mode during $t = [0.985, 1.16]$ s is listed in table 4.4 for completeness. χ in table 4.4 (evaluated based on equation (4.5)), however, only considers the evolution between B and C marked in figure 4.13, i.e. without the coexistence of the 3/2 mode. This covers most part of the 2/1 mode evolution along with the power-ramp, while excluding the uncertainties of the exact values of $\bar{\rho}_{mn}\Delta'_{32}$. It can be seen that smaller k tends to fit better w_{exp} along with the ramp-up of the co-ECCD power (i.e. $I_{\text{cd,tot}}/I_p$),

though $k = 2 \sim 6$ can fit reasonably w_{exp} (with $\chi \leq 20\%$). This is similar to the observations in simulating #59151 (table 4.2), where lower k tends to fit better the $w(t)$ above the noise level. The value of α , as discussed in section 4.3.1, affects the detailed w dependence of $\bar{\rho}_{mn}\Delta'$ and thus the time evolution of w (and χ). $\bar{\rho}_{mn}\Delta'_{\text{ohmic0}}$ is shown to depend mainly on k , whereas the variation of $\alpha = 5 \sim 15$ only leads to a change of $\bar{\rho}_{mn}\Delta'_{\text{ohmic0}}$ of the order of 10^{-2} (table 4.4). This is consistent with the discussions in section 4.3.1, where instances with $\alpha = 3 \sim 30$ approximately lie on the same fitted curve of $\bar{\rho}_{mn}\Delta'_{\text{ohmic0}} - k$ (dashed black line in figure 4.8).

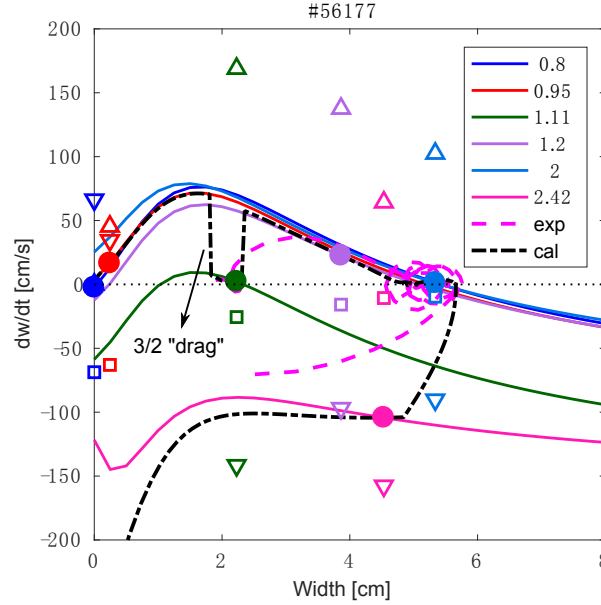


Figure 4.14. $\frac{dw}{dt}(w)$ traces at different time slices of the simulation with $k = 2$, $\alpha = 10$ and an additional $\bar{\rho}_{mn}\Delta'_{32} = -0.36$ (dashed red curve in figure 4.13). Solid traces: $\frac{dw}{dt}$ evaluated at various time slices (as indicated by the numbers in the legend) and different w ; solid circles with corresponding colors: $\frac{dw}{dt}$ at the w_{cal} of each time slice. $\bar{\rho}_{mn}\Delta'_{32}$ (downward-pointing triangles), $\bar{\rho}_{mn}\Delta'_{BS}$ (upward-pointing triangles) and $\bar{\rho}_{mn}\Delta'_{GGJ}$ (squares) at the w_{cal} of each time slice, divided by $\tau_R/\bar{\rho}_{mn}$, are also listed. Dash-dot black: $\frac{dw_{\text{cal}}}{dt}(w_{\text{cal}})$ from the simulation; dashed magenta: $\frac{dw_{\text{exp}}}{dt}(w_{\text{exp}})$ taken from the measurement.

To investigate the $\bar{\rho}_{mn}\Delta'_{\text{ohmic0}} - k$ mapping with a different density level (i.e. $n_{el} = 1.45 \times 10^{19} \text{ m}^{-3}$ versus $1.72 \times 10^{19} \text{ m}^{-3}$), the instances from table 4.4 have been included in figure 4.8, as marked by the magenta triangles (some data points are overlapped). It can be seen that $\bar{\rho}_{mn}\Delta'_{\text{ohmic0}} - k$ mappings with different densities are approximately parallel, where the dash-dotted curve is a rigid shift of the dashed line by -1.5 . This shows that the choice of k will not change the trend of $\bar{\rho}_{mn}\Delta'_{\text{ohmic0}} - n_{el}$ mapping that will be inferred from various power-ramp experiments with different densities. Note that the difference of I_p in the test discharges (-110 kA versus -90 kA) only leads to a rigid shift of the $\bar{\rho}_{mn}\Delta'_{\text{ohmic0}} - n_{el}$ mapping as well, as will be detailed in the next section. It should also be noted that even though smaller k (e.g. 2) leads to smaller χ in the simulations (tables 4.2 and 4.4), it tends to cause a lull in the simulated evolution of $w(t)$ at small w (figure 4.6), which is less plausible based on

experimental observations of mode occurrence, as discussed in section 4.3.1. Given these discussions and without losing generality, $k = 6$ (i.e. the medium value between 2 and 10) and $\alpha = 3 \sim 15$ will be used in the rest of the thesis.

Table 4.4. Key parameters for simulating the 2/1 mode evolution of #56177

k	α	a_2	$\bar{\rho}_{mn}\Delta'_{\text{ohmic0}}$	$\bar{\rho}_{mn}\Delta'_{\text{sat}}$	χ	$\bar{\rho}_{mn}\Delta'_{32}$
2	5	1.5	-0.58	-0.700	5.76%	-0.52
4	5	1.5	-1.53	-0.696	11.92%	-0.54
6	5	1.5	-2.48	-0.682	19.58%	-0.56
10	5	1.5	-4.38	-0.672	38.04%	-0.57
2	10	1.5	-0.56	-0.610	4.60%	-0.36
4	10	1.5	-1.50	-0.610	5.20%	-0.37
6	10	1.5	-2.45	-0.610	7.52%	-0.38
10	10	1.5	-4.35	-0.604	15.52%	-0.39
2	15	1.5	-0.52	-0.592	4.66%	-0.33
4	15	1.5	-1.45	-0.592	4.53%	-0.33
6	15	1.5	-2.40	-0.592	5.19%	-0.33
10	15	1.5	-4.30	-0.592	8.95%	-0.33

Power ramp-up with $I_p \approx -90$ kA

With a narrower range of MRE coefficients determined, simulations of more power-ramp experiments with $I_p \approx -90$ kA (i.e. the same as #59151, figure 4.2) are performed to estimate the $\bar{\rho}_{mn}\Delta'_{\text{ohmic0}}-n_{el}$ mapping for $I_p \approx -90$ kA. A series of power ramp-up experiments with different n_{el} are selected: TCV #59318 with $n_{el} = 1.84 \times 10^{19} \text{ m}^{-3}$, #59358 with $n_{el} = 1.1 \times 10^{19} \text{ m}^{-3}$ and #59360 with $n_{el} = 2.46 \times 10^{19} \text{ m}^{-3}$, respectively.

The same EC settings (power traces, angles, etc.) are applied in the three experiments, and shown in figure 4.15 (a) is an example of the EC power traces. In these three discharges, $L4$ and $L6$ are used to drive co-ECCD near the plasma center, reaching a maximum total EC power of 0.96 MW at the end of the power ramp-up. In the case of #59318, as shown in figure 4.15 (b), a 2/1 mode is triggered along with the ramp-up of the EC power and appears at $t = 1.29$ s. In the other two experiments with lower or higher n_{el} (#59358 and #59360), however, no NTMs are observed in the entire discharges, requiring $\bar{\rho}_{mn}\Delta'_0 \leq 0$ in these two cases. Simulations of these three experiments have been performed with the MRE, with fixed $k = 6$ as discussed before. Based on the Δ'_0 model (equation (4.2)) and following the same procedures as in previous examples (#59151 and #56177), $\bar{\rho}_{mn}\Delta'_{\text{ohmic0}}$ is estimated to be -1.37 for #59318.

Based on the onset condition of triggerless NTMs (equation (4.4)), the fact that no mode occurs in #59358 or #59360 means

$$\bar{\rho}_{mn}\Delta'_0 \equiv \bar{\rho}_{mn}\Delta'_{\text{ohmic0}} + k \frac{I_{\text{cd,tot}}}{I_p} \leq -\bar{\rho}_{mn}\Delta'_{GGJ} \quad (4.6)$$

in both cases, where $\bar{\rho}_{mn}\Delta'_{GGJ}$ is stabilizing (i.e. negative) as defined in equation (3.7). With the $I_{cd,tot}$ taken from the outputs of TORAY-GA, $\bar{\rho}_{mn}\Delta'_{GGJ}$ calculated by equation (3.7) and the fixed $k = 6$, equation (4.6) estimates the corresponding range of $\bar{\rho}_{mn}\Delta'_{ohmic0}$ in each case. For #59358 ($n_{el} = 1.1 \times 10^{19} \text{ m}^{-3}$), equation (4.6) gives $\bar{\rho}_{mn}\Delta'_{ohmic0} \leq -3.6$ and we take $\bar{\rho}_{mn}\Delta'_{ohmic0} = -4.6$ for example to stay away from marginal stability, based on the observations that no mode has been triggered with this low density in various similar discharges. For #59360 ($n_{el} = 2.46 \times 10^{19} \text{ m}^{-3}$), equation (4.6) gives $\bar{\rho}_{mn}\Delta'_{ohmic0} \leq -1.2$ and we take $\bar{\rho}_{mn}\Delta'_{ohmic0} = -1.2$ to be around the marginal stability at this density level. This is based on experimental observations that the 2/1 mode, once triggered with central co-ECCD with a different n_{el} level, can be sustained with $n_{el} = 2.4 \times 10^{19} \text{ m}^{-3}$ even after turning off the EC power (i.e. ohmic plasmas) in our test discharges. This trend of $\bar{\rho}_{mn}\Delta'_{ohmic0}$ with increasing n_{el} is also consistent with earlier studies that higher n_{el} is more prone to the onset of TMs in ohmic TCV discharges [Kirneva et al. 2015].

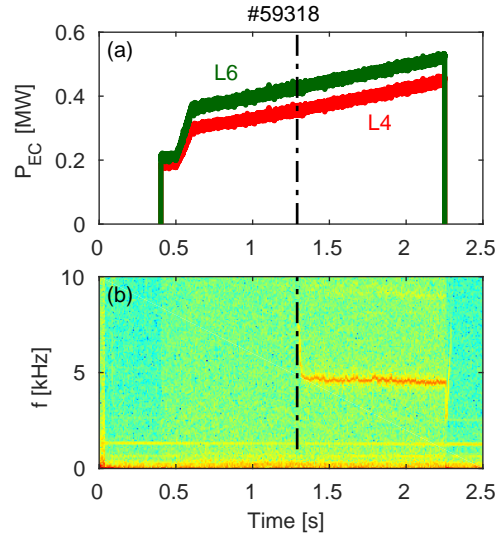


Figure 4.15. Experimental overview of an EC power ramp-up experiment with constant $n_{el} = 1.84 \times 10^{19} \text{ m}^{-3}$ and $I_p \approx -90 \text{ kA}$: (a) EC power traces; (b) 2/1 NTM spectrogram. Figure from [Kong et al. 2020].

To study $\bar{\rho}_{mn}\Delta'_{ohmic0}$ at higher densities (e.g. $n_{el} > 2.46 \times 10^{19} \text{ m}^{-3}$) that will allow interpolation for n_{el} up to $3 \times 10^{19} \text{ m}^{-3}$ as shown in figure 4.1, interpretative ASTRA simulations have been performed for an ohmic discharge with similar plasma shape and constant $I_p \approx -110 \text{ kA}$ (#58097). As shown in figure 4.16 (a), n_{el} ramps from 1×10^{19} to $4 \times 10^{19} \text{ m}^{-3}$ in this discharge. No NTM is observed during the entire density-ramp. The ASTRA results show that the local magnetic shear at 2/1 surface (s_{21}) increases along with n_{el} -ramp from 1×10^{19} to about $2.4 \times 10^{19} \text{ m}^{-3}$, whereas it stays relatively constant when n_{el} further ramps from 2.4×10^{19} to $4 \times 10^{19} \text{ m}^{-3}$, as illustrated in figure 4.16 (b). This is expected to be linked with the classical stability of the plasma ($\bar{\rho}_{mn}\Delta'_{ohmic0}$ in this case), as discussed in appendix A, and $\bar{\rho}_{mn}\Delta'_{ohmic0}$ is thus taken as a constant for $n_{el} \in [2.46, 4] \times 10^{19} \text{ m}^{-3}$, i.e. $\bar{\rho}_{mn}\Delta'_{ohmic0} = -1.2$ following

#59360.

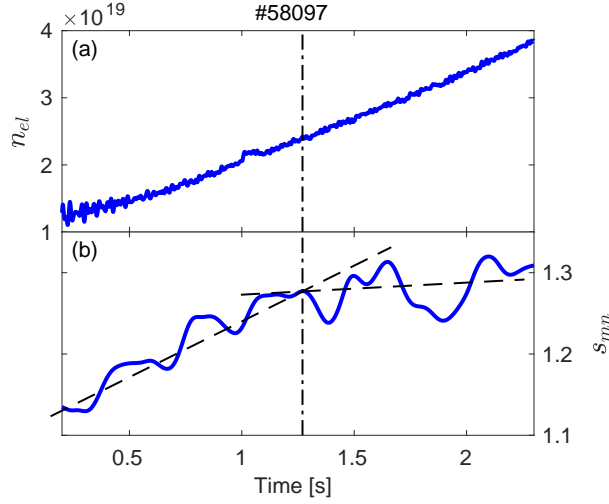


Figure 4.16. Overview of an ohmic discharge with density-ramp and $I_p \approx -110$ kA: (a) n_{el} trace from the experiment; (b) s_{21} inferred from ASTRA outputs. The two dashed black curves in (b) are included to guide the eyes.

Together with those estimated by simulations of #59151 ($I_p \approx -90$ kA, table 4.3), figure 4.17 summarizes $\bar{\rho}_{mn}\Delta'_{ohmic0}(n_{el})$ for $I_p \approx -90$ kA obtained from simulations with $k = 6$ and $a_3 = 1$ presented so far (blue circles). Apart from $\bar{\rho}_{mn}\Delta'_{ohmic0}$, a_3 in equation (3.7) is also expected to play a role in the triggerless onset of NTMs: a_3 affects the amplitude of $\bar{\rho}_{mn}\Delta'_{GGJ}$, which is another component of the mode onset condition (equation (4.4)).

To investigate the sensitivity of $\bar{\rho}_{mn}\Delta'_{ohmic0}-n_{el}$ mapping on a_3 , similar interpretative simulations of the power ramp-up experiments presented have been performed with $a_3 = 0.25$, following the value used in [Kong et al. 2019]. This generates a new set of $\bar{\rho}_{mn}\Delta'_{ohmic0}(n_{el})$, as marked by the black crosses in figure 4.17, which tend to be more negative than those estimated with $a_3 = 1$ (blue circles). This is as expected from the Δ'_0 model (equation (4.2)) used: with the same $kI_{cd,tot}/I_p$ but a smaller a_3 (thus a smaller $-\bar{\rho}_{mn}\Delta'_{GGJ}$ in equation (4.4)), $\bar{\rho}_{mn}\Delta'_{ohmic0}$ needs to be more negative to fit the occurrence of NTMs in the experiments. The shape of the $\bar{\rho}_{mn}\Delta'_{ohmic0}-n_{el}$ dependence, however, is very similar, as indicated by the cyan circles in figure 4.17, which are a shift of corresponding blue circles by -0.35 . This corresponds to an average value of the difference of $\bar{\rho}_{mn}\Delta'_{GGJ}$ with $a_3 = 0.25$ and 1 and confirms that for the triggerless onset of these NTMs, using a different a_3 mainly introduces a rigid shift to the absolute values of $\bar{\rho}_{mn}\Delta'_{ohmic0}$ to be used in the simulations, while the trend of the dependence and the main physics are retained.

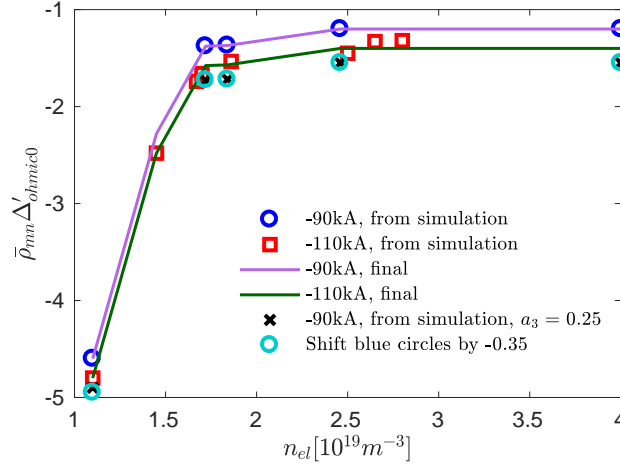


Figure 4.17. $\bar{\rho}_{mn}\Delta'_{ohmic0}$ — n_{el} mapping for different I_p (with $k = 6$), showing $\bar{\rho}_{mn}\Delta'_{ohmic0}(n_{el})$ for $I_p \approx -90$ kA (blue circles - estimated by simulating power-ramp experiments, purple curve - final mapping used, as will be discussed in section 4.3.3), and for $I_p \approx -110$ kA (red squares - estimated by power and density ramp experiments, green curve - a rigid shift of the purple curve by -0.2). Black crosses are obtained by simulating power-ramp and density-ramp experiments with $a_3 = 0.25$ and cyan circles are a rigid shift of the blue circles by -0.35 . Figure from [Kong et al. 2020]

4.3.3 Density-ramp experiments with constant EC power

To investigate the underlying mechanisms of the observed density range in figure 4.1, where all the discharges have $I_p \approx -110$ kA, $\bar{\rho}_{mn}\Delta'_{ohmic0}$ — n_{el} mapping for $I_p \approx -110$ kA is needed. This can in principle be carried out by simulating power-ramp experiments with $I_p \approx -110$ kA and different n_{el} levels, similar to sections 4.3.1 and 4.3.2. However, only two EC power ramp-up experiments with $I_p \approx -110$ kA are available so far, with constant $n_{el} = 1.45 \times 10^{19} m^{-3}$ (#56177) and $2.65 \times 10^{19} m^{-3}$ (#56605), respectively. Simulation of #56177 with $k = 6$ and $a_3 = 1$ estimates $\bar{\rho}_{mn}\Delta'_{ohmic0} = -2.48$ (table 4.4, $\alpha = 5$); following the same procedures as in previous sections, simulations of #56605 generate $\bar{\rho}_{mn}\Delta'_{ohmic0} = -1.33$ with $k = 6$ and $a_3 = 1$ (not detailed here for conciseness). Given the lack of power-ramp experiments with $I_p \approx -110$ kA, more $\bar{\rho}_{mn}\Delta'_{ohmic0}(n_{el})$ points can be inferred from simulations of density ramp-up or ramp-down experiments at constant EC power with $I_p \approx -110$ kA, where NTMs are typically triggered during the density ramp.

An iterative method used to get $\bar{\rho}_{mn}\Delta'_{ohmic0}$ — n_{el} mappings for different I_p

For simulations of each density-ramp experiment, a time-varying $\bar{\rho}_{mn}\Delta'_{ohmic0}$ (given its dependence on the time-varying n_{el}) is used, based on the linear interpolation of the mapping given in figure 4.17 (blue circles, with $I_p \approx -90$ kA and $a_3 = 1$), plus a small rigid shift (Δ'_{shift}) of

the interpolated $\bar{\rho}_{mn}\Delta'_{\text{ohmic0}}$ to consider different plasma conditions (e.g. different I_p), i.e.

$$\bar{\rho}_{mn}\Delta'_{\text{ohmic0}}(n_{el}) = \bar{\rho}_{mn}\Delta'_{\text{ohmic0,interp}}(n_{el}) + \bar{\rho}_{mn}\Delta'_{\text{shift}}, \quad (4.7)$$

where $\bar{\rho}_{mn}\Delta'_{\text{ohmic0,interp}}(n_{el})$ is the direct linear interpolation based on a given $\bar{\rho}_{mn}\Delta'_{\text{ohmic0}}(n_{el})$ mapping, $\bar{\rho}_{mn}\Delta'_{\text{shift}}$ a constant (with respect to n_{el} and thus time) shift added to match the appearance of the mode in the density-ramp experiment, and $\bar{\rho}_{mn}\Delta'_{\text{ohmic0}}(n_{el})$ the mapping used in the simulations eventually.

Based on simulations of different density-ramp experiments, table 4.5 summarizes the n_{el} level around mode onset at each experiment, the $\bar{\rho}_{mn}\Delta'_{\text{shift}}$ used and the resulting $\bar{\rho}_{mn}\Delta'_{\text{ohmic0}}$ at the n_{el} near mode onset. For power ramp-up experiments #56177 and #56605, no shift is added and $\bar{\rho}_{mn}\Delta'_{\text{ohmic0}}$ is determined following the same procedures presented in sections 4.3.1 and 4.3.2, as discussed previously. The "Original $\bar{\rho}_{mn}\Delta'_{\text{shift}}$ " in table 4.5 refers to the rigid shift added to fit the appearance of the mode in each experiment (with $I_p \approx -110$ kA), based on the direct interpolation of the $\bar{\rho}_{mn}\Delta'_{\text{ohmic0}}-n_{el}$ mapping for $I_p \approx -90$ kA given in figure 4.17 (blue circles). The resulting $\bar{\rho}_{mn}\Delta'_{\text{ohmic0}}$ for $I_p \approx -110$ kA at each n_{el} is labeled as "Original $\bar{\rho}_{mn}\Delta'_{\text{ohmic0}}$ " in table 4.5. Note that no mode is observed for #56291 in table 4.5 with a very low density $n_{el} = 1.1 \times 10^{19} \text{ m}^{-3}$; the corresponding $\bar{\rho}_{mn}\Delta'_{\text{ohmic0}}$ at this n_{el} level is estimated with the same method as used for the low density case #59358 discussed in section 4.3.2.

Table 4.5. $\bar{\rho}_{mn}\Delta'_{\text{ohmic0}}(n_{el})$ for $I_p \approx -110$ kA with $k = 6$ and $a_3 = 1$. Table from [Kong et al. 2020]

$n_{el} [10^{19} \text{ m}^{-3}]$	1.1	1.45	1.67	1.7	1.86	2.5	2.65	2.8
Original $\bar{\rho}_{mn}\Delta'_{\text{shift}}$	-0.2	N/A	-0.1	-0.17	-0.17	-0.25	N/A	-0.12
Original $\bar{\rho}_{mn}\Delta'_{\text{ohmic0}}$	-4.8	-2.48	-1.66	-1.55	-1.535	-1.45	-1.33	-1.32
Final $\bar{\rho}_{mn}\Delta'_{\text{shift}}$	-0.2	N/A	-0.18	-0.28	-0.17	-0.25	N/A	-0.12
Final $\bar{\rho}_{mn}\Delta'_{\text{ohmic0}}$	-4.8	-2.48	-1.74	-1.66	-1.535	-1.45	-1.33	-1.32
Based on #	56291	56177	58510	56044	56124	56607	56605	56593

The fact that the "Original $\bar{\rho}_{mn}\Delta'_{\text{shift}}$ " values (from -90 kA to -110 kA) in table 4.5 are negative at all n_{el} levels is consistent with the observations that TMs are more stable with larger I_p values [Kim 2015]. In addition to the sign, the "Original $\bar{\rho}_{mn}\Delta'_{\text{shift}}$ " at different n_{el} is also quite similar, e.g. with an average shift of about -0.168 . This confirms that $I_p \approx -110$ kA mainly leads to a rigid shift of the $\bar{\rho}_{mn}\Delta'_{\text{ohmic0}}-n_{el}$ mapping compared to that with $I_p \approx -90$ kA, which can actually be used in turn to estimate the corresponding $\bar{\rho}_{mn}\Delta'_{\text{ohmic0}}$ at a certain n_{el} with $I_p \approx -90$ kA. For example, with an opposite shift of $+0.168$ of the $\bar{\rho}_{mn}\Delta'_{\text{ohmic0}}$ at $n_{el} = 1.45 \times 10^{19} \text{ m}^{-3}$ and $I_p \approx -110$ kA (i.e. -2.48 as listed in table 4.5, #56177), an extra point at $n_{el} = 1.45 \times 10^{19} \text{ m}^{-3}$ can be added for $I_p \approx -90$ kA, i.e. with $\bar{\rho}_{mn}\Delta'_{\text{ohmic0}} = -2.312$.

The updated $\bar{\rho}_{mn}\Delta'_{\text{ohmic0}}-n_{el}$ mapping for $I_p \approx -90$ kA can then be interpolated and shifted again to simulate the density ramp-up experiments listed in table 4.5. A new set of $\bar{\rho}_{mn}\Delta'_{\text{shift}}$ is thus generated, leading to a new average $\bar{\rho}_{mn}\Delta'_{\text{shift}}$ to be used to infer the $\bar{\rho}_{mn}\Delta'_{\text{ohmic0}}$ at $n_{el} = 1.45 \times 10^{19} \text{ m}^{-3}$ for $I_p \approx -90$ kA, and so on. After three iterations, $\bar{\rho}_{mn}\Delta'_{\text{shift}}$ converges to

the order of 10^{-4}), so does the average $\bar{\rho}_{mn}\Delta'_{\text{shift}}$ and the updated mapping for $I_p \approx -90$ kA. The “Final $\bar{\rho}_{mn}\Delta'_{\text{shift}}$ ” and “Final $\bar{\rho}_{mn}\Delta'_{\text{ohmic0}}$ ” in table 4.5 represent the final values obtained after these iterations, with an average $\bar{\rho}_{mn}\Delta'_{\text{shift}}$ of -0.2 . The resulting $\bar{\rho}_{mn}\Delta'_{\text{ohmic0}}(n_{el})$ for $I_p \approx -110$ kA is plotted as the red trace with squares in figure 4.17, while the updated mapping for $I_p \approx -90$ kA (i.e. with one extra point at $n_{el} = 1.45 \times 10^{19} \text{ m}^{-3}$) is shown by the purple curve. The green curve in figure 4.5 is a rigid shift of the dashed purple trace by the average shift -0.2 and represents the final $\bar{\rho}_{mn}\Delta'_{\text{ohmic0}} - n_{el}$ mapping for $I_p \approx -110$ kA, which will be used in section 4.4 to study the observed density range for mode onset in the test discharges (figure 4.1).

A density-ramp experiment with constant EC power

To better illustrate the density-ramp experiments and simulations mentioned above, this section presents a density ramp-up experiment in TCV with constant total EC power (#56044 in table 4.5). The onset and evolution of 2/1 NTMs with varying n_{el} through interpretative simulations with the MRE will also be discussed. As shown in figure 4.18, EC power is switched on at $t = 0.4$ s and kept constant at 0.96 MW during $t = [0.45, 2.4]$ s. Similar to the experiments shown in previous sections, all the EC launchers are set to drive co-ECCD near the plasma center with constant $I_p \approx -110$ kA. A 2/1 mode is triggered during the density ramp-up and appears at $t = 0.835$ s with $n_{el} \approx 1.7 \times 10^{19} \text{ m}^{-3}$. The 2/1 mode is then sustained and evolves along with the density-ramp and disappears quickly when completely turning off the EC power at $t = 2.4$ s.

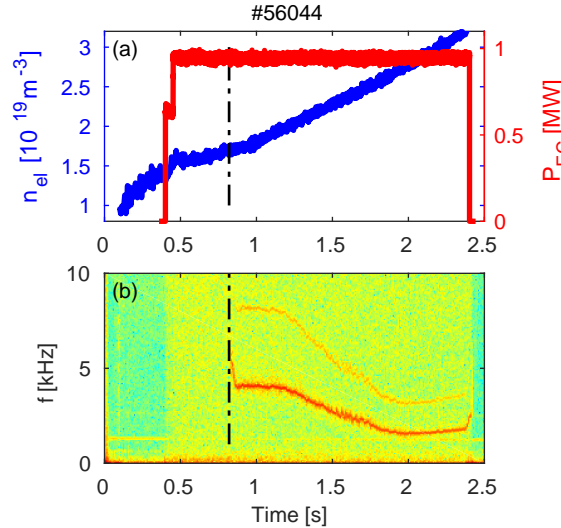


Figure 4.18. Experimental overview of a density ramp-up experiment with constant EC power (0.96 MW) during $t = [0.45, 2.4]$ s and $I_p \approx -110$ kA. (a) n_{el} trace (blue) and the total EC power from all the EC launchers (red); (b) NTM spectrogram. $I_{cd,tot}$ during the density-ramp, taken from TORAY-GA outputs, can be inferred from the dash-dotted red curve in figure 4.21. Figure from [Kong et al. 2020].

As shown in figure 4.19 and similar to the discussions in previous sections, two measurement points labeled as “A” and “B” are used as the constraints determining $\bar{\rho}_{mn}\Delta'_{\text{ohmic0}}$ (the rigid $\bar{\rho}_{mn}\Delta'_{\text{shift}}$ in this case) and $\bar{\rho}_{mn}\Delta'_{\text{sat}}$ in the simulations. “A” represents the first measurement point available and “B” is at $t = 1$ s, i.e. before a faster ramp of n_{el} . The corresponding χ of each simulation, as defined by equation (4.5), is evaluated with all the measurement points between “A” and “C” to consider the entire w evolution during the density ramp. Similar to previous simulations, a_2 has been adjusted to match the experimental $\frac{dw}{dt}$ trace, as illustrated in figure 4.20, where $a_2 = 1$ has been used. Constant $k = 6$ and $a_3 = 1$ are fixed as discussed before, while α is adjusted to minimize χ .

 Table 4.6. #56044, parameters for simulations with different a_3

a_3	k	α	a_2	$\bar{\rho}_{mn}\Delta'_{\text{ohmic0,interp}}$	$\bar{\rho}_{mn}\Delta'_{\text{shift}}$	$\bar{\rho}_{mn}\Delta'_{\text{sat}}$	χ
1	6	5.5	1.0	Purple trace in figure 4.17	-0.28	-0.57	3.36%
0.25	6	3.3	1.0	Black crosses in figure 4.17	-0.23	-0.67	3.74%

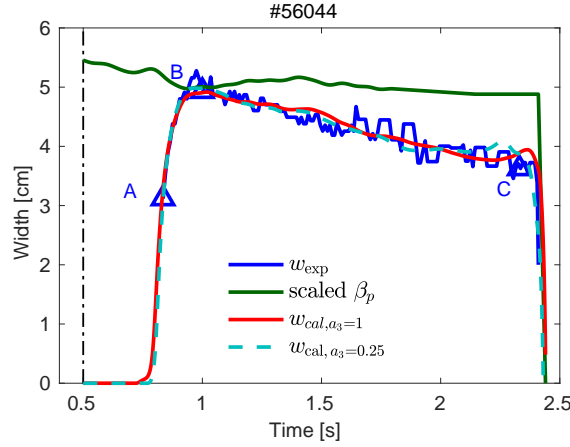


Figure 4.19. Island width evolution of #56044 (figure 4.18). Solid blue: measurement; solid green: scaled β_p based on equation (4.3), with $t_{\text{ref}} = 1$ s and $\beta_p(t_{\text{ref}}) = 0.77$; solid red: simulation with $a_3 = 1$ and parameters in table 4.6; dashed cyan: simulation with $a_3 = 0.25$ and parameters in table 4.6. Blue triangles labeled as A and B: the two constraints used to determine $\bar{\rho}_{mn}\Delta'_{\text{ohmic0}}$ and $\bar{\rho}_{mn}\Delta'_{\text{sat}}$; A to C: the range within which χ (equation (4.5)) in table 4.6 is evaluated. Figure from [Kong et al. 2020].

The best fit obtained is plotted as the solid red curve in figure 4.19, with $\chi = 3.36\%$. As mentioned in section 4.3.2, simulation has also been performed with $a_3 = 0.25$, together with the corresponding $\bar{\rho}_{mn}\Delta'_{\text{ohmic0}} - n_{el}$ mapping for $a_3 = 0.25$ (black crosses in figure 4.17) and a rigid shift to fit the appearance of NTMs in the experiment. The set of parameters used in these two simulations of #56044 are listed in table 4.6, and the best fit with $a_3 = 0.25$ is depicted by the dashed cyan curve in figure 4.19. It can be seen that $a_3 = 0.25$ (with the corresponding $\bar{\rho}_{mn}\Delta'_{\text{ohmic0}}$ in figure 4.17) can also fit well the w evolution, confirming that the exact value of a_3 is not playing a dominant role in the w evolutions in our discharges. This is consistent with the w -dependence and relative amplitude of each term in the MRE: once NTMs appear, the amplitude of $\bar{\rho}_{mn}\Delta'_{GGJ}$ decreases sharply given its $1/w$ dependence

(equation (3.7)); the $\bar{\rho}_{mn}\Delta'_{GGJ}$ at finite w (e.g. 2 ~ 6 cm) is much smaller than $\bar{\rho}_{mn}\Delta'$ and $\bar{\rho}_{mn}\Delta'_{BS}$ in our test discharges. Therefore, the island width evolution after the mode occurs is dominated by $\bar{\rho}_{mn}\Delta'$ and $\bar{\rho}_{mn}\Delta'_{BS}$ and is not affected much by a_3 . One would need accurate w measurements at [0, 1.5] cm to see the difference.

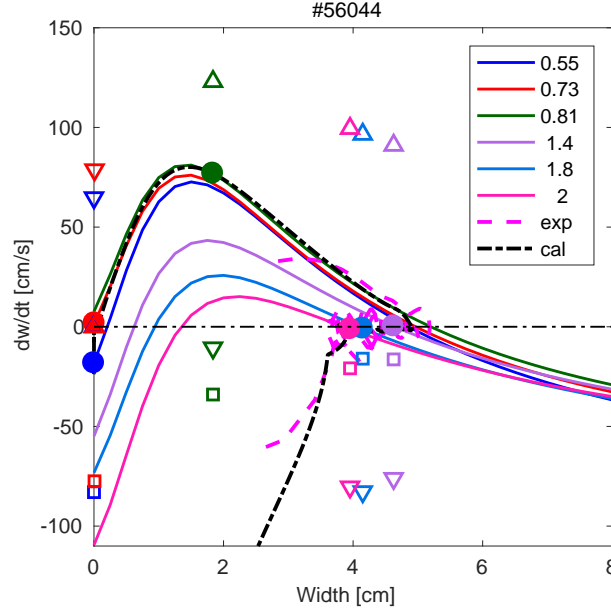


Figure 4.20. $\frac{dw}{dt}(w)$ traces at several time slices of the simulation with $a_3 = 1$ (solid red curve in figure 4.19), showing EC-heated plasma without mode ($t = 0.55$ s), 2/1 mode onset with $\frac{dw}{dt}(w = 0) > 0$ ($t = 0.73$ s), mode grows to about 2 cm quickly with large $\frac{dw}{dt}$ ($t = 0.81$ s), $w_{\text{sat}} \approx 4.8$ cm ($t = 1.4$ s) and $w_{\text{sat}} \approx 4$ cm ($t = 1.8$ s and $t = 2$ s). Dash-dotted black curve: $\frac{dw_{\text{cal}}}{dt}(w_{\text{cal}})$ from the simulation; dashed magenta: $\frac{dw_{\text{exp}}}{dt}(w_{\text{exp}})$ taken from measurement. $\frac{dw}{dt}$ at the w_{cal} of each time slice are marked by the solid circles with corresponding colors. $\bar{\rho}_{mn}\Delta'$ (downward-pointing triangles), $\bar{\rho}_{mn}\Delta'_{BS}$ (upward-pointing triangles) and $\bar{\rho}_{mn}\Delta'_{GGJ}$ (squares) at the w_{cal} of each time slice, divided by $\tau_R/\bar{\rho}_{mn}$, are also listed.

To better illustrate the simulated mode onset and the time evolution of $\bar{\rho}_{mn}\Delta'_0$ along with the ramp-up of density, various components of $\bar{\rho}_{mn}\Delta'_0$ (equation (4.2)) of the simulation with $a_3 = 1$ (solid red curve in figure 4.19) are depicted in figure 4.21. As indicated by the dashed blue curve, time-varying $\bar{\rho}_{mn}\Delta'_{\text{ohmic0}}$ is used in the simulation along with the ramp-up of density, based on an interpolation of the $\bar{\rho}_{mn}\Delta'_{\text{ohmic0}} - n_{el}$ mapping for $I_p \approx -90$ kA (solid purple curve in figure 4.17) and a constant $\bar{\rho}_{mn}\Delta'_{\text{shift}} = -0.28$. $kI_{\text{cd,tot}}/I_p$ (dash-dotted red trace) decreases along with the ramp-up of density due to a drop of current drive efficiency (thus $I_{\text{cd,tot}}$) with higher density and constant power. This is the main drive for the decrease of w between B and C (figure 4.19) and explains why w_{sat} does not follow the β_p trace (green curve in figure 4.19). 100% absorption of the EC beams is maintained up to $t = 2$ s when n_{el} reaches about $2.8 \times 10^{19} \text{ m}^{-3}$, and then quickly drops along with the further increase of n_{el} , explaining the observed faster decrease of $I_{\text{cd,tot}}/I_p$ after $t = 2$ s (dash-dotted curve in figure 4.21). $\bar{\rho}_{mn}\Delta'_0$ shown by the solid green trace results from the sum of the blue and red curves,

as defined by equation (4.2). $\bar{\rho}_{mn}\Delta'_{GGJ}$ varies with w and time, but only the amplitude at $w = 0$ (e.g. at mode onset) is shown in figure 4.21 (dotted black line). Based on the onset condition (equation (4.4)), $\bar{\rho}_{mn}\Delta'_0$ counteracts the stabilizing $\bar{\rho}_{mn}\Delta'_{GGJ}$ at $w = 0$, leading to $\frac{dw}{dt}(w = 0) > 0$ at $t = 0.78$ s and thus the onset of the mode. The finite w then modifies $\bar{\rho}_{mn}\Delta'$ based on its w dependence, defined in equation (3.25), and deviates from $\bar{\rho}_{mn}\Delta'_0$ after mode onset (at $t = 0.78$ s).

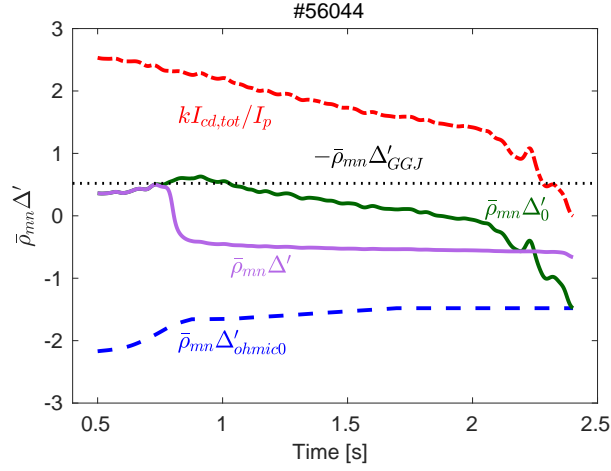


Figure 4.21. Various components of $\bar{\rho}_{mn}\Delta'_0$ for the simulation with $a_3 = 1$ (solid red curve in figure 4.19). Dashed blue: time-varying ohmic contribution to $\bar{\rho}_{mn}\Delta'_0$ based on the $\bar{\rho}_{mn}\Delta'_{ohmic0} - n_{el}$ mapping shown by the purple curve in figure 4.17 and a constant $\bar{\rho}_{mn}\Delta'_{shift} = -0.28$; red dash-dotted: the contribution of ECCD to $\bar{\rho}_{mn}\Delta'_0$; solid green: $\bar{\rho}_{mn}\Delta'_0$ based on the sum of the ohmic and ECCD contribution (equation (4.2)); dotted black: the amplitude of $\bar{\rho}_{mn}\Delta'_{GGJ}$ at $w = 0$; solid purple: $\bar{\rho}_{mn}\Delta'$ (equation (3.25)), deviating from $\bar{\rho}_{mn}\Delta'_0$ (solid green) after mode onset (at $t = 0.78$ s) based on its w dependence. Figure from [Kong et al. 2020].

Similar density ramp-up experiments with higher EC power or density ramp-down experiments at different EC power levels have also been performed, for example as listed in table 4.5. Following the same procedures shown in this section, corresponding interpretative simulations with the MRE prove to fit well the evolution of 2/1 NTMs in all the cases, not detailed here for conciseness. As mentioned, the $\bar{\rho}_{mn}\Delta'_0$ model developed in this section has also been applied in the interpretative simulations of NTM control experiments in TCV, as will be presented in chapter 5, for NTM stabilization and prevention cases where both central and off-axis co-ECCD are involved.

4.4 Recovery of the observed density range

It is interesting to explore the density effect on the triggerless onset of NTMs observed in numerous TCV discharges (section 4.2.2) with the Δ'_0 model developed in section 4.3. We have obtained the n_{el} -dependence of $\bar{\rho}_{mn}\Delta'_{ohmic0}$ in section 4.3 (table 4.5 and figure 4.17 for $I_p \approx -110$ kA), it remains to determine the n_{el} -dependence of $I_{cd,tot}$ in equation (4.2). This

can be inferred from $I_{cd,tot}$ at various n_{el} levels computed by TORAY-GA.

As shown in figure 4.22, a linear dependence of $I_{cd,tot}$ on $P_{ec,tot}/n_{el}$ is obtained based on various TCV discharges with different central co-ECCD power and n_{el} but similar plasma shape:

$$\frac{I_{cd,tot}}{I_{ref}} = c \cdot \frac{P_{ec,tot}}{P_{ec,ref}} \frac{n_{el}}{n_{el,ref}}, \quad (4.8)$$

where $P_{ec,tot}$ is the total absorbed EC power of all the EC beams. Note that the n_{el} dependence in equation (4.8) is as expected from the current drive efficiency of ECCD beams [Cohen 1987; Lin-Liu et al. 2003, and references therein]. With $I_{ref} = -110$ kA, $n_{el,ref} = 1.72 \times 10^{19} \text{ m}^{-3}$ and $P_{ec,ref} = 1$ MW, the fitting gives $c = 0.356$, as indicated by the dashed black line in figure 4.22. To investigate the range and effects of c , linear curves with $c = 0.32$ and 0.39 (i.e. $\pm 10\%$ with respect to $c = 0.356$) are shown by the dotted black lines.

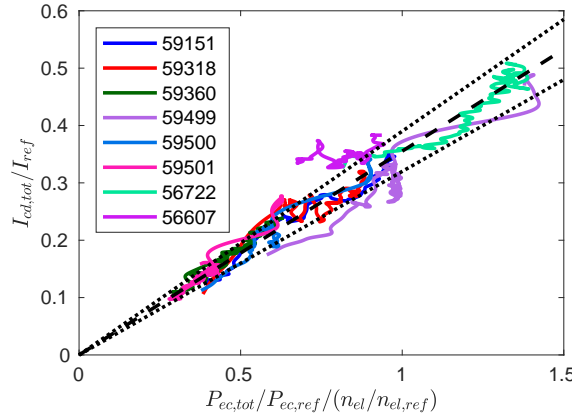


Figure 4.22. Linear dependence of $I_{cd,tot}$ (from TORAY-GA) on $P_{ec,tot}/n_{el}$ in the test discharges, based on the fitting of various TCV experiments (shown in the legend). #56722 and #56607 are with $I_p \approx -110$ kA, while all the other discharges have $I_p \approx -90$ kA. The fit with $c = 0.356$ is shown by the dashed black curve, while fits with $c = 0.32$ and 0.39 (i.e. $\pm 10\%$ with respect to $c = 0.356$) are shown by the dotted black lines. Figure from [Kong et al. 2020].

Based on equation (4.8) and the $\bar{\rho}_{mn}\Delta'_{ohmic0} - n_{el}$ mapping for $I_p \approx -110$ kA (green trace in figure 4.17), Δ'_0 can be evaluated for each given $n_{el} \in [1.1, 3] \times 10^{19} \text{ m}^{-3}$. Figure 4.23 shows $\frac{dw}{dt}(w=0)$, i.e. $\bar{\rho}_{mn}\Delta'_0 + \bar{\rho}_{mn}\Delta'_{GGJ}$ at different n_{el} and EC power levels, with a fixed $\bar{\rho}_{mn}\Delta'_{GGJ} = -0.5$, which is an average value of the test discharges before mode onset (i.e. $w = 0$) with $a_3 = 1$. The dashed lines in figure 4.23 represent the $kI_{cd,tot}/I_p$ contribution to $\bar{\rho}_{mn}\Delta'_0$ evaluated at different EC power and n_{el} levels based on equation (4.8), with $I_p = -110$ kA (as used in the discharges shown in figure 4.1), fixed $k = 6$ and $c = 0.356$. The solid magenta curve depicts the sum of $\bar{\rho}_{mn}\Delta'_{ohmic0}$ evaluated based on the interpolation of the $\bar{\rho}_{mn}\Delta'_{ohmic0} - n_{el}$ mapping for $I_p \approx -110$ kA (green trace in figure 4.17) and the constant $\bar{\rho}_{mn}\Delta'_{GGJ} = -0.5$, i.e. representing the $\frac{dw}{dt}(w=0)$ in ohmic plasmas. The sum of different dashed lines with the solid magenta curve generates the total $\frac{dw}{dt}(w=0)$ at different EC power levels, as indicated by the solid

lines in corresponding colors. $\frac{dw}{dt}(w=0) > 0$ predicts the triggerless onset of NTMs while $\frac{dw}{dt}(w=0) \leq 0$ predicts stable plasmas. The EC power levels have been chosen to facilitate the comparison between figure 4.23 and figure 4.1.

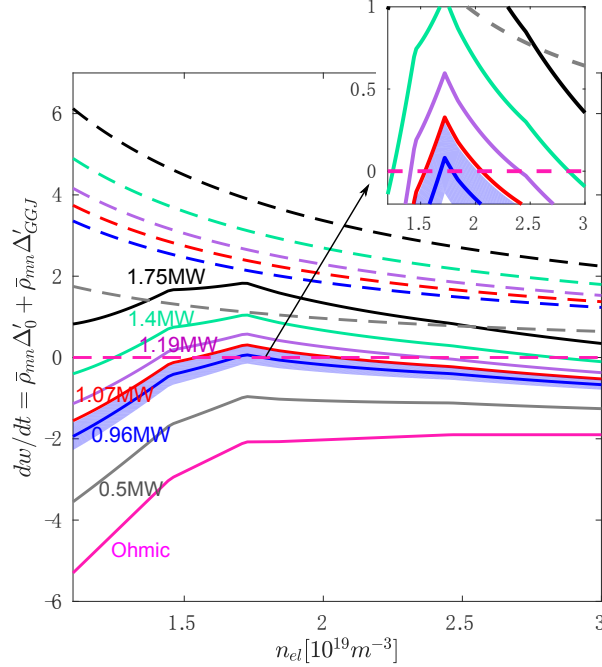


Figure 4.23. Model predictions for mode onset at $I_p \approx -110$ kA (figure 4.1), i.e. $\frac{dw}{dt}(w=0) \equiv \bar{\rho}_{mn}\Delta'_0 + \bar{\rho}_{mn}\Delta'_{GGJ}$ evaluated at different n_{el} and $P_{ec,tot}$, based on the Δ'_0 model (equation (4.2)). Dashed lines: the $kI_{cd,tot}/I_p$ contribution to $\bar{\rho}_{mn}\Delta'_0$ with different $P_{ec,tot}$ and n_{el} levels based on equation (4.8) (with $k=6$ and $c=0.356$); solid magenta curve: the sum of $\bar{\rho}_{mn}\Delta'_{ohmic0}$ evaluated by the interpolation of the $\bar{\rho}_{mn}\Delta'_{ohmic0}-n_{el}$ mapping for $I_p \approx -110$ kA (green trace in figure 4.17) and a constant $\bar{\rho}_{mn}\Delta'_{GGJ} = -0.5$, i.e. representing the total $\frac{dw}{dt}(w=0)$ in ohmic plasmas; other solid traces in corresponding colors as the dashed ones: the sum of different dashed lines with the solid magenta curve, representing the total $\frac{dw}{dt}(w=0)$ with different $P_{ec,tot}$ levels. Filled light blue area: the estimated density range for $P_{ec,tot} = 0.96$ MW with $c \in [0.32, 0.39]$. Figure from [Kong et al. 2020].

It can be seen that figure 4.23 reproduces well the observed n_{el} and $P_{ec,tot}$ dependence of the triggerless onset of 2/1 NTMs in TCV (with $I_p \approx -110$ kA, figure 4.1), i.e. NTMs only occur within a certain range of n_{el} and this range tends to broaden with higher $P_{ec,tot}$. As summarized in table 4.7, for $I_p \approx -110$ kA, triggerless NTMs are predicted to occur with $n_{el} \in [1.65, 1.8] \times 10^{19} \text{ m}^{-3}$ for $P_{ec,tot} = 0.96$ MW (blue), $n_{el} \in [1.55, 2.1] \times 10^{19} \text{ m}^{-3}$ for $P_{ec,tot} = 1.07$ MW (red), $n_{el} \in [1.4, 2.4] \times 10^{19} \text{ m}^{-3}$ for $P_{ec,tot} = 1.19$ MW (purple), and $n_{el} \in [1.25, 2.8] \times 10^{19} \text{ m}^{-3}$ for $P_{ec,tot} = 1.4$ MW (cyan). With $P_{ec,tot} = 1.75$ MW (black), NTMs are expected to occur within the entire tested range ($n_{el} = 1.1 \sim 3 \times 10^{19} \text{ m}^{-3}$). All of these are in close agreement with the experiments summarized in figure 4.1. Note that the slightly narrower density ranges predicted by the model than those observed in the experiments (e.g. for $P_{ec,tot} = 0.96$ MW and $P_{ec,tot} = 1.07$ MW) can be explained by the error bars of fitting the $I_{cd,tot}(P_{ec,tot}/n_{el})$ dependence (figure 4.22). With a slightly different coefficient c in equation (4.8), the exact values of the density

ranges are affected. As an example, the computed density range for NTM onset with $P_{\text{ec,tot}} = 0.96 \text{ MW}$ and $c \in [0.32, 0.39]$ is depicted by the filled light blue area in figure 4.23.

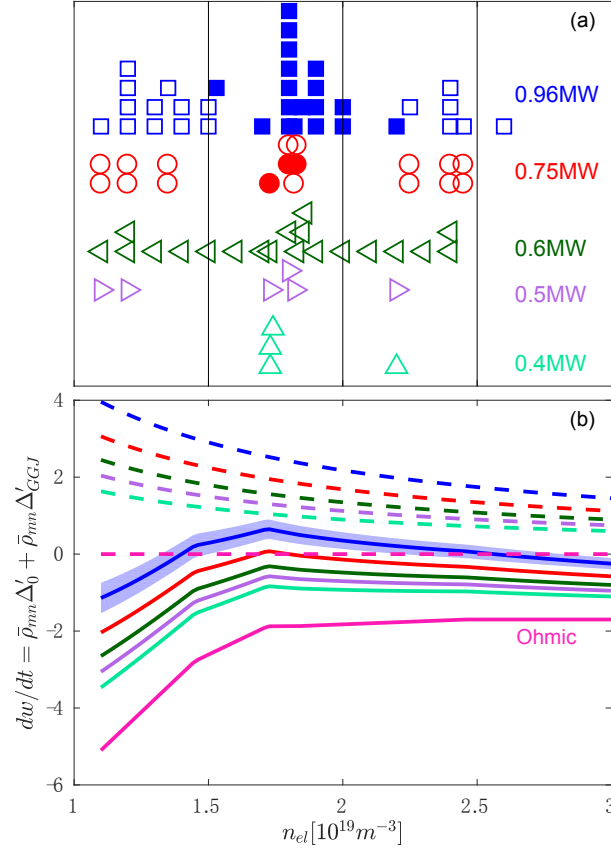


Figure 4.24. Experimental observations (a) and model predictions (b) of the density range for mode onset at $I_p \approx -90 \text{ kA}$. (a) A collection of 88 stationary instances taken from 42 TCV discharges with $I_p \approx -90 \text{ kA}$ and different n_{el} and $P_{\text{ec,tot}}$. Solid symbols: 2/1 NTM triggered; open symbols: no NTMs. (b) $\frac{dw}{dt}(w=0) \equiv \bar{\rho}_{mn}\Delta'_0 + \bar{\rho}_{mn}\Delta'_{\text{GGJ}}$ evaluated at different n_{el} and $P_{\text{ec,tot}}$, based on the Δ'_0 model (equation (4.2)). Dashed lines: $kI_{\text{cd,tot}}/I_p$ contribution to $\bar{\rho}_{mn}\Delta'_0$ at different $P_{\text{ec,tot}}$ and n_{el} levels (with $k = 6$ and $c = 0.356$); solid magenta: the sum of $\bar{\rho}_{mn}\Delta'_{\text{ohmic0}}$ (evaluated based on the $\bar{\rho}_{mn}\Delta'_{\text{ohmic0}} - n_{el}$ mapping for $I_p \approx -90 \text{ kA}$ shown by the purple trace in figure 4.17) and a constant $\bar{\rho}_{mn}\Delta'_{\text{GGJ}} = -0.5$; other solid lines with corresponding colors as the dashed ones: the sum of different dashed lines with the solid magenta curve, i.e. the total $\frac{dw}{dt}(w=0)$ at different $P_{\text{ec,tot}}$ levels. Filled light blue area: estimated density range for $P_{\text{ec,tot}} = 0.96 \text{ MW}$ with $c \in [0.32, 0.39]$ and $I_p \approx -90 \text{ kA}$. Figure from [Kong et al. 2020].

A similar exercise has been performed for discharges with $I_p \approx -90 \text{ kA}$, as illustrated in figure 4.24 and summarized in table 4.7. Similar to figure 4.1, figure 4.24 (a) displays 88 instances taken from 42 TCV discharges with $I_p \approx -90 \text{ kA}$ at different n_{el} and $P_{\text{ec,tot}}$ levels, exhibiting similar effects: there is a density range for the triggerless onset of these NTMs and the range tends to broaden with increasing $P_{\text{ec,tot}}$. Compared to the case with $I_p \approx -110 \text{ kA}$ and $P_{\text{ec,tot}} = 0.96 \text{ MW}$ (i.e. blue squares in figure 4.1), the fact that there is a slightly wider n_{el} range for mode onset (i.e. $[1.53, 2.2] \times 10^{19}$ versus $[1.54, 2] \times 10^{19} \text{ m}^{-3}$), and that the case with $I_p \approx -90 \text{ kA}$ is less

marginal for mode onset with the same EC power (i.e. only solid symbols are involved within the given n_{el} range) indicate the plasma is more unstable to TMs with smaller amplitude of I_p , which justifies the proposed $I_{cd,tot}/I_p$ dependence in equation (4.2).

Following the same procedures and as shown in figure 4.24 (b), the onset of NTMs with $I_p \approx -90$ kA also proves to be well reproduced by the Δ'_0 model. Different colors represent different EC power levels, the same as used in figure 4.24 (a). The $\bar{\rho}_{mn}\Delta'_{ohmic0}-n_{el}$ mapping for $I_p \approx -90$ kA is used to evaluate $\bar{\rho}_{mn}\Delta'_{ohmic0}$ at different n_{el} , as indicated by the solid magenta trace, which corresponds to the purple curve in figure 4.17 plus a constant $\bar{\rho}_{mn}\Delta'_{GGJ} = -0.5$, similar to that in figure 4.23. The dashed traces represent $kI_{cd,tot}/I_p$ contribution to $\bar{\rho}_{mn}\Delta'_0$ evaluated at different EC power and n_{el} levels based on equation (4.8) with $I_p = -90$ kA, $k = 6$, $I_{ref} = -110$ kA and $c = 0.356$. The sum of different dashed lines with the solid magenta curve generates the total $\frac{dw}{dt}(w = 0)$ at different EC power levels, as indicated by the solid lines in corresponding colors. Similarly, the computed density range for NTM onset with $P_{ec,tot} = 0.96$ MW and $c \in [0.32 \ 0.39]$ is depicted by the filled light blue area in figure 4.24 (b).

Table 4.7. Predicted n_{el} range for mode onset at different central EC power levels

I_p [kA]	Central EC power [MW]	n_{el} range for mode onset [10^{19} m^{-3}]
110	0.96	Marginal mode onset within [1.65, 1.8]
	1.07	[1.55, 2.1]
	1.19	[1.4, 2.4]
	1.4	[1.25, 2.8]
	1.75	wider than [1.1, 3]
90	< 0.75	Unconditionally stable to all n_{el}
	0.75	1.8
	0.96	[1.53, 2.2]

It can be seen that figure 4.24 (b) reproduces well the observed n_{el} and $P_{ec,tot}$ dependence of the triggerless onset of 2/1 NTMs shown in figure 4.24 (a), in terms of the n_{el} range for $P_{ec,tot} = 0.96$ MW (blue), the NTM onset only at $n_{el} \approx 1.8 \times 10^{19} \text{ m}^{-3}$ with $P_{ec,tot} = 0.75$ MW (red) and no mode with even lower near-axis co-ECCD power (green, purple and cyan). From these discussions, one can see that the observed n_{el} -range for the triggerless onset of NTMs in the tested discharges is consistent with the n_{el} -dependence of the stability of ohmic plasmas and the n_{el} -dependence of the current drive efficiency of co-ECCD beams predicted by our model. The Δ'_0 model defined by equation (4.2), appearing simple, proves to describe well the main variations of Δ'_0 at different density and EC power levels. More theoretical inputs that can link the proposed dependence more directly with the details of q and j profiles, such as ρ_{mn} and s_{mn} , are desired to further understand this model.

4.5 Discussions

4.5.1 Effects of rotation on the triggerless onsets of NTMs in TCV

Previous studies show that plasma rotation may play a role in the onset of NTMs [Gerhardt et al. 2009; Buttery et al. 2008, and references therein]. To explore the possible effects of rotation on the onset of 2/1 NTMs in the test discharges, dedicated power-scan and density-scan experiments have been performed, along with the measurements of rotation profiles by a charge exchange recombination spectroscopy (CXRS) system in TCV [Marini 2017]. The experiments have been programmed such that a certain density or EC power is kept constant for a sufficiently long time, typically 0.5 s, i.e. much longer than the resistive time scale in the discharges ($0.05 \sim 0.1$ s). $I_p \approx -90$ kA and similar plasma shapes have been used in all the experiments presented in this section. The measured toroidal velocity (v_{tor}) profiles of the carbon impurities at different EC power and density levels are shown in figures 4.25 (a) and (b), respectively, where each trace is taken from the average of several time slices with the same EC power and density level. ρ_ψ in the figures refers to the normalized radial location based on the square root of the poloidal flux Ψ .

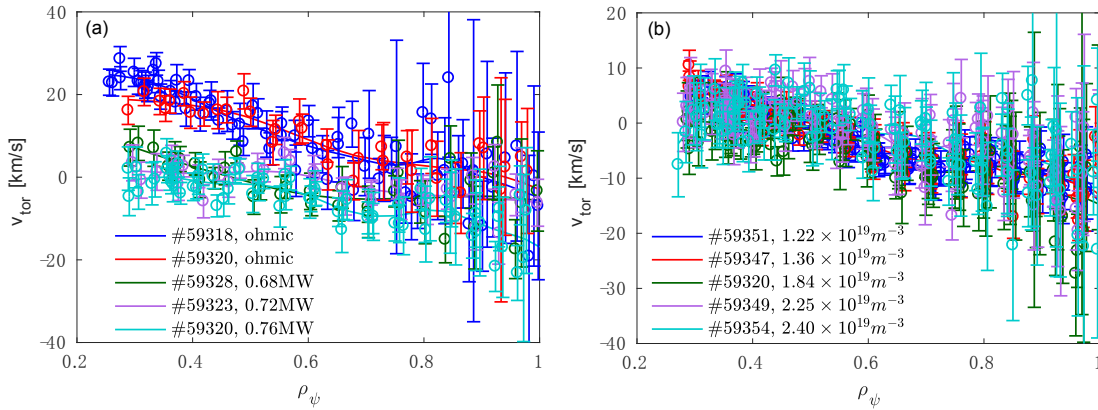


Figure 4.25. Toroidal rotation profiles (a) with constant $n_{el} = 1.84 \times 10^{19} \text{ m}^{-3}$ but various EC power levels as indicated by the legend and (b) with constant $P_{\text{ec,tot}} = 0.76 \text{ MW}$ but various n_{el} levels as indicated by the legend. Measurements at several time slices (without the appearance of NTMs) are used in each case. Figure from [Kong et al. 2020].

In figure 4.25 (a), the series of experiments have the same $n_{el} = 1.84 \times 10^{19} \text{ m}^{-3}$, whereas different near-axis co-ECCD power levels are involved. The EC power threshold for triggering 2/1 NTMs in these cases is about 0.76 MW, determined by the power ramp-up experiment (#59318) shown in figure 4.15. Based on #59318, constant EC power around 0.76 MW has been used in #59328, #59323 and #59320. No NTMs were observed in ohmic plasmas (i.e. $P_{\text{ec,tot}} = 0$), #59328 (0.68 MW) or #59323 (0.72 MW), whereas 2/1 mode occurred about 0.1 s after reaching $P_{\text{ec,tot}} = 0.76 \text{ MW}$ in #59320, as expected. As we only consider here the effects of rotation on mode onset (i.e. before the occurrence of a mode), the v_{tor} profile with $P_{\text{ec,tot}} = 0.76 \text{ MW}$ in #59320 (i.e. the cyan trace in figure 4.25 (a)) is averaged over the time slices *before* the

appearance of the mode to avoid introducing the modifications of rotation profile by NTMs discussed in [Lazzaro et al. 2015].

It can be seen from figure 4.25 (a) that ν_{tor} is driven towards the co- I_p direction (more negative values) with the application of co-ECCD beams, similar to previous observations in TCV [Lazzaro et al. 2015; Sauter et al. 2010]. Within the error bars, the rotation profiles near the threshold of mode onset (green, purple and cyan traces in figure 4.25 (a)) largely overlap, i.e. there is no noticeable change of rotation right before the onset of these NTMs. This indicates that plasma rotation is not playing a dominant role in the onset of NTMs in our discharges. Meanwhile, the fact that no mode is triggered with the relatively large change of rotation profiles from ohmic to EC-heated plasmas also implies a less important role of rotation on the mode onset in these discharges - there is a larger change in the rotation profile from ohmic plasmas (blue and red) to $P_{\text{ec,tot}} = 0.68 \text{ MW}$ case (green) than with a further increase of $P_{\text{ec,tot}}$.

Figure 4.25 (b) illustrates the ν_{tor} profiles at different n_{el} levels, with constant $P_{\text{ec,tot}} = 0.76 \text{ MW}$ in all cases. NTMs only occurred in #59320 with $n_{\text{el}} = 1.84 \times 10^{19} \text{ m}^{-3}$ and we take the time slices before the mode onset to get the ν_{tor} profile in this case, as discussed above. It can be seen that the rotation profiles with different density levels once again overlap with each other within the error bars, confirming that rotation does not play a dominant role in the onset of NTMs in the discharges presented in this chapter. It is Δ'_0 that dominates the mode onset, as detailed in previous sections. Note that with the existence of NTMs (i.e. after mode onset), the rotation profiles become non-monotonic with a vanishing shear around the mode location (not involved in the figures) due to a neoclassical toroidal viscosity effect [Lazzaro et al. 2015], but is not discussed here as we only concentrate on how the rotation profile affects mode onset instead of *vice versa*.

4.5.2 Contribution of pure heating to the triggerless onset of NTMs

As discussed in section 4.3 and section 4.4, the simple model for Δ'_0 (equation (4.2)) has proven to explain well the triggerless onset of NTMs observed in TCV discharges with strong near-axis central co-ECCD. Further improvement of the model is foreseen with more theoretical inputs and more experiments with different settings. For example, heating effects from ECH or ECCD beam depositions are also expected to affect the current density and q profiles, thus affecting Δ'_0 and the triggerless onset of NTMs. Note that the deposition of ECCD beams leads to both current drive and heating effects that can affect the stability of plasmas, which in equation (4.2) have been incorporated by the $kI_{\text{cd,tot}}/I_p$ term. In this section, a first attempt to separate the effect of heating and current drive on Δ'_0 is presented, by using

$$\bar{\rho}_{mn}\Delta'_0 = \bar{\rho}_{mn}\Delta'_{\text{ohmic0}} + k_{cd}\frac{I_{\text{cd,tot}}}{I_p} + k_h\frac{P_{\text{ec,tot}}}{P_{\text{ref}}}, \quad (4.9)$$

where k in equation (4.2) has been separated into k_{cd} and k_h , and at this stage, the total absorbed EC power ($P_{\text{ec,tot}}$) has been chosen as a representation of the heating effect. The

coefficients k_{cd} and k_h can be estimated by interpretative simulations of experiments where different combinations of heating and current drive are involved.

In this respect, a series of EC power ramp-up experiments presented in [Lazzaro et al. 2015] - #48836, #48837 and #48841 are selected and preliminary simulations are performed. Constant $I_p \approx -115$ kA and $n_{el} = 1.72 \times 10^{19} \text{ m}^{-3}$ were kept in these three experiments, with the same plasma triangularity $\delta \approx 0.25$ as used in the experiments shown in this chapter but a slightly larger elongation κ (1.42 instead of 1.3). Three independent EC launchers were used in each experiment, depositing EC beams near the plasma center. The EC power traces were kept the same among the three experiments, whereas different toroidal angles were set to allow for different combinations of ECH and ECCD. Specifically, all three launchers were set to drive co-ECCD in #48836, while #48837 has two co-ECCD and one counter-ECCD and #48841 has one co-ECCD, one counter-ECCD and one ECH. The $I_{cd,tot}$ increases along with the ramp-up of the EC power and has an amplitude of $|I_{cd,tot}^{36}| > |I_{cd,tot}^{37}| > |I_{cd,tot}^{41}| \approx 0$ at each time slice, as expected. Along with the ramp-up of the total EC power (reaching a maximum of about 1.2 MW before turning off), 2/1 NTMs were triggered in #48836 and #48837, with a later timing in #48837 (figure 4.26) when the total EC power ramped up to a higher value than #48836, whereas no NTM has been observed in #48841 during the entire power-ramp.

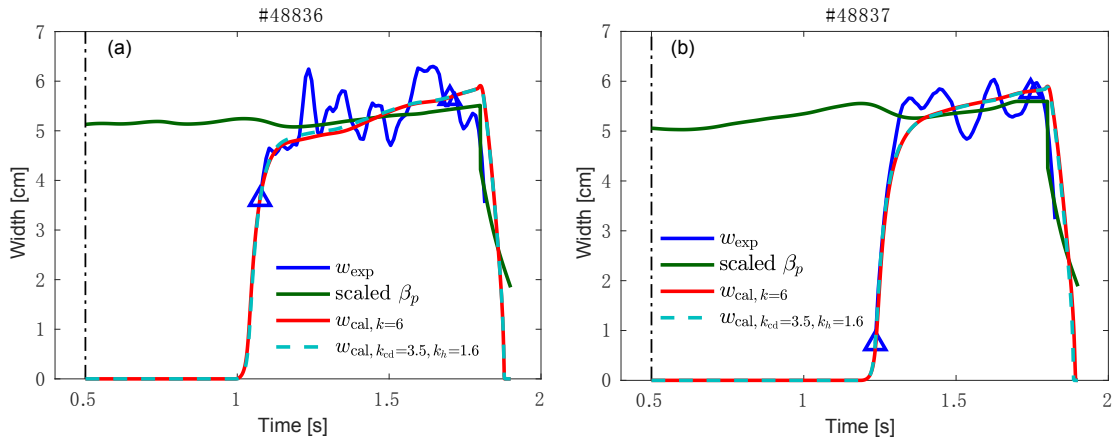


Figure 4.26. $w(t)$ evolution of power-ramp experiment (a) #48836 (with three co-ECCD) and (b) #48837 (with two co-ECCD and one counter-ECCD). Solid blue: measurement; solid green: scaled β_p based on equation (4.3), with $\beta_p(t_{ref} = 1.7) = 0.91$ for #48836 and $\beta_p(t_{ref} = 1.75) = 0.96$ for #48836; solid red: simulation with $k = 6$ in equation (4.2); dashed cyan: simulation with $k_{cd} = 3.5$ and $k_h = 1.6$ in equation (4.9). Two blue triangles: the two constraints used to determine $\bar{\rho}_{mn}\Delta'_{ohmic0}$ and $\bar{\rho}_{mn}\Delta'_{sat}$ as well as the time range within which χ is evaluated. Figure from [Kong et al. 2020].

To be comparable with previous simulations presented in section 4.3, simulations are performed with the original Δ'_0 model (equation (4.2)) and $k = 6$ for #48836 and #48837, where co-ECCD beams are involved. The simulated island width evolution of the 2/1 NTM, as shown by the solid red curves in figure 4.26, fits well the measurement (with $\chi < 10\%$ as seen in table 4.8). For simulations separating the heating effect (with equation (4.9)), the range of k_h to be used can be estimated based on #48841, where $I_{cd,tot}^{41} \approx 0$. Setting $k_{cd} = 0$ in equation (4.9) and

based on the observation that no NTMs were triggered in this discharge, k_h is found to be smaller than 2 when choosing $P_{\text{ref}} = 1.5 \text{ MW}$. More constraints on k_{cd} and k_h can be found along with the simulations of #48836 and #48837 (i.e. with different ECCD levels). Given the uncertainties and oscillations of various experimental data (e.g. w_{exp} , $I_{\text{cd,tot}}$, etc.), only pairs of k_{cd} and k_h can be estimated at this stage. The set of parameters used in the simulations as well as the corresponding χ for each simulation are summarized in table 4.8. a_2 has been adjusted to fit better the experimental $\frac{dw}{dt}$ in each discharge, as discussed in previous sections. It can be seen that different pairs of k_{cd} and k_h can fit reasonably the measurements ($\chi < 20\%$). As an example, simulations with $k_{cd} = 3.5$ and $k_h = 1.6$ ($P_{\text{ref}} = 1.5 \text{ MW}$) in equation (4.9) are shown by the dashed cyan curves in figure 4.26.

Table 4.8. List of the key parameters used in simulations with different Δ'_0 models

Shot #	k	k_{cd}	k_h	α	a_2	$\bar{\rho}_{mn}\Delta'_{\text{ohmic0}}$	$\bar{\rho}_{mn}\Delta'_{\text{sat}}$	χ
48836	6	N/A	N/A	15	1.7	-0.75	-1.26	8.48%
	N/A	4.5	0.95	15	1.7	-0.84	-1.26	8.32%
	N/A	4	1.25	15	1.7	-0.86	-1.26	8.26%
	N/A	3.5	1.6	15	1.7	-0.91	-1.25	8.13%
	N/A	3	1.9	15	1.7	-0.93	-1.25	8.08%
48837	6	N/A	N/A	15	1.7	-0.21	-1.18	7.47%
	N/A	4.5	0.95	15	1.7	-0.50	-1.26	7.11%
	N/A	4	1.25	15	1.7	-0.59	-1.20	7.22%
	N/A	3.5	1.6	15	1.7	-0.71	-1.20	7.35%
	N/A	3	1.9	15	1.7	-0.80	-1.20	7.43%
59151	6	N/A	N/A	10	1.0	-1.33	-0.484	5.08%
	N/A	4.5	0.95	10	1.0	-1.33	-0.484	6.08%
	N/A	4	1.25	10	1.0	-1.32	-0.484	6.13%
	N/A	3.5	1.6	10	1.0	-1.33	-0.484	5.34%
	N/A	3	1.9	10	1.0	-1.32	-0.484	5.43%

To investigate the contribution of each component to $\bar{\rho}_{mn}\Delta'_0$ in the simulations, the various terms of equation (4.9) for the three experiments are depicted in figure 4.27, with $k_{cd} = 3.5$ and $k_h = 1.6$ for each simulation. Different discharges are distinguished by different colors - #48836 in blue, #48837 in red and #48841 in green. Given the constant n_{el} in each discharge, constant $\bar{\rho}_{mn}\Delta'_{\text{ohmic0}}$ is used in the simulations, as indicated by the horizontal dashed lines in figure 4.27. The $\bar{\rho}_{mn}\Delta'_{\text{ohmic0}}$ of #48841 is set to equal that of #48837 (overlapped). The dotted lines refer to the contribution of heating to $\bar{\rho}_{mn}\Delta'_0$, i.e. $k_h \frac{P_{\text{ec,tot}}}{P_{\text{ref}}}$, and largely overlap among various discharges since the same injected EC power and similar absorption rate are involved. The dash-dotted lines represent the contribution of current drive to $\bar{\rho}_{mn}\Delta'_0$, i.e. $k_{cd} \frac{I_{\text{cd,tot}}}{I_p}$. Note that the $I_{\text{cd,tot}}$ of these discharges have been recalculated with TORAY-GA to adapt recent updates in the equilibrium solver LIUQE since the publication of [Lazzaro et al. 2015]. The new $I_{\text{cd,tot}}$ of #48841 shows an overall co-ECCD, but quite small indeed. The solid lines represent the sum of the three components, i.e. the $\bar{\rho}_{mn}\Delta'_0$. The average $-\bar{\rho}_{mn}\Delta'_{GGJ}$ in these experiments are indicated by the horizontal solid black line. The onset of mode

occurs when $\bar{\rho}_{mn}\Delta'_0 > -\bar{\rho}_{mn}\Delta'_{GGJ}$ (equation (4.4)), as indicated by the vertical dashed lines with corresponding colors.

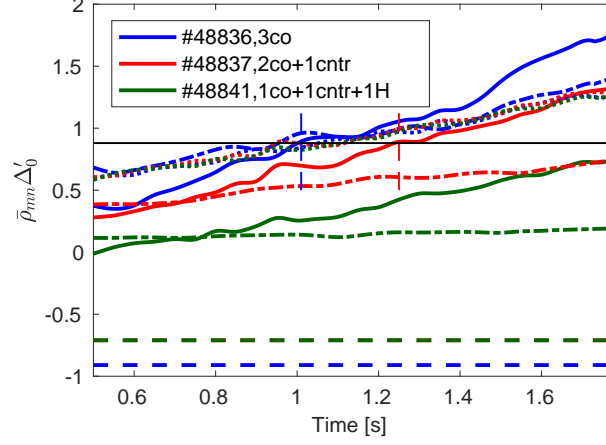


Figure 4.27. Time-varying $\bar{\rho}_{mn}\Delta'_0$ for #48836 (blue), #48837 (red) and #48841 (green) based on equation (4.9). Horizontal dashed lines: $\bar{\rho}_{mn}\Delta'_{ohmic0}$ used in the simulations, the same for #48837 and #48841 (overlapped); dotted lines: $k_h \frac{P_{ec,tot}}{P_{ref}}$, contribution of heating to $\bar{\rho}_{mn}\Delta'_0$ in different discharges; dash-dotted: contribution of current drive to $\bar{\rho}_{mn}\Delta'_0$; solid curves in corresponding colors: sum of the three components, i.e. the final $\bar{\rho}_{mn}\Delta'_0$ for each discharge. Horizontal solid black line: the average amplitude of $\bar{\rho}_{mn}\Delta'_{GGJ}$ in the experiments; vertical dashed lines: the time slices of the onset of the mode in #48836 and #48837.

Simulations have also been performed for a previous example #59151 (figure 4.2) with equation (4.9), as shown in table 4.8. The simulation with $k = 6$ is taken from table 4.2. As indicated by the χ values in table 4.8, the simulations with k_{cd} and k_h can fit well the measured island width evolution for this discharge as well. The difference of $\bar{\rho}_{mn}\Delta'_{ohmic0}$ between #59151 and #48836, with similar $n_{el} = 1.72 \times 10^{19} \text{ m}^{-3}$ and the same $k = 6$, can be explained by the different plasma conditions in these two different series of discharges (e.g. different I_p and κ). For #48837, where a large heating effect is involved given the settings of the EC launchers (2 co-ECCD and 1 counter-ECCD), the $\bar{\rho}_{mn}\Delta'_{ohmic0}$ required to fit the experiments with $k = 6$ is less negative than #48836, where the current-drive effect is dominant. This indicates that the original $\bar{\rho}_{mn}\Delta'_0$ model (equation (4.2)), developed based on discharges with dominant current-drive effect (e.g. with all the launchers in strong co-ECCD), underestimates the contribution of heating to $\bar{\rho}_{mn}\Delta'_0$, especially for cases where the heating contribution may be comparable to the current-drive effect, as expected.

A better separation of the heating and current-drive contribution to $\bar{\rho}_{mn}\Delta'_0$ would require detailed NTM onset experiments with pure ECH and corresponding simulations. Due to the limitations of the total EC power available at the time of the experiments, no 2/1 NTMs have been observed so far with pure central ECH in similar plasmas. However, as indicated by the solid green curve in figure 4.27, a further increase of the total EC power (e.g. reaching above 1.5 MW) would lead to the onset of NTMs with central pure heating. This can be tested soon

with new EC gyrotrons being commissioned. Further studies about the effects of heating on the triggerless onset of NTMs are left as future work.

4.6 Summary

Triggerless 2/1 NTMs have been observed reproducibly in low-density TCV discharges with strong near-axis co-ECCD. The underlying physics of this type of NTMs, from the onset as a TM at $w = 0$ to the saturation as an NTM up to w_{sat} , has been studied in detail in this chapter, through dedicated experiments with various density and EC power levels as well as interpretative simulations with the modified Rutherford equation (MRE). Given the Δ' -triggered nature of these NTMs (L -mode plasmas with $q_{95} > 5$ and no/tiny sawteeth) and the difficulties of calculating Δ' reliably, a simple model for the stability index *at* $w = 0$, i.e. Δ'_0 (equation (4.2)), has been developed based on experiments and interpretative simulations. Together with the w -dependence of Δ' (equation (3.25)), it provides a *complete* model of Δ' for all w (including $w = 0$) and has reproduced self-consistently the entire time-evolution of triggerless NTMs at various plasma conditions.

An unexpected density dependence of the onset of triggerless NTMs has been newly and experimentally observed in TCV: there is a certain range of density within which triggerless NTMs can occur, and the range is found to broaden with increasing central co-ECCD power. The underlying mechanisms of the observed phenomena have been explored using the Δ'_0 model that is developed with a different set of experiments and simulations. It is found that the formation of the density range results from the density dependence of the stability of ohmic plasmas, being more unstable at higher density, and of the ECCD efficiency, driving less current at higher densities hence less destabilizing. Both effects are consistent with increasing magnetic shear at the $q = 2/1$ surface, as obtained from interpretative ASTRA simulations, being more unstable. However, its exact value is not accurate enough at this stage to be used directly in the Δ'_0 model. The simulations have also highlighted that ohmic plasmas are much more stable ($\Delta'_0 \ll 0$) at low density than at medium to high densities.

A detailed study of various parameters involved in the simulations with the MRE has also been presented, which clarifies their main effects and constrains better the range of parameters to be used. For example, a_2 , the coefficient affecting the bootstrap contribution (equation (3.4)), is found to dominate the amplitude of the growth rate of w at medium to large w , where measurements are available, and can be constrained well by comparing with the experimental data; k in the Δ'_0 model (equation (4.2)) affects both the onset of NTMs and the detailed time-evolution of w up to w_{sat} , given the w -dependence of Δ' defined by equation (3.25); α affects the slope of the w dependence of Δ' at small w , thus playing a role in the evolution that is mainly below the noise level of measurements in the test discharges. The sensitivity of NTM onset and evolution to a_3 that affects $\bar{\rho}_{mn}\Delta'_{GGJ}$ (equation (3.7)) in the MRE has also been investigated. Different a_3 values only lead to a rigid shift of the $\bar{\rho}_{mn}\Delta'_{\text{ohmic0}}(n_{el})$ mapping to be used to fit the experiments, whereas the main physics proves to be well retained. Following

table 3.1 and the discussions in this chapter, ranges of the key coefficients and parameters involved in simulations with the MRE are summarized in table 4.9.

Table 4.9. List of key MRE coefficients and parameters

Item	Relevant equation	Range
a_2	(3.4)	tuned based on experimental $\frac{dw}{dt}(w)$, typically [1, 2]
a_3	(3.7)	1
a_4	(3.9)	[0.3, 0.65], based on table 5.3 (chapter 5)
a_5	(3.10)	0.9, based on table 5.3 (chapter 5)
Δ'_{sat}	(3.25)	tuned based on a_2 and measured w_{sat} : a_2/Δ'_{sat} determines w_{sat} (equation (3.20))
k	(4.2)	[2, 10], typically set to 6
Δ'_{ohmic0}	(4.2)	tuned based on the measured occurrence of NTMs with a fixed $k(= 6)$
α	(3.25)	[3, 15], tuned to minimize χ (equation (4.5))

A “lull” region characterized by a very slow growth rate at a certain range of w has been observed in simulations with small k and/or large α . This could explain a similar behavior firstly described in [Brennan et al. 2003]. More detailed study on the existence of the lull region and the range of parameters used requires better measurements of w at very small w , and needs improved diagnostics. Further improvement of the Δ'_0 model is also foreseen. For example, a first attempt has been made to separate the contribution of heating to the onset of these NTMs with available data, while more detailed experiments with higher ECH power will allow quantifying better different effects.

The possible effects of plasma rotation on the onset of these NTMs in TCV have also been explored through dedicated power-scan and density-scan experiments with careful rotation measurements. No noticeable change of rotation can be observed around the onset threshold of these NTMs, indicating that rotation is not playing a dominant role in the NTM onset in the test discharges. This confirms that the dominant effect is the dependence of Δ'_0 on n_{el} and $I_{\text{cd,tot}}/I_p$.

The new Δ'_0 model (equation (4.2)) developed in this chapter is generic in separating Δ'_0 into the classical stability of ohmic plasmas and the contribution of auxiliary heating and current drive. The proposed density dependence of each term also remains general: destabilization of 2/1 NTMs at high density is found to be the main mechanism causing density limit of tokamak plasmas for the cases examined [Kirneva et al. 2015], while the current drive efficiency of ECCD is expected to depend inversely on density [Cohen 1987; Lin-Liu et al. 2003, and references therein]. However, to cover all the plasma scenarios in various tokamaks, a more general model that directly links Δ'_0 (and Δ') with the details of q and j profiles such as the radial

location of the considered $q = m/n$ surface and the local magnetic shear, is needed. A detailed sensitivity study of Δ' discussed in appendix A presents an example of such a model (equation (A.5)), while more comprehensive sensitivity study that covers a wider range of q and j profiles or analytical derivations would provide better estimations.

The Δ'_0 model has facilitated the study of triggerless NTMs in TCV and explain well various experimental observations (including the unexpected density range for mode onset). The underlying physics of triggerless NTMs studied in detail in this chapter can inspire investigations of triggerless NTMs observed in other devices and is important for ITER. In particular, from interpretative simulations with ASTRA, it is observed that discharges with increasing radial location of the $q = 2/1$ surface and/or increasing magnetic shear at the $2/1$ surface tend to be more unstable for TMs, for example with increasing density from 1×10^{19} to $2.4 \times 10^{19} \text{ m}^{-3}$ (for ohmic plasmas) or with increasing central $I_{cd,tot}$ in the test discharges.

It is worth emphasizing that Δ'_0 , though being a key parameter in the simulated onset of NTMs (below the noise level of measurements), only has a high-order effect on the time evolution of island width (especially the part above the noise level), given the strong w -dependence of Δ' (equation (3.25)) that eventually enters the MRE (equation (3.3)). This means that the exact value of Δ'_0 does not affect much the fitting of experimental results and tuning Δ'_0 based on the measured occurrence (i.e. the first measurement point available) of NTMs is good enough in terms of simulating $w(t)$. This method is applicable to simulations of any discharge, for instances discharges that will be presented in the next chapter where both NTM stabilization and prevention cases are involved. Similarly, Δ'_0 can be adapted automatically based on real-time w measurements in real-time simulations with the MRE, as will be discussed in chapter 6 (section 6.4).

The detailed discussions about the effects of various coefficients (such as a_2 and a_3) on NTM evolutions (section 4.3.1) are of importance for simulations with the MRE in general. The standard terms used in the MRE and the simulations involving finite island widths are also relevant for NTMs seeded by other mechanisms. As summarized in table 4.9, the key coefficients and parameters for simulating any TCV discharges with the MRE can be determined as follows. Note that one should check that the parameters are within the range defined in chapters 4 and 5 (summarized in table 4.9). A similar procedure has been shown to be valid for simulating an AUG discharge, as discussed in chapter 6 (section 6.4.5).

- Determining a_2 by fitting the experimental $\frac{dw}{dt}(w)$ trace. Note that a_2 is typically within $[1, 2]$ based on simulations of TCV discharges (table 4.9)
- $a_3 = 1$; $a_6 = 0$ (neglecting the polarization current term)
- $a_5 = 0.9$ (relevant when off-axis EC beams are involved, details in chapter 5). A range of $[0.2, 1.6]$ is found to be compatible with TCV experiments (equation (5.2), section 5.5), though $a_5 = 0.9$ generates the best fit of the experiments so far
- Tuning a_4 based on the measured stabilization/prevention of NTMs, but within $[0.3, 0.65]$

with $a_5 = 0.9$ (relevant when off-axis EC beams are involved, details in chapter 5). Ranges of a_4 at different a_5 are summarized in table 5.3

- Tuning $\bar{\rho}_{mn}\Delta'_{\text{sat}}$ (within $[-m, 0)$) to fit the measured w_{sat}
- $k = 6$. A range of $[2, 10]$ has been determined (section 4.3.1)
- Tuning $\bar{\rho}_{mn}\Delta'_{\text{ohmic0}}$ based on the measured occurrence of NTMs
- Tuning α (within $[3, 15]$) to minimize χ (equation (4.5))

5 Stabilization and prevention of 2/1 NTMs with EC beams in TCV

5.1 Introduction

Apart from the detailed study on the onset of 2/1 NTMs presented in the previous chapter, the control of 2/1 NTMs has also been investigated within the scope of this thesis and is the main topic of this chapter. Two main methods of NTM control, i.e. NTM stabilization and NTM prevention are explored, through dedicated TCV experiments and interpretative simulations with the MRE. Similar to the actuators for future NTM control in ITER, (off-axis) EC beams are applied in the NTM control experiments in TCV, apart from the near-axis EC beams that are used for the onset of NTMs as discussed in the previous chapter. Effects of EC beams on the stability and control of NTMs are twofold: by modifying the current density profile and thus the classical stability of plasmas (i.e. Δ'), and by replacing the missing bootstrap current within the magnetic island through direct current drive or indirect heating effect [Hegna and Callen 1997].

Although similar physics is involved in 3/2 and 2/1 NTMs, the control of 2/1 NTMs is more challenging due to their typically larger growth rate and proximity to the plasma edge, which on one hand increases the chance of mode locking and disruptions and on the other hand decreases the current drive efficiency. The reliable and efficient control of 2/1 NTMs is thus a major concern for ITER and needs to be ensured. In this respect, more experimental efforts are still needed to carefully isolate different effects, assess the range of validity of theoretical models and improve the control algorithms. With the relatively short time scale of TCV (confinement time ~ 5 ms and resistive time $50 \sim 100$ ms) and its flexible EC system, different plasma conditions and various aspects of NTM control are explored in the experiments, as will be detailed in this chapter.

The MRE (equation (3.3)), including the Δ'_0 model developed in chapter 4 (equation (4.2)), is applied in interpreting the experimental results presented in this chapter. For instance, dynamic evolutions of 2/1 NTMs along with time-varying deposition locations of the control beam are studied in detail; effects of heating and current drive on the stabilization of 2/1 NTMs are quantified carefully; the entire island width evolution, starting from zero width (i.e.

no island) and including both NTM stabilization and prevention cases, is reproduced in the simulations. These simulations meanwhile facilitate the comparison of various effects and the validation of theoretical models, as will be discussed in this chapter.

The rest of the chapter is organized as follows. The plasma scenario and experimental setup are briefly introduced in section 5.2. Section 5.3 discusses about the self-stabilization of NTMs through a slow ramp-down of the near-axis destabilizing ECCD power. In section 5.4, the evolution of a 2/1 NTM along with a large variation of the deposition location of the control beam (between the plasma center and edge) is discussed, constraining better the theoretical model (especially the form of the G_{cd} term in equation 3.15) used in the simulations. Section 5.5 compares the effects of co-ECCD, counter-ECCD and ECH on the stabilization of 2/1 NTMs, with various effects quantified by detailed simulations with the MRE. The efficiency of NTM prevention and that of NTM stabilization, in terms of the minimum EC power required in each case, are compared in section 5.6. In section 5.7, effects of the misalignment of EC beams with respect to the target mode location are discussed. Section 5.8 summarizes the main contents of this chapter.

5.2 Plasma scenario and experimental setup

Limited L -mode plasmas with constant plasma current ($I_p \approx -110$ kA) and toroidal magnetic field ($B_0 = -1.44$ T) are used, similar to the scenarios used in the studies of mode onset described in section 4.2.1. $q_{95} \approx 7$, $\delta \approx 0.25$ and $\kappa \approx 1.32$ are kept in the discharges. Relatively constant low density is kept in each experiment to ensure 100% absorption of EC beams, with the n_{el} ranges from $1.4 \times 10^{19} \text{ m}^{-3}$ to $2 \times 10^{19} \text{ m}^{-3}$ in various experiments.

As illustrated in figure 5.1 (a), two X2 EC gyrotrons with a nominal power of 0.5 MW each are applied to deposit power near the plasma center and drive co-ECCD using two launchers ($L4$ and $L6$) with independent steerable mirrors. As discussed in the previous chapter, 2/1 NTMs are typically destabilized about 100 ms (i.e. the resistive time scale on TCV) after turning on the near-axis EC power, through a modification of the current density profile, i.e. a Δ' effect. The mode then grows dominated by the effects of neoclassical perturbed bootstrap current (i.e. NTMs).

A third X2 gyrotron with a nominal power of 0.75 MW and an independent launcher ($L1$) is used for control purposes. The toroidal angles of these launchers are set before the experiment to allow for co-ECCD, counter-CD or ECH, while their poloidal angles can be controlled by feedforward or feedback commands to vary their deposition locations during each discharge. The EC power and poloidal angle traces in the experiments presented in this chapter were pre-programmed, while the real-time application of the NTM control scheme will be discussed in chapter 6. EC-relevant parameters such as the power absorption rate, deposition location and driven current of the beams from each launcher are computed by TORAY-GA [Matsuda 1989]. Shown in figure 5.1 (b) is an example of the deposited power density profiles of the three launchers.

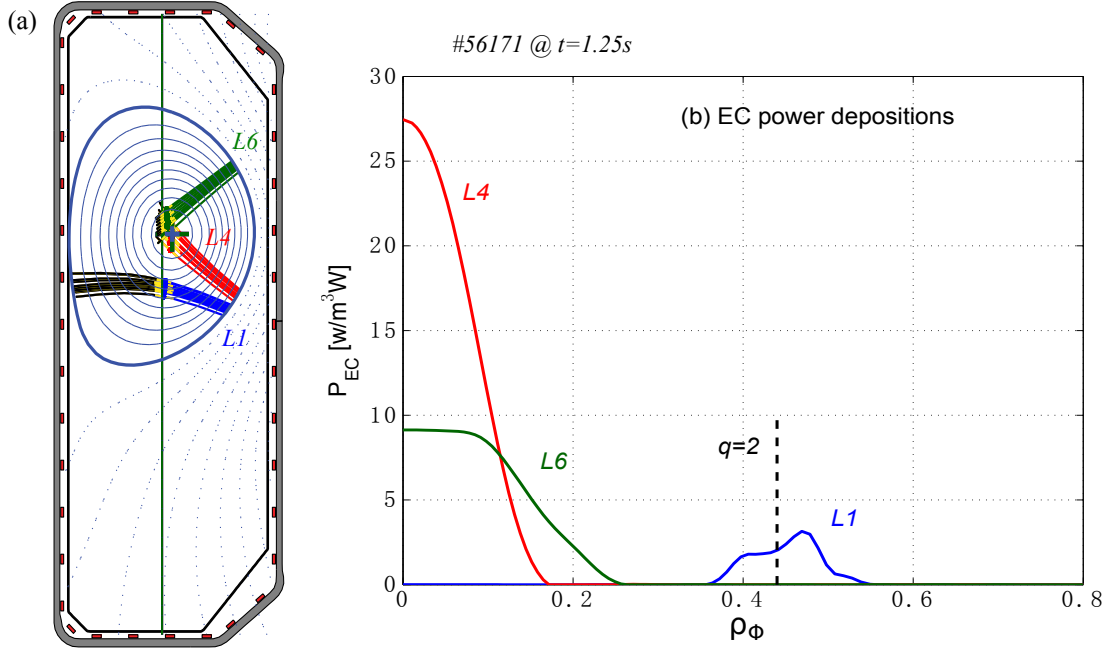


Figure 5.1. Illustration of the plasma scenario and experimental setup: (a) a poloidal cross section of TCV showing one poloidal array of 38 magnetic probes (red rectangles on the wall), flux surfaces computed by LIUQE and EC traces from TORAY-GA; (b) deposited EC power density profiles per injected power computed by TORAY-GA, with the $q = 2$ location from ASTRA marked as the dashed vertical line. The example is taken from #56171 at $t = 1.25$ s. Figure from [Kong et al. 2019].

5.3 Self-stabilization: slow ramp-down of near-axis co-ECCD power

As illustrated in figure 3.3 (section 3.2), full stabilization of NTMs occurs when the maximum of the total island width growth rate $\frac{dw}{dt} \leq 0$, i.e. $\frac{dw}{dt}(w = w_{\text{marg}}) \leq 0$. To investigate the amplitude of w_{marg} of the test discharges, an experiment with a slow ramp-down of the near-axis co-ECCD power (i.e. the destabilizing power) has been performed, as shown in figure 5.2. About 0.96 MW of X2 EC power in total is turned on at 0.4 s and deposits co-ECCD near the plasma center through $L4$ and $L6$ in this discharge, similar to NTM onset experiments presented in the previous chapter. Relatively constant $I_p \approx -110$ kA and $n_{el} \approx 1.8 \times 10^{19} \text{ m}^{-3}$ are kept in this discharge.

A transient 3/2 NTM exists at $t \in [0.45 \text{ } 0.55]$ s, while a 2/1 NTM appears at about 0.5 s, 100 ms after switching on the EC power and is sustained. Starting from $t = 1.2$ s, the EC power is slowly ramped down and reaches a total power of about 0.35 MW at $t = 2.11$ s when the mode self-stabilizes (without the application of off-axis EC power). During the slow ramp-down of the EC power, the island width slowly decreases (with a small negative growth rate $\frac{dw}{dt}$ as indicated by the dashed magenta curve in figure 5.5) and quickly drops below the noise level at $w \approx 1.9$ cm, as shown by the solid blue trace in figure 5.3. This provides an estimation of $w_{\text{de}} \approx w_{\text{marg}} \approx 1.9$ cm in the test discharge, consistent with that calculated by equation (3.6)

(with $\chi_{\parallel, mn} \approx 6 \times 10^7 \text{ m}^2/\text{s}$ and $\chi_{\perp, mn} \approx 1 \text{ m}^2/\text{s}$), where w_{de} represents the stabilizing effect at small w in equation (3.4).

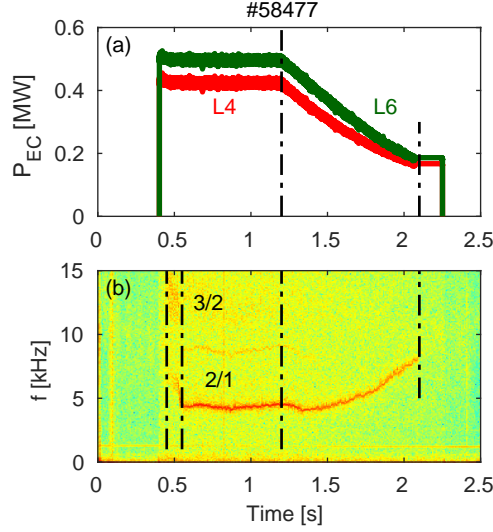


Figure 5.2. Experimental overview of an EC power ramp-down experiment with constant $n_{el} \approx 1.8 \times 10^{19} \text{ m}^{-3}$ and $I_p \approx -110 \text{ kA}$: (a) EC power traces; (b) NTM spectrogram. Reproduced from [Kong et al. 2019].

To quantify the effects of various terms on w evolution, simulations of the 2/1 NTM are performed with the MRE presented in section 3.4. Following the discussions in section 4.3, fixed $k = 6$ is used in all the simulations shown in this chapter while $\bar{\rho}_{mn} \Delta'_{\text{sat}}$ is adjusted so that w_{cal} crosses point “B” in figure 5.3, corresponding to measured w_{sat} before the ramp-down of near-axis ECCD power. $\bar{\rho}_{mn} \Delta'_{\text{ohmic0}}$ can in principle be estimated based on the appearance of NTMs, i.e. to cross point “A” in figure 5.3, as used in the previous chapter. However, the sudden change of T_e and n_e (especially near the plasma center) when turning on the near-axis EC power at $t = 0.4$ s causes a sudden increase of the total driven current $I_{\text{cd,tot}}$, thus a sudden increase of the computed $\bar{\rho}_{mn} \Delta'_0$ with equation (4.2). This happens on a time scale that is faster than the current redistribution time scale of the plasma and would predict an earlier timing of mode onset than in the experiments.

As an illustration, figure 5.4 depicts the time evolution of the local magnetic shear s_{mn} and the normalized radial location of the $q = m/n$ surface ρ_{mn} (i.e. $\bar{\rho}_{mn}/a$) from interpretative ASTRA simulations, as well as the $I_{\text{cd,tot}}$ from TORAY-GA outputs. The timing of turning on the EC power (i.e. at $t = 0.4$ s) is marked by the vertical dash-dotted black line. One can see that there is a fast increase of the amplitude of $I_{\text{cd,tot}}$ (within 30 ms) once switching on the EC power, whereas the change of s_{mn} and ρ_{mn} (thus $\bar{\rho}_{mn} \Delta'_0$) is on a slower time scale (about 100 ms). On the other hand, with a slower change of the EC power (thus $I_{\text{cd,tot}}$) since $t = 1.2$ s, similar to the power-ramp and density-ramp experiments presented in the previous chapter, $I_{\text{cd,tot}}/I_p$ can follow well the evolution of s_{mn} and ρ_{mn} , i.e. the proposed $\bar{\rho}_{mn} \Delta'_0$ model in equation (4.2) in this case can reproduce well the trend of $\bar{\rho}_{mn} \Delta'_0$.

5.3. Self-stabilization: slow ramp-down of near-axis co-ECCD power

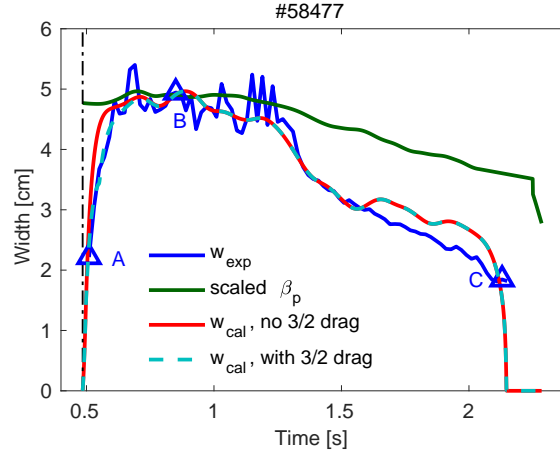


Figure 5.3. Island width evolution of #58477 (figure 5.2). Solid blue: measurement; solid green: scaled β_p based on equation (4.3), with $t_{\text{ref}} = 0.85\text{s}$ and $\beta_p(t_{\text{ref}}) = 0.76$; solid red: simulation without the “drag” from 3/2 mode; dashed cyan: simulation with a constant 3/2 drag $\bar{\rho}_{mn}\Delta'_{32} = -0.25$ during the coexistence of 3/2 and 2/1 modes. The first measurement point is marked by the triangle labeled as A and the constraint used to determine $\bar{\rho}_{mn}\Delta'_{\text{sat}}$ is represented by B; the range within which χ (equation (4.5)) is evaluated is from B to C.

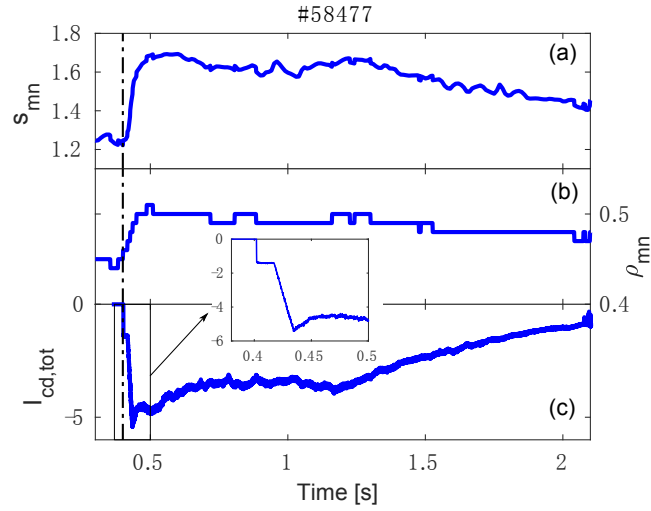


Figure 5.4. Time evolution of (a) local magnetic shear at $q = m/n$ surface, (b) normalized radial location of $q = m/n$ surface and (c) total driven current of #58477 shown in figure 5.2 and 5.3. s_{mn} and ρ_{mn} are taken from interpretative ASTRA simulations while $I_{\text{cd,tot}}$ is from TORAY-GA outputs. $I_{\text{cd,tot}}$ exhibits a faster change when turning on the EC power (around $t = 0.4\text{s}$) than that of s_{mn} and ρ_{mn} , whereas it can follow well the evolution of s_{mn} and ρ_{mn} during the slow power ramp-down after $t = 1.2\text{s}$.

The faster change of $I_{\text{cd,tot}}$ when turning on the EC power makes it difficult to fit point A by adjusting $\bar{\rho}_{mn}\Delta'_{\text{ohmic0}}$: the mode would occur either before $t = 0.43\text{s}$ (when $I_{\text{cd,tot}}$ reaches the peak) or not at all in the simulations. Instead, a different approach is adopted: determining $\bar{\rho}_{mn}\Delta'_{\text{ohmic0}}$ based on a direct interpolation of the $\bar{\rho}_{mn}\Delta'_{\text{ohmic0}} - n_{el}$ mapping for $I_p \approx -110\text{kA}$

given in the previous chapter (dashed-dotted green curve with squares in figure 4.17), while starting the simulation from a timing near point A (e.g. 25 ms before A in this case). As mentioned in the previous chapter, one would need to add an extra model (to our existing model) to consider the different time scales between the time-evolution of $I_{cd,tot}$ (and EC power) and the effective change of the q profile to solve this problem more systematically.

The value of a_2 can be estimated by comparing the experimental $\frac{dw}{dt}(w)$ trace to measurements, as discussed in the previous chapter. However, the uncertainties of $\bar{\rho}_{mn}\Delta'_{ohmic0}$ mentioned above (thus $\bar{\rho}_{mn}\Delta'_0$ and $\bar{\rho}_{mn}\Delta'$) as well as the coexistence of the 3/2 mode that can exert a negative “drag” ($\bar{\rho}_{mn}\Delta'_{32}$) on the evolution of 2/1 mode inevitably introduce uncertainties on a_2 . Without losing generality, constant $a_2 = 1.5$ is used in the simulations of #58477, which is a medium value of a_2 used in the previous chapter. The corresponding $\bar{\rho}_{mn}\Delta'_{sat}$ used to fit point B in figure 5.3 is -0.78 and $\alpha = 8$ is tuned to minimize χ defined in equation (4.5). $a_3 = 1$ is used in all the simulations in this chapter, whereas a_4 and a_5 are not discussed here since only near-axis EC beams are involved in this test, i.e. $\bar{\rho}_{mn}\Delta'_{CD} \approx 0$ and $\bar{\rho}_{mn}\Delta'_H \approx 0$ in equation (3.3). The simulated w without considering the drag from 3/2 mode is depicted by the solid red curve in figure 5.3, while the one with an additional $\bar{\rho}_{mn}\Delta'_{32} = -0.25$ added to $\bar{\rho}_{mn}\Delta'$ during the coexistence of both modes ($t \in [0.5, 0.55]$ s) is plotted as the dashed cyan curve in figure 5.3. χ is evaluated between B and C, i.e. excluding the effects of the uncertainties of $\bar{\rho}_{mn}\Delta'_{32}$ on χ , and gives $\chi = 9.67\%$ for both cases.

$\frac{dw}{dt}(w)$ traces at various time slices (as indicated by the numbers in the legend) of the simulation with the additional $\bar{\rho}_{mn}\Delta'_{32} = -0.25$ during the coexistence of 2/1 and 3/2 modes (dashed cyan curve in figure 5.3) are depicted by the solid curves with corresponding colors in figure 5.5, while the simulated w_{cal} at each time slice is denoted by a solid circle with the same color. The $\frac{dw_{cal}}{dt}(w_{cal})$ trace taken from the simulation is depicted by the dash-dotted black curve, which crosses the solid circles as expected. The $\frac{dw_{exp}}{dt}(w_{exp})$ trace taken from the measurement is shown by the dashed magenta curve. With $a_2 = 1.5$ and considering the 3/2 drag, the simulated $\frac{dw_{cal}}{dt}(w_{cal})$ trace fits well the measurements. The values of $\bar{\rho}_{mn}\Delta'$, $\bar{\rho}_{mn}\Delta'_{BS}$ and $\bar{\rho}_{mn}\Delta'_{GGJ}$ evaluated with the corresponding w_{cal} at each time slice, divided by $\tau_R/\bar{\rho}_{mn}$, are indicated by the open downward-pointing triangles, upward-pointing triangles and squares in figure 5.5, respectively. The sum of these terms recovers the total $\frac{dw}{dt}$ at each time slice, i.e. solid circles with corresponding colors.

One can see that at $t = 0.485$ s, $\frac{dw}{dt} > 0$ at $w = 0$ (due to a positive $\bar{\rho}_{mn}\Delta'$) and the mode starts to grow, representing the onset of the mode; at $t = 0.5$ s, with the additional $\bar{\rho}_{mn}\Delta'_{32}$, w reaches about 2 cm; at $t = 1$ s, $\frac{dw}{dt} \approx 0$ at $w_{sat} = 5$ cm; from $t = 1.2$ s, the EC power is ramped down slowly and $\frac{dw}{dt} \lesssim 0$ is sustained with decreasing w_{sat} . The decrease of the central ECCD power has two main effects: on one hand it reduces $I_{cd,tot}$, changes the q profile and hence $\bar{\rho}_{mn}\Delta'$ (captured through equation (4.2)), on the other hand it lowers the $\bar{\rho}_{mn}\Delta'_{BS}$ term that is sustaining the mode. At $t \approx 2.11$ s, the maximum of $\frac{dw}{dt}$ goes just below 0 with $w \approx 1.9$ cm and the mode is fully stabilized; after turning off the EC power at $t = 2.25$ s, the entire $\frac{dw}{dt}$ curve remains negative and the plasma is stable to NTMs.

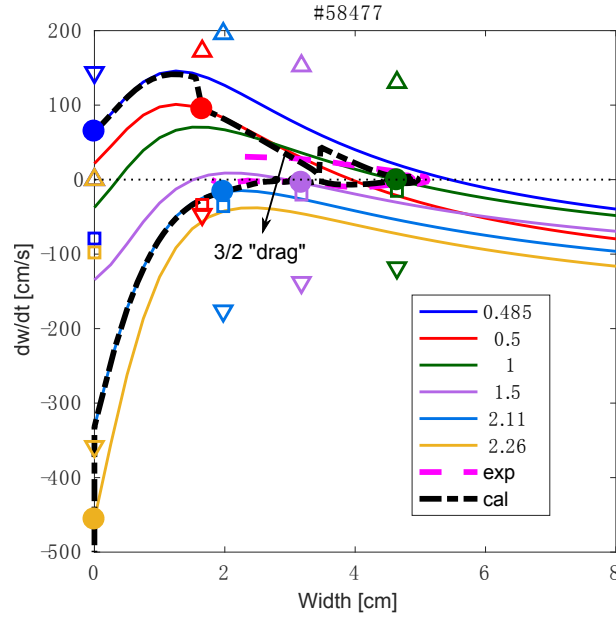


Figure 5.5. $\frac{dw}{dt}(w)$ traces at different time slices (as indicated by the numbers in the legend) of the simulation with an additional $\bar{\rho}_{mn}\Delta'_{32} = -0.25$ during the coexistence of 2/1 and 3/2 modes (dashed cyan curve in figure 5.3), showing $\frac{dw}{dt}$ evaluated at various time slices and w (solid traces), and $\frac{dw}{dt}$ at the w_{cal} of each time slice (solid circles). $\bar{\rho}_{mn}\Delta'$ (downward-pointing triangles), $\bar{\rho}_{mn}\Delta'_{BS}$ (upward-pointing triangles) and $\bar{\rho}_{mn}\Delta'_{GGJ}$ (squares) at the w_{cal} of each time slice, divided by $\tau_R/\bar{\rho}_{mn}$, are also listed. $\frac{dw_{\text{cal}}}{dt}(w_{\text{cal}})$ from the simulation is plotted as the dash-dotted black curve (labeled as “cal”) while $\frac{dw_{\text{exp}}}{dt}(w_{\text{exp}})$ from measurement is shown by the dashed magenta trace (“exp”).

5.4 Stabilization of NTMs with varying co-ECCD depositions

Highly reproducible active 2/1 NTM stabilization experiments have been carried out in TCV with off-axis co-ECCD beams, showing a strong stabilization effect when the beams reach the target mode location. Shown in figure 5.6 is one example of such an experiment (TCV #56027). In this discharge, EC power is turned on at $t = 0.4$ s and deposits co-ECCD near the plasma center through $L4$ and $L6$, which triggers a 2/1 NTM at about $t = 0.5$ s. The control co-ECCD beam is switched on at $t = 0.7$ s and deposits through a third launcher ($L1$) with 0.75 MW power. As shown in figure 5.6 (b) and (c), the deposition location of $L1$ is varied, causing a variation of the mode amplitude and frequency. The radial location of the $q = 2$ surface from the ASTRA output is indicated by the dashed black curve in figure 5.6 (b), as used in the simulations with the MRE. ρ_Φ refers to the normalized radial location based on the square root of the toroidal flux Φ .

A partial stabilization effect can be seen when the EC beam reaches the mode location ($q = 2$ surface) for the first time at $t = 1.15$ s. The mode amplitude recovers (but reaches a lower value) once the beam moves away (figure 5.8) and is fully stabilized when the beam crosses the $q = 2$ surface for the second time at $t = 1.53$ s. $I_{\text{cd,tot}}$ then increases along with the movement

of $L1$ from outside the $q = 2$ surface to the plasma center, but no mode is triggered any more due to a decrease of n_{el} and a more stable $\bar{\rho}_{mn}\Delta'_{ohmic0}$ in equation (4.2). The deposition width of each beam (w_{dep}) can be inferred from TORAY-GA outputs, for instance, the example shown in figure 5.1 shows a full e^{-1} width about $0.2 \times 25 \text{ cm} = 5 \text{ cm}$ for $L4$ and $L6$ while $w_{dep} \approx 3 \text{ cm}$ for $L1$. w_{dep} can vary with varying deposition locations, but a fixed and constant $w_{dep} = 5 \text{ cm}$, unless otherwise stated, is used for all the launchers for simplicity as well as considering the possible beam broadening effects [Nikkola et al. 2003; Poli et al. 2015, and references therein] that are not included in TORAY-GA.

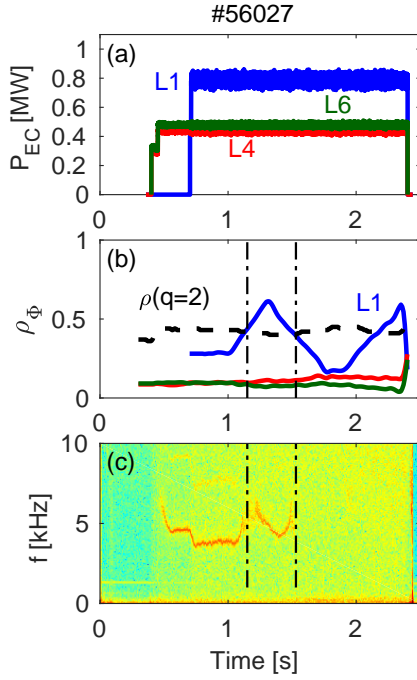


Figure 5.6. Experimental overview of an NTM stabilization experiment with varying co-ECCD depositions under constant $n_{el} \approx 1.5 \times 10^{19} \text{ m}^{-3}$ and $I_p \approx -110 \text{ kA}$: (a) EC power traces; (b) normalized deposition locations; and (c) 2/1 NTM spectrogram. Figure from [Kong et al. 2019].

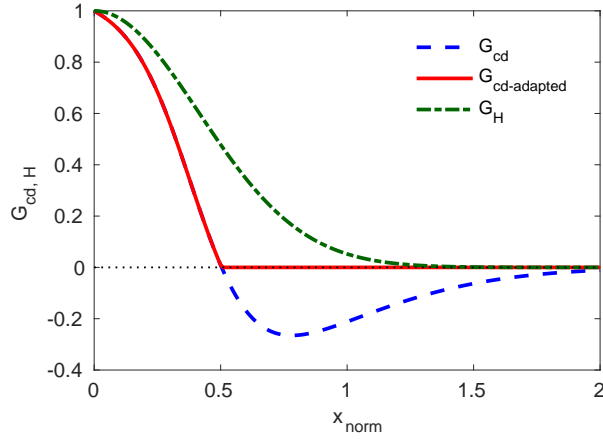


Figure 5.7. $G_{cd,H}$ terms with $w/w_{dep} = 1$, showing theoretical (full) G_{cd} that is characterized by a negative (destabilizing) part at relatively large misalignment (e.g. $x_{norm} \geq 0.5$ of the dashed blue curve), an adapted G_{cd} without the negative part (solid red) and G_H from theory (dash-dotted green). Figure from [Kong et al. 2019].

Simulations with the MRE are performed and it is necessary to specify $\bar{\rho}_{mn}\Delta'_{CD}$ and $\bar{\rho}_{mn}\Delta'_H$ in equation (3.3) since small values of x_{norm} (thus large G_{cd} and G_H) are covered along with the movement of $L1$. As described in section 3.4, G_H and G_{cd} are approximated by equations (3.14) and (3.15), respectively. The shapes of these two curves are shown in figure 5.7 for $w/w_{dep} \approx 1$ (as the ones involved here). As depicted by the dashed blue curve, the theoretical G_{cd} is characterized by a strong negative (destabilizing) part at $0.5 \leq x_{norm} \leq 1$ and stays around 0 for $x_{norm} \geq 1.5$. However, no such destabilizing effects have been observed experimentally so far in numerous NTM stabilization experiments with varying EC beam deposition locations in

TCV, where a wide range of x_{norm} is covered (e.g. $x_{\text{norm}} \in [0, 1.5]$ in figure 5.7) in each discharge, similar to #56027 shown here. For example, the experiments presented in [Felici et al. 2012, figures 1, 3 and 4] demonstrate full NTM stabilization when the deposition location of the control co-ECCD beam reaches close enough to mode location ($x_{\text{norm}} < 0.5$) from either inside or outside the $q = m/n$ surface.

As shown in [Felici et al. 2012, figure 3 (#40411 and #40418)], near monotonic decrease of the measured island width is observed along with the movement of control beams from $x_{\text{norm}} > 0.5$ to $x_{\text{norm}} < 0.5$, without any local increases of w , which does not seem to support the predicted $G_{cd} < 0$ part shown in figure 5.7. This phenomenon, as observed in other TCV experiments (e.g. discharges in section 5.5), may be explained by the finite or even strong heating contribution from the EC beams (i.e. $\bar{\rho}_{mn}\Delta'_H$) in small to medium size tokamaks [De Lazzari and Westerhof 2009; Bertelli et al. 2011] that counteracts this destabilizing effect. It may also be that the destabilizing effect, if any [Isayama et al. 2009], is not as strong as predicted by theory.

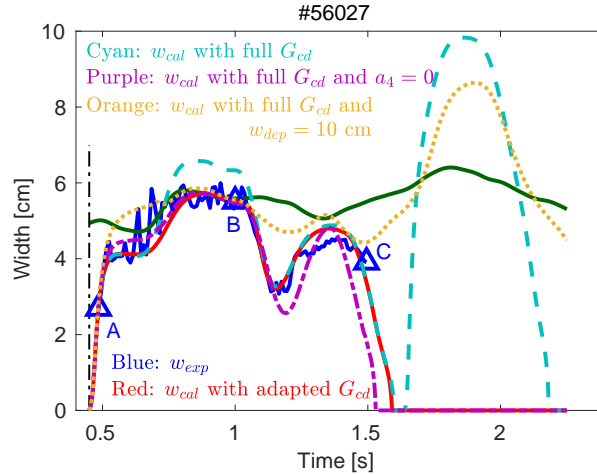


Figure 5.8. Island width evolution of #56027 illustrated in figure 5.6. Solid blue: measurement; solid green: scaled β_p based on equation (4.3), with $t_{\text{ref}} = 1$ s and $\beta_p(t_{\text{ref}}) = 0.85$; solid red (case 1 in table 5.1): simulation with the adapted G_{cd} curve in figure 5.7, i.e. without the negative part of G_{cd} ; dash cyan (case 2): simulation with the same parameters as the solid red curve, except with the theoretical (full) G_{cd} curve in figure 5.7; dashed-dotted purple (case 3): simulation with the theoretical G_{cd} curve, $a_4 = 0$ and $a_5 = 4.5$; dotted orange trace (case 4): simulation with the theoretical G_{cd} curve and $w_{\text{dep}} = 10$ cm. A: the first measurement point available; B: the constraint used to determine $\bar{\rho}_{mn}\Delta'_{\text{sat}}$; A to C: the time range within which χ (equation (4.5)) is evaluated.

Another evidence that favors zero/weak negative part of the G_{cd} curve is NTM onset experiments with varying EC deposition locations. One example of these experiments is shown in figure 5.9 (#56751). In this discharge, two co-ECCD EC beams ($L4$ and $L6$) are switched on at $t = 0.3$ s, with a constant total power of 0.96 MW until $t = 2.3$ s, when the beams are switched off. The deposition locations of the EC beams, as shown in figure 5.9 (a), are varied from $\rho_\phi \approx 0.6$ to 0.1. $x_{\text{norm}} \in [0, 2]$ is covered in this discharge, whereas no mode is triggered until

the EC beams reach close enough to the plasma center ($\rho_{\text{dep}} \approx 0.2$ as seen in figure 5.9 (b)), with $x_{\text{norm}} \geq 1.5$. Simulations of #56751, following the same procedures as in the previous chapter but with the $\bar{\rho}_{mn}\Delta'_{CD}$ and $\bar{\rho}_{mn}\Delta'_H$ terms included (as small x_{norm} thus large amplitude of G_{cd} is involved in this discharge), show that the strong negative part of G_{cd} would have caused an earlier onset of the mode at $t \approx 1.93$ s when x_{norm} reaches around 0.75, i.e. the minimum (most destabilizing) value of G_{cd} (dashed blue trace in figure 5.7).

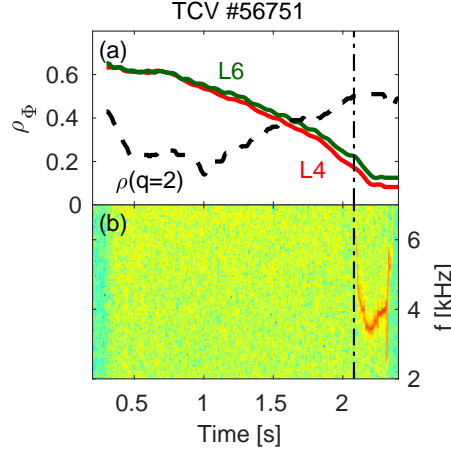


Figure 5.9. Experimental overview of an NTM onset experiment with varying co-ECCD depositions and constant EC power: (a) normalized deposition locations; and (b) 2/1 NTM spectrogram.

Table 5.1. Parameters for simulating #56027 with fixed $k = 6$, $a_3 = 1$ and $w_{\text{de}} = 1.9$ cm

Case No.	α	a_2	a_4	a_5	w_{dep} [cm]	With $G_{cd} < 0$	$\bar{\rho}_{mn}\Delta'_{\text{ohmic0}}$	$\bar{\rho}_{mn}\Delta'_{\text{sat}}$
1	8	2	0.4	0.9	5	N	figure 4.17, green	-1.02
2	8	2	0.4	0.9	5	Y	figure 4.17, green	-1.02
3	8	2	0	4.5	5	Y	figure 4.17, green	-0.94
4	8	2	0.25	1.6	10	Y	figure 4.17, green	-0.80

To better clarify these phenomena and isolate the effect of the negative part of G_{cd} on w evolution, an adapted G_{cd} curve (red trace in figure 5.7) is tested in the simulations of the NTM stabilization experiment #56027 (figure 5.6), removing the $G_{cd} < 0$ part while retaining the stabilizing effect. Similar to #58477 (figures 5.2 - 5.5), where a fast change of $I_{\text{cd,tot}}$ upon switching on the near-axis EC power is involved, $\bar{\rho}_{mn}\Delta'_{\text{ohmic0}}$ in the simulations is also taken from a direct interpolation of the $\bar{\rho}_{mn}\Delta'_{\text{ohmic0}} - n_{el}$ mapping for $I_p \approx -110$ kA (green curve in figure 4.17). $a_2 = 2$ is chosen to fit better the experimental $\frac{dw}{dt}(w)$ trace (dashed magenta curve in figure 5.10) while $\alpha = 8$ is tuned to minimize χ . The set of coefficients and parameters used in various simulations of #56027 are summarized in table 5.1. $\bar{\rho}_{mn}\Delta'_{\text{sat}}$ of cases 1, 3 and 4 are tuned based on the constraint exerted by point B in figure 5.8, following the same procedures as used in previous simulations, whereas the value for case 2 is taken directly from case 1 to illustrate better the effect of the $G_{cd} < 0$ part, as will be discussed later.

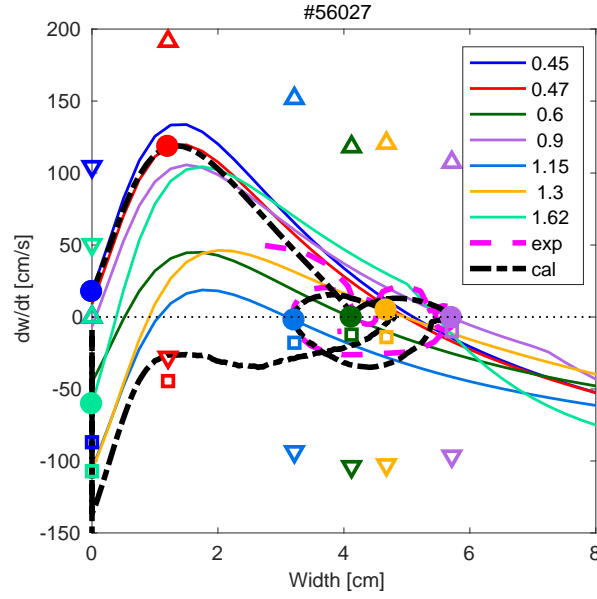


Figure 5.10. $\frac{dw}{dt}(w)$ traces at different time slices (as indicated by the numbers in the legend) of the simulation depicted by the solid red curve in figure 5.8, showing $\frac{dw}{dt}$ evaluated at various time slices and w (solid traces), and $\frac{dw}{dt}$ at the w_{cal} of each time slice (solid circles). $\bar{\rho}_{mn}\Delta'_D$ (downward-pointing triangles), $\bar{\rho}_{mn}\Delta'_{BS}$ (upward-pointing triangles) and $\bar{\rho}_{mn}\Delta'_{GGJ}$ (squares) at the w_{cal} of each time slice, divided by $\tau_R/\bar{\rho}_{mn}$, are also listed. $\frac{dw_{\text{cal}}}{dt}(w_{\text{cal}})$ from the simulation is plotted as the dash-dotted black curve while $\frac{dw_{\text{exp}}}{dt}(w_{\text{exp}})$ from measurement is shown by the dashed magenta trace.

The ranges of a_4 (for $\bar{\rho}_{mn}\Delta'_{CD}$) and a_5 (for $\bar{\rho}_{mn}\Delta'_H$) are summarized in equation (5.2) and table 5.3 through detailed NTM stabilization experiments with co-ECCD, counter-ECCD and ECH beams as well as corresponding simulations, as will be discussed in the next section. Within that range and with the adapted G_{cd} curve (i.e. removing the destabilization effect), $a_4 = 0.4$ and $a_5 = 0.9$ provide the best fit of the measurement so far (with $\chi = 6.54\%$). As shown by the solid red curve in figure 5.8, the simulation fits very well the entire w evolution, in terms of the initial mode growth, the w_{sat} , the partial stabilization as well as the full stabilization. It is emphasized that the above-mentioned coefficients are fixed during the entire discharge simulation. The $\frac{dw}{dt}(w)$ traces of this simulated w evolution are depicted in figure 5.10.

With the same coefficients as the above simulation (case 1 in table 5.1), another simulation is performed with the theoretical G_{cd} curve that includes the destabilizing effect (case 2), and is shown as the dashed cyan curve in figure 5.8. The x_{norm} (defined by equation (3.16)) of different EC beams as well as the corresponding G_{cd} and G_H of the simulation with adapted G_{cd} (case 1) are depicted in figure 5.11, whereas the corresponding values of case 2 are shown by the dashed blue traces (focusing on the control beam $L1$). The difference in x_{norm} of the two cases results from the difference of w_{cal} , for example at $t \in [0.72 \text{ s}]$ and $t \geq 1.65 \text{ s}$ when comparing the solid red and dashed cyan curves in figure 5.8, which enters the definition of x_{norm} (equation (3.16)) and in turn affects G_H . Note that G_{cd} and G_H (solid curves) are very small at $t = 1 \text{ s}$ and 1.3 s when $L1$ just starts to move towards the mode location, so the

control beam does not have obvious effects on the mode evolution until $t \approx 1.1$ s and $t \approx 1.4$ s, respectively, when the beam is close enough to the mode location. This is in accordance with the observed mode evolution in figures 5.6 and 5.8.

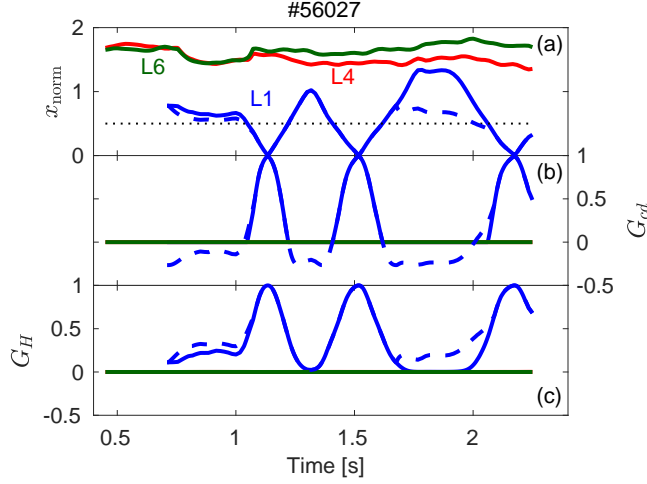


Figure 5.11. Misalignment levels (x_{norm}) of EC beams and the corresponding G_{cd} and G_H for the simulations shown by the solid red and dashed cyan curves in figure 5.8 (case 1 and 2 in table 5.1, respectively). (a) solid curves: x_{norm} evolutions of different EC beams, evaluated with the w_{cal} from the simulation with the adapted G_{cd} ; dashed blue: the corresponding x_{norm} of L1, evaluated with the w_{cal} from the simulation with the theoretical G_{cd} ; dotted black: $x_{\text{norm}} = 0.5$, where the theoretical G_{cd} value changes its sign with $w/w_{\text{dep}} \approx 1$, as shown in figure 5.7. (b) G_{cd} of different beams: evaluated based on the adapted G_{cd} curve in figure 5.7 and corresponding x_{norm} in (a) (solid), or based on the theoretical G_{cd} curve and corresponding x_{norm} in (a) (dashed). (c) G_H evaluated based on equation (3.14) and the corresponding x_{norm} shown in (a).

As indicated by the dashed curves in figure 5.11 (b), there are strong destabilizing effects of the EC beam (i.e. $G_{cd} < 0$) when depositing on both sides of the $q = 2$ surface (i.e. $0.7 \text{ s} \leq t \leq 1.05 \text{ s}$ and $1.22 \text{ s} \leq t \leq 1.4 \text{ s}$) in the simulation, causing a strong increase of w as seen from the dashed cyan curve in figure 5.8. Note that the product of the coefficients in front of G_{cd} (equation (3.9)) is larger when the beam deposits inside the $q = 2$ surface than outside, leading to a stronger destabilizing $\bar{\rho}_{mn} \Delta'_{CD}$ and explaining the significant increase of the simulated w only when $0.7 \text{ s} \leq t \leq 1.05 \text{ s}$. The destabilizing effect from G_{cd} also leads to a $\bar{\rho}_{mn} \Delta'_{CD} > 0$ at $1.62 \text{ s} \leq t \leq 2.05 \text{ s}$ when L1 is moving towards the plasma center and would have triggered the mode again, which is not observed in the experiment.

Efforts are made to simulate w evolution with the theoretical G_{cd} curve by tuning different parameters, e.g., a_4 , a_5 and w_{dep} . For $w_{\text{dep}} = 5 \text{ cm}$, it is found that even with a very small ECCD effect ($a_4 = 0.1$) and very large heating term ($a_5 = 4.5$), the mode would have been triggered when L1 moves towards the plasma center. Reasonable fit of the measured w can be achieved with $a_4 = 0$ and $a_5 = 4.5$ (dashed purple trace in figure 5.8, case 3 in table 5.1), but it is not physical as on one hand ECCD is expected to play a role (a_4 should be finite) and on the other hand $a_5 = 4.5$ is already out of the range of a_5 defined in the next section (equation (5.2)). Doubling the w_{dep} of L1 to 10 cm and using $a_4 = 0.25$ and $a_5 = 1.6$, which are the limits

of the ranges summarized in equation (5.2) and table 5.3, the simulation cannot recover the observed localized partial or full stabilization effects when $L1$ reaches the mode location, as indicated by the dashed orange curve in figure 5.8.

Similar exercises have also been performed for the above-mentioned experiments (#40411 and #40418) shown in [Felici et al. 2012, figure 3]. The full NTM stabilization from inside and outside the rational surface in those two experiments defines well the actual location of the $\bar{\rho}_{mn}$, while the fast decrease of measured w before full stabilization determines w_{de} in the experiments, as discussed in [Felici et al. 2012]. Detailed simulations show that the $G_{cd} < 0$ part of the theoretical curve would cause a sudden increase of the simulated w before full stabilization, especially for the case where the control beam moves from inside the rational surface (#40411) and thus having a larger product of the coefficients in front of G_{cd} . Even with a wide $w_{dep} = 10$ cm for the $\bar{\rho}_{mn}\Delta'_H$ term (while retaining the narrow w_{dep} for $\bar{\rho}_{mn}\Delta'_{CD}$) as well as the maximum $a_5 = 1.6$ from equation (5.2), the destabilizing effect from $G_{cd} < 0$ cannot be counteracted. This once again questions the existence or at least the level of the destabilization part in the G_{cd} curve, emphasizing the necessity of more theoretical investigations in this respect, in particular including the self-consistent modifications of q profiles on transport and current redistribution time scales.

Given the large heating effects entangled in the experiments and the uncertainties in the measurement of w , it is not possible to quantify the level of the negative part of G_{cd} (if any) in more details yet, but we have shown that it is not dominant in our experiments and the adapted G_{cd} curve (without the negative part) will be used in all the following discussions for simplicity. It should also be noted that although tuning the fixed free coefficients does allow matching the largest experimental w_{sat} , the good match of the entire time evolution of w , with constant coefficients, means that the parametric dependencies of the various terms used in the MRE match well the experiments.

5.5 NTM stabilization with co-ECCD, counter-ECCD or ECH

A series of NTM stabilization experiments have been carried out with the control beam in co-ECCD, counter-ECCD or ECH, respectively, to better separate the contribution of heating ($\bar{\rho}_{mn}\Delta'_H$) and current drive ($\bar{\rho}_{mn}\Delta'_{CD}$) to 2/1 NTM stabilization in the test discharges. $n_{el} \in [1.8, 2.3] \times 10^{19} \text{ m}^{-3}$ and $I_p \approx -110 \text{ kA}$ are maintained in these discharges. As shown in figure 5.12, about 0.96 MW of X2 EC power is switched on at $t = 0.4$ s and deposits co-ECCD near the plasma center through $L4$ and $L6$. 2/1 NTMs are triggered at about $t = 0.5$ s in the discharges, similar to previous examples. $L1$ with a power of 0.75 MW is switched on at $t = 0.8$ s and moved towards the mode location from $t = 1$ s to stabilize the modes. The toroidal angle of $L1$ is set such that it can drive co-ECCD (#56171, figure 5.12 (a)-(c)), counter-ECCD (#56172, figure 5.12 (d)) or ECH (#56173, figure 5.12 (e)), respectively, while the poloidal angle remains the same for the three discharges.

$L4$ and $L6$ deposit near the plasma center with a slow ramp-down of their power from $t = 0.9$ s

and reach a total power of 0.6 MW at $t = 2.25$ s, which would still sustain the mode if $L1$ were not present, as indicated by the example shown in figure 5.2. For the case with co-ECCD (figure 5.12 (c)), 2/1 NTM is fully stabilized at $t = 1.25$ s when $L1$ crosses the mode location for the first time. Note that $L1$ then continues depositing around the $q = 2$ surface and no mode is destabilized. For the case with counter-ECCD (figure 5.12 (d)) and with similar amount of driven current as in the co-ECCD case, partial stabilization effect can be observed. For the case with ECH, partial stabilization is kept until $t = 2.37$ s, when $L1$ beam reaches the mode location for the third time and fully stabilizes the mode just before turning off the EC power at $t = 2.4$ s, as illustrated in figure 5.12 (e).

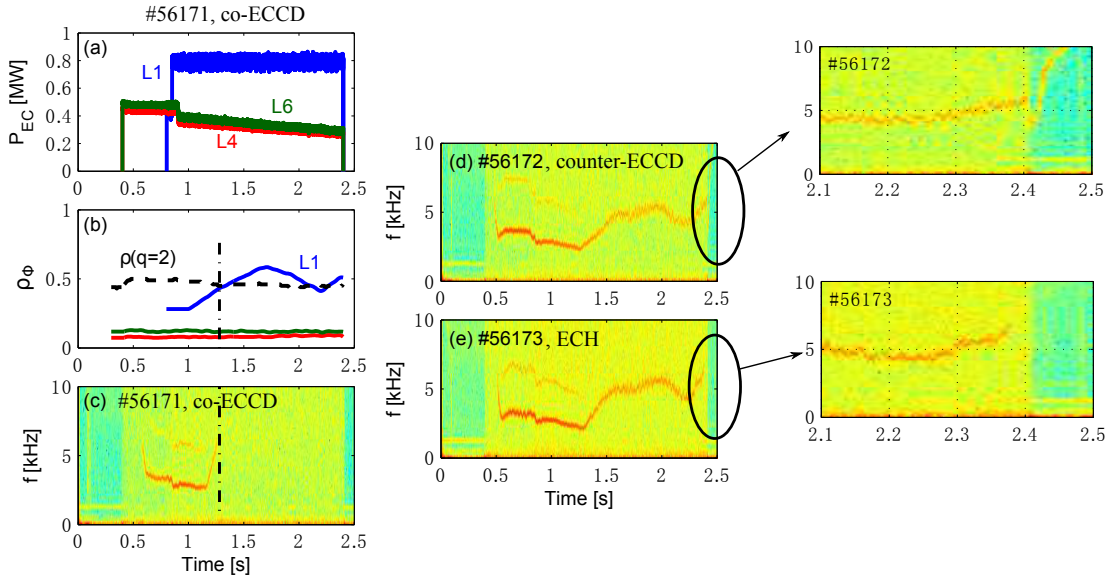


Figure 5.12. Experimental overview of a series of NTM stabilization experiments with co-ECCD, counter-ECCD and ECH for control: (a) EC power traces (same in the three discharges, with power off at $t = 2.4$ s); (b) EC deposition locations (the three discharges share the same poloidal angles, similar deposition locations and $q = 2$ surface locations); (c) 2/1 NTM spectrogram for #56171 ($L1$ in co-ECCD), exhibiting full NTM stabilization with the first crossing of the mode location at $t = 1.25$ s; (d) 2/1 NTM spectrogram for #56172 ($L1$ in counter-ECCD), showing partial stabilization; (e) 2/1 NTM spectrogram for #56173 ($L1$ in ECH), illustrating full stabilization with the third crossing of mode location at $t = 2.37$ s. Figure from [Kong et al. 2019].

The relative importance of heating ($\bar{\rho}_{mn}\Delta'_H$) and current driven ($\bar{\rho}_{mn}\Delta'_{CD}$) on mode evolution can be estimated through simulating these three discharges with the MRE. The cost function χ defined in equation (4.5) is used to quantify the accuracy of simulations without involving full stabilization (e.g. for #56172 and #56173), while

$$\chi^2 = \frac{1}{M} \sum_{i=1}^M \left(\frac{w_{cal}(t_i) - w_{exp}(t_i)}{w_{exp}(t_i)} \right)^2 + c_{weight} \left(\frac{t_{stab,cal} - t_{stab,exp}}{t_{norm}} \right)^2 \quad (5.1)$$

is used for simulations involving full NTM stabilization. M refers to the total number of measurement points at which $w_{cal}(t_i) \geq \min(w_{exp}(t_{i=1,2,\dots,N}))$, where N is the total number

of measurement points within the simulation time window, $w_{\text{cal}}(t_i)$ the simulated island width evaluated at the measurement time point $t = t_i$ and $w_{\text{exp}}(t_i)$ the measured w at t_i ; $t_{\text{stab,exp}}$ stands for 100 ms after mode drops below the noise level of measurements, which is about the time for w to reach 0 from the noise level as seen in figure 5.14; $t_{\text{stab,cal}}$ is the time at which w_{cal} reaches 0 again after onset; $c_{\text{weight}} = 1.8$ and $t_{\text{norm}} = 1$ s are chosen so that a $\Delta t = |t_{\text{stab,cal}} - t_{\text{stab,exp}}| = 0.15$ s offset in the stabilization timing would lead to a $\chi \geq 20\%$. In this way, χ is not affected differently by “earlier” or “later” stabilization in the simulations as long as Δt is the same.

Simulations with the MRE are performed for these three discharges with constant coefficients in all the simulations. The ranges of a_4 and a_5 in equation (3.3) can be estimated by optimizing χ in the three discharges. For instance, the range of a_5 can be determined by simulating #56173 (i.e. L1 in ECH) as $\bar{\rho}_{mn}\Delta'_{CD} \approx 0$ in this case, and we get

$$0.2 \leq a_5 \leq 1.6 \quad (5.2)$$

to keep $\chi \leq 20\%$, i.e. within the error bar of w measurement. The best fit achieved for this discharge is with $a_5 = 0.9$, resulting $\chi \approx 6.5\%$, as shown by the solid red curve in figure 5.13 (a). Stronger oscillations along with the movement of L1 are seen in the simulation than the measurement, indicating a possibly larger w_{dep} than the one used here (5 cm).

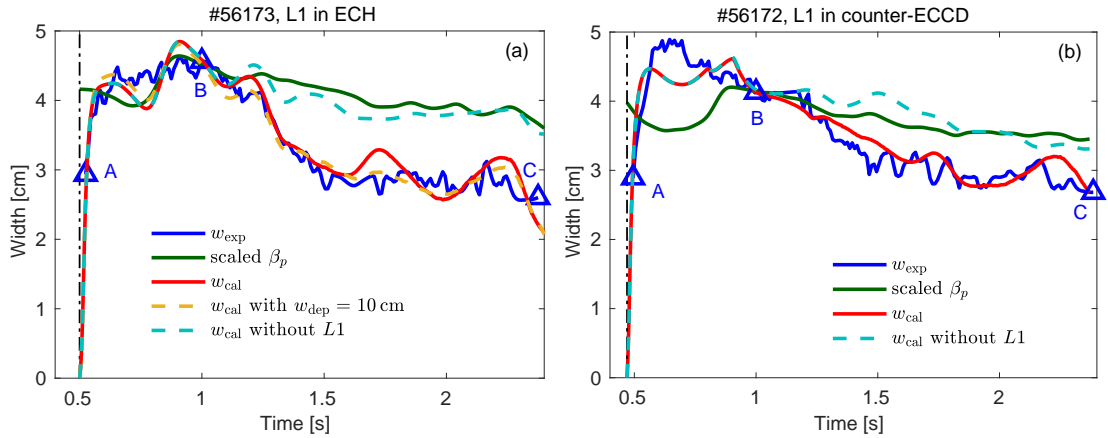


Figure 5.13. Island width evolution of NTM stabilization (a) with ECH and (b) with counter-ECCD. Solid blue: measurements; solid green: scaled β_p based on equation (4.3), with $t_{\text{ref}} = 1$ s, $\beta_p(t_{\text{ref}}) = 0.9$ for (a) and $\beta_p(t_{\text{ref}}) = 0.91$ for (b). (a) solid red: simulation with parameters listed as case 5 in table 5.2; dashed orange: case 6 (with doubling w_{dep} for L1); dashed cyan: case 7 (assuming no stabilization effect from L1). (b) solid red: simulation with the parameters listed as case 3 in table 5.2; dashed cyan: case 4 (assuming no stabilization effect from L1). A in both (a) and (b): the first measurement point available; B: the constraint used to determine $\bar{\rho}_{mn}\Delta'_{\text{sat}}$; A to C: the time range within which χ (equation (4.5)) is evaluated.

Doubling the w_{dep} of L1 to 10 cm, a better fit with $\chi \approx 4.5\%$ can be achieved, as indicated by the dashed orange curve in figure 5.13 (a). This implies a possibly stronger broadening of the

beam in the near perpendicular injection (ECH), but the details of this are out of the scope of this thesis. Note that the slight ramp-down of the near-axis power used for triggering NTMs ($L4$ and $L6$) that reaches a minimum total power around 0.6 MW in these three experiments, is not able to fully stabilize the NTMs, as indicated by the dashed cyan curves in figures 5.13 and 5.14, where simulations have been performed assuming no stabilization effect from $L1$ and the mode would have stayed. This is consistent with the experiment shown in figure 5.2, where the self-stabilization is only obtained when the total central power ramps down to around 0.35 MW. The list of parameters used in the simulations are summarized in table 5.2 (case 5 to 7 for #56173).

Table 5.2. List of the key parameters used to simulate #56171, #56172 and #56173, with fixed $k = 6$, $a_3 = 1$ and $w_{de} = 1.9$ cm

Case No.	Discharge #	α	a_2	a_4	a_5	w_{dep} [cm]	$\bar{\rho}_{mn}\Delta'_{ohmic0}$	$\bar{\rho}_{mn}\Delta'_{sat}$	χ
1	56171	8	1.5	0.4	0.9	5	figure 4.17, green	-1.1	6.2%
2	56171	8	1.5	0	0	5	figure 4.17, green	-1.1	> 20%
3	56172	8	1.5	0.3	0.9	5	figure 4.17, green	-1.12	6.3%
4	56172	8	1.5	0	0	5	figure 4.17, green	-1.12	> 20%
5	56173	5	1.5	0.4	0.9	5	figure 4.17, green	-1.32	6.5%
6	56173	5	1.5	0.4	1.8	10	figure 4.17, green	-1.24	4.5%
7	56173	5	1.5	0	0	5	figure 4.17, green	-1.32	> 20%

Table 5.3. Ranges of a_4 with various a_5 values

Fixed a_5 chosen based on equation (5.2)	Range of a_4 to keep $\chi \leq 20\%$ for #56171	Range of a_4 to keep $\chi \leq 20\%$ for #56172	Overlapped ranged of a_4 to keep $\chi \leq 20\%$ for both shots
0.2	[0.5 3]	[0.1 0.2]	No overlap
0.5	[0.4 3]	[0.1 0.4]	0.4
0.9	[0.3 2.9]	[0.1 0.65]	[0.3 0.65]
1.2	[0.2 2.8]	[0.15 0.85]	[0.2 0.85]
1.6	[0.1 2.6]	[0.25 1.1]	[0.25 1.1]

With a fixed value of a_5 taken from equation (5.2), the range of a_4 can be determined by simulating the co-ECCD and counter-ECCD experiments and ensuring $\chi \leq 20\%$ for both discharges. Various a_5 values are tested, with the corresponding range of a_4 summarized in table 5.3. Note that the minimum of a_4 has been set to 0.1 in these simulations as $\bar{\rho}_{mn}\Delta'_{CD}$ is expected to play a role (i.e. a_4 should be finite). It can be seen that with increasing a_5 (thus a larger stabilizing term $\bar{\rho}_{mn}\Delta'_H$), both the lower and upper bounds of a_4 decrease for the co-ECCD case #56171, meaning that less stabilizing effect from $\bar{\rho}_{mn}\Delta'_{CD}$ is required to fit the measured full stabilization of NTMs, as expected; the trend is opposite for the counter-ECCD case #56172, in accordance with the fact that larger destabilization effect from $\bar{\rho}_{mn}\Delta'_{CD}$

(counter-ECCD) can be tolerated with a larger stabilizing $\bar{\rho}_{mn}\Delta'_H$ term (with increasing a_5). With $a_5 = 0.9$ (the best fit for the ECH case, #56173), $a_4 = 0.4$ gives the best fit for #56171 (case 1 in table 5.2), while $a_4 = 0.3$ for #56172 (case 3 in table 5.2), as depicted by the red curves in figure 5.13 (b) and 5.14, respectively.

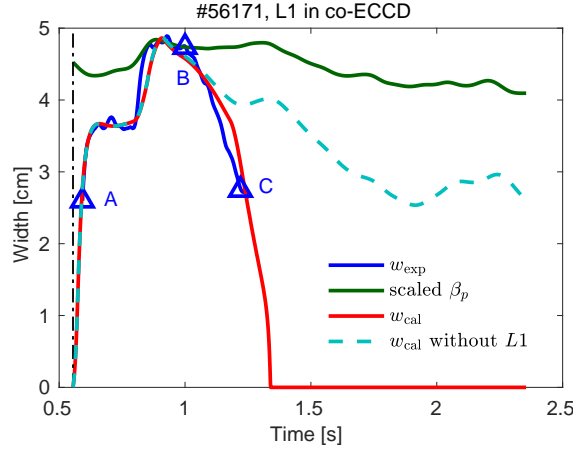


Figure 5.14. Island width evolution of discharge #56171 illustrated in figure 5.12. Solid blue: measurement; solid green: scaled β_p based on equation (4.3), with $t_{\text{ref}} = 1$ s and $\beta_p(t_{\text{ref}}) = 0.84$; solid red: simulation with the parameters listed as case 1 in table 5.2; dashed cyan: case 2 (assuming no stabilization effect from $L1$). A: the first measurement point available; B: the constraint used to determine $\bar{\rho}_{mn}\Delta'_{\text{sat}}$; A to C: the range within which χ (equation (4.5)) is evaluated.

Simulations assuming no stabilization effect from $L1$ (i.e. the dashed cyan curves) in figure 5.13 also highlight the different effects of heating ($\bar{\rho}_{mn}\Delta'_H$) and current drive ($\bar{\rho}_{mn}\Delta'_{CD}$) on NTM stabilization. Note that both ECH and counter-ECCD have a stabilizing heating effect (i.e. $\bar{\rho}_{mn}\Delta'_H < 0$). The fact that there is a larger difference between the dashed cyan curve and the solid blue or red curve in the case of ECH (#56173, figure 5.13 (a)) than in the case of counter-ECCD (#56172, figure 5.13 (b)) indicates that ECH is more effective than counter-ECCD on NTM stabilization, as expected. This is because counter-ECCD has a destabilizing current drive effect (i.e. $\bar{\rho}_{mn}\Delta'_{CD} > 0$), which counteracts its stabilizing heating effect ($\bar{\rho}_{mn}\Delta'_H < 0$) and displays an overall less effective stabilizing effect than the ECH case that has $\bar{\rho}_{mn}\Delta'_H < 0$ and $\bar{\rho}_{mn}\Delta'_{CD} \approx 0$. Simulations indicate a slightly larger amplitude of the heating effect ($|\bar{\rho}_{mn}\Delta'_H|$) than current drive effect ($|\bar{\rho}_{mn}\Delta'_{CD}|$) in #56172 (counter-ECCD), explaining the overall stabilizing effect observed in this discharge.

The co-ECCD beam ($L1$) used in #56171 (figure 5.14) has $\bar{\rho}_{mn}\Delta'_H < 0$ and $\bar{\rho}_{mn}\Delta'_{CD} < 0$ (i.e. both stabilizing), thus exhibiting the strongest overall stabilization effect among the three experiments. Figure 5.15 shows $\frac{dw}{dt}(w)$ traces at several interesting time slices of the best fit of #56171 (solid red curve in figure 5.14), concerning mode onset ($t = 0.55$ s), $w_{\text{sat}} = 3.5$ cm ($t = 0.72$ s), $w_{\text{sat}} = 5$ cm ($t = 0.9$ s), full stabilization ($t = 1.25$ s), EC-heated plasma without mode ($t = 2$ s) as well as the ohmic plasma after turning off the EC power ($t = 2.28$ s).

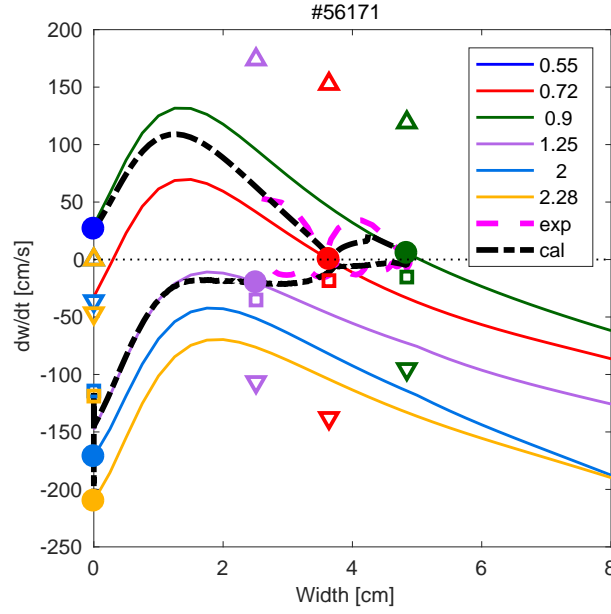


Figure 5.15. $\frac{dw}{dt}(w)$ traces at different time slices (as indicated by the numbers in the legend) of the simulation shown by the solid red curve in figure 5.14 (case 1 in table 5.2), showing $\frac{dw}{dt}$ evaluated at various time slices and w (solid traces), and $\frac{dw}{dt}$ at the w_{cal} of each time slice (solid circles). $\bar{\rho}_{mn}\Delta'$ (downward-pointing triangles), $\bar{\rho}_{mn}\Delta'_{BS}$ (upward-pointing triangles) and $\bar{\rho}_{mn}\Delta'_{GGJ}$ (squares) at the w_{cal} of each time slice, divided by $\tau_R/\bar{\rho}_{mn}$, are also listed. $\frac{dw_{\text{cal}}}{dt}(w_{\text{cal}})$ from the simulation is plotted as the dash-dotted black curve while $\frac{dw_{\text{exp}}}{dt}(w_{\text{exp}})$ from measurement is shown by the dashed magenta trace.

To investigate the increase of the inductive (ohmic) current due to the deposition of EC powers in these experiments, it is feasible to use $\eta_H P_l$ in equation (3.10), where η_H refers to the efficiency with which the EC power is converted into a perturbative inductive current as defined in section 3.4 and P_l the absorbed EC power. The $\eta_H P_l$ of the control beam L1 has been evaluated, giving 3kA \sim 6kA in these three experiments. This is slightly higher than the current driven (I_{cd}) by the control beam L1 when it reaches the $q = m/n$ surface, which is 2kA \sim 3kA in the case of co-ECCD (#56171). Note that there are other parameters in front of $\eta_H P_l$ and I_{cd} for the calculation of $\bar{\rho}_{mn}\Delta'_H$ (equation (3.10)) and $\bar{\rho}_{mn}\Delta'_{CD}$ (equation (3.9)), and simulations give $\bar{\rho}_{mn}\Delta'_{CD}(\approx -0.4) \leq \bar{\rho}_{mn}\Delta'_H(\approx -0.15) < 0$ in the case of co-ECCD (#56171).

It is also useful to evaluate the current density driven at the mode location (i.e. $j_{cd}(\rho = \rho_{mn})$) as it is expected to compensate the missing bootstrap current density at the rational surface (i.e. $j_{bs}(\rho = \rho_{mn})$) caused by the mode. Following the conventions in the literature [Sauter et al. 2010; Zohm et al. 2007; Poli et al. 2015; Bertelli et al. 2011], we define $\eta_{\text{NTM}} \equiv \frac{j_{cd}(\rho=\rho_{mn})}{j_{bs}(\rho=\rho_{mn})}$ to quantify this effect. Figure 5.16 summarizes the level of η_{NTM} of five TCV experiments to give an indication of the η_{NTM} required for 2/1 NTM stabilization in the test discharges.

Similar to the EC power settings in #56027 (figure 5.6 (a)) and #56171 (figure 5.12 (a)), a third co-ECCD beam was switched on after the onset of 2/1 NTMs for NTM stabilization in #55106,

#58248 and #58249 involved in figure 5.16. Different deposition locations of the control co-ECCD beam are covered in the tests, as indicated by the abscissa ($x_{\text{norm,sign}}$) of figure 5.16, where $x_{\text{norm,sign}} = \frac{(\bar{\rho}_{\text{dep}} - \bar{\rho}_{mn})}{\max(w, w_{\text{dep}})}$ is similar to x_{norm} (equation (3.16)) but defined here to distinguish depositions on different sides of the $q = m/n$ surface. For instance, it can be seen that the control co-ECCD beam of #56027, #56171 and #55106 deposits around the $q = m/n$ surface (with $-0.5 \leq x_{\text{norm,sign}} \leq 0.5$) and displays a peak of η_{NTM} when reaching near the $q = m/n$ surface, due to a peak in $j_{cd}(\rho = \rho_{mn})$, as expected. In #58248 and #58249, however, the control co-ECCD beam deposits far from the $q = m/n$ surface (by pre-programming) with $x_{\text{norm,sign}} < -0.45$ (i.e. inside the rational surface, more towards the plasma center) and $x_{\text{norm,sign}} > 0.45$ (i.e. outside the rational surface, more towards the plasma edge), respectively. They are taken from a series of NTM-EC misalignment experiments that will be discussed in section 5.7. #58248 and #58249 confirm that only very small $j_{cd}(\rho = \rho_{mn})$ and η_{NTM} can be obtained with this level of beam misalignment and that no full stabilization of NTMs can be reached.

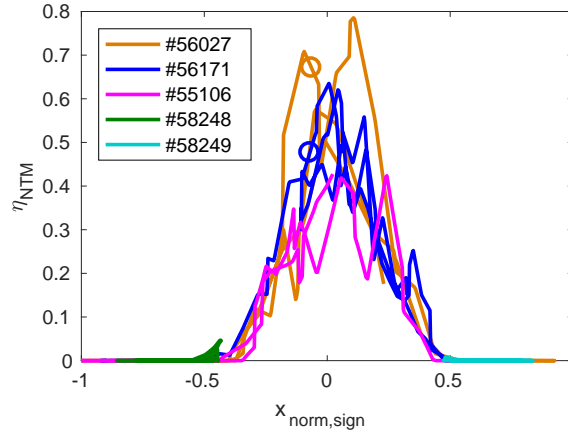


Figure 5.16. A collection of $\eta_{\text{NTM}} \equiv \frac{j_{cd}(\rho = \rho_{mn})}{j_{bs}(\rho = \rho_{mn})}$ reached in various 2/1 NTM stabilization experiments in TCV. $x_{\text{norm,sign}}$ indicates the deposition location of the control beam with respect to the 2/1 rational surface. The two open circles represent the instances with full stabilization (in #56027 and #56171), yielding $\eta_{\text{NTM}} = 0.6 \pm 0.2$ is required to fully stabilize 2/1 NTMs in these TCV experiments. In #58248 and #58249, the large misalignment ($|x_{\text{norm,sign}}| > 0.45$) of the control beam was programmed on purpose. Figure from [Kong et al. 2019].

Full stabilization of 2/1 NTMs are only observed in #56027 and #56171, as marked by the open circles with corresponding colors in figure 5.16. This gives $\eta_{\text{NTM}} > 0.45$ for full 2/1 NTM stabilization in these TCV experiments, with the perturbed bootstrap current density of the order of 10^5 A/m^2 . However, in addition to the uncertainties of the evaluation of j_{cd} and j_{bs} , there is an uncertainty of the exact relative position of EC beams with respect to the mode (i.e. $x_{\text{norm,sign}}$) at the time of full stabilization. Therefore, it could be more consistent to consider that the modes are stabilized at $x_{\text{norm,sign}} = 0$, which would give $\eta_{\text{NTM}} \geq 0.6$ based on figure 5.16. Overall we have $\eta_{\text{NTM}} = 0.6 \pm 0.2$ for full NTM stabilization from these analyses.

This η_{NTM} value is lower than the predicted requirement for ITER [Sauter et al. 2010; Zohm et al. 2007; Poli et al. 2015], which does not consider $\bar{\rho}_{mn}\Delta'_H$ explicitly in the calculations, as $\bar{\rho}_{mn}\Delta'_{CD}$ is predicted to dominate in ITER [De Lazzari and Westerhof 2009, 2010]. As shown by the MRE simulations in this section, the amplitude of $\bar{\rho}_{mn}\Delta'_H$ is comparable to that of $\bar{\rho}_{mn}\Delta'_{CD}$ in our NTM stabilization experiments with co-ECCD, contributing significantly to the stabilization of NTMs and reducing the requirement of η_{NTM} for full NTM stabilization. Similar and lower values of η_{NTM} have been observed in other tokamaks [Isayama et al. 2009] and are consistent with theoretical predictions considering $\bar{\rho}_{mn}\Delta'_H$ explicitly [Bertelli et al. 2011].

5.6 NTM stabilization versus prevention

The prevention of NTMs with localized preemptive ECCD, as another method of NTM control, has been explored in TCV as well. In principle NTM prevention allows avoiding NTMs altogether and can be the preferred control method, but it penalizes Q (ratio between fusion energy and input energy) and may be prohibitive for some scenarios [Sauter et al. 2010]. An example of NTM prevention experiments is shown in figure 5.17, where $L1$ is switched on at $t = 0.3\text{s}$ and sweeps around the 2/1 rational surface sinusoidally. The small sinusoidal sweeping of the control beam ($L1$) is applied to facilitate the comparison between NTM prevention and stabilization (#58254, figure 5.18), by increasing the chance of covering the correct location in both cases despite possibly different plasma evolutions. As shown in figure 5.16, covering $x_{\text{norm}} \approx 0$ is crucial for NTM control.

$L4$ and $L6$ are switched on at $t = 0.4\text{s}$ and deposit near the plasma center for NTM onset, as used in previous examples. All the launchers are set to drive co-ECCD in this experiment. A ramp-down of $L1$ (i.e. the control beam) power is applied to estimate the minimum power required for NTM prevention (i.e. without the onset of NTMs). It can be seen from figure 5.17 that no 2/1 NTM is triggered until completely turning off $L1$ at $t \approx 1.1\text{s}$ when $L1$ power ramps down to 0.36MW, meaning that 2/1 NTM is successfully prevented with only 0.36MW.

In a comparable NTM stabilization discharge shown in figure 5.18, similar plasma scenario and settings as in #58256 are used, except that $L1$ is turned on after NTM onset and with a ramp-up of its power to estimate the minimum power required for full NTM stabilization. In this discharge, mode cannot be fully stabilized even with 0.75MW. This shows a higher efficiency for NTM prevention than stabilization, in terms of the EC power required in each case, similar to observations on other tokamaks [Nagasaki et al. 2005]. However, prevention of NTMs may require a much longer temporal duration of the EC power and thus a larger total input energy than NTM stabilization, which needs to be taken into account in the selection of NTM control strategies. The successful NTM prevention with sinusoidal sweeping (misalignment) around the rational surface also supports the use of the adapted G_{cd} term (figure 5.7) in the simulations. Further experiments with different but constant EC powers for NTM prevention and stabilization are needed to better quantify their comparison.

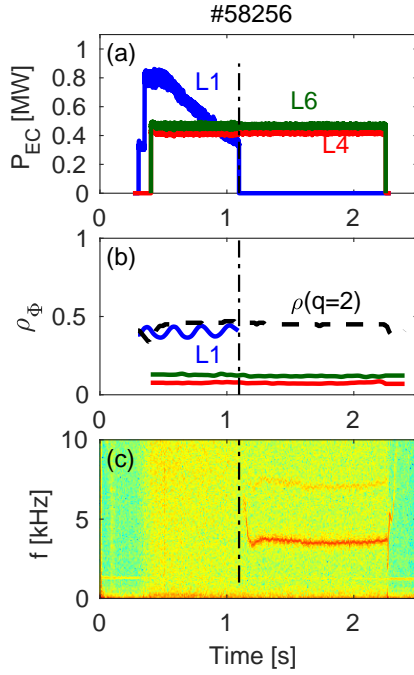


Figure 5.17. Overview of an NTM prevention experiment with off-axis co-ECCD: (a) EC power traces, where $L1$ is switched on before turning on the destabilizing near-axis power; (b) EC deposition locations, with $L1$ sweeping sinusoidally around the mode location; and (c) 2/1 NTM spectrogram. Figure from [Kong et al. 2019].

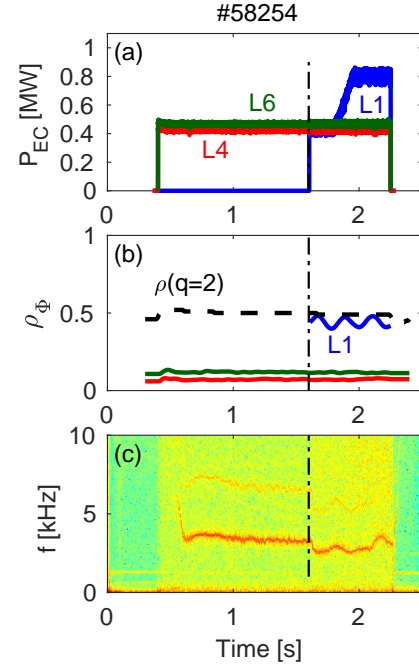


Figure 5.18. Overview of an NTM stabilization experiment with off-axis co-ECCD: (a) EC power traces, where $L1$ is switched on after mode onset; (b) EC deposition locations, with $L1$ sweeping sinusoidally around the mode location; and (c) 2/1 NTM spectrogram. Figure from [Kong et al. 2019].

Following the same procedures used in the previous chapter where NTMs occur in the middle of power-ramp or density-ramp, simulations are performed for the NTM prevention experiment shown in figure 5.17 (#58256). As shown in figure 5.19, simulations start from $t = 0.25$ s (i.e. ohmic plasma before turning on the EC power) with $w = 0$. Based on the discussions in section 5.5, $a_4 = 0.65$ and $a_5 = 0.9$ are used in the simulation shown by the solid red trace in figure 5.19. $\bar{\rho}_{mn}\Delta'_{\text{ohmic0}}$ and $\bar{\rho}_{mn}\Delta'_{\text{sat}}$ are tuned to satisfy the two constraints marked as “A” and “B” in figure 5.19, requiring a rigid shift of $\bar{\rho}_{mn}\Delta'_{\text{shift}} = -0.19$ in equation (4.7) based on the $\bar{\rho}_{mn}\Delta'_{\text{ohmic0}} - n_{el}$ mapping for $I_p \approx -110$ kA (dashed-dotted green curve with squares in figure 4.17) and $\bar{\rho}_{mn}\Delta'_{\text{sat}} = -0.84$. $a_2 = 1.4$ has been chosen to fit better the experimental $\frac{dw}{dt}(w)$ trace (dashed magenta in figure 5.20). It can be seen that the simulated red curve fits very well the timing of NTM onset and the island saturation after NTM triggering, with $\chi \approx 3.3\%$.

The prevention effect is found to result from the local effects of off-axis co-ECCD as well as the favorable curvature that all together counteracts the positive $\bar{\rho}_{mn}\Delta'_0$ that tends to trigger the mode. Note that $\bar{\rho}_{mn}\Delta'_0$ is actually higher before turning off the prevention power ($L1$), due to a higher total $I_{cd,\text{tot}}$ with three launchers in equation (4.2), but the mode has still been able to be preempted. This emphasizes the local effects of off-axis ECCD on NTM prevention and the

importance of covering the correct mode location for NTM control. It also explains why the mode is triggered relatively fast (within 20 ms) after turning off the preemptive EC power.

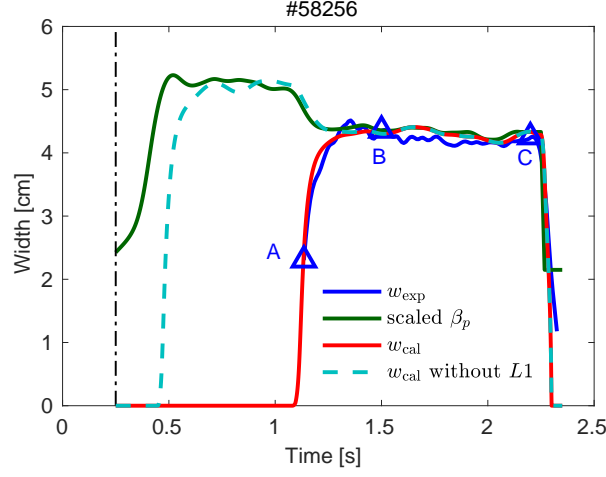


Figure 5.19. Island width evolution of #58256 (figure 5.17). Solid blue: measurement; solid green: scaled β_p based on equation (4.3), with $\beta_p(t_{\text{ref}} = 1.5) = 0.74$; solid red: simulation including the prevention effect from L1; dashed cyan: assuming no L1. A and B: the two constraints used to determine $\bar{\rho}_{mn}\Delta'_{\text{ohmic}0}$ and $\bar{\rho}_{mn}\Delta'_{\text{sat}}$; A to C: the time range within which χ (equation (4.5)) is evaluated.

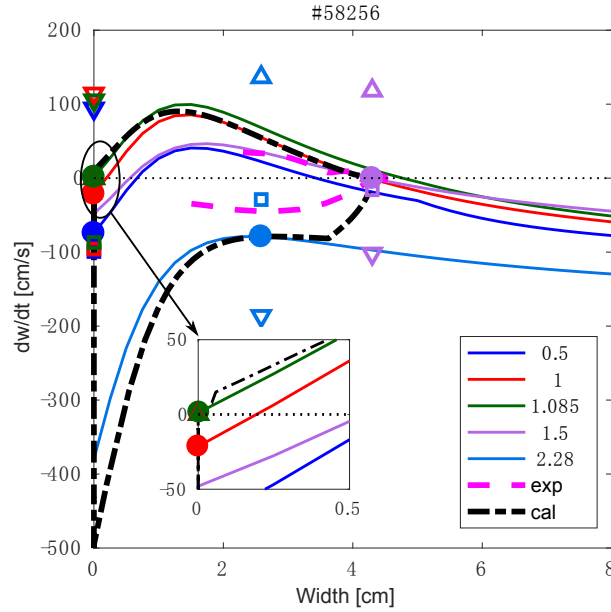


Figure 5.20. $\frac{dw}{dt}(w)$ traces at different time slices (as indicated by the numbers in the legend) of the simulation shown by the solid red curve in figure 5.19, showing $\frac{dw}{dt}$ evaluated at various time slices and w (solid traces), and $\frac{dw}{dt}$ at the w_{cal} of each time slice (solid circles). Full prevention (no mode, $t = 0.5$ s and $t = 1$ s), NTM onset ($t = 1.085$ s), $w_{\text{sat}} = 4.5$ cm ($t = 1.5$ s), and ohmic plasma ($t = 2.28$ s) are shown respectively. $\bar{\rho}_{mn}\Delta'$ (downward-pointing triangles), $\bar{\rho}_{mn}\Delta'_{BS}$ (upward-pointing triangles) and $\bar{\rho}_{mn}\Delta'_{GGJ}$ (squares) at the w_{cal} of each time slice, divided by $\tau_R/\bar{\rho}_{mn}$, are also listed. Dash-dotted black: $\frac{dw_{\text{cal}}}{dt}(w_{\text{cal}})$ from the simulation; dashed magenta: $\frac{dw_{\text{exp}}}{dt}(w_{\text{exp}})$ from measurement.

The $\frac{dw}{dt}(w)$ traces at several interesting time slices are shown in figure 5.20. One can see that before turning off $L1$, for example at $t = 0.5$ s and $t = 1$ s, the total $\frac{dw}{dt}$ values are negative at $w = 0$ (i.e. no mode onset), as indicated by the solid blue and red circles in the figure. At $t = 1.085$ s (green), $\frac{dw}{dt}$ goes just above 0 at $w = 0$ and leads to the onset of the NTM. At $t = 1.5$ s (purple), $w_{\text{sat}} = 4.5$ cm is reached, while plasma is stable to NTMs after turning off the near-axis ECCD power, for instance at $t = 2.28$ s. To investigate the prevention effect, another simulation has been performed with the same parameters but assuming no $L1$, as shown by the dashed cyan curve in figure 5.19. The mode would have been triggered at $t \approx 0.5$ s in this case, similar to NTM onsets shown in previous examples. Note that it is our complete MRE model including TMs that has allowed us to simulate and explain the role of ECCD in preemptive experiments.

5.7 Effects of EC misalignment on the stabilization and prevention of NTMs

As seen from the MRE (equation (3.3)) and the discussions in previous sections, the alignment of EC beams with respect to the mode location (i.e. beam-mode alignment/misalignment) plays an important role in the effectiveness of NTM control. To further illustrate this effect, this section discusses about dedicated experiments carried out on TCV with different misalignment levels of EC beams and corresponding simulations with the MRE. To start with, section 5.7.1 presents three representative NTM stabilization experiments that have different beam-mode misalignment levels (towards the center or edge of the plasma, or on target) and exhibit distinct effects on the island width evolution, the underlying physics of which is explored through simulations with the MRE. Section 5.7.2 shows the statistics of the effects of misalignment based on more TCV experiments, concerning both NTM stabilization and prevention cases, with or without a sinusoidal sweeping of the control EC beam.

5.7.1 A series of NTM stabilization experiments with different EC misalignment

Three representative NTM stabilization experiments (#58247-#58249) with similar settings as in previous sections but different beam-mode misalignment levels are shown in figure 5.21. The same EC power traces (figure 5.21 (a)) are used in the three discharges, while the poloidal angle of $L1$, thus its radial deposition location is different in the three discharges, as illustrated in figure 5.21 (b). The radial location of the $q = 2$ surface taken from ASTRA outputs, as indicated by the dashed black traces in (b), largely overlaps for the three discharges.

The difference in beam-mode alignment causes different evolution of NTMs: with enough power from $L1$, good alignment (#58247) leads to a full stabilization of 2/1 NTMs; slight misalignment towards the edge of the plasma leads to a partial stabilization of the mode, whereas slight misalignment towards the plasma center causes an increase of mode amplitude, as shown by the spectrogram in figure 5.21 and/or the measured island width in figures

5.22 and 5.23 (solid blue traces). The different deposition location of $L1$ meanwhile leads to different driven current from $L1$, thus the total driven current from the three EC launchers: more inward deposition (with a higher local T_e/n_e) drives more current, as depicted in figure 5.21 (d).

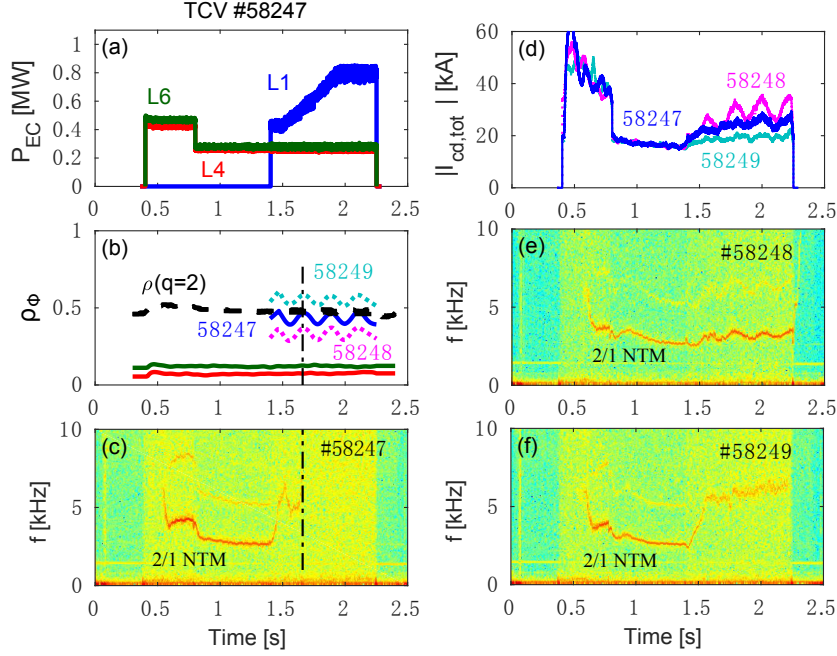


Figure 5.21. Experimental overview of a series of 2/1 NTM stabilization experiments with different beam-mode misalignment levels: (a) EC power traces, the same for the three discharges; (b) deposition locations of EC beams computed by TORAY-GA and $\rho(q=2)$ from ASTRA; (c) NTM spectrogram of #58247; (d) amplitude of the total driven current from all EC launchers, computed by TORAY-GA; (e) NTM spectrogram of #58248 and (f) NTM spectrogram of #58249.

To better understand the observed differences in mode evolution and quantify various effects, interpretative simulations with the MRE are performed for the three discharges. Shown in figure 5.22 are the results for the case with more inward deposition of $L1$ (#58248), where the measured w (solid blue) increases upon switching on $L1$ at $t = 1.4$ s. Following the same procedures as summarized in section 3.5 and used in previous sections, $a_2 = 1.5$, $a_3 = 1$, $a_4 = 0.3$, $a_5 = 0.9$, $\alpha = 5$, $w_{de} = 1.9$ cm and $w_{dep} = 5$ cm are used in the simulations, while $\bar{\rho}_{mn}\Delta'_{sat} = -0.83$ is fitted based on the w_{sat} at $t = 1.35$ s (the second blue triangle), i.e. before switching on the off-axis beam $L1$. Similar to #58477 (figure 5.2), a transient 3/2 NTM co-exists with the 2/1 mode at the beginning of the 2/1 mode evolution (not shown in figure 5.21), and adding a constant 3/2 “drag” fits better w_{exp} , as shown by the solid red curve in figure 5.22.

The overall destabilizing effect observed when turning on $L1$ in #58248 is found to result from various competing destabilizing and stabilizing effects: the higher total EC power upon switching on $L1$ leads to an increase of β_p that amplifies the destabilizing $\bar{\rho}_{mn}\Delta'_{BS}$, as indicated by the solid green trace in figure 5.22; the increase of the total driven current $I_{cd,tot}$ leads to

5.7. Effects of EC misalignment on the stabilization and prevention of NTMs

an increase of $\bar{\rho}_{mn}\Delta'_0$ (equation (4.2)), which eventually increases $\bar{\rho}_{mn}\Delta'$ (equation (3.25)), i.e. less stabilizing effect from $\bar{\rho}_{mn}\Delta'$; the misalignment meanwhile decreases the stabilizing effects from $\bar{\rho}_{mn}\Delta'_{CD}$ and $\bar{\rho}_{mn}\Delta'_H$, which are not sufficient to overcome the destabilizing effects and w eventually increases. Note that there is a larger increase of $I_{cd,tot}$ when the deposition is more towards the plasma center (figure 5.21 (d)), causing a more evident overall destabilizing effect. The existence and possible role of the destabilizing effect from $G_{cd} < 0$ (blue curve in figure 5.7) can be better isolated by simulations of experiments involving a wide range of x_{norm} (i.e. with EC beam sweeping from the edge to the center of the plasma in each discharge), as has been discussed in detail in section 5.4. It has been shown that $G_{cd} < 0$, if any, may not be as strong as predicted by theory and does not play an important role in the test discharges. The destabilizing effect resulting from altering q and j profiles (thus modifying $\bar{\rho}_{mn}\Delta'$) with EC beams has been included in our $\bar{\rho}_{mn}\Delta'$ model (equations (3.25) and (4.2)) consistently.

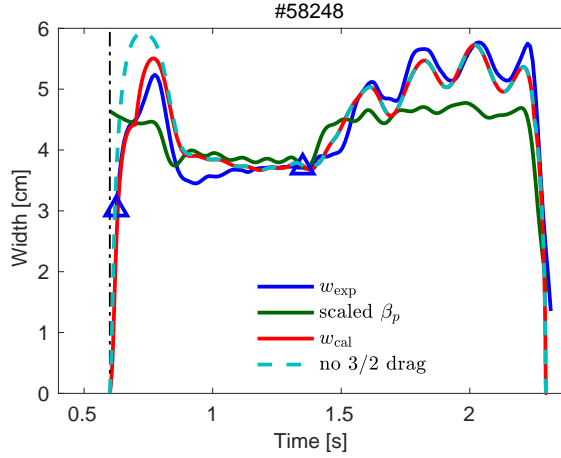


Figure 5.22. w evolution of #58248 shown in figure 5.21. Solid blue: measurement; solid green: scaled β_p based on equation (4.3), with $t_{ref} = 1.35$ s and $\beta_p(t_{ref}) = 0.65$; solid red: simulation including the “drag” from a co-existent 3/2 mode; dashed cyan: simulation without adding the 3/2 drag.

Simulations have also been performed for #58247 and #58249, where full or partial stabilization of 2/1 NTMs has been observed, respectively. The results for #58247 are shown in figure 5.23 (a), where the dashed cyan curve represents the simulation with the same parameters as #58248 presented above, except with $a_4 = 0.65$, i.e. the upper bound of a_4 with $a_5 = 0.9$ (table 5.3). This is seen to maximize the stabilizing effect from co-ECCD beams ($\bar{\rho}_{mn}\Delta'_{CD}$ and $\bar{\rho}_{mn}\Delta'_H$), but the full stabilization of NTM cannot be reproduced even in this simulation. Efforts have been made to better fit w_{exp} by tuning different parameters, including trying small rigid shifts of $\rho(q = 2)$ within its error bars, but without success. The main difficulty stems from the relatively slow and large drop of w upon switching on L1 (i.e. from $t = 1.4$ s to 1.5 s), which cannot be explained by the stabilizing effects from $\bar{\rho}_{mn}\Delta'_{CD}$ and $\bar{\rho}_{mn}\Delta'_H$, even with very large a_4 and a_5 that are already outside the ranges defined in table 5.3.

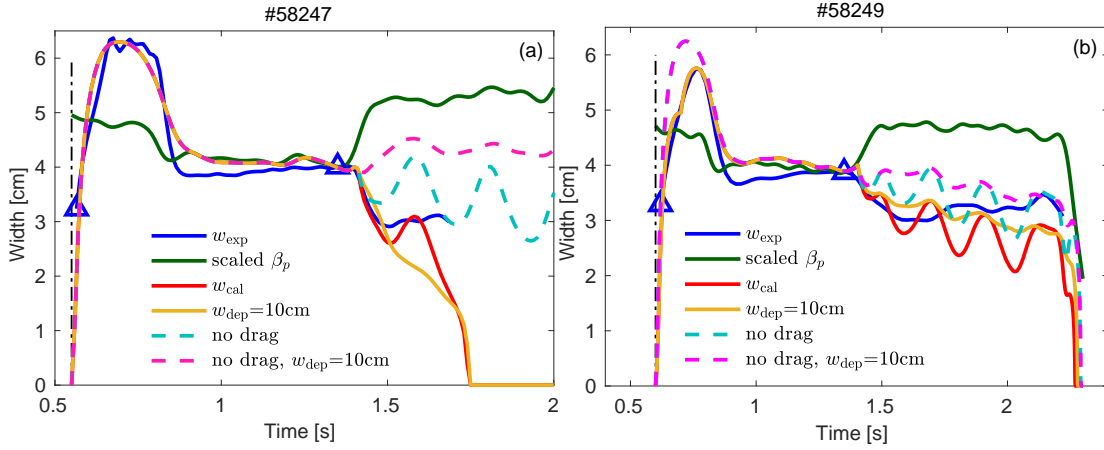


Figure 5.23. w evolution of (a) #58247 and (b) #58249 shown in figure 5.21. Solid blue: measurements; solid green: scaled β_p based on equation (4.3), with $\beta_p(t_{\text{ref}} = 1.35) = 0.65$; dashed cyan: simulation with the same parameters as in #58248, except with $a_4 = 0.65$; solid red: simulation with the same parameters as the dashed cyan curve, but with an extra $\bar{\rho}_{mn}\Delta'_{\text{extra}}$ (and a 3/2 drag as well for (b)); dashed magenta: simulation with the same parameters and settings as the dashed cyan curve, but with $w_{\text{dep}} = 10$ cm instead of 5 cm; solid orange in (a): simulation with the same parameters and settings as the solid red curve, except with $w_{\text{dep}} = 10$ cm and $\min(\bar{\rho}_{mn}\Delta'_{\text{extra}}) = -0.5$; solid orange in (b): simulation with the same parameters and settings as the solid red curve, but with $w_{\text{dep}} = 10$ cm.

Similar phenomenon has been observed in numerous similar TCV discharges (e.g. those shown in the next section), where a sudden switch-on of EC power at or outside $\rho(q = 2)$ is involved. This indicates that the abrupt switch-on of EC beams at more off-axis position may exert an extra effect on mode evolution, for example by changing the condition of the wall (e.g. recycling rate) that will affect the details of the q profile and thus $\bar{\rho}_{mn}\Delta'$. Note that this is different from the cases discussed in sections 5.4 and 5.5 (figures 5.6 and 5.12), where the off-axis beam is typically switched on well inside $\rho(q = 2)$, moves towards $\rho(q = 2)$ and sweeps around it - it is the sudden switch-on of EC power near or outside $\rho(q = 2)$ that plays a role.

To further investigate this phenomenon, an *ad hoc* $\bar{\rho}_{mn}\Delta'_{\text{extra}}$ term is added to the right hand side of the MRE (equation (3.3)), similar to the additional drag $\bar{\rho}_{mn}\Delta'_{32}$ added during the coexistence of the 3/2 mode. To take into the account the time scale of the variation of $\bar{\rho}_{mn}\Delta'$ (resistive time), $\bar{\rho}_{mn}\Delta'_{\text{extra}}$ is set to drop from 0 to a more negative value (-0.25 for the simulations of #58247) from $t = 1.4$ s to 1.5 s and remains constant (at -0.25) afterward. As a comparison, the simulation with the same parameters as the dashed cyan curve but adding the extra $\bar{\rho}_{mn}\Delta'_{\text{extra}}$ is shown by the solid red trace, where the full stabilization of the 2/1 NTM can be reproduced. It is worth emphasizing that the full stabilization here still results from the localized effect of EC beams when they reach close enough to the mode, i.e. from $\bar{\rho}_{mn}\Delta'_{CD}$ and $\bar{\rho}_{mn}\Delta'_{H'}$, whereas the $\bar{\rho}_{mn}\Delta'_{\text{extra}}$ added only mimics the change of plasma condition that slowly converges to a new equilibrium with more negative $\bar{\rho}_{mn}\Delta'$.

Considering the possible broadening of w_{dep} as discussed in previous sections, simulations are also performed assuming a wider w_{dep} of $L1$ (10 cm instead of 5 cm), with or without

5.7. Effects of EC misalignment on the stabilization and prevention of NTMs

the $\bar{\rho}_{mn}\Delta'_{\text{extra}}$, as shown by the solid orange and dashed magenta curves in figure 5.23 (a), respectively. Similar to the simulation with $w_{\text{dep}} = 5$ cm (dashed cyan), the case without $\bar{\rho}_{mn}\Delta'_{\text{extra}}$ (dashed magenta, $w_{\text{dep}} = 10$ cm) cannot reproduce the full stabilization of NTMs observed in this experiment either (figure 5.21 (c)); including the $\bar{\rho}_{mn}\Delta'_{\text{extra}}$ term and with a more negative value (-0.5 instead of -0.25) than the case with $w_{\text{dep}} = 5$ cm (solid red), the simulation with $w_{\text{dep}} = 10$ cm (solid orange) can reproduce the full stabilization, but with a larger χ than the simulation with $w_{\text{dep}} = 5$ cm (solid red).

Shown in figure 5.23 (b) are the results of #58249, where only partial stabilization is observed in the experiment (until completely turning of the EC power at $t = 2.25$ s). Simulations are performed with the same parameters as #58247 (with $a_4 = 0.65$ as well), with or without $\bar{\rho}_{mn}\Delta'_{\text{extra}}$, as shown by the solid red and dashed cyan curves, respectively. It shows that adding a $\bar{\rho}_{mn}\Delta'_{\text{extra}}$ tends to fit better the evolution from $t = 1.4$ s to 1.5 s. This is more evident in simulations with $w_{\text{dep}} = 10$ cm, as indicated by the solid orange and dashed magenta curves. A wider w_{dep} in this case decreases the oscillations of the simulated w and fits better the measurements, indicating a possible broadening of w_{dep} when the EC beam deposits closer to the plasma edge, which is not included in the computations with TORAY-GA. There is also a co-existent 3/2 mode at the beginning of the 2/1 evolution in this discharge, similar to #58248, and an extra 3/2 drag is included in the simulations with $\bar{\rho}_{mn}\Delta'_{\text{extra}}$ (i.e. solid red and orange curves in 5.23 (b)).

The series of experiments presented in this section illustrate the effect of beam-mode misalignment on the stabilization of NTMs: while a good alignment (with sufficient EC power) leads to the full stabilization of NTMs and a slight misalignment towards the edge of the plasma leads to partial stabilization, the misalignment towards the center of the plasma causes an increase of the island width. Based on corresponding MRE simulations, the overall destabilizing effect is found to result from a large increase of β_p (thus Δ'_{BS}) and Δ' (less stabilizing, through a larger $I_{\text{cd,tot}}$ value), as well as the decrease of the local stabilizing effects from off-axis EC beams when misaligned.

5.7.2 Statistics of the effect of beam-mode misalignment on the stabilization and prevention of NTMs

Misalignment tests with sweeping

The strong correlation of w with beam-mode alignment presented in the previous section has motivated further experimental studies on this topic, covering a larger range of beam-mode misalignment and testing both NTM stabilization and prevention cases. The experimental settings are illustrated in figure 5.24. For NTM stabilization shown in (a), $L4$ and $L6$ deposit near the plasma center for mode onset, while $L1$ is switched on after mode onset and sinusoidally sweeps around the mode location (dashed black curve in the middle panel, based on LIUQE outputs) with a normalized full sweeping amplitude of 0.1. ρ_ψ in the figures refers to the normalized radial location based on the square root of the poloidal flux Ψ . In the example

shown here where a good beam-mode alignment is maintained (#60208), full stabilization of the 2/1 mode is achieved right after turning on $L1$. Figure 5.24 (b) illustrates an NTM prevention experiment, where $L1$ is switched on before turning on the central EC beams, preventing the onset of NTMs. It can be seen that 2/1 NTM is successfully prevented in this discharge, i.e. the mode does not occur until completely turning off the prevention power.

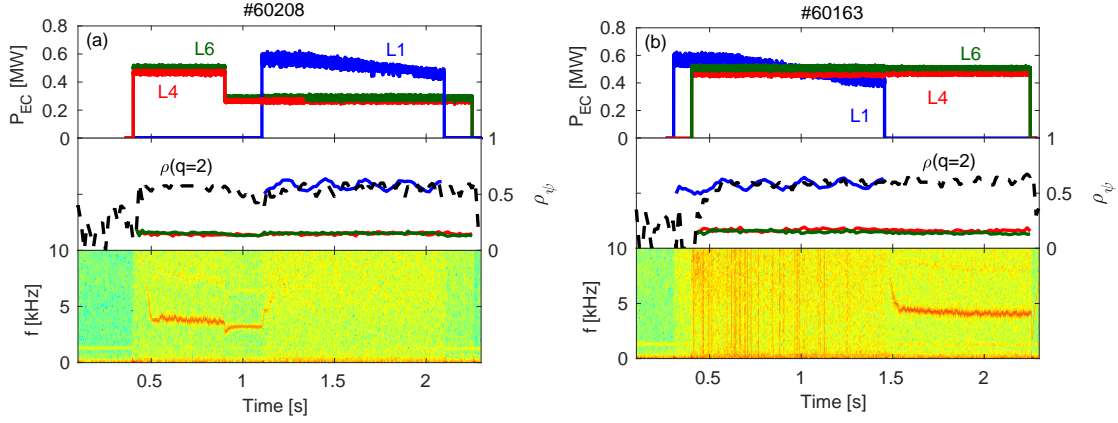


Figure 5.24. Experimental overview of two misalignment tests with sinusoidal sweeping: (a) 2/1 NTM stabilization; (b) 2/1 NTM prevention. The dashed black curve in the middle panel represents the radial location of the $q = 2$ surface based on LIUQE outputs.

Similar experiments have been carried out, except with different misalignment levels of $L1$ that can be quantified by the averaged offset of the center of sweeping with respect to the target mode location. Following the definition of x_{norm} in equation (3.16), a $x_{\text{norm,avg}}$ is defined as

$$x_{\text{norm,avg}} \equiv \frac{\bar{\rho}_{\text{offset}}}{w_{\text{dep}}}, \quad (5.3)$$

where $\bar{\rho}_{\text{offset}}$ represents the averaged offset of the center of sweeping with respect to the $q = 2$ surface, i.e. the average of $\bar{\rho}_{\text{dep}} - \bar{\rho}_{mn}$ in a given discharge, and w_{dep} the full e^{-1} width.

The effects of $L1$ on w in each discharge can also be quantified. For NTM stabilization tests,

$$\eta_{\text{stab}} \equiv \frac{w_{\text{exp},0} - w_{\text{exp},1}}{w_{\text{exp},0}}, \quad (5.4)$$

where $w_{\text{exp},0}$ is the measured saturated island width before turning on the control beam $L1$ and $w_{\text{exp},1}$ the measured saturated island width after turning on $L1$: $\eta_{\text{stab}} = 1$ thus represents full stabilization, $\eta_{\text{stab}} = 0$ no effect, $\eta_{\text{stab}} \in (0, 1)$ partial stabilization and $\eta_{\text{stab}} < 0$ overall destabilizing effect. For NTM prevention tests, the effects are quantified by η_{prevent} , which is either 0 (no prevention) or 1 (successful prevention, i.e. no NTM onset when $L1$ is still on).

η_{stab} and η_{prevent} obtained from a group of experimental scans (performed in the same experimental week) are summarized in figure 5.25, with a fixed $w_{\text{dep}} = 5$ cm in equation (5.3). For

the NTM prevention cases (red curve with open circles), successful prevention can only be achieved when $x_{\text{norm,avg}} \in (-0.5, 0.5)$, i.e. within half of w_{dep} and having finite deposition at the $q = 2$. For the NTM stabilization cases (blue curve with solid squares), there seems to be an offset of the center of relative symmetry compared to the prevention cases, at $x_{\text{norm,avg}} \approx 0.3$ instead of 0, corresponding to an offset of about 0.06 in ρ_ψ . This can be explained by the uncertainty of the radial location of $q = 2$ reconstructed by LIUQE, especially with the existence of an NTM (e.g. in the case of NTM stabilization), which affects local T_e and n_e and eventually q profiles as well. Another possible explanation is that the island itself can be asymmetric with respect to $q = 2$, as observed in ASDEX Upgrade [Meskat et al. 2001], but not enough diagnostic data is available in these discharges to check this point further.

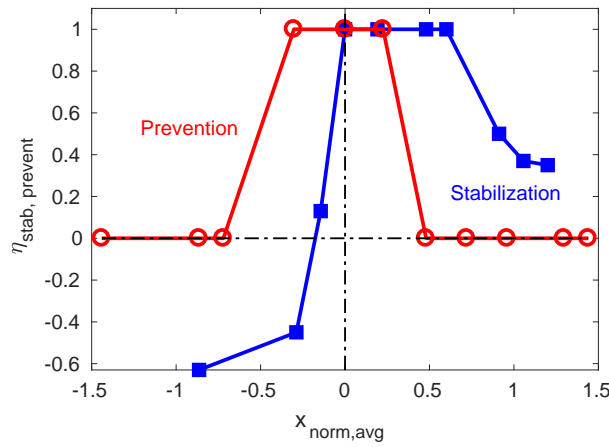


Figure 5.25. Summary of the effects of beam-mode misalignment on 2/1 NTM stabilization and prevention, taken from a series of experiments with sinusoidally sweeping control beam and different misalignment levels with respect to the $q = 2$ surface.

Another observation of the stabilization cases in figure 5.25 is that misalignment towards the plasma center can be destabilizing ($\eta_{\text{stab}} < 0$), while misalignment towards the plasma edge can lead to partial stabilization, or at least no destabilizing effects have been observed, consistent with the discussions in the previous section. Considering the difficulty of obtaining perfect alignment, these observations show that it is better to align the control beam outside the target rational surface than inside. Note that there is still finite deposition of EC power and current inside the island for the rightmost case with $x_{\text{norm,avg}} = 1.2$ (#60122), when the EC beam passes through the plasma for the first time (*first-pass*), considering $w_{\text{exp}} \approx w_{\text{dep}} = 5$ cm, the sweeping used and the uncertainty of the radial location of $q = 2$ from LIUQE (thus the actual value of $x_{\text{norm,avg}}$). Moreover, the incomplete first-pass EC absorption in these more outward cases (e.g. around 50% in #60122) result in the reflection of EC beams by the inner vessel wall, which may lead to more EC depositions at the mode location and contribute to the observed partial stabilization, as will be discussed further in the next section.

Misalignment tests without sweeping

Dedicated misalignment experiments have also been conducted *without* the sinusoidal sweeping (in another experimental week), for both NTM stabilization and preventions cases. These experiments have exactly the same settings as those shown in figure 5.24, except that poloidal angle of the control beam $L1$ is fixed and no sweeping is added. Following the same procedures discussed above, η_{stab} and η_{prevent} obtained from different discharges are summarized in figure 5.26, with a fixed $w_{\text{dep}} = 5$ cm as well.

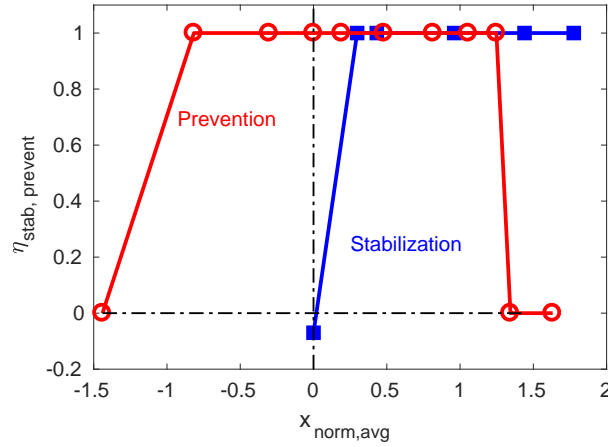


Figure 5.26. Summary of the effects of beam-mode misalignment on 2/1 NTM stabilization and prevention, taken from a series of experiments with a fixed poloidal angle of the control beam (no sweeping) and different misalignment levels with respect to the $q = 2$ surface.

Similar to figure 5.25, the stabilization cases in figure 5.26 (blue squares) exhibit an outward shift of the center of relative symmetry compared to the prevention cases, at $x_{\text{norm,avg}} \geq 1$ instead of 0. This could be one of the possible explanations of the observed full NTM stabilization in the cases with very outward depositions (e.g. $x_{\text{norm,avg}} > 1.3$), otherwise the EC beams would not have any depositions within the island, at least when they pass through the plasma for the first time. To further verify the experimental observations shown in figure 5.26, two standard NTM stabilization experiments, #60324 and #60311 shown in figure 5.27, where the control beam is moved slowly from inside or outside the $q = 2$ surface to $q = 2$ have been performed in the same experimental week as these misalignment experiments (with a fixed poloidal angle thus near constant deposition location of $L1$) shown in figure 5.26. It can be seen that the localized stabilization effects of the control EC beam, i.e. full stabilization only when the beam crosses the mode location presented in section 5.4 to section 5.7.1 or in [Felici et al. 2012] cannot be reproduced in #60311. The EC beam from $L1$ has $x_{\text{norm,avg}} \approx 1.95$ when fully stabilizes the mode at $t \approx 1.4$ s in #60311, which is already very far from the $q = 2$ surface even when considering the possible uncertainties in the determination of $q = 2$ and $x_{\text{norm,avg}}$.

5.7. Effects of EC misalignment on the stabilization and prevention of NTMs

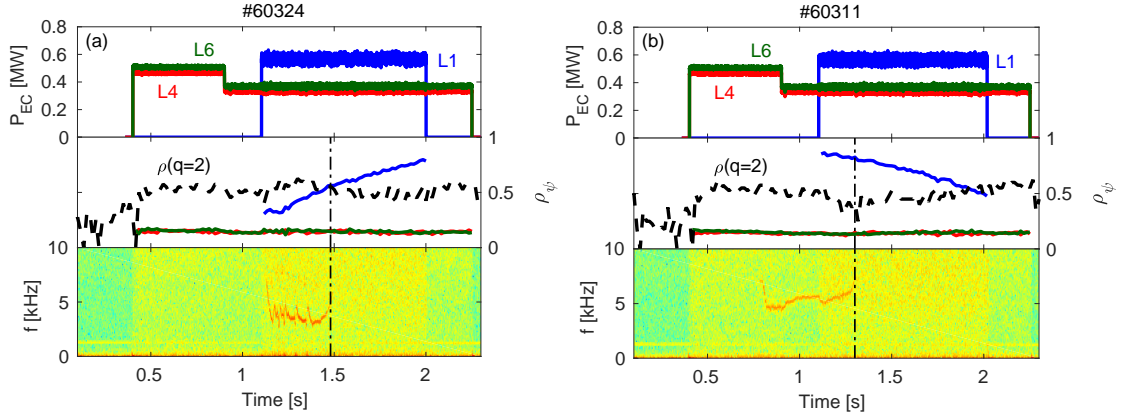


Figure 5.27. Experimental overview of two standard NTM stabilization experiments on TCV, carried out in the same experimental week as the misalignment experiments summarized in figure 5.26: (a) 2/1 NTM stabilization from inside $q = 2$; (b) 2/1 NTM stabilization from outside $q = 2$. The dashed black curve in the middle panel represents the radial location of the $q = 2$ surface based on LIUQE outputs.

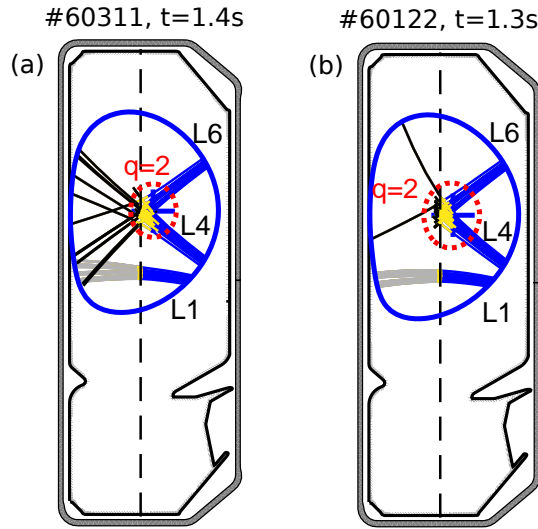


Figure 5.28. A poloidal view of the deposition paths of different EC beams in (a) #60311 (figure 5.27) and (b) #60122 (the rightmost blue square in figure 5.25), respectively. The EC-relevant results are taken from TORAY-GA outputs and the flux surfaces from LIUQE.

Another possible explanation for the observed full NTM stabilization in these cases with very outward EC depositions is the incomplete absorption of EC beams when they pass through the plasma for the first time and the consequent reflections by the vacuum vessel that may lead to an effective deposition at the mode location. As an illustration, a poloidal view of the EC traces of #60311 at $t = 1.4$ s are shown in figure 5.28 (a), based on the outputs of TORAY-GA. It can be seen that there is no deposition of L1 at the mode location when the beam passes through the plasma for the first time. The first-pass EC absorption rate in this case is about 50% (from TORAY-GA) and the remaining EC rays can be reflected by the wall and

effectively deposit inside the island. More detailed TORAY-GA calculations that consider these possible reflections and multiple passes through the plasma can be performed to verify this point further. Similarly, the observed partial stabilization for the cases with more outward depositions (with sweeping) shown in figure 5.25 may also be explained by the reflection and effective deposition within the island, in addition to the uncertainties of LIUQE and the estimation of $x_{\text{norm,avg}}$. An example of these is shown in figure 5.28 (b).

Note that the absorption rates and paths of EC rays depend on detailed plasma conditions, e.g. the temperature and density profiles, and may vary in different experiments, especially when incomplete first-pass absorption and subsequent reflections of EC beams are involved. The discussions in this section shed light on the possible role of these effects on the partial/full stabilization of 2/1 NTMs, when the EC beams are misaligned well outside the $q = 2$ surface. Further experimental studies on beam-mode misalignment should take these effects into consideration. In particular, they should be planned such that the reflected EC beams stay away from the $q = 2$ surface, since far off-axis EC beams will typically only have partial first-pass absorption. Moreover, comprehensive MRE simulations that assume different misalignment levels, with/without sweeping, different frequency and amplitude of the sweeping, etc., will be able to better compare the sweeping and non-sweeping techniques and are left as future work.

5.8 Summary

In this chapter, the physics and control of 2/1 NTMs have been studied experimentally and numerically in TCV. The self-stabilization of NTMs through a slow ramp-down of the near-axis co-ECCD power estimates the level of w_{marg} of NTMs involved in the test discharges. The observed dynamic evolution of 2/1 NTMs along with varying deposition locations of the co-ECCD beam has been reproduced well in the simulations with MRE. This constrains better the theoretical models used, for example the discussions about the existence of the negative part of G_{cd} in section 5.4.

With the aim of quantifying the contribution of heating and current drive to the stabilization of 2/1 NTMs, a series of NTM control experiments with different current drive settings have been performed, with the control beam in co-ECCD, counter-ECCD or ECH, respectively. Corresponding interpretative simulations estimate the range of the coefficients and parameters to be used in the MRE (i.e. a_4 and a_5) and quantifies the contribution of heating and current drive. It has been shown that pure heating exhibits a comparable effect as current drive on NTM stabilization in our test discharges, in accordance with theoretical predictions for relatively small machines.

As another method of NTM control, the prevention of 2/1 NTMs by means of preemptive ECCD has also been explored. The prevention effect is found to come from the local effects of heating and current drive of the off-axis beam (i.e. $\bar{\rho}_{mn}\Delta'_H$ and $\bar{\rho}_{mn}\Delta'_{CD}$), as well as the stabilizing effect from favorable curvature ($\bar{\rho}_{mn}\Delta'_{GGJ}$), instead of a global change of the classical stability of plasmas (i.e. Δ'). The small sinusoidal sweeping of the radial deposition location of the

control EC beam around the target mode location has proven to be effective for both NTM stabilization and NTM prevention cases. Along with the sweeping, power-ramp experiments have shown that NTM prevention is much more efficient than NTM stabilization in the test discharges, in terms of the minimum EC power required.

The effect of beam-mode misalignment on NTM evolution has been studied in detail. It is observed that misalignment towards the plasma center can be destabilizing, due to a larger increase of β_p and Δ' , as well as a decrease of the stabilizing effects from the EC beams caused by the misalignment. Small misalignment towards the plasma edge, on the other hand, can lead to partial stabilization, or at least no destabilization effects have been observed. Given the difficulty of keeping perfect beam-mode alignment, this observation motivates to align the control beam slightly outside the target rational surface, instead of inside. These misalignment studies based on many TCV discharges also shed light on the possible role of incomplete first-pass EC absorption and consequent reflections and multiple passes through the plasma on the stabilization of 2/1 NTMs, especially when the EC beams are misaligned well outside the $q = 2$ surface. Further experimental studies on beam-mode misalignment should take these effects into account.

It is worth emphasizing that the MRE presented in section 3.4, together with the simple Δ'_0 model proposed and developed in detail in the previous chapter (section 4.3) has been used in all the simulations involved in this chapter and proves to work well for the rather complicated set of experiments (NTM prevention, stabilization, sweeping, co-ECCD, counter-ECCD, ECH, etc.) with very similar fixed coefficients that are determined based on the procedures summarized in section 4.6. As a review, the key coefficients and parameters used in the simulations of the main discharges presented in this chapter are summarized in table 5.4. The interpretative simulations presented in chapters 4 and 5 also highlight the possibility of applying the MRE in real-time (RT), for example, to compute the amount of EC power required to stabilize or prevent a given NTM in RT and to predict its evolution, contributing to the overall RT integrated control strategy. A first example of such a RT-capable MRE module will be presented in the next chapter.

Table 5.4. List of the coefficients and parameters used in the best fits of various TCV discharges, with fixed $k = 6$, $a_3 = 1$, $w_{de} = 1.9$ cm and $w_{dep} = 5$ cm

Shot #	α	a_2	a_4	a_5	$\bar{\rho}_{mn}\Delta'_{ohmic0}$	$\bar{\rho}_{mn}\Delta'_{sat}$	χ
58477	8	1.5	N/A	N/A	figure 4.17, green	-0.78	9.67%
56027	8	2	0.4	0.9	figure 4.17, green	-1.02	6.54%
56171	8	1.5	0.4	0.9	figure 4.17, green	-1.1	6.20%
56172	8	1.5	0.3	0.9	figure 4.17, green	-1.12	6.30%
56173	5	1.5	0.4	0.9	figure 4.17, green	-1.32	6.50%
58256	8	1.4	0.65	0.9	figure 4.17, green (and shifted by -0.19)	-0.84	3.30%
58248	5	1.5	0.4	0.9	figure 4.17, green	-1.32	6.50%

6 Real-time NTM control and integrated multi-actuator plasma control in TCV

6.1 Introduction

Different aspects of NTMs have been discussed in previous chapters from the physics point of view, with the aim of clarifying the underlying mechanisms. In this chapter, focus will be given to real-time (RT) control aspects, as well as how the physics study has contributed or will contribute to a better RT control of NTMs and the overall integrated plasma control.

To start with, RT control of NTMs in TCV will be presented in section 6.2, concerning the main challenges of NTM control in general (section 6.2.1), the feedback NTM control algorithms implemented in TCV (section 6.2.2) and one simple example of TCV RT NTM control experiments (section 6.2.3). The integration of NTM control algorithm with other control algorithms will be the subject of section 6.3, with several experimental examples illustrated. In section 6.4, the RT application of the modified Rutherford equation (MRE) discussed in previous chapters (i.e. RT-MRE) will be presented. As will be demonstrated for the first time, the RT-MRE is capable of providing valuable RT information, not only for NTM control, but also for the overall integrated control. Detailed examples will be shown in section 6.4.1 to section 6.4.5. The implementation of the RT-MRE in the plasma control system (PCS) will be discussed in section 6.4.6. Summary and outlook of the chapter will be given in section 6.5.

6.2 Real-time control of NTMs in TCV

6.2.1 Main challenges of real-time NTM control

One of the main challenges of real-time (RT) NTM control is to find and maintain good alignment of the EC beam(s) with respect to the target mode location under different plasma scenarios and complicated plasma evolutions. This typically requires accurate detection of the mode location and determination of the deposition location of EC beams in RT, where the latter can be inferred from computations with RT ray-tracing codes (e.g. a RT version of TORBEAM [Reich et al. 2015; Poli et al. 2018a]), though inevitably with uncertainties.

In terms of the determination of mode location, different methods have been explored on various tokamaks. For example, RT equilibrium reconstruction (with or without motional Stark effect measurements of the pitch angle of magnetic field lines) [Ferron et al. 1998; Moret et al. 2015] has been used as a standard tool to estimate the location of a certain m/n mode, i.e. radial location of the $q = m/n$ surface. Despite inherent uncertainties, this information provides the first estimation of mode location, whereas it becomes the only measurement available regarding mode location in the case of preventing NTMs (i.e. before the occurrence of NTMs) [La Haye et al. 2005].

Multi-channel electron cyclotron emission (ECE) radiometers have been utilized in several tokamaks such as JT60-U [Isayama et al. 2003], DIII-D [Park and Welandar 2006], and ASDEX Upgrade [Reich et al. 2012] as a complementary diagnostic of mode location, based on the amplitude and phase of localized temperature fluctuations caused by the motion of magnetic islands, as detailed in these references. In addition, a new scheme that combines an ECE diagnostic in the same sight line with the steerable ECRH/ECCD antenna used for NTM control, namely a line-of-sight ECE or inline ECE has been implemented and tested in experiments on TEXTOR [Oosterbeek et al. 2008; Hennen et al. 2010] and ASDEX Upgrade [Van Den Brand et al. 2019]. This has the advantage that the alignment is obtained without requiring RT equilibrium reconstruction or ray-tracing, though it can be technically challenging to separate the typically MW-level EC beam from the mW-level ECE signal. A similar scheme, with the same poloidal (toroidal) angle for ECE and EC beam antennas but different toroidal (poloidal) aiming (i.e. quasi-in-line ECE), has been implemented and tested experimentally in DIII-D [Volpe et al. 2009] and TCV [Rispoli et al. 2019].

Another method used to estimate mode location is based on the responses of measured island width to varying EC deposition locations, seeking the minimum of the island width or growth rate [Humphreys et al. 2006; Wehner and Schuster 2012; Rapson et al. 2014; Kolemen et al. 2014; Kim et al. 2015]. Even though the island width growth rate has a more direct relation with the beam-mode misalignment (e.g. from the MRE discussed in section 3.4), it is also more sensitive to the noise of measurements and difficult to ensure robust control [Rapson et al. 2016]. Recently, attention has been drawn to the *data fusion* technique that combines estimations from various methods to get a better overall estimation. For instance, estimations from equilibrium reconstruction, RT ECE diagnostic and minimum-seeking method have been fused into a single estimation of mode location and proven promising in experiments on ASDEX Upgrade [Rapson et al. 2017b].

On TCV, a simple and robust sweeping technique has been proposed, which adds a small (sinusoidal) oscillation to the deposition location of the control EC beam, i.e. sweeps the EC beam around the estimated mode location [Kim 2015]. Though less efficient than perfect alignment (that is almost impossible to obtain), it ensures that the correct mode location is crossed at least from time to time. In particular, in terms of NTM prevention, this technique relaxes the strict requirement on RT equilibrium reconstruction that is the only information available on mode location. The sweeping technique has proven to be effective for NTM

stabilization and prevention on TCV and ASDEX Upgrade [Kim 2015; Kong et al. 2019; Reich et al. 2014]. A better estimation of the mode location, for example with the data fusion method discussed above or with a RT version of the MRE that will be presented in section 6.4, can decrease the sweeping amplitude required.

Another main element of RT NTM control is to evaluate the EC power needed to control a given mode, in RT. Unfortunately, not much research has been performed on this topic so far and a typical practice in RT NTM control experiments is to simply use the maximum power of the selected control beam(s). In terms of NTM stabilization, an upgraded scheme that makes use of RT island width measurements has been proposed, in an “ask for more if not enough” fashion, i.e. an extra EC launcher is added in RT if the total power from existing EC launcher(s) used for stabilization is not sufficient to fully suppress a given NTM. This has been successfully applied in experiments on ASDEX Upgrade [Reich et al. 2014] for stabilizing 3/2 NTMs and recently implemented and tested on TCV for suppressing 2/1 NTMs [Kong et al. 2017]. In the near future, as will be discussed in this chapter, RT physics-model-based computations (e.g. RT-MRE) can be included to provide a better first estimation of the required power, contributing to a faster stabilization of NTMs that can grow and get locked quickly.

6.2.2 Feedback NTM control algorithms in TCV

Feedback NTM control algorithms have been implemented in the distributed digital control system (SCD) of TCV, which consists of a set of independent nodes linked via shared reflective memory [Anand et al. 2017; Galperti et al. 2017]. As discussed in chapter 2, the SCD receives various diagnostic inputs (e.g. from magnetic probes, soft X-ray, far infrared interferometer, etc.) and actuator outputs (e.g. for gas valves, EC systems, etc.). In particular, a new advanced RT magnetic analyses code based on the singular value decomposition (SVD) of fast magnetic signals [Galperti et al. 2014] has been implemented on a newly installed RT node of the SCD [Anand et al. 2017; Galperti et al. 2017]. This provides RT information about the likelihood of each m/n mode and their rotating frequencies, generating RT trigger signals when combined with user-specified thresholds.

Similar to those described in [Kim 2015], the first version of the RT NTM control algorithm in TCV takes the target q value (q_{target}), the $q(\rho)$ profile and user-specified configuration parameters as inputs, and outputs commands concerning the radial deposition location (ρ_{cmd}) and power (P_{cmd}) of EC beams. q_{target} is typically m/n for controlling an m/n NTM, whereas finite offsets (denoted as q_{offset}) can be added to allow performing RT misalignment experiments, i.e. with $q_{\text{target}} \equiv m/n + q_{\text{offset}}$. The $q(\rho)$ profile is taken from a RT version of the Grad-Shafranov equilibrium reconstruction code LIUQE that has been implemented in the SCD, with a sub-ms cycle time that is compatible with RT applications [Moret et al. 2015].

ρ_{cmd} is either the direct interpolation based on q_{target} and $q(\rho)$ profile, or in the case of *robust* control, the sum of the interpolated ρ with a small sinusoidal sweeping. The amplitude and frequency of the sweeping are specified by the user before a discharge, but future work can

be done to adapt these parameters in RT, for example based on evaluating the beam-mode alignment with the RT-MRE (section 6.4.2). ρ_{cmd} is then translated into the corresponding poloidal angle (θ_{cmd}) of the EC launcher, through a look-up table built with offline simulations of similar plasmas with TORAY-GA [Matsuda 1989] or through RT-TORBEAM [Reich et al. 2015; Poli et al. 2018a] when available. P_{cmd} is typically taken as the maximum power of a given EC launcher, or as newly implemented, in an “ask for more if not enough” fashion for NTM stabilization (examples in sections 6.3.2 and 6.3.3).

As the first illustration of the feedback NTM control algorithm discussed above, a simple RT NTM stabilization experiment will be presented in the next section. Recently, a more generic interface of the NTM controller has been implemented, thanks to the development of a new PCS framework that will be discussed in section 6.3.1. Experiments with the new framework and interface will be presented in section 6.3.2 and 6.3.3 after introducing the new PCS.

6.2.3 A simple real-time NTM stabilization experiment in TCV

This section illustrates an RT NTM stabilization experiment with fixed EC power: the maximum power of the selected launcher for NTM control, as shown in figure 6.1. Two EC launchers ($L4$ and $L6$) are involved in this discharge: the power from both launchers is controlled by feedforward waveforms and has approximately the same value as the two launchers share the same power unit; the toroidal angles of both launchers are set before the discharge to drive co-ECCD; the poloidal angle of $L4$ (θ_4) is fixed during the discharge to deposit power and current near the plasma center, following a (constant) feedforward waveform, while the angle $L6$ (θ_6) is feedback controlled by the NTM controller. This assignment of EC launchers (i.e. $L6$ for NTM control and $L4$ for central co-ECCD) is pre-programmed before the discharge.

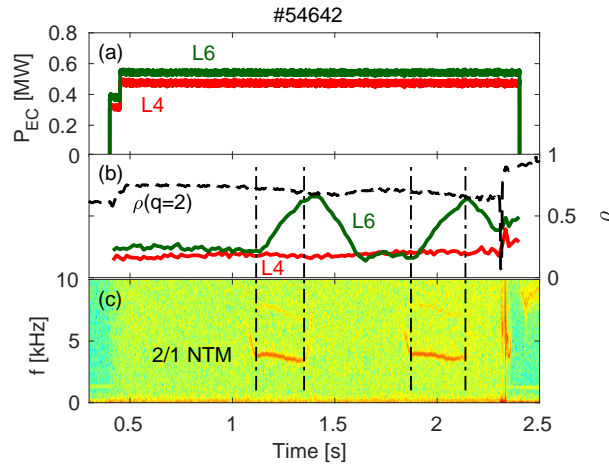


Figure 6.1. Experimental overview of an RT NTM control experiment with fixed EC power: (a) EC power traces; (b) radial deposition locations of EC beams and RT ρ_{ψ} ($q = 2$); and (c) NTM spectrogram. Vertical dash-dotted lines in (b) and (c) represent the “on” and “off” of RT trigger signals for 2/1 NTM taken from magnetic analyses, indicating the detected onset and full stabilization of the mode.

SVD analyses of magnetic signals [Galperti et al. 2014, 2017] are preformed in RT and provide the likelihood of each m/n mode. Together with user-defined thresholds, these generate time-varying RT trigger signals (1 or 0) for each m/n mode, representing the existence or absence of a given mode. As shown in figure 6.1 (c), a 2/1 NTM is detected and fully stabilized twice during the flat-top of this discharge (until 2.3 s), with the “on” and “off” of corresponding RT trigger signals marked by the vertical dash-dotted lines. q_{target} is set to 2/1 (i.e. $q_{\text{offset}} = 0$) in this discharge and corresponding ρ_{cmd} is obtained based on the $q(\rho)$ profile from RT-LIUQE (dashed black curve in figure 6.1 (b)). This ρ_{cmd} is eventually translated into θ_{cmd} for L6 through a look-up table, since RT-TORBEAM was not available in this discharge. In the absence of NTMs, θ_{cmd} of L6 is taken from feedforward waveforms to deposit near the plasma center, leading to the “suppress & return” type of movement of L6 shown in figure 6.1 (b) (solid green trace), i.e. the assigned launcher is moved towards q_{target} to *suppress* a given NTM and *return* to its initial location (the plasma center in this example) after suppressing the mode. Note that there are physical limits on the speed of moving the mechanical components of launchers, thus the steering of θ , so it takes time to move L6 in between $\rho(q = 2)$ and the plasma center.

This discharge (#54642) highlights the localized stabilization effects of off-axis EC beam(s), i.e. the 2/1 mode is fully stabilized as soon as and only when the co-ECCD beam reaches the target mode location, similar to the examples shown in the previous chapter. In terms of mode onset, the fact that no mode is triggered until both co-ECCD beams reach and remain at the plasma center (i.e. with a total central power of 0.96 MW) for a while indicates that it is marginal to trigger these 2/1 modes with 0.96 MW in this discharge, where $n_{el} \approx 1.7 \times 10^{19} \text{ m}^{-3}$ and $I_p \approx -110 \text{ kA}$ are kept. This is consistent with the predictions of the density range in chapter 4 (figure 4.23). Note also that no destabilization effects are observed when the co-ECCD beam is still near $q = 2$ after fully suppressing the mode, similar to the observations in chapter 5.

6.3 Integrated multi-actuator plasma control in TCV

The normal operation of tokamaks requires the reliable control of many physics parameters, ranging from the control of plasma current, density and shape, to the control of MHD instabilities, plasma β and q profiles. It is not rare that the same actuators are required to perform several control tasks simultaneously, leading to conflicting requests of actuators. For example, EC systems can be demanded by both impurity accumulation control and q profile control. This is especially true for future long-pulse devices like ITER, where a large amount of important control requirements need to be fulfilled with only a limited set of actuators [Snipes et al. 2014; Humphreys et al. 2015]. Moreover, off-normal events such as NTMs and vertical displacements events, or faults such as power supply failures may occur and need to be handled properly in RT [Eidietis et al. 2018; Blanken et al. 2019]. Therefore, the plasma control system (PCS) for a tokamak reactor should be able to decide which plasma quantities to be controlled not only based on the pulse schedule, but also on RT plasma and actuator states. It should also be able to take correct measures when unexpected events or faults happen and

decide on future actions.

In this respect, a promising solution is to use the combination of a supervisory controller and an actuator manager in the design of the PCS [Rapson et al. 2015; Maljaars and Felici 2017]. The supervisory controller makes RT high-level decisions on how to continue the discharge and prioritizes all considered control tasks based on the states of the plasma; the actuator manager computes in RT the actuator allocations accordingly. While important progress has been made in the design and implementation of supervisory controller and actuator manager under different PCS architectures [Rapson et al. 2015; Treutterer et al. 2014; Eidietis et al. 2018, and references therein], the links between RT diagnostics and event handling algorithms as well as the resource allocations are mostly hard-coded. Adding new functionalities or new diagnostics typically requires substantial modifications of existing codes. The dependence on specific diagnostics and actuators also makes it difficult to port the algorithms from one tokamak to another. Given these difficulties, a generic PCS structure has been newly proposed, implemented and experimentally tested on TCV, with generic supervisory controller and actuator manager [Blanken et al. 2019; Vu et al. 2019], as will be detailed in the next section.

6.3.1 A new generic plasma control system (PCS) framework

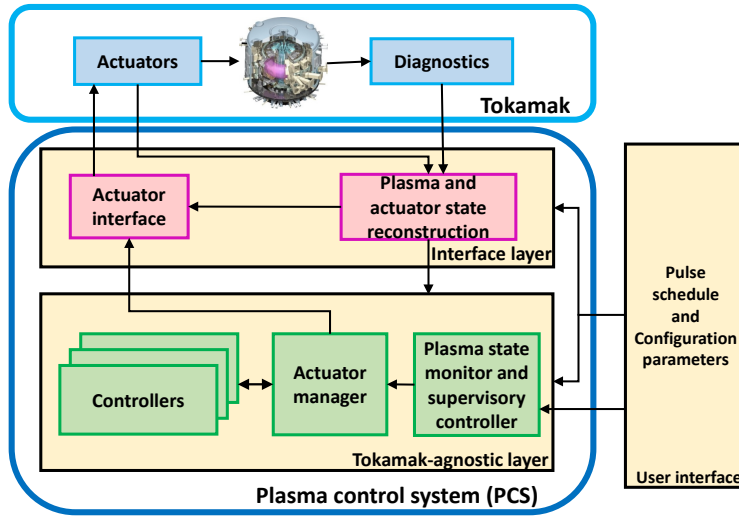


Figure 6.2. Overview of the new generic PCS framework, reproduced from [Vu et al. 2019].

The new framework is illustrated in figure 6.2, where the PCS is separated into an *interface layer* and a *tokamak-agnostic layer*. The interface layer translates RT signals from tokamak-specific diagnostics and actuators into generic outputs to be used by the tokamak-agnostic layer. For example, a generic *plasma and actuator state reconstruction* block uses RT diagnostics and simulations to generate a continuous generic representation of plasma and actuator states. In TCV, the plasma and actuator state reconstruction contains RT SVD analyses of magnetic perturbations [Galperti et al. 2014, 2017], RT-LIUQE [Moret et al. 2015] and RT-TORBEAM

[Reich et al. 2015; Poli et al. 2018a]; the RAPTOR observer [Felici et al. 2011, 2016] has been included as well to estimate the electron temperature (T_e) and q profiles; the RAPDENS-observer [Blanken et al. 2018] has been used to reconstruct electron density profiles, etc. As will be illustrated in section 6.4.6, more functionalities can be easily added thanks to the generic feature of the framework.

In the tokamak-agnostic layer, only tokamak-independent control tasks such as 2/1 NTM stabilization, β control and q profile control are considered, i.e. in a *task-based* manner. The pulse schedule and configuration parameters for each control task, on the other hand, are tokamak- and scenario-dependent: they are set by the user before a discharge using a standardized *user interface*. The continuous-valued plasma and actuator states from the interface layer are translated by a generic *plasma state monitor* into a discrete finite-state representation of plasma and actuator conditions, with state transitions triggered by user-defined thresholds [Blanken et al. 2019]. Based on the defined tasks, the pulse schedule and the discrete states, a generic *supervisory controller* [Blanken et al. 2019] activates relevant tasks/controllers, prioritizes all considered tasks and communicates the parameters specific to each control task. An advanced task-based *actuator manager* [Vu et al. 2019] then optimizes the actuator allocations for each task based on the priorities and requests from all control tasks as well as the plasma and actuator states and limits.

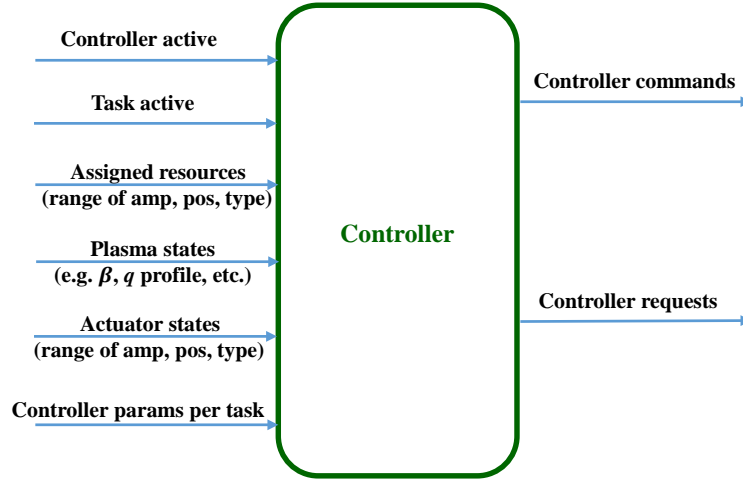


Figure 6.3. Generic controller with standardized interface, reproduced from [Vu et al. 2019].

The control tasks are performed by generic *controllers* in the tokamak-agnostic layer, the mapping between which are defined by the user through the user interface: a controller can perform several control tasks, whereas a control task can be only assigned to one controller. The tokamak-agnostic layer provides a layer of abstraction for physics operators as they only need to specify generic control tasks, without having to consider the functionalities of each specific controller.

All the controllers in the tokamak-agnostic layer share the same standardized interface [Vu et al. 2019], as shown in figure 6.3. *Controller active* and *task active* represent the activation signals for the controller and the various control tasks associated with this controller, respectively; *assigned resources* are the assigned virtual actuator resources per task, i.e. the range of amplitude (e.g. minimum and maximum of the EC power available), position (e.g. reachable deposition location of EC beams) and type (e.g. co-ECCD); *plasma states* are the full representation of plasma conditions that are the same for all controllers; each controller will then use the subset of the plasma states that it requires to fulfill its tasks; *actuator states* are the states of the assigned actuators to each controller; *controller params per task* are parameters of the concerned tasks, which are defined in the pulse schedule but can be modified by the supervisory controller in RT when necessary.

In the outputs, *controller commands* are the commands for each task that are sent to the actuators at the present time step and remain within the limit of the assigned resources at the present time step; *controller requests* are the requests for each task that are sent to the actuator manager to get the resource allocation for the next time step; they are not necessarily within the limit of the assigned virtual resources at the present time step. Examples of these will be given along with the experiments shown in next sections.

6.3.2 Integrated control experiment with preliminary plasma supervision and actuator allocations

The generic PCS framework presented in the previous section has been successfully implemented in the SCD of TCV. Using the first version of the system, with a preliminary supervisory controller and actuator manager, RT integrated control of NTMs, β and model-estimated q profiles has been demonstrated experimentally in TCV. Note that the q profiles used in this experiment are estimations from RAPTOR [Felici et al. 2011, 2016] due to the absence of internal current density measurements in TCV. Three control tasks, namely 2/1 NTM stabilization, β and q profile control are involved, with two controllers: the NTM controller discussed in section 6.2 to perform the 2/1 NTM stabilization task and a profile controller [Maljaars et al. 2017; Vu et al. 2016; Mavkov et al. 2017] to perform β and q profile control tasks.

As shown in figure 6.4, three EC launchers ($L1$, $L4$ and $L6$) have been used as actuators to perform these control tasks. As mentioned, $L4$ and $L6$ share the same power unit and always convey approximately the same power, while their deposition locations can be different. In this experiment, $L4$ and $L6$ are set to drive co-ECCD with a nominal power of 0.5MW each and can be assigned to the three tasks based on their RT priorities and requests; $L1$ is set to drive counter-ECCD and reserved only for β and q profile control, with a nominal power of 0.75MW. The priorities of the control tasks are defined such that 2/1 NTM stabilization takes the highest priority (i.e. 1) once a 2/1 NTM is detected, otherwise β control takes the highest priority. The default priority of each control task is specified by the user, which is then used by the supervisory controller to compute RT priorities based on RT plasma states (e.g. the

sudden occurrence of an NTM).

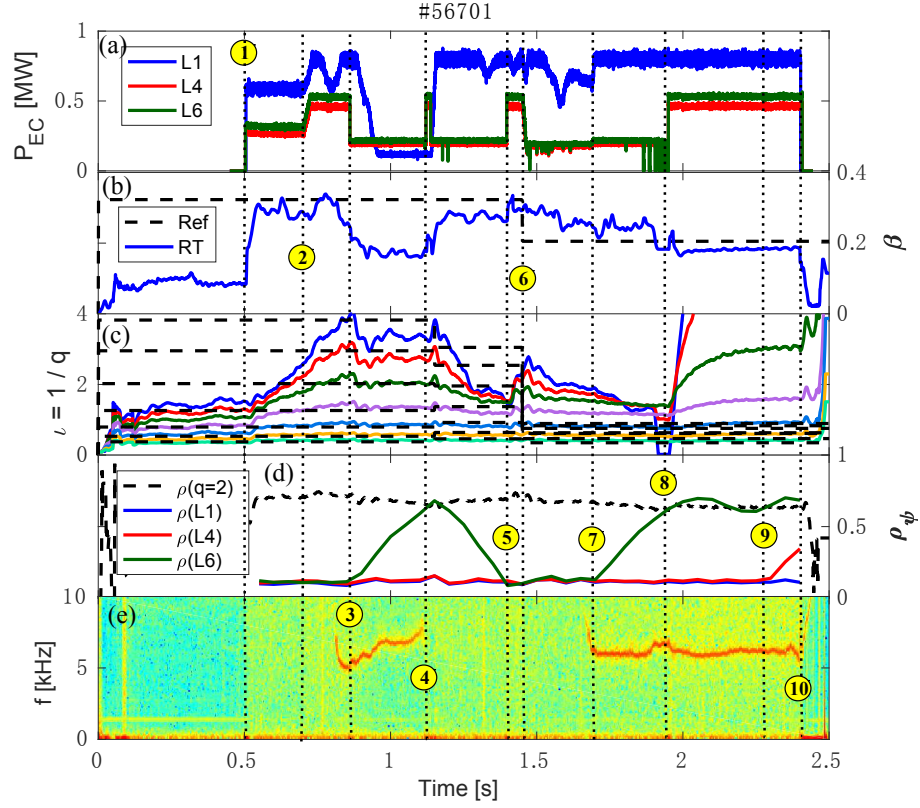


Figure 6.4. Integrated control of NTMs, β and model-estimated q profiles in TCV with a preliminary supervisory controller and actuator manager: (a) EC power traces; (b) reference (dashed black) and RT β ; (c) $\iota \equiv q^{-1}$ profiles - different dashed/solid curves represent the reference/RT-estimated ι values at different radial locations; (d) $\rho(q=2)$ (dashed black) and deposition locations of different launchers; and (e) 2/1 NTM spectrogram. Reproduced from [Kong et al. 2019].

EC power is switched on at ① in this experiment, with all three launchers depositing near the plasma center following feedforward waveforms, before starting RT control at ②. A 2/1 NTM is detected by RT magnetic measurements (i.e. above the user-specified threshold) at ③. The 2/1 NTM stabilization task and NTM controller are thus activated and 2/1 NTM stabilization gets the highest priority. $L6$ is assigned to NTM stabilization that requests a maximum power of 0.5 MW and moves towards the $q = 2$ surface. The power of $L6$ (thus $L4$ as well since it shares the same power supply) is reduced to its minimum during its movement between plasma center and $q = 2$ (e.g. ③ - ④ in figure 6.4 (a) and (d)) and recovers 0.5 MW once the deposition is close enough to the target position (e.g. at ④). The NTM is fully stabilized and β control thus takes the highest priority, which increases the power of $L6$ and $L4$ at ⑤ (i.e. when $L6$ reaches close to the plasma center) to follow better the β reference (⑤ - ⑥ in figure 6.4 (b)). At ⑥, as seen in figure 6.4 (a) - (c), β and q profile control change their power commands in response to a change of the β and q references at that time.

It is worth mentioning that the approach of using minimized EC power during the movement of EC beams between the plasma center and the $q = 2$ surface in this discharge is based on several considerations. Firstly, it serves as a comprehensive test of the RT control of EC power. Secondly, it reduces the total power consumed when the EC beam is not located at the requested deposition location of the considered control task. Moreover, at the time of the experiment, it was conjectured that depositing ECCD near the $q = 2$ surface (after mode stabilization) could be destabilizing for 2/1 NTMs, so this technique can be beneficial in the sense that it reduces the potential destabilizing effect. However, as clarified through dedicated TCV experiments and corresponding simulations with the MRE discussed in chapter 5 (section 5.4), no such local destabilization effects have been observed so far in our studies on TCV, so it is not necessary to decrease the EC power for this purpose. In fact, as shown in figure 6.4 (b) and (c), the imposed low EC power makes it difficult to follow the β and q references even in the absence of NTMs (e.g. from shortly after ④ to ⑤). Therefore, this technique of decreasing EC power during its movement needs to be taken with caution in future integrated control experiments, especially when the control of q profiles is involved, which requires the active control of off-axis EC beams itself.

2/1 NTM is triggered again at ⑦, so 2/1 NTM stabilization task takes again the highest priority and requests a power of $[0, 0.5]$ MW. $L6$ is assigned to this task and moved towards the mode location similarly. The sweeping technique and the “asking for more if not enough” scheme discussed in section 6.2 have been combined and applied in this discharge: once the mode stays longer than a given time (one sweeping cycle in this case) after $L6$ reaches the mode location, the 2/1 NTM stabilization task requests a power of $[0, 1]$ MW and $L4$ is also assigned (⑨); $L4$ starts to move towards the mode location, but not enough time is left in this discharge to reach the target position and fully stabilize the mode. EC power is turned off at ⑩ and the mode is self-stabilized. During the control of NTMs where no co-ECCD power is available for β and q profile control, β and q profile references cannot be followed very well.

In this example, the priority and the resource allocation of control tasks are computed in RT, but in an *ad hoc* way: only a preliminary supervisory controller and actuator manager are involved, which act more like a switch combining relevant outputs based on given conditions. A more generic and advanced supervisory controller and actuator manager have been developed ever since and applied routinely in the integrated control experiments in TCV, as will be discussed in the next section.

6.3.3 Integrated control experiments with advanced plasma supervision and actuator allocations

NTM stabilization with real-time EC allocations

In the example shown in figure 6.5, two control tasks, namely 2/1 NTM stabilization and central co-ECCD are considered. They both are assigned to the new generic NTM controller with standardized interface presented in section 6.3.1 (figure 6.3). The priority of each control

task is computed in RT by a new generic supervisory controller with standardized inputs, outputs and transition conditions [Blanken et al. 2019]. It uses both the default values from the user-interface as well as RT plasma states: 2/1 NTM stabilization is given its user-defined priority 1 once a 2/1 NTM is detected, whereas central co-ECCD (with a user-defined priority 0.8) has the highest priority in the absence of 2/1 mode, as shown in figure 6.5 (a). Three co-ECCD actuators ($L1$, $L4$ and $L6$) are used in this discharge: the poloidal angle and power of $L1$ are controlled by feedforward waveforms to deposit co-ECCD near the plasma center, whereas those of $L4$ and $L6$ are in feedback control.

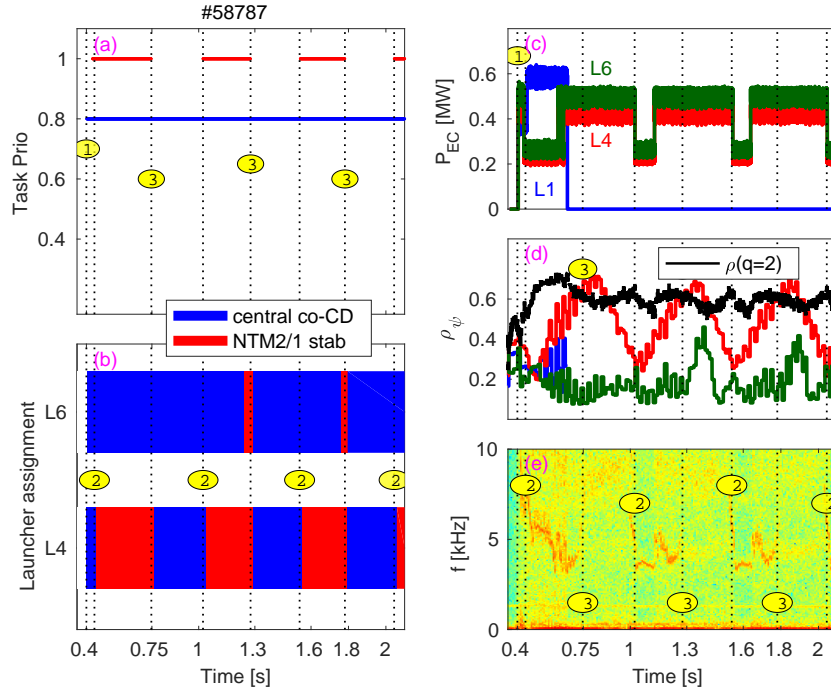


Figure 6.5. Experimental overview of a RT NTM stabilization experiment with RT EC allocations: (a) RT priorities of the two control tasks; (b) RT allocations of $L4$ and $L6$ to the control tasks; (c) EC power traces; (d) normalized deposition locations of EC beams (from RT-TORBEAM) and the location of $q = 2$ surface (from RT-LIUQE); and (e) 2/1 NTM spectrogram. Vertical dotted lines labeled by ① - beginning of RT feedback control; ② - the “on” of RT trigger signals for 2/1 NTM, indicating the detected onset of the 2/1 mode; ③ - the “off” of RT trigger signals, indicating the full suppression of 2/1 mode.

The allocation of $L4$ and $L6$ to the two control tasks, shown in figure 6.5 (b), is computed in RT by a new advanced actuator manager that solves an optimization problem based on the RT priority and actuator requests of each task [Vu et al. 2019]. For example, the central co-ECCD task always requests $[0, 1]$ MW co-ECCD power and is assigned both $L4$ and $L6$ if it has the highest priority (i.e. no 2/1 NTM is present); once a 2/1 NTM is detected, as indicated by the vertical dotted black lines marked with ②, the 2/1 NTM stabilization task is given its user-defined priority (i.e. 1, figure 6.5 (a)) and assigned one launcher ($L4$, figure 6.5 (b)) as it requests $[0, 0.5]$ MW co-ECCD power at the beginning, while only $L6$ is assigned to the central co-ECCD task even though it requests higher power. $L4$ is then moved towards the $q = 2$

surface following the ρ_{cmd} of the 2/1 NTM stabilization task while $L6$ remains near the plasma center when it is assigned to the central co-ECCD task (with a $\rho_{\text{cmd}} = 0.2$ in this discharge), as seen in figure 6.5 (d).

As mentioned in section 6.3.1, we distinguish between task “requests” and “commands” in the new PCS [Vu et al. 2019]: the requests of each control task contain ranges of power (e.g. $[0, 1]$ MW), location (e.g. $[0, 0.2]$) and current drive direction (e.g. $[-1, -0.2]$ for co-ECCD with negative I_p) that are sent to the actuator manager to get the actuator allocation for the next time step; the commands are the actual P_{cmd} (e.g. 0.5 MW), ρ_{cmd} (e.g. 0.2) and current drive direction (e.g. -1 for co-ECCD) sent to the actuators at the present time step (within the limits of the assigned virtual resources), similar to the example shown in section 6.2.3 (#54642). However, in contrast to #54642 (figure 6.1), the allocations of $L4$ and $L6$ are computed in real-time and their power is in feedback control in this discharge (#58787) .

A sinusoidal sweeping is added to the deposition locations of the EC launchers that are assigned to the 2/1 NTM stabilization task and have reached close enough (within ± 0.05 in this case) to the target $q = 2$ surface; more power ($[0, 1]$ MW instead of $[0, 0.5]$ MW) is requested if the mode still sustains after all the assigned launchers have finished more than half a cycle of sweeping. The threshold of the proximity of EC beam to mode location that is used to start sweeping, as well as the number of sweeping cycles to finish before asking for more power are user-defined parameters specified before a discharge. $L6$ is then assigned to the 2/1 NTM stabilization task (figure 6.5 (b) and moves towards $\rho(q = 2)$ as well. Note that there is a delay in the response and movement of the mechanical components of EC launchers, causing an actual movement of $L6$ only after the full stabilization of NTMs in this experiment (e.g. at $t \approx 1.3$ s and 1.8 s in figure 6.5 (d)). 2/1 NTM is fully suppressed three times during the discharge, effectively with $L1$ only, indicating that a longer waiting time (e.g. one sweeping cycle instead of the half cycle used here) before requesting more power would have avoided switching the allocation of $L6$ to NTM control. This meanwhile highlights the importance of obtaining a better RT estimation of the EC power required for NTM control in view of more reliable and efficient integrated control. A promising method in this respect is to use a RT version of the validated MRE discussed in previous chapters, as will be demonstrated for the first time in section 6.4.

The $\rho(q = 2)$ shown in figure 6.5 (d) is taken from RT-LIUQE, while RT-TORBEAM that was available in this discharge has been used in two different ways: “backward” simulations to convert ρ_{cmd} (i.e. either 0.2 from the central co-ECCD task or $\rho(q = 2)$ from 2/1 NTM stabilization task) to θ_{cmd} ; and “forward” simulations to estimate in RT the actual deposition location of each EC launcher. Given the absence of RT measurement of EC poloidal angles in TCV, their values are estimated by linear models taken into account the speed of the movement of each launcher and used as inputs for “forward” RT-TORBEAM runs. The resulting deposition locations are shown in figure 6.5 (d) and are in good accordance with offline simulations with TORAY-GA, not shown in the figure for conciseness. The power of $L4$ (thus $L6$ as well) is decreased to its minimum (around 0.2 MW) during its movement between the plasma center

and $\rho(q = 2)$ in this case to minimize the perturbation on the central co-ECCD task, i.e. by minimizing off-axis co-ECCD power. However, this technique needs to be taken with caution in future experiments as discussed in the previous section.

Integrated control of NTMs and β with real-time EC allocations

In another example shown in figure 6.6, three control tasks are involved: 2/1 NTM stabilization, β control and central co-ECCD. Three controllers are used to perform these tasks, as shown in table 6.1. The task-controller mapping as well as the active time and default priority of each control task (table 6.1) are specified by the user through the user-interface. It can be seen that the central co-ECCD task has the lowest priority among the three tasks and is only active at the beginning of the discharge to establish the operational equilibrium; the 2/1 NTM stabilization task is only activated when a 2/1 NTM is detected/present and has the highest priority once activated; the β control task is active from $t = 0.5$ s and has a lower priority than the 2/1 NTM stabilization task. Similar to #58787 discussed in the previous section, the new generic supervisory controller and actuator manager have been used in this discharge.

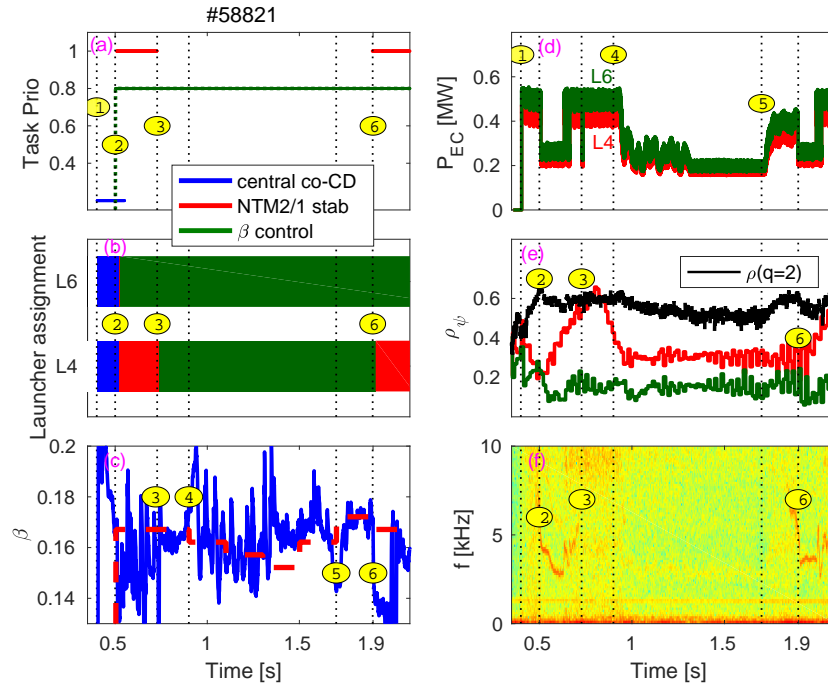


Figure 6.6. Experimental overview of integrated control of NTMs and β , reproduced from [Vu et al. 2019]: (a) RT priorities of the three control tasks; (b) RT allocations of $L4$ and $L6$ to the control tasks; (c) reference and RT β ; (d) EC power traces; (e) normalized deposition location of EC beams (from RT-TORBEAM) and the location of $q = 2$ surface (from RT-LIUQE); and (f) 2/1 NTM spectrogram.

Two EC launchers ($L4$ and $L6$) are used to perform these three tasks, based on RT allocations determined by the actuator manager. Both launchers are set to drive co-ECCD and have a

nominal power of 0.5 MW each. The central co-ECCD and β control task request a power of [0, 1] MW each; the 2/1 NTM stabilization task requests [0, 0.5] MW when active, but reserves the ability to ask for more power as discussed before.

Table 6.1. Settings for #58821 shown in figure 6.6

Task	Priority	Active time [s]	Controller
Central co-ECCD	0.2	[0.4, 0.55]	Feedforward
2/1 NTM stabilization	1	[0.5, 2.5]	NTM
β control	0.8	[0.5, 2.5]	Performance

As shown in figure 6.6 (a) and (b), the central co-ECCD task is the only active task during ① to ② and is assigned both launchers based on its power request ([0, 1] MW). A 2/1 NTM is detected at ② and $L4$ is assigned to the 2/1 NTM stabilization task by the actuator manager, given its highest priority and requested power ([0, 0.5] MW); β control task has lower priority and receives $L6$ even though it requests [0, 1] MW; with the lowest priority, no actuators are available for the central co-ECCD task during [0.5, 0.55] s. $L4$ then moves towards the $q = 2$ surface, following the command of the NTM stabilization task, while $L6$ remains near the plasma center as commanded by the β control task. Again, the power of $L4$ (thus $L6$ as well) is decreased before it reaches close to the $q = 2$ surface.

2/1 NTM is fully suppressed at ③ and β control is the only active task until another 2/1 NTM is detected at ⑥. Both launchers are assigned to β control during ③ - ⑥ based on its requested power ([0, 1] MW). As shown in figure 6.6 (c), RT β follows quite well the reference during ③ - ④ and ⑤ - ⑥; during ④ - ⑤, RT β cannot follow well the reference, since the reference is so low that the lower limit of actuator power is reached (i.e. 0.2 MW), as indicated in (d).

6.4 Inclusion of Modified Rutherford Equation in the plasma control system

The determination of the required power to control a given NTM in the experiments, as presented in previous sections, remains *ad hoc*, i.e. requires several trials and errors. For future long-pulse tokamaks, it is advantageous to build more intelligence into NTM controller that is aware of the resources it needs to fulfill its tasks. This can be done by including a solver for the MRE presented in previous chapters in the PCS, which is also valuable for the integrated control in general. For example, the better knowledge of the required power would allow better allocations of EC actuators; predictions of NTM evolution with the RT-MRE facilitate the decision-making of the supervisory controller, e.g. NTM prevention or disruption avoidance tasks may be activated if the supervisory controller foresees a dangerous mode or one that cannot be stabilized in time. In this respect, a versatile RT-MRE is newly proposed within the scope of this thesis. Its various capabilities have been tested extensively by offline simulations and will be presented in the following sections. The implementation of the RT-MRE in the PCS will also be discussed.

6.4.1 Real-time determination of the coefficients in the MRE

The MRE used in the interpretative simulations of NTM island width w in chapters 4 and 5 is rewritten below for convenience:

$$\frac{\tau_R}{\bar{\rho}_{mn}} \frac{dw}{dt} = \bar{\rho}_{mn} \Delta' + \bar{\rho}_{mn} \Delta'_{BS} + \bar{\rho}_{mn} \Delta'_{GGJ} + \bar{\rho}_{mn} \Delta'_{CD} + \bar{\rho}_{mn} \Delta'_H, \quad (6.1)$$

where coefficients a_2 to a_5 are involved in $\bar{\rho}_{mn} \Delta'_{BS}$, $\bar{\rho}_{mn} \Delta'_{GGJ}$, $\bar{\rho}_{mn} \Delta'_{CD}$ and $\bar{\rho}_{mn} \Delta'_H$, respectively (equation (3.4) - equation (3.10) in chapter 3), while other parameters such as Δ'_{sat} , k and α are involved in $\bar{\rho}_{mn} \Delta'$ (equations (3.25) and (4.2)). As presented in previous chapters, these coefficients need to be specified before any application of the MRE.

In chapters 4 and 5, it has been demonstrated that constant coefficients can fit well a rather complicated set of experiments, and more importantly, the range and main effects of each coefficient are well-defined (as summarized in section 4.6): a_2 has a large impact on the island width growth rate ($\frac{dw}{dt}$) at relatively large w where measurements are available, and $a_2 \in [1, 2]$ has been used in the simulations of various TCV discharges; Δ' , defined in equation (3.25), contains information both on the onset of NTMs (Δ'_0 in terms of triggerless NTMs, equation (4.2)) and the saturation at large w (Δ'_{sat} , equation (3.25)), where Δ'_0 can be estimated based on the measured appearance of NTMs and Δ'_{sat} based on the measured w_{sat} (and the a_2 used); $k = 6$ and $\alpha = 3 \sim 15$ have been determined based on detailed simulations in chapter 4 (sections 4.3.1 and 4.3.2), while in this chapter $\alpha = 10$ and 15 will be used in the simulations of TCV #56171 (sections 6.4.1 to 6.4.4) and AUG #30594 (sections 6.4.5), respectively; $a_3 \equiv 1$; ranges of a_4 and a_5 have been determined from a series of NTM stabilization experiments with co-ECCD, counter-ECCD or ECH, and $a_4 \in [0.3, 0.65]$ along with a fixed $a_5 = 0.9$ (table 5.3) have been used in all the simulations.

This means that it should also be possible to use a set of constant coefficients for the RT-MRE, but then the main question is if and how one can find the optimal set of coefficients for each discharge, *in RT*. The answer to this question stems from the understanding of the key effects of each coefficient on NTM dynamics and the usage of RT measurements available (e.g. w). Following the discussions above, there are two main coefficients/parameters to be determined in RT: Δ'_0 that affects the onset timing of triggerless NTMs and a_2 (with a given $\bar{\rho}_{mn} \Delta'_{\text{sat}}$) that affects w_{sat} . These two parameters (especially a_2) dominate the simulated $w(t)$ evolution in all cases, whereas the effects of a_4 when off-axis co-ECCD beams are involved will be discussed in the next section.

Δ'_0 and a_2 can be determined by comparing RT simulations with RT w measurements. For Δ'_0 , the simple model of Δ'_0 (equation (4.2)) provides the first guess, while the rigid shift $\bar{\rho}_{mn} \Delta'_{\text{shift}}$ (equation (4.7)) used to consider different plasma conditions (e.g. plasma shapes) can be adapted based on the measured appearance of NTMs in RT. a_2 is adjusted by comparing the simulated $w(t)$ evolution during a small time interval to the measured $w(t)$ over the same interval. To better illustrate these, examples based on the TCV discharge #56171 (presented in

section 5.5 of chapter 5, figure 5.12) are shown.

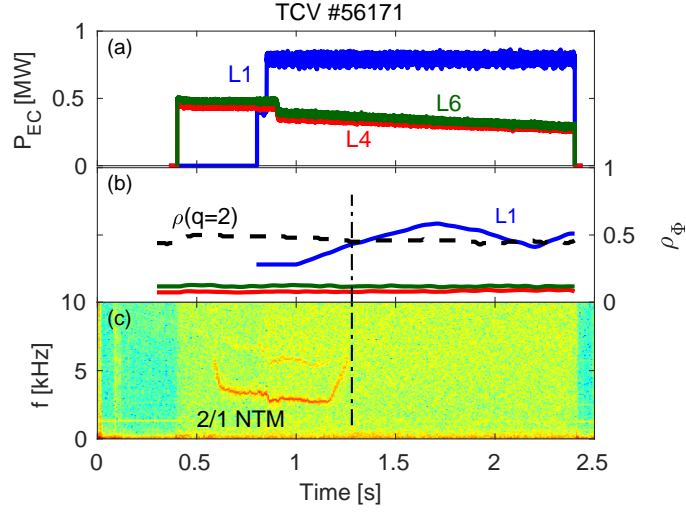


Figure 6.7. 2/1 NTM stabilization with co-ECCD, taken from figure 5.12 of chapter 5: (a) Feedforward EC power traces; (b) EC deposition locations taken from TORAY-GA and $\rho(q=2)$ from ASTRA; (c) NTM spectrogram.

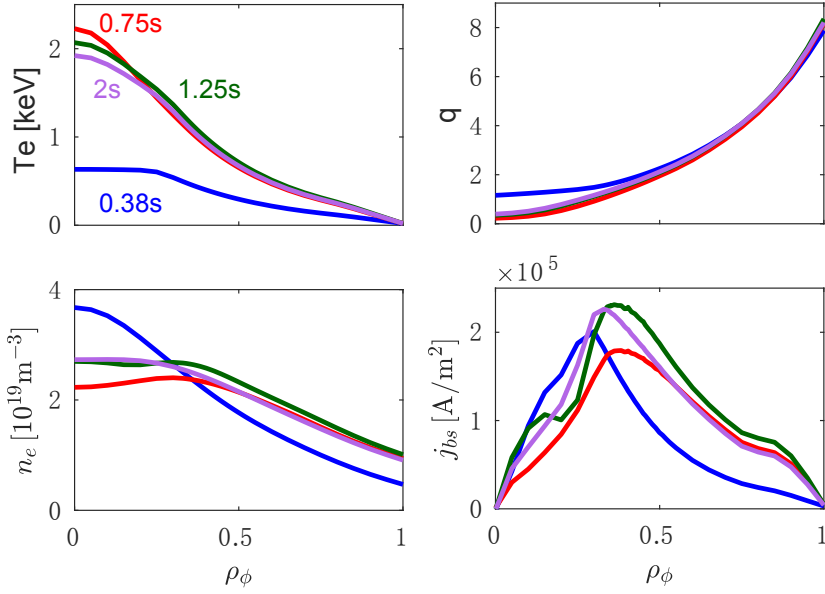


Figure 6.8. T_e , n_e , q and j_{bs} profiles at several different time steps of #56171, taken from interpretative RAPTOR simulations that solve equation (4.1).

As a reminder and shown in figure 6.7, in this discharge two co-ECCD launchers (L4 and L6) deposit near the plasma center and lead to the onset of a 2/1 NTM, due to a Δ' effect as discussed. Another co-ECCD launcher L1 is switched on at $t = 0.8\text{ s}$ and fully suppresses the NTM once it reaches the mode location. To better mimic RT situations, relevant profiles such as T_e ,

q and various current density components are taken from interpretative simulations with the fast RT transport code RAPTOR, following the same procedures described in [Teplukhina 2018]. Examples of the T_e , n_e , q and j_{bs} profiles are shown in figure 6.8, at $t = 0.38$ s (blue, ohmic plasma), 0.75 s (red, two central co-ECCD with NTMs), 1.25 s (green, full stabilization with off-axis co-ECCD) and 2 s (purple, no mode with off-axis co-ECCD). EC-relevant parameters such as the deposition location, absorbed power and driven current used in the MRE simulations are from TORAY-GA, but can be replaced by corresponding outputs from RT-TORBEAM in RT.

Adaptation of Δ'_{shift} based on mode onset

After obtaining the first guess of $\bar{\rho}_{mn}\Delta'_0$ from the $\bar{\rho}_{mn}\Delta'_0$ model (equation (4.2)), $\bar{\rho}_{mn}\Delta'_{\text{shift}}$ (thus the final $\bar{\rho}_{mn}\Delta'_0$) is adapted based on the measured w at each considered time: $\bar{\rho}_{mn}\Delta'_{\text{shift}}$ is adjusted (when necessary) such that the total $\frac{dw}{dt}$ ($w = 0$) ≤ 0 if no mode is detected by the measurements (i.e. below the noise level); in the case where a mode with width w_{measure} is detected, $\bar{\rho}_{mn}\Delta'_{\text{shift}}$ is adjusted (when necessary) to make sure the simulated total $\frac{dw}{dt}$ remain positive for $w \in [0, w_{\text{measure}}]$.

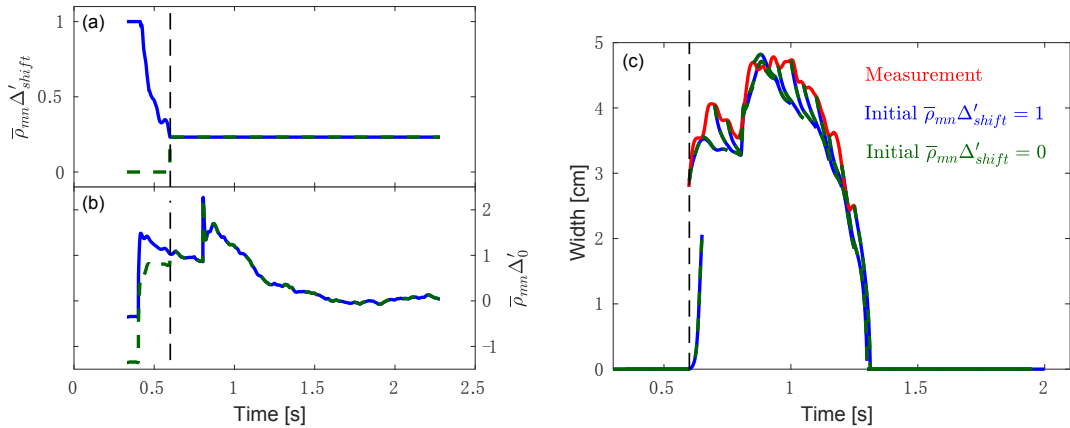


Figure 6.9. Illustration of the adaptation of Δ'_{shift} based on TCV #56171 (figure 6.7): (a) $\bar{\rho}_{mn}\Delta'_{\text{shift}}$ traces; (b) final $\bar{\rho}_{mn}\Delta'_0$ traces, i.e. the sum of $\bar{\rho}_{mn}\Delta'_0$ from $\bar{\rho}_{mn}\Delta'_0$ model (equation (4.2)) and the adapted $\bar{\rho}_{mn}\Delta'_{\text{shift}}$; and (c) w from measurements and simulations. Solid blue - simulation with initial $\bar{\rho}_{mn}\Delta'_{\text{shift}} = 1$; dashed green - with initial $\bar{\rho}_{mn}\Delta'_{\text{shift}} = 0$; red (in (c)) - measurement.

Two examples of these are shown in figure 6.9, where the initial $\bar{\rho}_{mn}\Delta'_{\text{shift}}$ is set to 1 (solid blue) or 0 (dashed green), respectively. At each selected time t_N (i.e. every 50 ms in this case for illustration purposes, figure 6.9 (c)), the MRE is called to compute the $w(t)$ evolution during $t \in [t_N - t_M, t_N]$, with the initial island width (w_0) taken from the measured w at $t_N - t_M$, where t_M is of the resistive time scale to cover the full dynamics of NTMs and set to 100 ms in this case. These configuration parameters can be set by the user before a discharge. Note that in these simulations, all the information used is from *previous and present* time steps, i.e. only making use of the available measurements and reconstructions. This means that the MRE in this case is simply *tracing* the $w(t)$ evolutions, similar to the interpretative simulations

presented in chapters 4 and 5, and making the RT tuning of the parameters feasible.

The resulting $\bar{\rho}_{mn}\Delta'_{\text{shift}}$ is shown in figure 6.9 (a), while the final $\bar{\rho}_{mn}\Delta'_0$ (i.e. the sum of $\bar{\rho}_{mn}\Delta'_0$ from the model (equation (4.2)) and the $\bar{\rho}_{mn}\Delta'_{\text{shift}}$) is shown in (b). For the case with initial $\bar{\rho}_{mn}\Delta'_{\text{shift}} = 1$ (solid blue), the simulated total $\frac{dw}{dt}(w=0) \equiv \bar{\rho}_{mn}\Delta'_0 + \bar{\rho}_{mn}\Delta'_{\text{GGJ}} > 0$ at the beginning of the discharge whereas no NTMs are detected by the measurements (red trace in (c)), so $\bar{\rho}_{mn}\Delta'_{\text{shift}}$ (solid blue trace in figure 6.9 (a)) is decreased such that the maximum $\frac{dw}{dt}(w=0)$ during the considered time interval ($[t_N - 0.1, t_N]$) remains below 0, until the appearance of NTMs (vertical dashed black lines in figure 6.9); for the case with initial $\bar{\rho}_{mn}\Delta'_{\text{shift}} = 0$ (dashed green trace), the simulated total $\frac{dw}{dt}(w=0) \leq 0$ at the beginning of the discharge, in accordance with the measurements, so $\bar{\rho}_{mn}\Delta'_{\text{shift}}$ (dashed green trace in figure 6.9 (a)) remains unchanged until the detection of the mode (vertical dashed black line), when $\bar{\rho}_{mn}\Delta'_{\text{shift}}$ is increased to make sure the simulated total $\frac{dw}{dt} > 0$ for $w \in [0, w_{\text{measure}}]$.

$\bar{\rho}_{mn}\Delta'_{\text{shift}}$ then remains constant, unless another adjustment is needed to match the measured appearance or disappearance of a mode. A fixed $a_2 = 1.3$ (with $\Delta'_{\text{sat}} = -1.4$) is used in these simulations, whereas the adaptation of a_2 will be illustrated below. It can be seen from figure 6.9 (c) that simulations with the adapted $\bar{\rho}_{mn}\Delta'_{\text{shift}}$ (with very different initial values) can follow well the measurements after the onset of NTMs. In particular, $\bar{\rho}_{mn}\Delta'_{\text{shift}}$ after mode onset (marked by the vertical dashed black curves in figure 6.9) thus the final $\bar{\rho}_{mn}\Delta'_0$ used in both simulations (green and blue traces in figure 6.9 (b)) reaches the same values after the adaptation of $\bar{\rho}_{mn}\Delta'_{\text{shift}}$ based on mode onset. With the exactly the same input profiles (e.g. T_e, q) and other coefficients (e.g. a_2) for the MRE, the simulations fully overlap, as shown by the blue and green traces in figure 6.9 (c). It is worth emphasizing that the exact values of $\bar{\rho}_{mn}\Delta'_{\text{shift}}$ (and $\bar{\rho}_{mn}\Delta'_0$) only have a higher-order effect, especially in RT applications, as they mainly affect w evolutions at very small w that are typically below the noise level of the measurements. The $w(t)$ evolution, as detailed in chapter 4, is quickly and significantly affected by neoclassical effects ($\bar{\rho}_{mn}\Delta'_{BS}$), highlighting the importance of adapting a_2 in RT.

Adaptation of a_2 based on $w(t)$

Similarly, the adaptation of a_2 is based on tracing $w(t)$ using the information from previous and present time steps, but by comparing with the measured $w(t)$ within each considered time interval $t \in [t_N - t_M, t_N]$. This is based on the fact that a_2 dominates the $w(t)$ evolution at medium to large w , where measurements are available, as discussed in chapter 4 (figures 4.3 and 4.5). In this section we present a simple and effective method of adapting a_2 based on the measured w_{sat} : at each selected time t_N , an evaluation is made to determine whether the measured $w(t)$ during $t \in [t_N - t_M, t_N]$ reaches a w_{sat} , e.g. by evaluating the variance of $w(t)$ with respect to the averaged w at the considered time interval and comparing the variance with a user-defined threshold; if w_{sat} is reached based on the user-specified criterion, the simulated $w(t)$ evolution at $t \in [t_N - t_M, t_N]$, using the a_2 value at the previous time step and $w_0 = w_{\text{measure}}(t = t_N - t_M)$, is compared with the measurement; if the simulation during $t \in [t_N - t_M, t_N]$ fits well the measurements, i.e. χ (equation (4.5)) is smaller than a

6.4. Inclusion of Modified Rutherford Equation in the plasma control system

user-specified threshold χ_{thres} , no adaptation is triggered and a_2 from the previous time step is kept; if $\chi > \chi_{\text{thres}}$, a_2 (with a fixed $\bar{\rho}_{mn}\Delta'_{\text{sat}}$) is adapted accordingly, e.g. based on the ratio of the average value of the simulated $w(t)$ to that of the measured $w(t)$; the new a_2 is then kept for future time steps until a new adaptation is triggered.

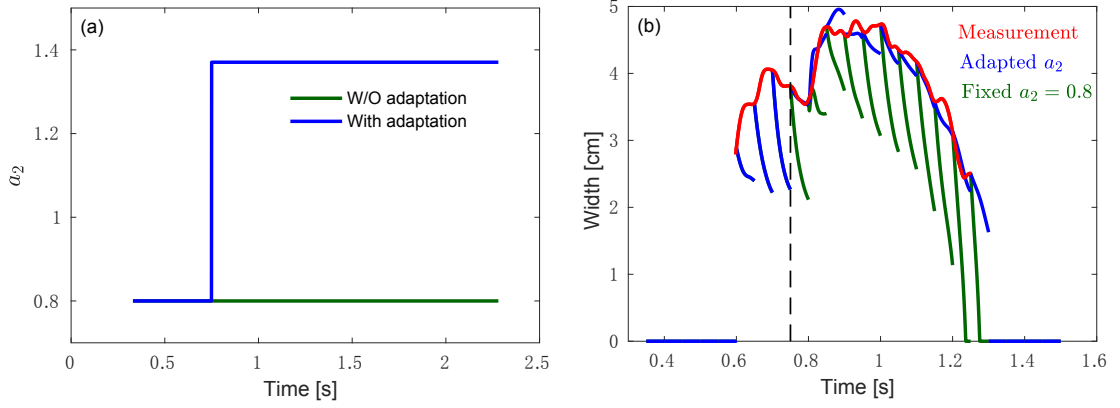


Figure 6.10. Illustration of the adaptation of a_2 base on TCV #56171 (figure 6.7): (a) a_2 traces; and (b) w from measurements and simulations. Blue - simulation with a_2 adaptation; green - with fixed $a_2 = 0.8$; red (in (b)) - measurement.

An example based on TCV #56171 (figure 6.7) is shown in figure 6.10, with a fixed $\bar{\rho}_{mn}\Delta'_{\text{sat}} = -1.4$. As presented in chapters 4 and 5, $\bar{\rho}_{mn}\Delta'_{\text{sat}} \in [-m, 0)$ is typically used in the simulations and it is the ratio between a_2 and $\bar{\rho}_{mn}\Delta'_{\text{sat}}$ that matters. As illustrated in figure 6.10, MRE simulations are performed every 50 ms, with a duration of 50 ms each. The adaptation of $\bar{\rho}_{mn}\Delta'_{\text{shift}}$ illustrated in figure 6.9 has been included in the simulations as well. Relevant (time-varying) profiles (e.g. T_e , n_e , q , j_{bs} , etc.) used in these simulations are taken from the outputs of interpretive simulations with RAPTOR (figure 6.8) with a time resolution of 1 ms.

A standard deviation of 20% is used in the simulations of #56171 (blue traces in figure 6.10 (b)) to determine whether $w(t)$ during each considered time interval reaches a w_{sat} ; if w_{sat} is reached, χ at the considered time interval is evaluated based on the simulated and measured $w(t)$; and a_2 is adapted only when $\chi > \chi_{\text{thres}} = 20\%$. This triggers the adaptation of a_2 at $t = 0.75$ s in this case (indicated by the vertical dashed black curve in figure 6.10 (b)) based on the simulated and measured $w(t)$ at $t \in [0.7, 0.75]$ s: a_2 is adapted from its initial value 0.8 to a new value 1.37, as shown by the blue curve in figure 6.10 (a). The specified criteria are not satisfied simultaneously in the rest of the discharge, explaining why a_2 is adapted only once in this example. A different threshold will affect the adaption of a_2 but can be specified flexibly by the user. It can be seen that simulations after the adaptation of a_2 can fit quite well the measurements (blue and red traces in (b)). As a comparison, simulations with a constant $a_2 = 0.8$, i.e. without the active adaptation of a_2 , are shown by the green curves in figure 6.10 (b), which systematically underestimates w .

The method of adapting a_2 based on w_{sat} shown in this section can be easily extended to

include more options. For example, one may choose to adapt a_2 even though w_{sat} is not reached - it is the evolution of $w(t)$ during each $t \in [t_N - t_M, t_N]$ that matters. However, in this case attention should be paid when off-axis EC beams (especially those close to the target mode location) are involved in the considered time interval, as these beams are able to largely affect $w(t)$ evolutions as well (see chapter 5). As an outlook, more advanced technique, e.g. the extended Kalman filter should be utilized in the RT adaptation of these coefficients.

6.4.2 Real-time information about beam-mode alignment

With more confidence about its coefficients, the RT-MRE can be applied in different ways to obtain valuable RT information. This section presents its application in estimating the alignment of EC beams with mode location, which can be obtained by tracing $w(t)$ (i.e. with information from previous and present time steps) assuming different deposition locations (ρ_{dep}) of the control EC beam.

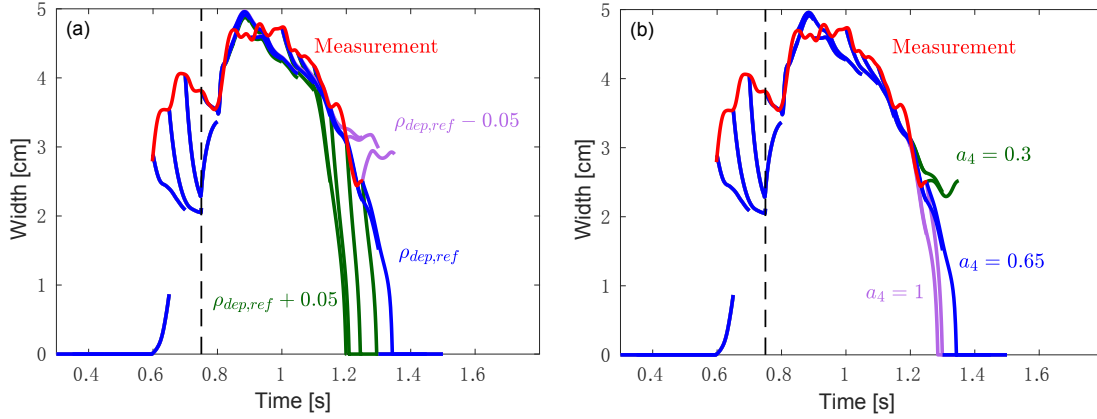


Figure 6.11. Based on TCV #56171 (figure 6.7): (a) Illustration of estimating beam-mode alignment through simulations with various ρ_{dep} and fixed $a_4 = 0.65$; (b) Illustration of the effect of a_4 on $w(t)$.

As illustrated in figure 6.11 (a), at each time t_N (every 50ms in this case), simulations of $w(t)$ during $t \in [t_N - 0.1, t_N]$ are performed, with three different ρ_{dep} of L1: $\rho_{\text{dep,ref}}$ as in the experiment (from ray-tracing calculations, blue curve in figure 6.7 (b)); and $\rho_{\text{dep,ref}} \pm \Delta\rho$, where $\Delta\rho \equiv \text{const}$ represents a rigid offset with respect to $\rho_{\text{dep,ref}}$ and can be set based on the uncertainties of ray-tracing computations. $\Delta\rho = 0.05$ is used in this case, and the adaptation of Δ'_{shift} and a_2 discussed in section 6.4.1 is included in all the simulations. The three simulations (blue, green and purple traces in figure 6.11 (a)) assuming different ρ_{dep} of L1 overlap until any ρ_{dep} used in the simulations reaches close enough to the mode location, i.e. earliest at $t \approx 1.15$ s for the case with $\rho_{\text{dep,ref}} + 0.05$ (green traces in figure 6.11 (a)). This is as expected from the $\bar{\rho}_{mn}\Delta'_{CD}$ and $\bar{\rho}_{mn}\Delta'_H$ terms defined in equations (3.9) and (3.10): $\bar{\rho}_{mn}\Delta'_{CD}$ and $\bar{\rho}_{mn}\Delta'_H$ terms are more negative (stabilizing) with less misalignment with respect to the mode location, leading to an earlier full stabilization of NTMs when the EC beam reaches the target location earlier. Fixed $a_4 = 0.65$ and $a_5 = 0.9$, i.e. coefficients for $\bar{\rho}_{mn}\Delta'_{CD}$ and $\bar{\rho}_{mn}\Delta'_H$ in equation (6.1),

respectively, are used in all the simulations shown in figure 6.11 (a).

Useful information can be drawn from the simulations with three different ρ_{dep} in figure 6.11 (a). For instance, at each time t_N , the beam-mode alignment can be improved by comparing the three simulations and identifying the one that has the minimum $\frac{dw}{dt}$: $\rho_{\text{dep,ref}} + 0.05$ in this case (green traces in figure 6.11 (a)), which indeed would lead to an earlier crossing of mode location as seen from the experiment (figure 6.7). Moreover, information concerning the uncertainties of $\rho_{\text{dep,ref}}$ evaluation can be estimated by comparing the three simulations to corresponding measurements at the same time interval: $\rho_{\text{dep,ref}}$ is a good estimation of the actual ρ_{dep} at the considered time interval if the simulation with $\rho_{\text{dep,ref}}$ indeed fits the best the measurements (i.e. with minimum χ as used in chapters 4 and 5); on the other hand, if the simulation with $\rho_{\text{dep,ref}} \pm \Delta\rho$ fits better the measurement, the uncertainty of $\rho_{\text{dep,ref}}$ is at least $\pm\Delta\rho$.

As mentioned in section 6.4.1, there is a range of a_4 that can be used with fixed $a_5 = 0.9$: $a_4 \in [0.3, 0.65]$ (table 5.3 in chapter 5). To illustrate the possible effect of a_4 on $w(t)$ evolution, simulations with $a_4 = 0.3, 0.65$ and 1 , respectively, are shown in figure 6.11 (b), where $a_4 = 1$ is actually already outside the defined range, but shown here for illustration purposes. It can be seen that larger a_4 , thus stronger stabilizing effect from $\bar{\rho}_{mn}\Delta'_{CD}$, leads to a faster stabilization of NTMs; the optimal a_4 or a narrower range of a_4 can be obtained by comparing different simulations with RT measurements. More importantly, the influence of a_4 on $w(t)$ is different from that of ρ_{dep} as seen from figure 6.11 (a) and (b), by comparing the green and purple traces to the (same) blue traces in each plot: a_4 only affects the level of the stabilizing effect when the EC beam reaches close enough to the mode location, whereas ρ_{dep} does not only affect the level of the stabilizing effect, but also the timing when the stabilizing effect starts to play a role. This is because ρ_{dep} determines the beam-mode misalignment level (quantified by x_{norm} defined in equation (3.16)) and affects both $\bar{\rho}_{mn}\Delta'_{CD}$ and $\bar{\rho}_{mn}\Delta'_H$, which have different dependence on x_{norm} (as illustrated in figure 5.7, chapter 5), whereas a_4 does not affect x_{norm} nor $\bar{\rho}_{mn}\Delta'_H$.

6.4.3 Real-time estimation of the EC power required for NTM control

The method of applying RT-MRE in estimating the required EC power (P_{req}) for NTM control will be presented in this section. As illustrated by figure 6.12, this is mainly based on the effects of EC power on the $\frac{dw}{dt}(w)$ plots of NTMs. Different situations are shown: partial stabilization, where the width of a given NTM (if larger than a user-specified w_{sat}) will be decreased to w_{sat} , or prevention of NTMs for a seed island width (w_{seed}) smaller than the critical island width w_{crit} ; marginal stabilization, where full stabilization of NTMs is obtained and featured by $\max(\frac{dw}{dt}) = 0$ at w_{marg} ; and “fast” stabilization, where full stabilization or prevention of NTMs is ensured, and featured by a faster full stabilization of NTMs when compared with the marginal case in terms of NTM stabilization. Both the “marginal” and “fast” cases are unconditionally stable, in the sense that the plasma is unconditionally stable to

NTMs, regardless of w_{seed} : $\frac{dw}{dt} \leq 0$ for all w .

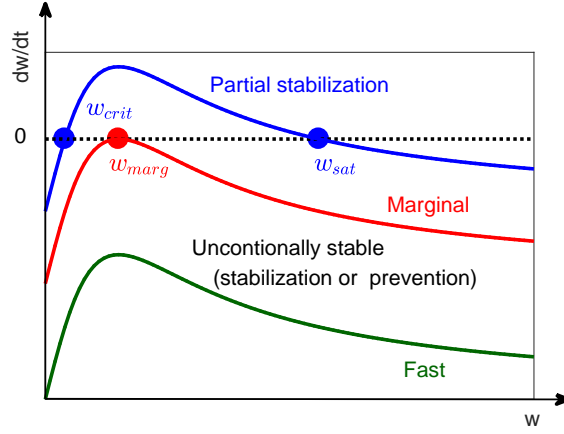


Figure 6.12. Illustration of $\frac{dw}{dt}(w)$ traces of various cases of NTM control: blue - partial stabilization to w_{sat} or prevention to $w_{seed} \leq w_{crit}$, featured by two zeros of $\frac{dw}{dt}(w)$ at w_{crit} and w_{sat} ; red - marginally stable, where the maximum of $\frac{dw}{dt}(w)$ equals 0 at w_{marg} ; green - “fast” stabilization, featured by more negative $\frac{dw}{dt}(w)$ that will lead to a faster stabilization of NTMs. Both the “marginal” and “fast” cases are unconditionally stable to NTMs, regardless of w_{seed} .

The estimation of the required power is then essentially the evaluation of the EC power needed to bring the present $\frac{dw}{dt}(w)$ to the requested $\frac{dw}{dt}(w)$, based on the dependence of various MRE terms (equation (6.1)) on the (off-axis) EC power (P_{EC}). As seen from equation (3.4) to equation (3.8), P_{EC} is expected to have implicit effects on $\bar{\rho}_{mn}\Delta'_{BS}$ and $\bar{\rho}_{mn}\Delta'_{GGJ}$ through the modifications of T_e profiles, q profiles etc., but the effects remain small since only off-axis EC beams are considered. Moreover, if needed, these effects can be included more self-consistently by predictive simulations (e.g. with the RAPTOR predictor [Felici et al. 2011] in RT). In terms of $\bar{\rho}_{mn}\Delta'$ (equation (3.25)), the main effect will be on $\bar{\rho}_{mn}\Delta'_0$ (equation (4.2)) given its dependence on I_{cd} , but can be easily included using the relation between P_{EC} and I_{cd} , i.e. current drive efficiency (η_{cd}) based on ray-tracing.

More evident effects of the off-axis P_{EC} on the MRE (thus the $\frac{dw}{dt}(w)$) are through its influence on $\bar{\rho}_{mn}\Delta'_{CD}$ and $\bar{\rho}_{mn}\Delta'_H$. Detailed forms of these two terms have been given in chapter 3 (equations (3.9) and (3.10)) and can be simplified as

$$\bar{\rho}_{mn}\Delta'_{CD} \propto -I_{cd}N_{cd}G_{cd} = -\eta_{cd}P_{EC}N_{cd}G_{cd} \quad (6.2)$$

and

$$\bar{\rho}_{mn}\Delta'_H \propto -\eta_H P_{EC} N_H G_H, \quad (6.3)$$

where I_{cd} is the driven current from the given EC launcher, η_H estimates the efficiency with which the EC power is converted into a perturbative inductive current, $N_{cd,H}$ represent the dependence on w and $G_{cd,H}$ represent the effect of beam-mode misalignment. The effect of

P_{EC} can thus be further simplified as

$$\bar{\rho}_{mn}(\Delta'_{CD} + \Delta'_H) = f_{EC}(w, \rho_{\text{dep}}) \cdot P_{EC}, \quad (6.4)$$

where $f_{EC}(w, \rho_{\text{dep}}) \propto -(\eta_{cd} N_{cd} G_{cd} + \eta_H N_H G_H)$ is the overall factor in front of P_{EC} that depends on w and ρ_{dep} and can be computed directly based on the detailed forms of each term (equations (3.11) to (3.15)). Note that η_{cd} and η_H should in principle depend on P_{EC} as well (e.g. through modifying T_e and n_e profiles), but these are only higher-order effects that do not affect much the results, or similarly, if needed, can be obtained self-consistently from ray-tracing computations based on predicted profiles with RAPTOR.

Equations (6.1) and (6.4) can be used to estimate P_{req} of different cases, based on user-specified w_{req} , ρ_{req} and t_{req} . w_{req} is the requested w , for example $w_{\text{req}} = 3$ cm to reach partial stabilization to 3 cm, -1 to reach unconditionally stable, etc.; ρ_{req} is the assumed deposition location of the control beam; t_{req} is only relevant for “fast” stabilization from a width larger than w_{req} , i.e., to reach w_{req} within t_{req} . The entire requirement is then interpreted as a generic functionality “evaluating P_{EC} needed to obtain w_{req} (within t_{req}) with EC beams depositing at ρ_{req} ”. Various examples of this will be shown in the rest of this section.

Unconditionally stable

One example of being unconditionally stable is marginally stable. As shown by the red curve in figure 6.12, the maximum of $\frac{dw}{dt}(w)$ reaches 0 at w_{marg} in this case. Substituting this into equations (6.1) and (6.4), and after simple rearrangements, P_{req} can be estimated by

$$P_{\text{req}} = -\frac{\bar{\rho}_{mn}(\Delta' + \Delta'_{BS} + \Delta'_{GGJ})|_{w=w_{\text{marg}}}}{f_{EC}(w_{\text{marg}}, \rho_{\text{dep}})} \approx -\frac{\bar{\rho}_{mn}(\Delta' + \Delta'_{BS} + \Delta'_{GGJ})|_{w=w_{\text{de}}}}{f_{EC}(w_{\text{de}}, \rho_{\text{dep}})}, \quad (6.5)$$

where $w_{\text{marg}} \approx w_{\text{de}}$ is used based on the derivative of MRE terms to w . This typically provides a good first estimate of P_{req} , then adjustments to P_{req} can be performed (when necessary) by evaluating $\frac{dw}{dt}$ around $w = w_{\text{de}}$ (typically within ± 0.5 cm with respect to w_{marg}) based on the MRE (equation (3.3)) and making sure the maximum equals or is just below 0.

With this method, P_{req} has been evaluated for TCV #56171 shown in figure 6.7, with $w_{\text{req}} = -1$ (will be replaced by $w_{\text{req}} = w_{\text{de}}$ in the simulations as w_{de} is computed within the MRE), $\rho_{\text{req}} = \rho_{mn}$ (assuming perfect alignment, i.e. different from the experimental trace shown in figure 6.7 (b)) and $t_{\text{req}} = -1$ (no requirement on t_{req}). In these simulations with the MRE, relevant time-varying profiles (e.g. T_e , n_e , q , j_{bs} , etc.) are taken from the outputs of RAPTOR simulations, while Δ'_0 and a_2 involved in the MRE are adapted as presented in section 6.4.1, with fixed $\Delta'_{\text{sat}} = -1.4$, $a_3 = 1$, $a_4 = 0.65$ and $a_5 = 0.9$. The results are shown by the red curves with crosses in figure 6.13 (a), where the symbols represent the time points when P_{req} is evaluated. Note that these estimations only require information at the present time step, different from the *tracing* presented in sections 6.4.1 and 6.4.2, where information at both

present and previous time steps is needed. As shown in figure 6.7, plasma conditions vary during this discharge, so does the P_{req} . As indicated by the vertical dashed black lines in figure 6.13 (a), $P_{\text{req}} \approx 0.7 \text{ MW}$ at $t = 1.25 \text{ s}$, in accordance with the experiment (full stabilization with 0.8 MW at around 1.25 s when crossing the mode location).

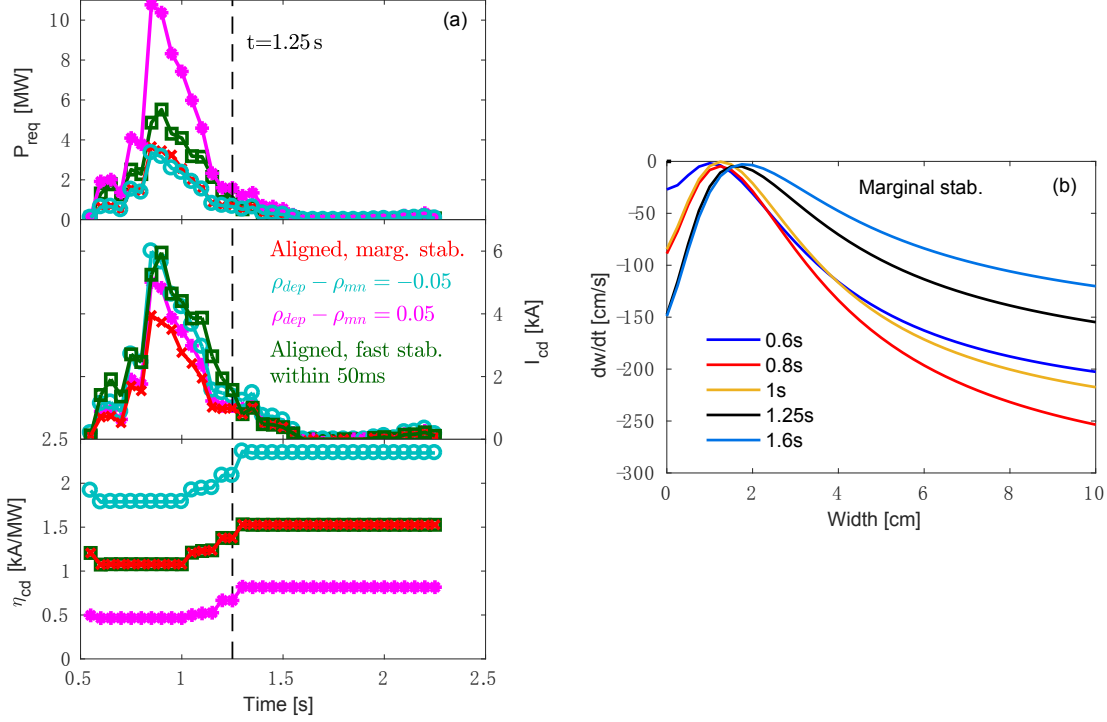


Figure 6.13. Simulations based on TCV #56171 (figure 6.7). (a) Top panel: P_{req} for being marginally stable with perfect alignment (red with crosses), $\rho_{\text{req}} - \rho_{mn} = -0.05$ (cyan with circles) and $\rho_{\text{req}} - \rho_{mn} = +0.05$ (magenta with asterisks); P_{req} for fast full stabilization within 50 ms (green with squares). Middle panel: corresponding I_{cd} , with the same line type as in the top panel. Bottom panel: η_{cd} of different cases. (b) $\frac{dw}{dt}(w)$ traces at various time slices shown in the legend, with the estimated P_{req} for marginal stabilization (with perfect alignment).

In these and following simulations, η_{cd} is taken based on the statistics of various experiments with similar plasma conditions (e.g. T_e , n_e , etc.) but different ρ_{dep} , and tends to decrease with increasing ρ_{dep} (i.e. towards the edge of the plasma), as expected. I_{cd} is then estimated by the product of η_{cd} and P_{req} . Similarly, P_{req} for reaching marginal stabilization with $\rho_{\text{req}} - \rho_{mn} = -0.05$ has been evaluated, as shown by the cyan curves with triangles. This case has higher η_{cd} due to its more inward deposition, while still having finite deposition within the mode (i.e. $G_{cd,H} \neq 0$); the higher η_{cd} leads to similar P_{req} as the perfect alignment case, but with higher I_{cd} (middle panel of figure 6.13 (a)). The case with $\rho_{\text{req}} - \rho_{mn} = 0.05$ (magenta traces), on the other hand, has lower η_{cd} and higher P_{req} . The resulting $\frac{dw}{dt}(w)$ traces with the estimated P_{req} for marginal stabilization (with perfect alignment) are shown in figure 6.13 (b). The maximum of $\frac{dw}{dt}(w)$ at all time slices equals or just below 0, as expected.

The green traces in figure 6.13 (a) are the estimations for “fast” full stabilization, assuming perfect alignment and with $t_{\text{req}} = 50$ ms. This requires solving $w(t)$ evolution with constant inputs (e.g. T_e , q profiles, etc.) taken from the present time step and an initial P_{req} (e.g. taken from the P_{req} for marginal stabilization); if the required time to reach $w = 0$ with the tested P_{req} is larger than 50 ms, P_{req} is increased, $w(t)$ re-evaluated, the requirement on t_{req} re-checked, and so on; after some iterations, the final P_{req} , i.e. the minimum power requested to reach full stabilization within t_{req} can be obtained. Note that this is only relevant for the time slices when the initial w_0 from the measurement is finite, otherwise P_{req} remains the same as that of the marginally stable case, as indicated in figure 6.13 (a).

The resulting $\frac{dw}{dt}(w)$ traces with the estimated P_{req} for fast full stabilization (with perfect alignment) are shown in figure 6.14 (a). It can be seen that at time slices when NTMs have finite w (i.e. during $t \in [0.5, 1.25]$ s in this discharge), $\frac{dw}{dt}(w)$ stay well below 0, whereas for time slices when w reaches 0 already (e.g. at $t = 1.6$ s), $\frac{dw}{dt}(w)$ stays just below 0, the same as the marginal stabilization case (figure 6.13 (b)). Examples of the $w(t)$ traces evaluated at different time slices (different from those shown in figure 6.14 (a)) with the P_{req} (green trace in the top panel of figure 6.13 (a)) are shown in figure 6.14 (b). It can be seen that full stabilization is achieved (for $w_0 \neq 0$) within 50 ms.

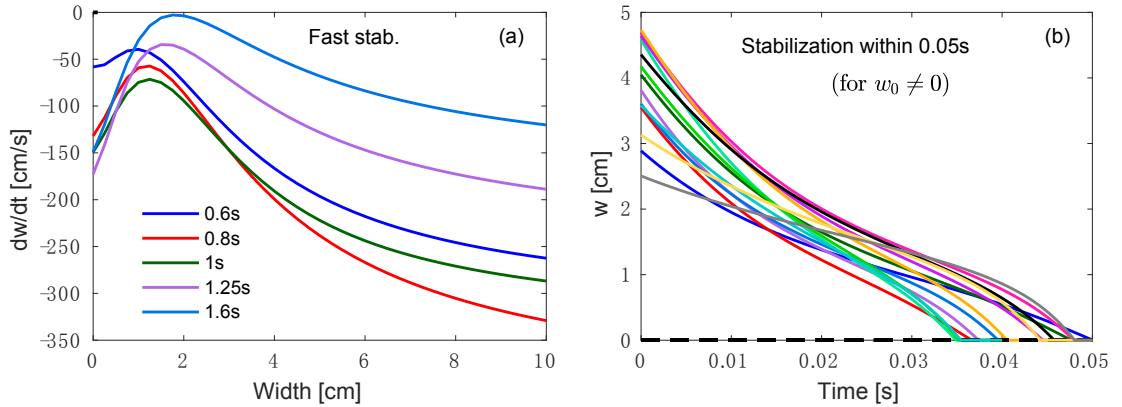


Figure 6.14. Simulations base on TCV #56171 (figure 6.7). (a) $\frac{dw}{dt}(w)$ traces at various time slices shown in the legend, with the estimated P_{req} for fast full stabilization within 50 ms with perfect alignment (green trace in the top panel of figure 6.13 (a)). (b) $w(t)$ traces evaluated based on the plasma conditions at different time slices (different from those shown in figure 6.14 (a)) with the final P_{req} .

Partial stabilization

As illustrated by the blue curve in figure 6.12, partial stabilization is characterized by $\frac{dw}{dt}(w = w_{\text{sat}}) = 0$, with $w_{\text{sat}} > w_{\text{marg}}$. Similar to equation (6.5), P_{req} to reach $w_{\text{req}} = w_{\text{sat}}$ can be estimated by

$$P_{\text{req}} = - \frac{\bar{\rho}_{mn}(\Delta' + \Delta'_{BS} + \Delta'_{GGJ})|_{w=w_{\text{sat}}}}{f_{EC}(w_{\text{sat}}, \rho_{\text{dep}})}. \quad (6.6)$$

Similarly, this is relevant only if the measured w at the considered time slice is larger than w_{sat} , assuming that one does not want to increase the island size, thus otherwise $P_{\text{req}} \equiv 0$. Note that the requested w_{sat} is compared to the w_{de} at each considered time that is computed within the MRE, and the requested partial stabilization will be replaced by full stabilization automatically if $w_{\text{sat}} \leq w_{\text{de}}$.

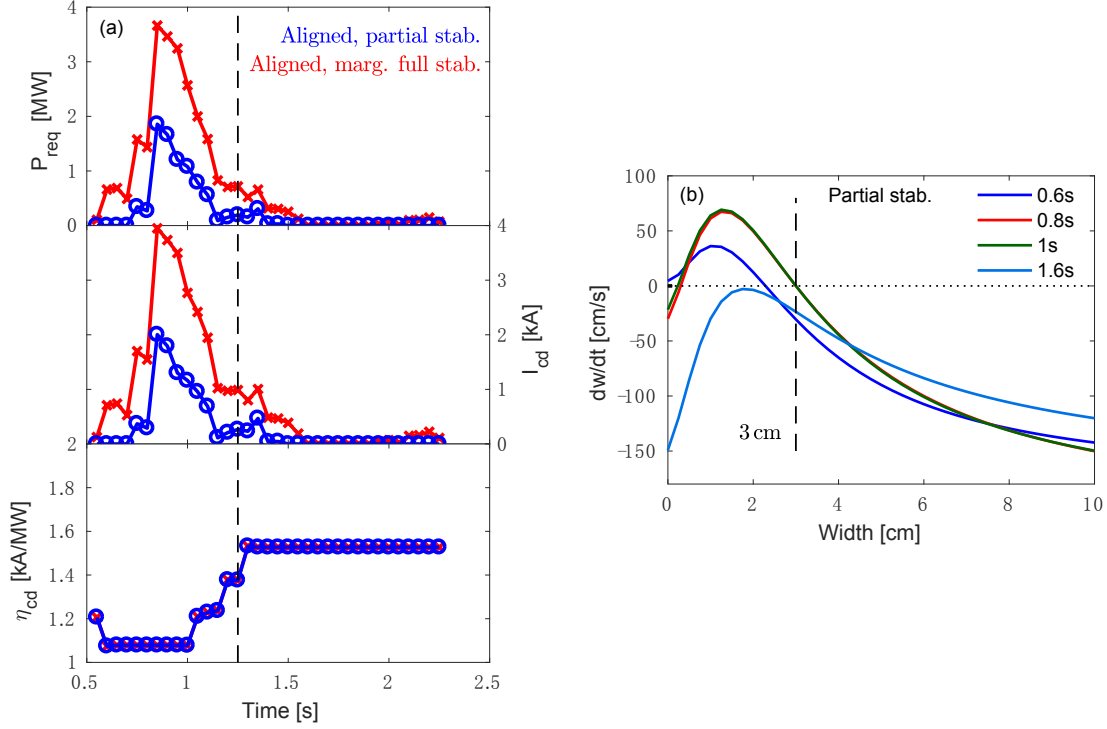


Figure 6.15. Simulations base on TCV #56171 (figure 6.7). (a) Top panel: P_{req} for partial stabilization to 3 cm with perfect alignment (blue with circles) and the case for marginal full stabilization (red with crosses, the same as in figure 6.13 (a)). Middle panel: corresponding I_{cd} , with the same line type as in the top panel. Bottom panel: η_{cd} of the two cases. (b) $\frac{dw}{dt}(w)$ traces at various time slices shown in the legend, evaluated with the estimated P_{req} for partial stabilization (with perfect alignment).

Estimations have been performed for TCV #56171 (figure 6.7) with $w_{\text{req}} = 3$ cm, $\rho_{\text{req}} = \rho_{mn}$ (perfect alignment) and $t_{\text{req}} = -1$ (no requirement on t_{req}), and the results are shown in figure 6.15 (a). It can be seen that partial stabilization (blue trace with circles) requires less EC power than full stabilization (red curve with crosses), as expected. The resulting $\frac{dw}{dt}(w)$ traces with the estimated P_{req} are shown in figure 6.15 (b). It can be seen that at time slices when the measured $w > 3$ cm (e.g. $t = 0.8$ s, 1 s), the application of P_{req} shifts the $\frac{dw}{dt}(w)$ so that $\frac{dw}{dt}(w = 3 \text{ cm}) = 0$.

RT estimations of the required EC power for partial stabilization have important implications in the overall integrated control. For instance, the supervisory controller can make a better decision on how to continue a discharge by comparing the difference in the power required by partial and full stabilization as well as considering the available actuators. With an idea of the

typical island width that causes mode locking (w_{lock}) in a given scenario, corresponding EC power can be evaluated and used in RT to avoid locked modes, by making sure $w_{\text{sat}} < w_{\text{lock}}$. Note also that a desired target w_{sat} can be determined by the maximum performance degradation allowed in a given discharge, based on the relation between w_{sat} and the degradation of the energy confinement time (equation (3.2) in chapter 3) [Chang and Callen 1990].

Prevention of NTMs with a given w_{seed}

The unconditionally stable cases discussed before are also applicable to the prevention of NTMs, where no NTMs will be triggered regardless of w_{seed} . However, this typically requires a rather high EC power. With a good knowledge of the possible w_{seed} of a given scenario, P_{req} can be lowered to prevent NTMs from being seeded by a given w_{seed} , instead of all w_{seed} . In terms of $\frac{dw}{dt}(w)$, this corresponds to the blue trace in figure 6.12, but considering w_{crit} instead of w_{sat} .

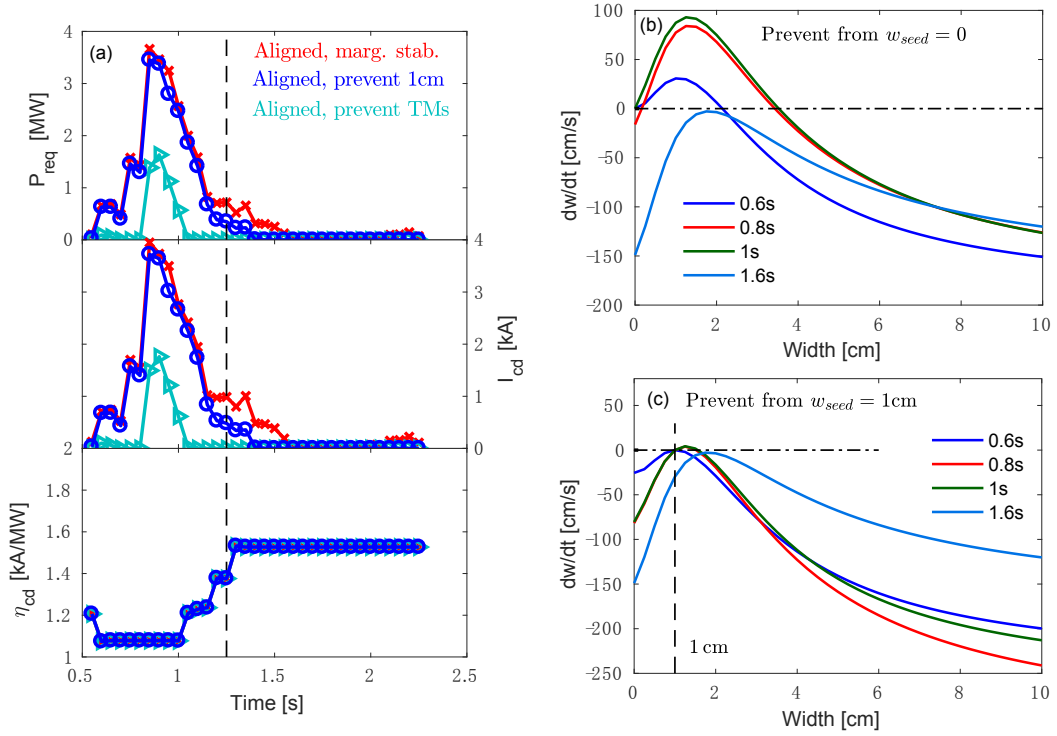


Figure 6.16. Simulations base on TCV #56171 (figure 6.7). (a) Top panel: P_{req} for preventing NTM onset from $w_{\text{seed}} = 0$ (cyan with triangles) and 1 cm (blue with circles), respectively; red curve with crosses - corresponding P_{req} for marginal full stabilization, the same as the red curve in figure 6.13 (a) and figure 6.15 (a). Middle panel: corresponding I_{cd} , with the same line type as in the top panel. Bottom panel: η_{cd} . (b) $\frac{dw}{dt}(w)$ traces for $w_{\text{req}} = 0$. (c) $\frac{dw}{dt}(w)$ traces for $w_{\text{req}} = 1$ cm.

Similar to the discussions about partial stabilization, the user-specified w_{seed} is also compared

to w_{de} at each considered time, and the request will be automatically replaced by being marginally stable if the requested $w_{seed} \geq w_{de}$. Otherwise, P_{req} to prevent NTM onset from a given w_{seed} is estimated by

$$P_{req} = -\frac{\bar{\rho}_{mn}(\Delta' + \Delta'_{BS} + \Delta'_{GGJ})|_{w=w_{seed}}}{f_{EC}(w_{seed}, \rho_{dep})}. \quad (6.7)$$

Estimations for TCV #56171 have been performed with $w_{req} = 0$ (i.e. triggerless NTMs originating from TMs) and 1 cm (standard seeded NTMs), respectively, as shown in figure 6.16 (a). ρ_{req} (i.e. the assumed ρ_{dep} of $L1$) in these simulations is set to ρ_{mn} , i.e. assuming perfect alignment of $L1$ in all the simulations (different from the experimental ρ_{dep} of $L1$ shown in figure 6.7 (b)). P_{req} of both cases are compared with that of marginal stabilization (the same as the red curves in figures 6.13 (a) and 6.15 (a)). It can be seen that much less power is needed to prevent triggerless NTMs than stabilizing them, in accordance with experimental observations (e.g. as discussed in section 5.6); P_{req} increases with larger w_{seed} , as expected, and the P_{req} for preventing $w_{seed} = 1$ cm is comparable to that for marginal full stabilization of NTMs in this discharge. This is because $\max(\frac{dw}{dt}) \approx 0$ with $w_{seed} = 1$ cm (figure 6.16 (c)), i.e. $w_{seed} = 1$ cm $\approx w_{marg}$ in this case.

Corresponding $\frac{dw}{dt}(w)$ traces at various time slices of preventing NTMs with $w_{seed} = 0$ and $w_{seed} = 1$ cm are presented in figure 6.16 (b) and (c), respectively, where $\frac{dw}{dt}(w \leq w_{seed}) \leq 0$ is kept. Note that no power is required for stabilization or prevention of NTMs at $t \geq 1.6$ s (figure 6.16 (a)). This is because the entire $\frac{dw}{dt}(w)$ curve reaches below 0 (i.e. unconditionally stable) along with the ramp-down of the central EC power in the experiment (figure 6.7) at $t \geq 1.6$ s. For example, the maximum of the $\frac{dw}{dt}(w)$ trace at $t = 1.6$ s (figure 6.16 (b) and (c)) just reaches 0, i.e. marginally stable.

The estimation of P_{req} for preventing NTMs is not only important for reliable NTM prevention, but also for the integrated control in general. For example, the supervisory controller may decide to perform NTM stabilization instead of prevention if the P_{req} for preventing NTMs from a given w_{seed} is comparable to that for the full stabilization of NTMs.

6.4.4 Prediction of island width evolution

Another useful application of the RT-MRE is to predict $w(t)$ evolution with given inputs, e.g. from pre-programmed waveforms. In contrast to the *tracing* discussed in sections 6.4.1 and 6.4.2, this *prediction* makes use of *present and future* information: at each time t_N , $w(t)$ during $t \in [t_N, t_N + t_M]$ is predicted, with the initial w_0 taken from the measured w at $t = t_N$. As an illustration, simulations have been performed for TCV #56171 (figure 6.7), assuming different situations of the control beam $L1$: vary the power of $L1$ while using the same ρ_{dep} as in the experiment (blue trace in figure 6.7 (b)), or vary ρ_{dep} with the same power of $L1$ as used in the experiment (800 kW, blue trace in figure 6.7 (a)). Corresponding simulation results are

6.4. Inclusion of Modified Rutherford Equation in the plasma control system

shown in figures 6.17. In these MRE simulations, relevant profiles (T_e , n_e , q , etc.) used are taken from interpretative simulations of #56171 (figure 6.7) with RAPTOR, instead of predictive transport simulations. Predictive transport simulations (e.g. with RAPTOR) would contribute to more self-consistent predictions, especially when a large change of plasma conditions is foreseen (e.g. a large change of the central heating power), and can be applied in the future when necessary.

In figure 6.17 (a), at each time t_N (every 30 ms, starting from $t = 0.75$ s), $w(t)$ evolution during $t \in [t_N, t_N + 0.2]$ is predicted, assuming different constant power from L1 (0, 200, 400, 800 kW) in each set of simulations, but using the same ρ_{dep} as in the experiment (blue trace in figure 6.7 (b)). It can be seen that with $P_{EC} = 800$ kW (as in the experiment), the NTM is predicted to be fully stabilized around $t = 1.25$ s, consistent with experimental observations, while no full stabilization is obtained with $P_{EC} \leq 400$ kW. Note that in these simulations with different P_{EC} , Δ'_0 is adjusted self-consistently based on the Δ'_0 model (equation (4.2)), by scaling I_{cd} with P_{EC} . This explains why the cases with lower P_{EC} tend to have a smaller increase of w (i.e. less increase of Δ'_0 and thus Δ') when turning on the control beam at around $t = 0.8$ s. The simulated $w(t)$ evolutions with lower P_{EC} (0, 200 and 400 kW) than actually used in the experiment (800 kW), i.e. the cyan, purple and green traces in figure 6.17 (a) thus tend to underestimate the measured $w(t)$ (red curve in figure 6.17 (a)) before $t = 1.25$ s.

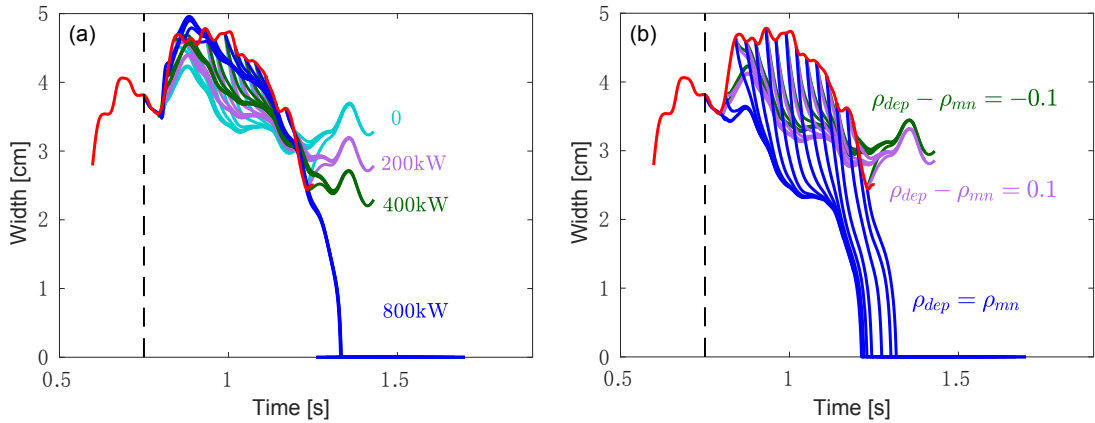


Figure 6.17. Predictions of $w(t)$ assuming different power or deposition location of the control beam L1 in TCV #56171 (figure 6.7): (a) predictions assuming different power of L1 with the same ρ_{dep} as shown by the blue trace in figure 6.7 (b); and (b) predictions assuming different ρ_{dep} of L1, but with fixed power 800 kW.

Simulations with fixed $P_{EC} = 800$ kW (as in the experiment) but different ρ_{dep} (perfect alignment or rigid offset with respect to ρ_{mn}) are shown in figure 6.17 (b). Similar to (a), the computations are carried out every 30 ms, with a duration of 200 ms each. Self-consistent Δ'_0 is used, by updating η_{cd} (thus I_{cd}) based on its relation with ρ_{dep} , which drops with increasing ρ_{dep} . For the simulations shown in figure 6.17 (b), η_{cd} at each ρ_{dep} is estimated based on a look-up table that is built based on the TORAY-GA outputs of several discharges that have similar settings as #56171 but different ρ_{dep} . This can be replaced by RT ray-tracing

calculations (e.g. from RT-TORBEAM) in the RT application. Comparing the simulations with different ρ_{dep} in figure 6.17 (b), faster full stabilization would be achieved if perfect alignment (i.e. $\rho_{\text{dep}} = \rho_{mn}$) were kept, while the slow decrease of w observed in the other two cases, where the beam-mode misalignment levels are large, are mainly from the slow ramp-down of the central co-ECCD power (from $L4$ and $L6$) in this discharge (figure 6.7). Note that the ρ_{dep} traces used in all these simulations are different from that used in the experiment (i.e. perfect alignment or rigid offset in the simulations versus a widely sweeping ρ_{dep} in the experiment), explaining the difference in the simulated and measured $w(t)$.

RT predictions of $w(t)$ evolutions can be used in different ways. For instance, with an estimation of $w(t)$ with different power and/or ρ_{dep} of the EC beam used for NTM stabilization, the supervisory controller may decide not to increase the power nor move the ρ_{dep} of the EC actuator(s) assigned to the NTM stabilization task if it foresees an acceptable degradation caused by the mode, even though the NTM stabilization task requests a higher EC power or a different ρ_{dep} . New control tasks can also be activated in RT based on the predictions. For example, the supervisory controller may activate the disruption avoidance or mitigation task if it foresees a $w(t)$ evolution to a large mode that risks to be locked easily.

6.4.5 Further tests of the RT-MRE based on an AUG discharge

The RT-MRE, built based on physics understanding, remains generic, i.e. it is applicable to different scenarios and tokamaks. The capabilities of the RT-MRE presented in section 6.4 have been tested comprehensively based on a discharge from ASDEX Upgrade - AUG #30594, and some examples will be shown in this section.

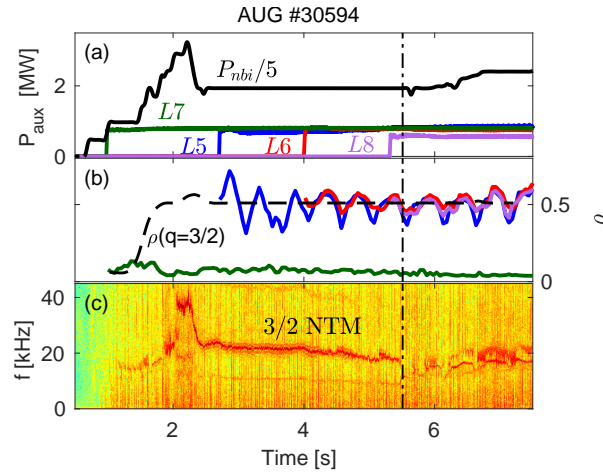


Figure 6.18. Experimental overview of an NTM stabilization experiment with varying co-ECCD depositions with $I_p \approx 1$ MA and relatively constant $n_{el} \approx 7 \times 10^{19} \text{ m}^{-3}$: (a) NBI and EC power traces; (b) normalized (wrt. a) deposition locations of EC beams and $\rho(q = 3/2)$; and (c) $3/2$ NTM spectrogram.

Following [Reich et al. 2014] and as shown in figure 6.18, a $3/2$ NTM is triggered during the

ramp-up of the central NBI power, through sawtooth crashes (i.e. a standard seeded NTM instead of triggerless NTM). RT NTM control of the 3/2 mode is conducted with three co-ECCD launchers, labeled as $L5$, $L6$ and $L8$, respectively. Another ECH launcher ($L7$) deposits near the plasma center, following feedforward waveforms. As seen from figure 6.18 (b), the robust sweeping technique and the ability of asking for more power are included in this discharge, similar to those presented in sections 6.2 and 6.3. The 3/2 NTM is fully stabilized by the three co-ECCD launchers at $t \approx 5.5$ s, with a total power of about 2.2 MW.

Before going into the tests of the RT-MRE, interpretative simulations similar to those presented in chapters 4 and 5 are performed for this discharge, as shown in figure 6.19. Relevant profiles such as T_e , n_e and q are taken from interpretative simulations with RAPTOR, following the same procedures as presented in [Teplukhina 2018]; EC-relevant parameters such as I_{cd} and ρ_{dep} are from TORBEAM. As indicated by the vertical dashed black line in figure 6.19, the simulations (except the magenta case that will be discussed later) start from $t = 2$ s with $w = 7$ cm, along with fixed $a_3 = 1$, $a_4 = 0.6$, $a_5 = 0.9$, $\bar{\rho}_{mn}\Delta'_0 = 0$ and $w_{de} = 2.5$ cm (with $\chi_{\parallel,mn} \approx 2.5 \times 10^7$ m²/s and $\chi_{\perp,mn} \approx 2$ m²/s in equation (3.6)). Similar to the simulations of TCV discharges, the w -dependence of $\bar{\rho}_{mn}\Delta'$ (equation (3.25)) is included in simulations of this AUG discharge, with $\alpha = 15$. The values of $\bar{\rho}_{mn}\Delta'_{sat}$ and a_2 used are discussed below.

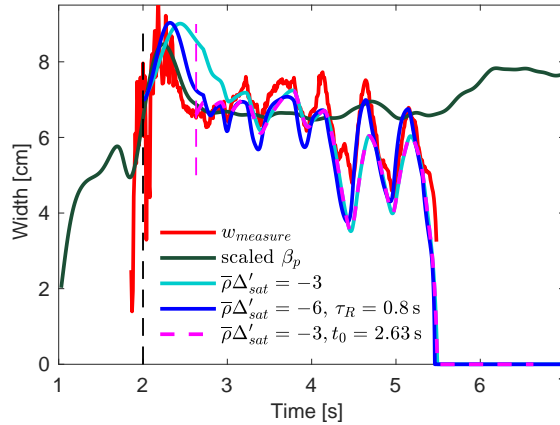


Figure 6.19. Island width evolution of AUG #30594 (figure 6.18): measurement (red), β_p scaled onto the same plot (green), simulation starting from $t = 2$ s and with $\bar{\rho}_{mn}\Delta'_{sat} = -3$ (cyan), simulation with $\bar{\rho}_{mn}\Delta'_{sat} = -6$ and modified τ_R (blue), and simulation starting from $t = 2.63$ s and with $\bar{\rho}_{mn}\Delta'_{sat} = -3$ (dashed magenta).

In the first simulation (cyan curve in figure 6.19), $\bar{\rho}_{mn}\Delta'_{sat} = -3$ (i.e. $-m$) together with $a_2 = 2.6$ are used, which fits well the oscillations and full stabilization of the NTM. However, the fast change of w along with the fast ramp-up and ramp-down of the NBI power (thus β_p as indicated by the green curve) at the beginning of the discharge cannot be recovered. A possible explanation for this is the uncertainty of the effective τ_R (equation (6.1)) used in the simulations, which may result from the computation of τ_R itself that is affected by local T_e and n_e , or from the uncertainty of the $\bar{\rho}_{mn}\Delta'_{sat}$ (and a_2) used.

Further simulations have been performed to investigate this effect, firstly by increasing the amplitude of $\bar{\rho}_{mn}\Delta'_{\text{sat}}$ (and a_2). This leads to an effectively smaller τ_R and faster NTM dynamics, as seen by dividing $\bar{\rho}_{mn}\Delta'_{\text{sat}}$ on both sides of the MRE (equation (6.1)). τ_R computed based on local T_e and n_e is then adjusted to fit better the measurements. With a very negative $\bar{\rho}_{mn}\Delta'_{\text{sat}} = -6$ (i.e. $-2m$), large $a_2 = 3.4$ and a large modification of the computed τ_R (0.8s instead of 2s), the simulation starting from $t = 2$ s can fit better the measurements, as indicated by the blue curve in figure 6.19. However, this already deviates from the standard set of parameters used in the simulations and involves too large modification of computed τ_R , which may not be physical.

A more feasible explanation is that there are transient effects caused by the fast change of central NBI power that are not included in the present MRE, for example, a large change of plasma rotation profiles, wall conditions, etc. As a further test, one simulation starting from $t = 2.63$ s, i.e. without the fast change of NBI power and right before turning on the first control launcher $L5$, is shown by the dashed magenta curve. The simulation fits reasonably the measurements with more standard $\bar{\rho}_{mn}\Delta'_{\text{sat}} = -3$ (i.e. $-m$) and $a_2 = 2.6$, and without any adjustment of the computed τ_R . $\bar{\rho}_{mn}\Delta'_{\text{sat}} = -3$ will be used in the simulations with RT-MRE discussed below.

Adaptation of a_2

As a further test of the functionalities of the RT-MRE presented in previous sections, similar simulations as in TCV #56171 have been performed for AUG #30594. Firstly, the capability of adapting a_2 is illustrated in figure 6.20. Fixed $a_3 = 1$, $a_4 = 0.6$, $a_5 = 0.9$, $\bar{\rho}_{mn}\Delta'_0 = 0$ and $\bar{\rho}_{mn}\Delta'_{\text{sat}} = -3$ are set, as discussed before.

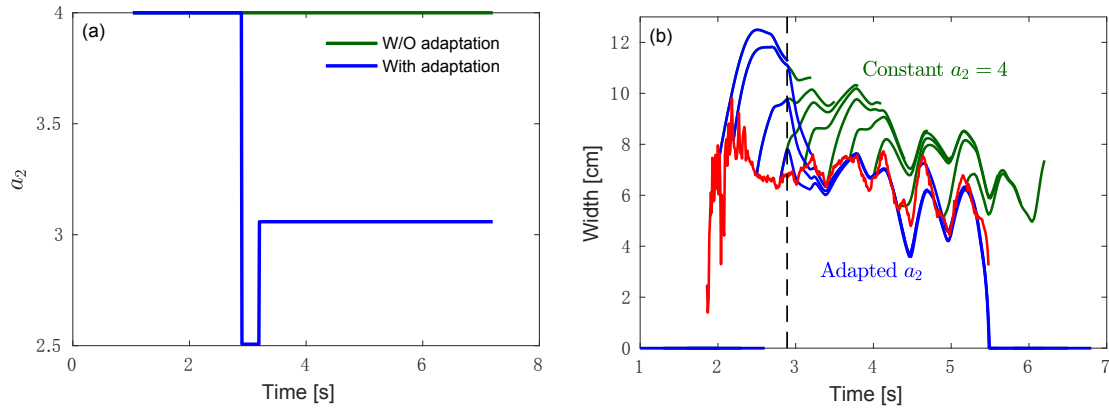


Figure 6.20. Illustration of adapting a_2 with RT-MRE for AUG #30594 (figure 6.18): (a) a_2 traces; and (b) w from measurements and simulations. Blue - simulation with a_2 adaptation; green - with fixed $a_2 = 4$; red (in (b)) - measurement.

Following the discussions in section 6.4.1, a_2 can be adjusted by comparing the simulated and measured $w(t)$ once the measured w reaches w_{sat} . In figure 6.20, simulations are performed at

each t_N (every 50 ms), tracing $w(t)$ during $t \in [t_N - 1, t_N]$ and comparing with corresponding measurements. To better illustrate the capability, a_2 is initialized with a high value 4 (figure 6.20 (a)), which would overestimate w , as indicated by the green traces in figure 6.20 (b). With the adaptation, a_2 is automatically adjusted at $t \approx 2.9$ s and 3.2 s, respectively (vertical dashed black lines in figure 6.20 (b)), when the measured w is detected to be stationary during $t \in [t_N - 1, t_N]$ (with a standard deviation less than 5%) and the simulated $w(t)$ deviates from the measurements by $\chi > 5\%$. As discussed in section 6.4.1, the thresholds for tuning a_2 can be specified by the user before a discharge. Simulations with the adapted a_2 fit better the measurements, as shown by the blue traces in figure 6.20 (b).

EC power required for NTM stabilization

As another example, P_{req} of obtaining marginal full stabilization has been evaluated for AUG #30594, following the same methods as described in section 6.4.3. $\rho_{\text{req}} = \rho_{mn}$ and $\rho_{\text{req}} - \rho_{mn} = -0.03$ are used, as shown by the blue and red curves in figure 6.21, respectively. It can be seen that $P_{\text{req}} \approx 1$ MW if the control beam is perfectly aligned with the mode location and $P_{\text{req}} \approx 2.5$ MW if misaligned by -0.03 . This is in accordance with the experimental observations shown in figure 6.18: a total power of about 2.2 MW (from three co-ECCD beams) is used to fully stabilize the 3/2 mode at $t \approx 5.5$ s, with the center of the deposition locations of control beams misaligned inside $q = 3/2$ surface by about -0.03 .

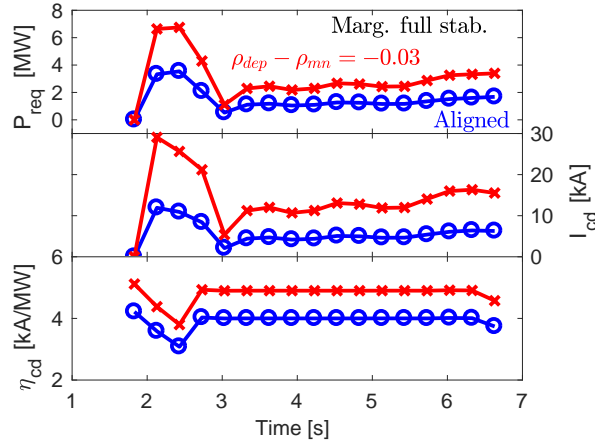


Figure 6.21. Simulations base on AUG #30594 (figure 6.18). Top panel: P_{req} for marginal full stabilization with perfect alignment (blue with circles) and $\rho_{\text{req}} - \rho_{mn} = -0.03$ (red with crosses), respectively. Middle panel: corresponding I_{cd} , with the same line type as in the top panel. Bottom panel: η_{cd} of the two cases.

6.4.6 Foreseen implementation of the RT-MRE in the PCS

The RT-MRE, verified with extensive simulations shown in previous sections, are foreseen to be implemented in the PCS and tested in experiments in the near future. In this section, the

implementation of the RT-MRE, or more specifically, the arrangement of various capabilities of the RT-MRE in the generic PCS presented in section 6.3.1 will be proposed.

Based on the understanding of the PCS and the RT-MRE capabilities, a first proposal is made within the scope of this thesis, as illustrated in figure 6.22. It is proposed to put the core MRE solver based on equation (6.1) as a stand-alone block outside the PCS, e.g. in an external library that can be linked with the PCS. This makes it easier to update the core model when necessary, and more importantly, any modifications of the model are synchronized in all the places automatically. Blocks that make use of the core MRE solver but remain generic can also be placed as external library blocks. For instance, function to estimate P_{req} and function to evaluate $w(t)$ evolutions can both be put in the library - their interfaces and functionalities remain generic.

These external library blocks can then be called by the PCS for different purposes, with corresponding set of inputs. In the *plasma and actuator state reconstruction* of the generic PCS (figure 6.2), two new blocks, namely the *MRE observer* and *MRE predictor* can be added to gain extra information about the plasma and actuator states from the MRE, before sending these states to the task-based *tokamak-agnostic layer*. The MRE observer, as indicated by its name, takes the information from *previous and present* time steps as well as relevant configuration parameters as inputs, and outputs information about the adapted coefficients (e.g. a_2) to be used, the uncertainty of the computed ρ_{dep} of a given EC launcher, the possible error of beam-mode alignment, etc. The MRE predictor, on the other hand, uses *present and future* information to predict the $w(t)$ evolutions and corresponding P_{req} that would be needed. These outputs are important for the decision-making of the supervisory controller, e.g. higher priority may be assigned to the NTM stabilization task, NTM prevention task can be activated, or disruption avoidance can be initialized if the supervisory controller foresees a dangerous mode based on these information.

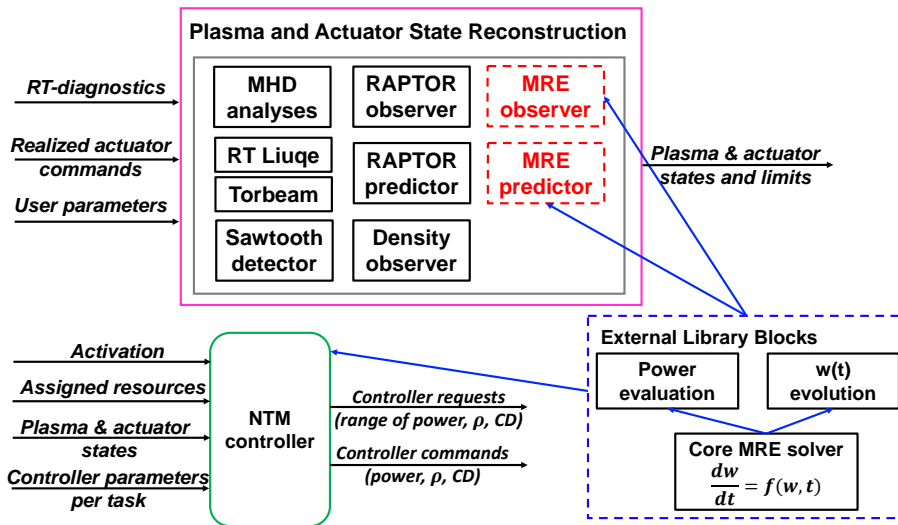


Figure 6.22. Implementation of the RT-MRE in the generic PCS shown in figure 6.2.

The generic NTM controller will be more intelligent as well: the P_{req} to perform a given task (e.g. 3/2 NTM stabilization, 2/1 NTM prevention, etc.) can be estimated by calling the external power evaluation library block. This will in turn facilitate the actuator allocation by the actuator manager and makes the best use of available resources to fulfill multiple tasks. It is also worth noting that the separation of a tokamak-agnostic layer and the generic feature of the new PCS make it very convenient to include the new functionalities of RT-MRE.

6.5 Summary and outlook

This chapter presented recent progress on the real-time (RT) control of NTMs and its integration with other control algorithms in TCV. Two main elements of reliable RT NTM control, namely the beam-mode alignment and the required EC power have been addressed. A new generic NTM controller has been built thanks to the development and implementation of a task-based generic plasma control system (PCS) framework discussed in section 6.3.1. The controller shares the same interface as the other controllers and is able to perform NTM control tasks by tracking the target location along with a small sinusoidal sweeping and by automatically increasing power request if the assigned power is not sufficient.

The capabilities of the NTM control algorithm have been demonstrated by RT NTM control and integrated control experiments on TCV. A more intelligent NTM controller will be built in the near future, which has a better knowledge of the power needed to perform a given task. This will be obtained by applying the MRE presented in previous chapters in RT (i.e. RT-MRE), as detailed and demonstrated for the first time in section 6.4. In particular, we have shown that MRE simulations can be adapted in RT (section 6.4.1) and thus accurate coefficients are not needed, assuming accurate enough RT measurements of island width are available. With a simple method of tracing measured $w(t)$ based on information from previous and present time steps, as discussed in section 6.4.1, MRE coefficients such as Δ'_{shift} and a_2 can be adapted effectively to fit well the measurements. More standard tools such as extended Kalman filter can be easily included in the future to adjust the coefficients systematically.

The RT-MRE has proven to be able to provide valuable information for the overall integrated control. For instance, the supervisory controller can make a better decision on how to continue a discharge by comparing the difference in the power required by partial and full stabilization as well as considering the available actuators. With an idea of the typical island width that causes mode locking (w_{lock}) in a given scenario, corresponding EC power can be evaluated and used in RT to avoid locked modes, by making sure $w_{\text{sat}} < w_{\text{lock}}$. The EC power can also be evaluated to constrain the performance degradation caused by NTMs within the allowed range in a given discharge, based on the relation between w_{sat} and the degradation of the energy confinement time (equation (3.2) in chapter 3) [Chang and Callen 1990]. With a good estimation of P_{req} for preventing NTMs, the supervisory controller may decide to perform NTM stabilization instead of prevention if the P_{req} for preventing NTMs from a given w_{seed} is comparable to that for the full stabilization of NTMs. The prediction of island width

Chapter 6. Real-time NTM control and integrated multi-actuator plasma control in TCV

evolution with the RT-MRE contributes to the decision-making of the supervisory controller. The capabilities of the proposed RT-MRE have been tested comprehensively based on one TCV discharge and one AUG discharge; the RT-MRE proves to work well for these distinct plasma conditions at different tokamaks.

The implementation of the RT-MRE, or more specifically, the arrangement of various capabilities of the RT-MRE in the PCS has been illustrated. The clear separation of different layers and the generic feature of the PCS makes it convenient to add the new capabilities of the RT-MRE to the PCS. The implementation of the RT-MRE in the SCD and corresponding experimental tests will be conducted on TCV in the near future. Implementation and experiments on other tokamaks such as AUG are also foreseen.

7 Conclusions

This thesis focused on the physics and control of neoclassical tearing modes (NTMs) as well as advanced integrated multi-actuator plasma control, which are essential for the high-performance operation of tokamaks.

Given the metastable nature of NTMs, i.e. the fact that a large enough seed island is required for the onset of NTMs, studies on mode onset can facilitate the avoidance of detrimental NTMs. In particular, this thesis (chapter 4) presented a detailed study of the onset of “triggerless” NTMs that stem from unstable current density and safety factor (q) profiles, i.e. the seed islands are provided by classical tearing modes (TMs) with a positive stability index Δ' . This is also relevant for other tokamaks, in particular for hybrid and advanced scenarios [Turco et al. 2018; Koslowski et al. 2001]. This study involves TCV experiments and corresponding simulations with the modified Rutherford equation (MRE), which has been widely used in interpreting island width (w) evolutions [Sauter et al. 1997, 2002c; La Haye 2006; De Lazzari and Westerhof 2009, 2010].

Electron cyclotron heating and current driven (ECH/ECCD) has proven to be a promising candidate in terms of the active control of NTMs in present and future tokamak devices, given its highly localized and flexible deposition [Isayama et al. 2003; La Haye 2006; Felici et al. 2012; Maraschek 2012; Henderson et al. 2015; Kong et al. 2019, and references therein]. Before going into the details of real-time (RT) control aspects in chapter 6, chapter 5 presented more physics-oriented experimental and numerical investigations of the dynamics of NTM island width under different plasma conditions, especially with varying power and/or deposition locations of the off-axis EC beams. Based on these studies of the onset and dynamic evolution of triggerless NTMs, a new model for Δ' (equations (3.25) and (4.2)), thus a new comprehensive MRE (equation (3.3)) has been developed in this thesis. It allows consistent simulations of all types of TMs and NTMs using the same model, and works for different plasma conditions and settings, including the stabilization and prevention of NTMs with ECH/ECCD.

The studies on NTM physics in turn facilitated a better RT control of NTMs, as discussed in chapter 6. For instance, ranges of the coefficients involved in the MRE have been well

determined through extensive simulations in chapters 4 and 5. This has contributed to the development of a RT-capable MRE module that is able to estimate the required EC power for NTM control and predict the evolution of NTMs in RT for the first time (section 6.4). These information from the RT-MRE is not only important for NTM control, but also for the overall integrated control where generic plasma state monitoring, supervision and actuator management are involved.

7.1 On the triggerless onset of NTMs

Triggerless NTMs have been observed in different tokamaks and plasma scenarios [Reimerdes et al. 2002; Fredrickson 2002; Brennan et al. 2007; Gerhardt et al. 2009; Ji et al. 2016; Turco et al. 2018]. In TCV, this type of NTMs have been observed reproducibly in low-density discharges with strong near-axis co-ECCD [Reimerdes et al. 2002; Nowak et al. 2014; Lazzaro et al. 2015; Kim 2015], providing an excellent opportunity for a systematic study of these modes. In this respect, dedicated experiments with various density and EC power levels and interpretative simulations with the MRE have been performed (chapter 4). These studies have contributed to the development of a model for the stability index at $w = 0$, i.e. Δ'_0 . Together with the w -dependence of Δ' (equation (3.25)), it provides a complete model of Δ' for all w (including $w = 0$) and has reproduced self-consistently the entire time-evolution of triggerless NTMs, from the onset as a TM at $w = 0$ to its saturation as an NTM up to w_{sat} under various plasma conditions.

An unexpected density dependence of the onset of triggerless NTMs has been newly observed along with the experiments in TCV, showing a certain range of density within which these NTMs can occur. The range is found to broaden with increasing central co-ECCD power and lower plasma current. The underlying physics of the observed phenomena has been explored using the Δ'_0 model, developed with a different set of experiments and simulations. It is found that the density range results from two competing effects: the density and plasma current dependence of the stability of ohmic plasmas (being more unstable at higher density and/or lower plasma current) and the monotonic density dependence of the ECCD efficiency (driving less current at higher density hence less destabilizing). The possible effects of plasma rotation on the onset of these NTMs in TCV have been explored through dedicated power-scan and density-scan experiments with careful rotation measurements. No noticeable change of rotation has been observed before and around the onset threshold of these NTMs, confirming that rotation is not playing an important role in the onset of NTMs and it is Δ'_0 that determines the onset of these modes.

The main effects and ranges of various parameters in the MRE have been clarified through the simulations. Especially, a_2 , the coefficient affecting the contribution of the perturbed bootstrap current (equation (3.4)), is found to dominate the amplitude of the growth rate of w at medium to large w , and can be constrained well by comparing with the experimental data (section 4.3.1). A “lull” region characterized by a very slow growth rate at a range of w has been

observed in simulations with certain sets of parameters (section 4.3.1), which could explain a similar behavior firstly described in [Brennan et al. 2003]. Further improvement of the Δ'_0 model is foreseen. For example, a first attempt has been made to separate the contribution of heating to the onset of these NTMs with available data (section 4.5.2). Improved diagnostics with better measurements of w at very small w would allow a better quantification of different effects, e.g. the contribution of the polarization current, the existence of the lull region, etc.

7.2 On the stabilization and prevention of NTMs

The physics of the stabilization and prevention of NTMs with off-axis EC beams has been explored in chapter 5. The simple model of Δ'_0 developed in chapter 4, together with the MRE presented in section 3.4, has been applied to simulate a rather complicated set of experiments (NTM prevention, stabilization, sweeping, co-ECCD, counter-ECCD, ECH, etc.) with very similar fixed coefficients. These simulations have tested further the theoretical model used and constrained better the coefficients in the MRE. For example, simulations of a series of NTM stabilization experiments with co-ECCD, counter-ECCD or ECH have quantified the contribution of heating and current drive to the stabilization of 2/1 NTMs, and estimated the range of corresponding coefficients in the MRE (section 5.5). Pure heating has proven to have a comparable effect as current drive on NTM stabilization in our test discharges, in accordance with theoretical predictions for relatively small machines [Bertelli et al. 2011].

As another method of NTM control, the prevention of 2/1 NTMs by means of preemptive ECCD has also been explored. The prevention effect is found to mainly come from the local effects of heating and current drive of off-axis EC beams, as well as the stabilizing effect from favorable curvature, instead of a global change of the classical stability of plasmas. The small sinusoidal sweeping of the radial deposition location of the control EC beam around the target mode location has proven to be effective for both NTM stabilization and NTM prevention cases. Along with the sweeping, power-ramp experiments have shown that NTM prevention is much more efficient than NTM stabilization in the test discharges, in terms of the minimum EC power required. It is worth emphasizing that this better physics understanding of NTM stabilization and prevention, including local sweeping or not, has been obtained thanks to the simulations with our new complete MRE.

The effects of beam-mode alignment on NTM evolution have been studied in detail. It has been observed that misalignment towards the plasma center can be destabilizing, due to a larger increase of β_p and Δ' , as well as a decrease of the stabilizing effects from the EC beams caused by the misalignment. Small misalignment towards the plasma edge, on the other hand, can lead to partial stabilization, or at least no destabilization effects have been observed. Given the difficulty of keeping perfect beam-mode alignment, this observation indicates that it is better to align the central location of the control beam slightly outside the target rational surface, instead of inside, and add a small sweeping around that location. However, note that this could be different in future devices like ITER and DEMO, where β_p and Δ' may not be

affected much by the local EC beams.

7.3 On the real-time NTM control and integrated plasma control

In addition to the physics-oriented studies presented in chapters 4 and 5, control-oriented studies have been carried out within the scope of this thesis, concerning both the RT control of NTMs and the integrated multi-actuator plasma control in TCV (chapter 6).

Two main elements of the reliable RT control of NTMs, namely the beam-mode alignment and the required EC power have been addressed. A new generic NTM controller has been built thanks to the development and implementation of a task-based generic plasma control system (PCS) framework [Blanken et al. 2019; Vu et al. 2019], involving advance plasma state monitoring, supervision and actuator management algorithms (section 6.3.1). The controller shares the same interfaces as the other controllers and is able to perform NTM control tasks by tracking the target mode location along with a small sinusoidal sweeping, and by automatically increasing its power request if the assigned power is not sufficient. The capabilities of the NTM control algorithm have been demonstrated by RT NTM control and integrated control experiments in TCV. A more intelligent NTM controller that has a better knowledge of the power needed to perform a given task will be built in the near future, based on a novel RT-capable MRE module newly developed within the scope of the thesis.

The RT-MRE has proven to be able to provide valuable information for the overall integrated control as well (section 6.4). For instance, the better estimation of the required power is useful for the actuator manager to optimize actuator allocations in RT; the prediction of island width evolution contributes to the decision-making of the supervisory controller. The capabilities of the proposed RT-MRE have been tested comprehensively based on one TCV discharge and one AUG discharge, proven to work well for these distinct plasma conditions. More importantly, we have demonstrated that MRE simulations can be easily adapted in RT, thus accurate coefficients are not needed, assuming that accurate enough RT measurements of w are available. The implementation of the RT-MRE, or more specifically, the arrangement of various capabilities of the RT-MRE in the PCS has been illustrated (section 6.4.6). The clear separation of different layers and the generic feature of the PCS make it convenient to add the new functionality of the RT-MRE to the PCS.

A A sensitivity study of Δ'

A.1 Introduction

As discussed in previous chapters, Δ' determines the onset of triggerless NTMs, but its value is very difficult to be estimated accurately or consistently given the uncertainties in equilibrium reconstructions and the sensitivity of Δ' to the details of q profiles. To gain some qualitative idea of the dependence of Δ' on local parameters at the considered rational surface such as the radial location (ρ_{mn}) and magnetic shear (s_{mn}), a dedicated sensitivity study has been performed based on artificial q profiles and perturbations. As will be seen in this appendix, this study meanwhile highlights the importance of global effects (i.e. with fixed local parameters) on Δ' .

The basic q profile used is $q(\rho) = 4.4\rho^2 - 0.6\rho + 1.2$, i.e. with $q_0 \equiv q(\rho = 0) = 1.2$, $\rho_{21} = 0.5$, $s_{21} = 0.95$, $ss_{21} = 1.208$ and $\bar{\rho}_{21}\Delta' = 3.23$, where ρ here is the normalized radial location with respect to $a = 0.24$ m, ss_{21} the “shear of the shear” at the $q = 2$ surface defined as $ss_{mn} = \frac{\rho}{s} \frac{ds}{d\rho} |_{mn}$, $\bar{\rho}$ the radial location in meter (i.e. $\bar{\rho} = \rho a$) and Δ' the stability at the $q = 2$ surface for simplicity. Analytical perturbations are then added to this basic q profile and corresponding $\bar{\rho}_{21}\Delta'$ can be calculated based on the definition of Δ' :

$$\Delta' = \lim_{\varepsilon \rightarrow 0} \frac{\frac{\partial \psi}{\partial \rho} |_{\rho_{mn} + \varepsilon} - \frac{\partial \psi}{\partial \rho} |_{\rho_{mn} - \varepsilon}}{\psi(\rho_{mn})}, \quad (\text{A.1})$$

where $\varepsilon > 0$ and ψ refers to the perturbed helical flux computed by [Wesson 2004]

$$\frac{d^2 \psi}{d\rho^2} + \frac{d\psi}{\rho d\rho} - \left(\frac{m^2}{\rho^2} + \frac{\frac{2\pi}{\rho} \frac{\partial j}{\partial \rho}}{\frac{1}{q} - \frac{n}{m}} \right) \psi = 0, \quad (\text{A.2})$$

assuming cylindrical geometry and a normalization $\frac{2\pi B_0}{\mu_0 R_0} = 1$. j in equation (A.2) refers to current density and is estimated by

$$j \approx \frac{B_0}{\mu_0 R_0} \left(\frac{2}{q} - \frac{\rho}{q^2} \frac{dq}{d\rho} \right), \quad (\text{A.3})$$

under the large aspect ratio assumption.

A.2 Scan of the radial location of localized perturbations

In each test presented in this section, a localized quadratic or cubic type perturbation with a full amplitude (amp) of 0.15 and full width (w_{full}) of 0.1 is added to the basic q profile. Some examples of the perturbations and resulting q profiles are shown in figure A.1 (with only one perturbation added in each test). Both positive ($amp > 0$, not shown in figure A.1) and negative ($amp < 0$, figure A.1 (a)) quadratic perturbations have been tested; for the cubic case (figure A.1 (b)), $amp > 0$ means that the amplitude of the perturbation is positive for $\rho > \rho_{center}$, where ρ_{center} is the central location of the perturbation added.

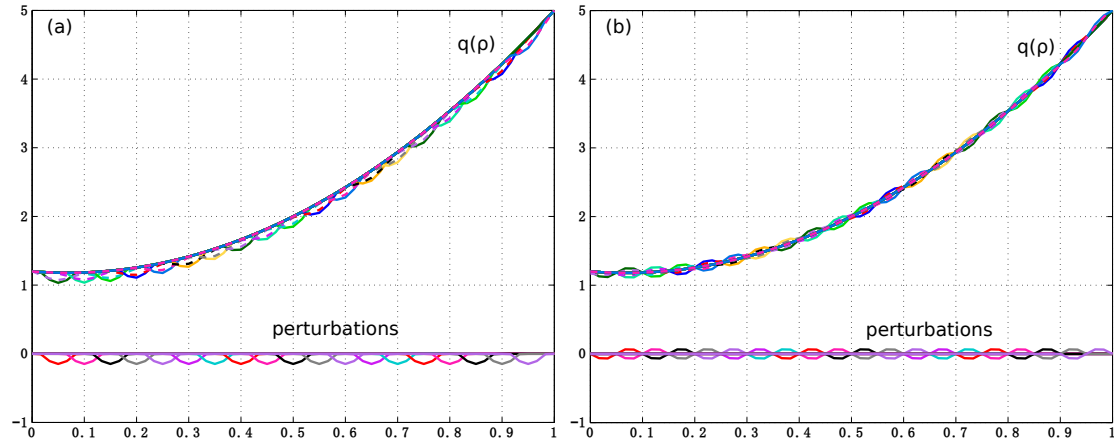


Figure A.1. Examples of the perturbation added and the resulting q profile: (a) $amp = -0.15$, $w_{full} = 0.1$, quadratic; and (b) $amp = 0.15$, $w_{full} = 0.1$, cubic.

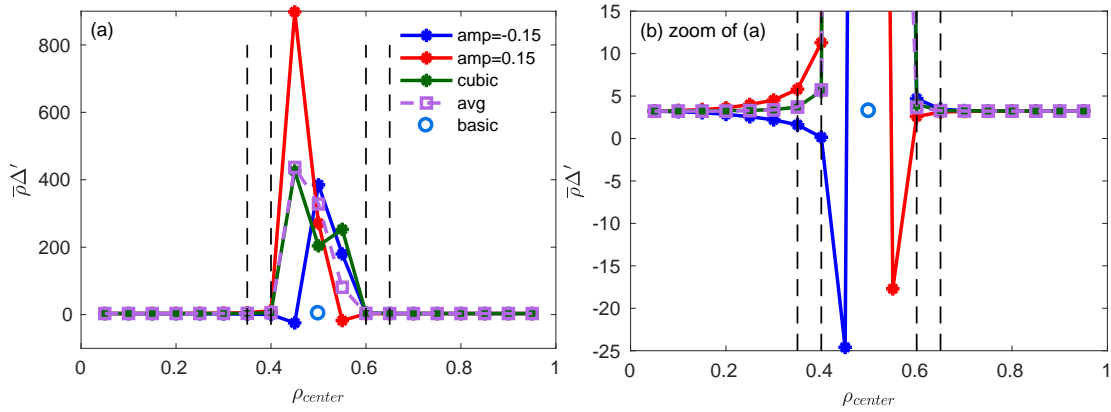


Figure A.2. Resulting $\bar{\rho}_{21}\Delta'$ of the location scan shown in figure A.1.

The computed $\bar{\rho}_{21}\Delta'$ is summarized in figure A.2. It can be seen that when ρ_{center} is within $[0.4, 0.6]$ (i.e. with $|\Delta\rho| \leq 0.1$, where $\Delta\rho \equiv \rho_{center} - \rho_{21}$), there is a sharp change of $\bar{\rho}_{21}\Delta'$,

A.2. Scan of the radial location of localized perturbations

indicating large effects of these local perturbations on the stability. The sum of the positive and negative quadratic cases (dashed purple curve with squares in figure A.2) matches quite well the cubic case (solid green).

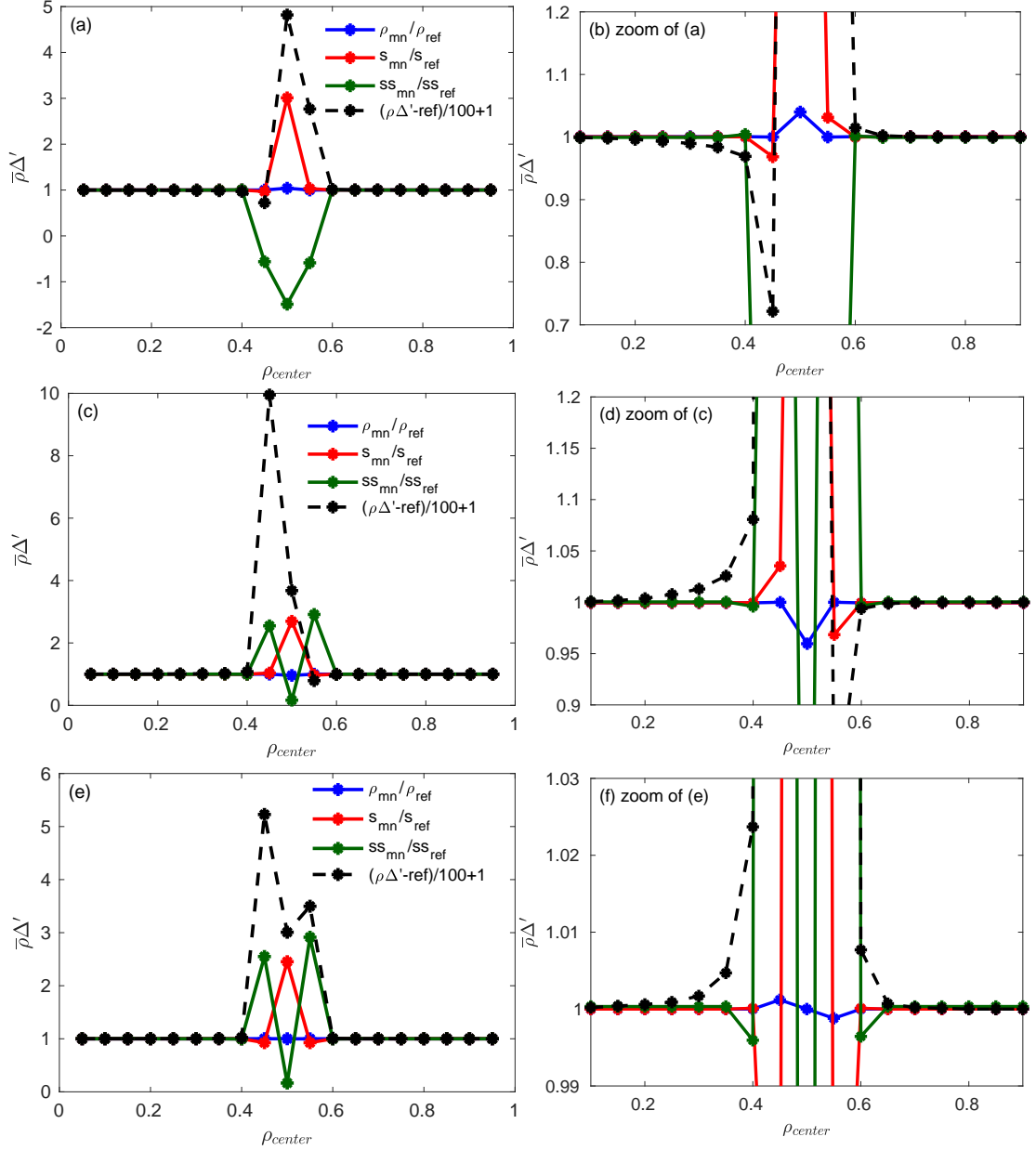


Figure A.3. Normalized local parameters at the $q = 2$ surface: (a) with quadratic perturbation and $amp = -0.15$ (figure A.1 (a)); (b) a zoom of (a); (c) with quadratic perturbation and $amp = 0.15$; (d) a zoom of (c); (e) with cubic perturbation and $amp = 0.15$ (figure A.1 (b)); (f) a zoom of (e).

To find out the key parameters that dominate the observed trend of $\bar{\rho}_{21}\Delta'$ in figure A.2, several normalized local parameters at the $q = 2$ surface, namely ρ_{21}/ρ_{ref} , s_{21}/s_{ref} and ss_{21}/ss_{ref} ,

Appendix A. A sensitivity study of Δ'

are depicted in figure A.3, with $\rho_{ref} = 0.5$, $s_{ref} = 0.95$ and $ss_{ref} = 1.208$ taken from the basic q profile (no perturbation). $\bar{\rho}_{21}\Delta'$ has been rescaled as “ $(\bar{\rho}_{21}\Delta' - \bar{\rho}_{21}\Delta'_{ref})/100 + 1$ ” and plotted in figure A.3 (dashed black curves), with $\bar{\rho}_{21}\Delta'_{ref} = 3.23$ taken from the basic q profile.

One can see that when the perturbation moves towards the $q = 2$ surface from $\rho < 0.35$ or $\rho > 0.65$, $\bar{\rho}_{21}\Delta'$ varies slowly whereas s_{21} , ρ_{21} and ss_{21} remain constant. This indicates that it is the global change of q that dominates the variations of Δ' in this case. Once the perturbation reaches closer (e.g. with $\rho_{center} \in [0.35, 0.4]$ or $[0.6, 0.65]$), ss_{21} (green curves) starts to vary while s_{21} and ρ_{21} still remain constant. It seems that $\bar{\rho}_{21}\Delta'$ increases with the increase of ss_{21} , for the case with $ss_{21} > 0$ (e.g. figure A.3 (c) and (e)). In (a), $\bar{\rho}_{21}\Delta'$ shows the same trend as ss_{21} for $\rho = [0.4, 0.45]$ (i.e. both decreasing), but then s_{21} starts to change as well and ss_{21} goes to negative values, and the trend varies. When the perturbation reaches even closer to the rational surface, ρ_{21} starts to change as well. The effects of ρ_{21} , s_{21} and ss_{21} on $\bar{\rho}_{21}\Delta'$ will be further discussed along with the amplitude and width scan of localized perturbations presented in section A.3.

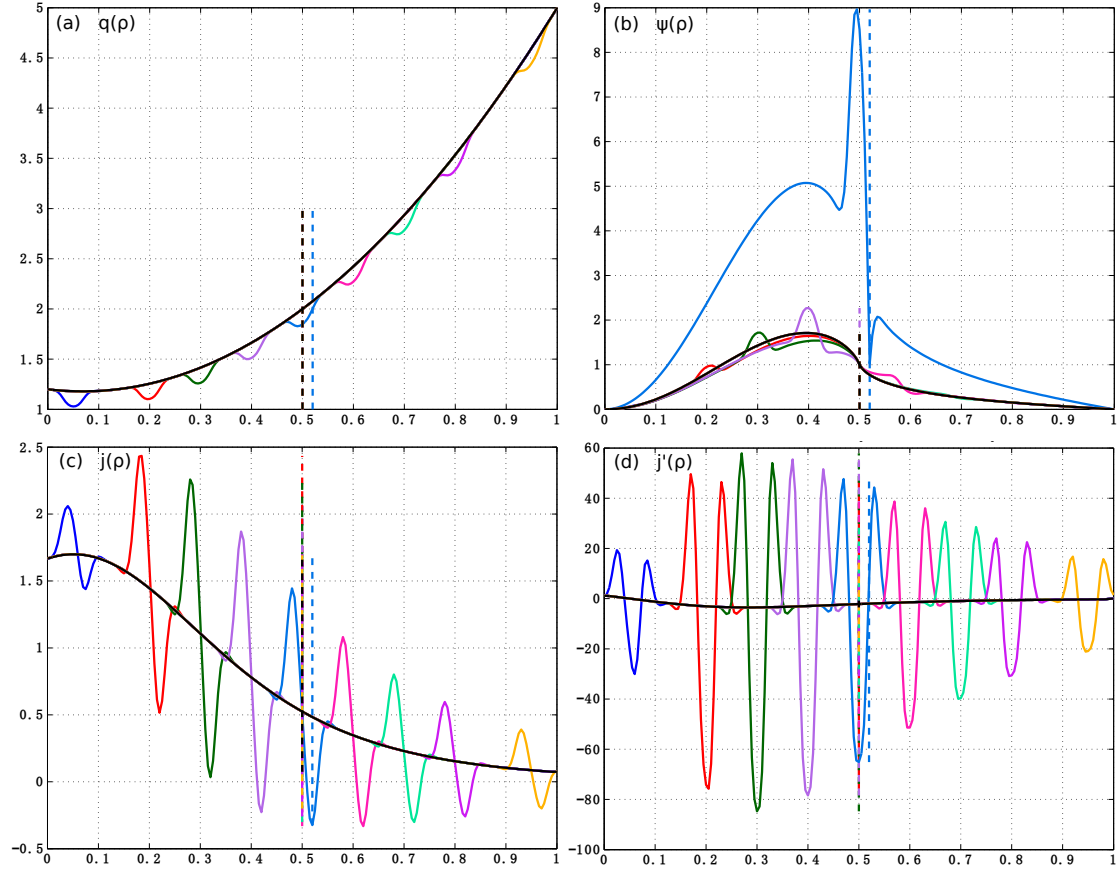


Figure A.4. ψ , j and j' profiles for tests with quadratic perturbations shown in (a). Each curve in (b) - (d) corresponds to the q profile with the same color in (a).

To have an idea of the resulting ψ profiles in these tests, several examples are shown in figure

A.2. Scan of the radial location of localized perturbations

A.4 and figure A.5, taken from the scan with quadratic perturbation ($amp = -0.15$) and cubic perturbation ($amp = 0.15$), respectively. The input q profiles and corresponding j (and $j' \equiv \frac{dj}{d\rho}$) profiles are depicted as well. The solid black traces in figure A.4 and A.5 represent relevant values for the case without any perturbation (i.e. from the basic q profile). ρ_{21} of each case is indicated by a vertical dashed line with the same color.

It can be seen that there is a larger perturbation on ψ profile when the perturbation gets closer to the $q = 2$ surface and the change of ψ is dramatic (not monotonic anymore around ρ_{21}) once the perturbation is centered at ρ_{21} . This is in accordance with the $\bar{\rho}_{21}\Delta'$ results shown in figure A.2, as expected. It is also seen that j is very sensitive to the perturbations of q profile, based on its dependence on q and q' (equation (A.3)), and in some cases $j < 0$ is involved. To isolate the possible effects of negative values on the results, another set of ρ_{center} scan has been performed with much smaller amplitude of perturbations (with $amp = 0.015$ instead of 0.15), for both the quadratic and cubic cases. Similar results as presented in this section have been obtained, not detailed here for conciseness.

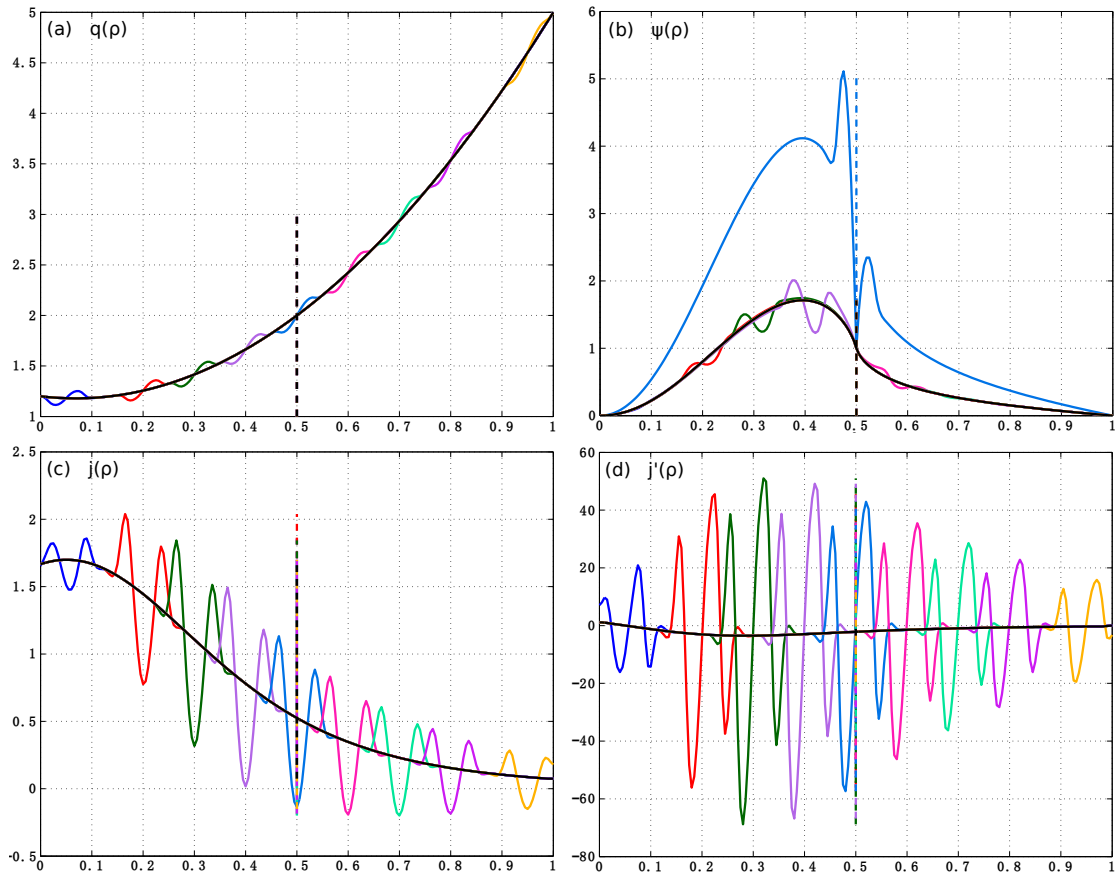


Figure A.5. ψ , j and j' profiles for tests with cubic perturbations shown in (a). Each curve in (b) - (d) corresponds to the q profile with the same color in (a).

A.3 Scan of the amplitude and width of localized perturbations

The scan of ρ_{center} presented in the previous section distinguishes two different regions that have different level of effects on $\bar{\rho}_{21}\Delta'$: the region “far” from ρ_{21} (with $\rho_{\text{center}} < 0.35$ or $\rho_{\text{center}} > 0.65$, i.e. $|\Delta\rho| > 0.15$) and the region around the $q = 2$ surface (e.g. with $\rho_{\text{center}} = \rho_{21}$). This section focuses on investigating the effects of the amplitude and width of perturbations on Δ' , with ρ_{center} at these two different regions, respectively.

A.3.1 Perturbation scan near the center or edge

As illustrated in figure A.6, perturbation scans have been performed with ρ_{center} far away from ρ_{21} , i.e. near the center or edge. *Quadratic-like* perturbations have been used in this section, to be comparable with the *cubic-like* perturbations used in section A.3.2 (figure A.12).

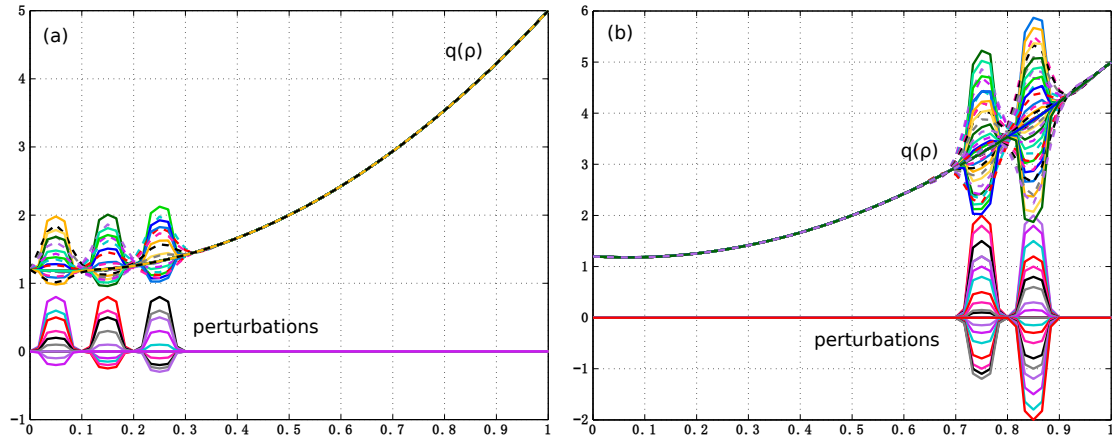


Figure A.6. Examples of the perturbations added (with different ρ_{center} , amplitude or width in each test) and the resulting q profiles: (a) perturbations near the center; (b) near the edge.

$\bar{\rho}_{21}\Delta'$ of a series of amplitude scan with $w_{\text{full}} = 0.1$ (i.e. the same as used in the ρ_{center} scan discussed in the previous section) is summarized in figure A.7, where different curves represent different perturbation amplitude, with the corresponding *amp* noted beside each curve in the same color. The right plot in figure A.7 is a zoom of the left plot around the tests near the edge. It can be seen that the perturbation near the center has a stronger influence on $\bar{\rho}_{21}\Delta'$ than that near the edge, though similar normalized amplitude of perturbation $\frac{\text{amp}}{q_{\text{local}}}$ has been used in both cases, where q_{local} is the local q value at ρ_{center} .

As different ρ_{center} is also involved in this series of tests, it is interesting to compare these results with the ρ_{center} scan shown in the previous section - marked by the open circles with corresponding colors (with the same *amp*). It can be seen that these results largely overlap, confirming that the quadratic-like shapes used here are similar to the quadratic ones presented before. In accordance with previous observations, the variation of $\bar{\rho}_{21}\Delta'$ (with respect to the reference value of the basic q profile, horizontal dashed black line in figure A.7) becomes

A.3. Scan of the amplitude and width of localized perturbations

larger when ρ_{center} is closer to ρ_{21} .

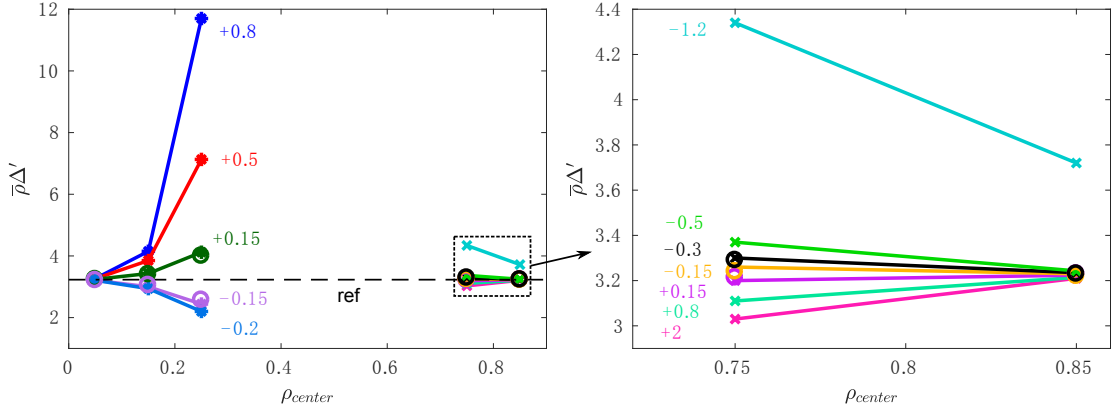


Figure A.7. Dependence of $\bar{\rho}_{21}\Delta'$ on the ρ_{center} and amplitude of quadratic-like perturbations shown in figure A.6. Solid curves with asterisks - scans near the center; with crosses - scans near the edge; numbers with the same color - amplitude of the perturbation; open circles with the same color - results taken from the ρ_{center} scan with quadratic perturbations and the same amplitude (section A.2).

In terms of the dependence of $\bar{\rho}_{21}\Delta'$ on amp , figure A.7 exhibits an increase of the variation of $\bar{\rho}_{21}\Delta'$ with increasing $|\text{amp}|$, as expected. However, an interesting dependence on the sign of amp is observed: for the perturbations near the center, $\text{amp} > 0$ leads to an increase of $\bar{\rho}_{21}\Delta'$ with respect to the reference value (i.e. more destabilizing), whereas for the perturbations near the edge, $\text{amp} > 0$ causes a decrease of $\bar{\rho}_{21}\Delta'$ (i.e. more stabilizing), as illustrated in figure A.8.

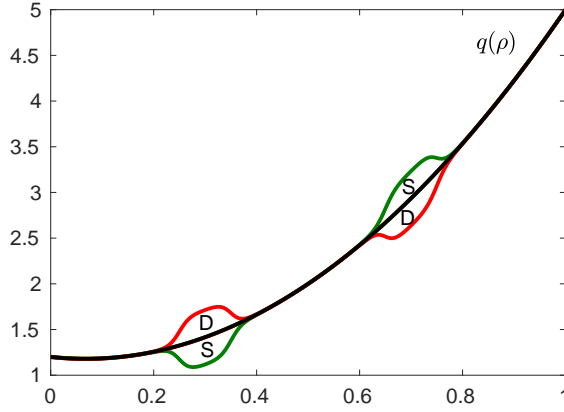


Figure A.8. Illustration of the stabilizing ("S") and destabilizing ("D") effects from different perturbations.

Different widths of the quadratic-like perturbations have been tested along with the amplitude and ρ_{center} scans, as summarized in figure A.9. For the perturbation with a width that covers the perturbed region of two narrower cases, e.g., the case with $\rho_{\text{center}} = 0.1$ and $w_{\text{full}} = 0.2$ (magenta curve with left-pointing triangles) with respect to the case with $\rho_{\text{center}} = 0.05$ and $w_{\text{full}} = 0.1$ (blue trace with asterisks) and with $\rho_{\text{center}} = 0.15$ and $w_{\text{full}} = 0.1$ (red trace with

Appendix A. A sensitivity study of Δ'

asterisks), the trend of $\bar{\rho}_{21}\Delta'$ is in between the two narrower cases and is affected more by the one closer to the $q = 2$ surface (i.e the red trace), indicating that the change of ρ_{center} affects more $\bar{\rho}_{21}\Delta'$ than the width of the perturbation, at least for the perturbations located far from the rational surface. With the same ρ_{center} , the larger the width, the stronger the effect on $\bar{\rho}_{21}\Delta'$, for example the purple curve with right-pointing triangles ($w_{\text{full}} = 0.3$) in comparison to the red curve ($w_{\text{full}} = 0.1$). However, this may be entangled with the fact that with wider width, the perturbation covers more the area closer to the rational surface. It can be further decoupled by the tests with $\rho_{\text{center}} = \rho_{21}$ presented in the next section, where we will see that the variation of $\bar{\rho}_{21}\Delta'$ actually decreases with increasing w_{full} .

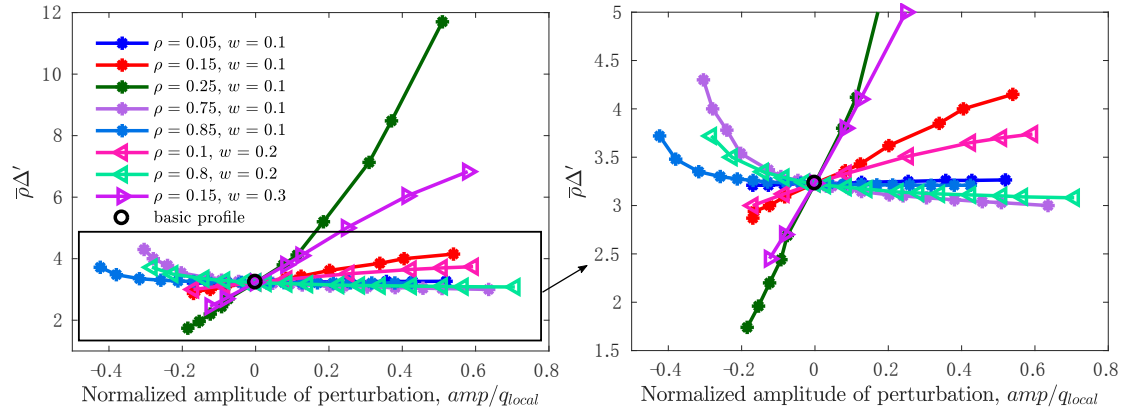


Figure A.9. $\bar{\rho}_{21}\Delta'$ with different amplitude and width of the perturbations far from the $q = 2$ surface.

For these tests with perturbations relatively far from the $q = 2$ surface, local parameters at the $q = 2$ surface remain unperturbed or at most with very small variations, as indicated by the second derivative ss_{21} shown in figure A.10. In combination with $\bar{\rho}_{21}\Delta'$ shown in figure A.9, no clear dependence of $\bar{\rho}_{21}\Delta'$ on ss_{21} can be seen at this stage. In terms of ρ_{21} and s_{21} , they remain unaffected by perturbations near the center (e.g. with $\rho_{\text{center}} = 0.05, 0.15$ or 0.25), so cannot explain the variations of $\bar{\rho}_{21}\Delta'$ observed in figure A.9. This indicates that it is the global effects that play a role in these cases. For the tests with perturbations near the edge, very small variations of ρ_{21} and s_{21} have been observed, but seem to correlate with the change of $\bar{\rho}_{21}\Delta'$ to some extent. To better illustrate this, a function $f(\rho_{mn}, s_{mn})$ defined as

$$f(\rho_{mn}, s_{mn}) = \bar{\rho}_{mn}\Delta'_{\text{ref}} + \text{coeff} \cdot \left(\sqrt{\frac{\rho_{mn}}{\rho_{\text{ref}}} \cdot \frac{s_{mn}}{s_{\text{ref}}}} - 1 \right) \quad (\text{A.4})$$

has been evaluated with the corresponding ρ_{21} and s_{21} of each test and a fixed $\text{coeff} = 300$, as shown by the dashed lines in figure A.11, where the solid curves are $\bar{\rho}_{21}\Delta'$ traces directly taken from figure A.9. $\rho_{\text{ref}} = 0.5$, $s_{\text{ref}} = 0.95$ and $\bar{\rho}_{mn}\Delta'_{\text{ref}} = 3.23$ are taken from the basic case without any perturbations, as discussed before. It seems that this $f(\rho_{mn}, s_{mn})$ can fit well the overall monotonic trend of $\bar{\rho}_{21}\Delta'$. A larger coeff would fit better the values of $amp > 0$ cases but still cannot reproduce the steep change of $\bar{\rho}_{21}\Delta'$ for the cases with $amp < 0$. These

A.3. Scan of the amplitude and width of localized perturbations

local effects (including that from ss_{21}) will be more evident when larger variations of local parameters are involved, for instance with $\rho_{\text{center}} = \rho_{21}$, and will be further discussed in section A.3.2. Nevertheless, the perturbation scan shown in this section, located relatively far from ρ_{21} (i.e. with minimized perturbations on the local parameters), highlights the importance of global effects on $\bar{\rho}_{21}\Delta'$ that are difficult to quantify.

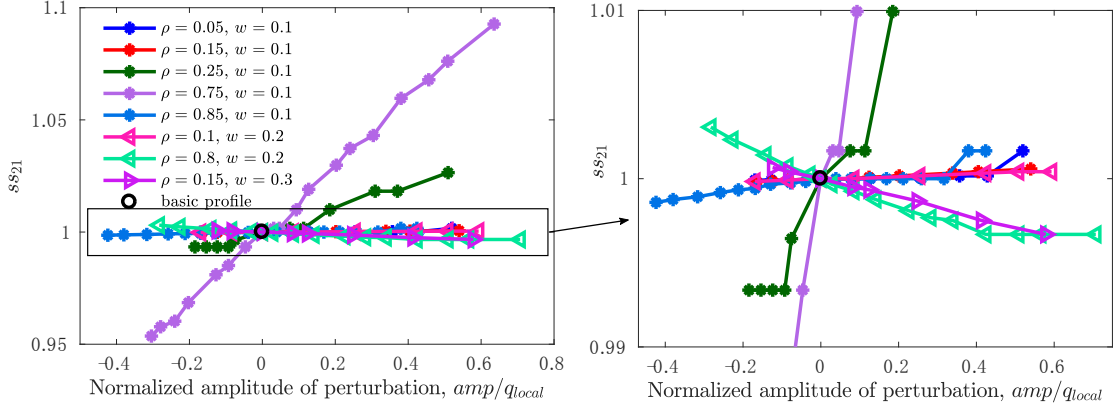


Figure A.10. ss_{21} of the amplitude and width scan with ρ_{center} far from the $q = 2$ surface.

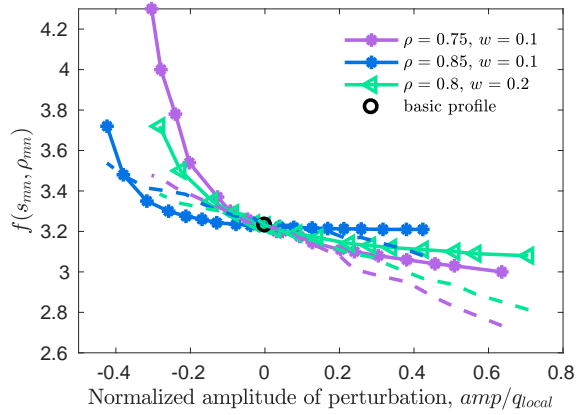


Figure A.11. $\bar{\rho}_{21}\Delta'$ (solid lines) of the amplitude and width scan with ρ_{center} near the edge and corresponding $f(s_{mn}, \rho_{mn})$ (dashed lines) evaluated based on equation (A.4).

A.3.2 Perturbation scan with $\rho_{\text{center}} = \rho_{21}$

This sections presents a series of amplitude and width scan of perturbations centered at ρ_{21} and with cubic-like or quadratic-like shapes, respectively.

With cubic-like perturbations

Examples of the cubic-like perturbations applied and the resulting q profiles are shown in figure A.12. The cubic-like shape is constructed by the combination of three different parts

Appendix A. A sensitivity study of Δ'

(each expressed by an analytical function): the part centered at ρ_{21} , and another two parts connecting to each side of the central part and used to adjust the full width of the perturbation. This facilitates retaining similar local parameters for the scan of w_{full} with fixed amp (e.g. figure A.12 (a)). The sum of the three functions with the basic q profile (i.e. the perturbed q profile) is smoothed to get the final q profile used in the computation of $\bar{\rho}_{21}\Delta'$, as indicated by the dashed lines in figure A.12.

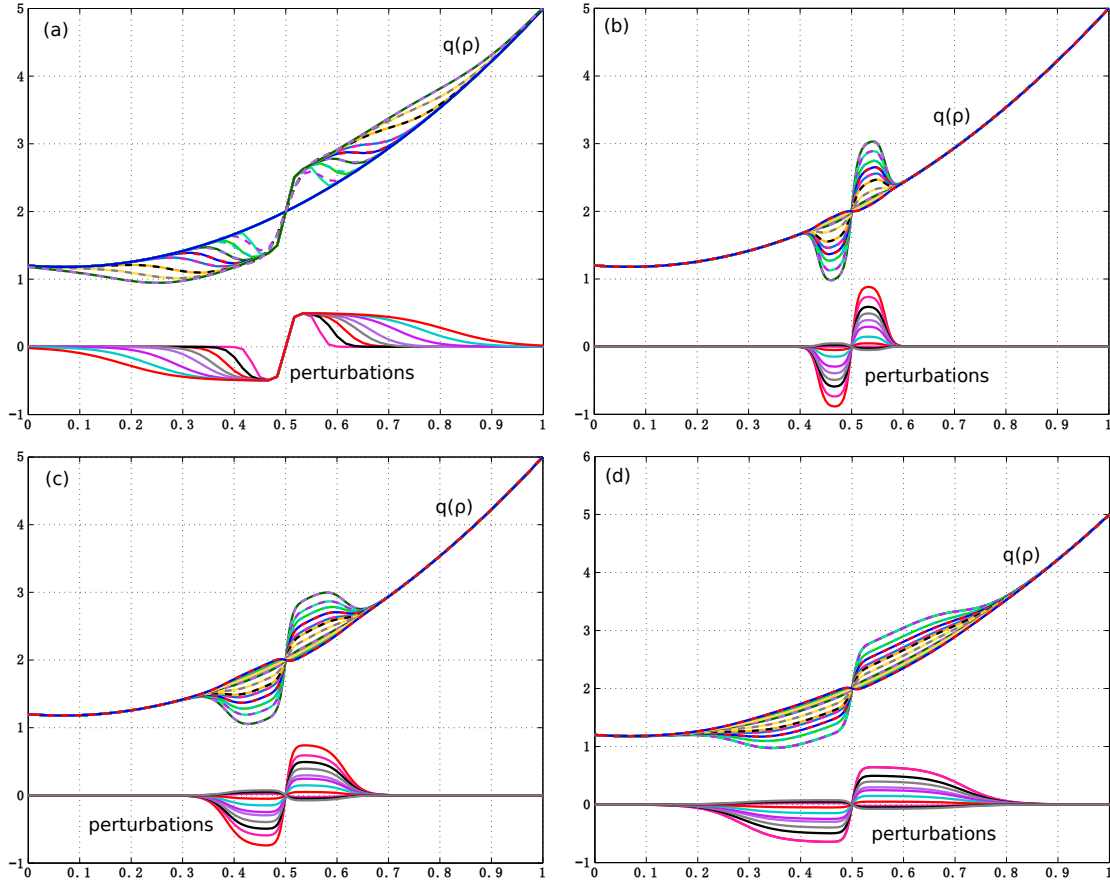


Figure A.12. Examples of the cubic-like perturbations added and the resulting q profiles: (a) perturbations with fixed amp but different w_{full} ; (b) - (d) with fixed w_{full} (wider from (b) to (d)) but different amp .

With the cubic-like perturbations, ρ_{21} remains unperturbed (i.e. keeps 0.5) in this series of tests, as expected. Local s_{21} and ss_{21} are shown in figure A.13: ss_{21} values for tests with different w_{full} largely overlap, while s_{21} exhibits two branches that are caused by the smoothing of q profiles before computation. Nevertheless, the dependence of s_{21} and ss_{21} on amp is very evident, which is interesting to be compared with the trend of $\bar{\rho}_{21}\Delta'$ shown in figure A.14.

A.3. Scan of the amplitude and width of localized perturbations

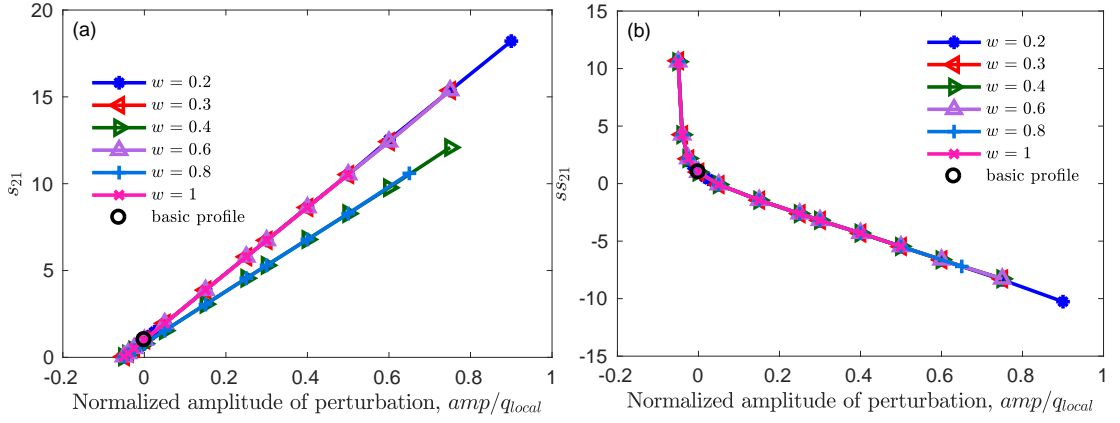


Figure A.13. (a) s_{mn} and (b) ss_{mn} from the amplitude and width scan of perturbations with $\rho_{center} = \rho_{mn}$ and cubic-like shape.

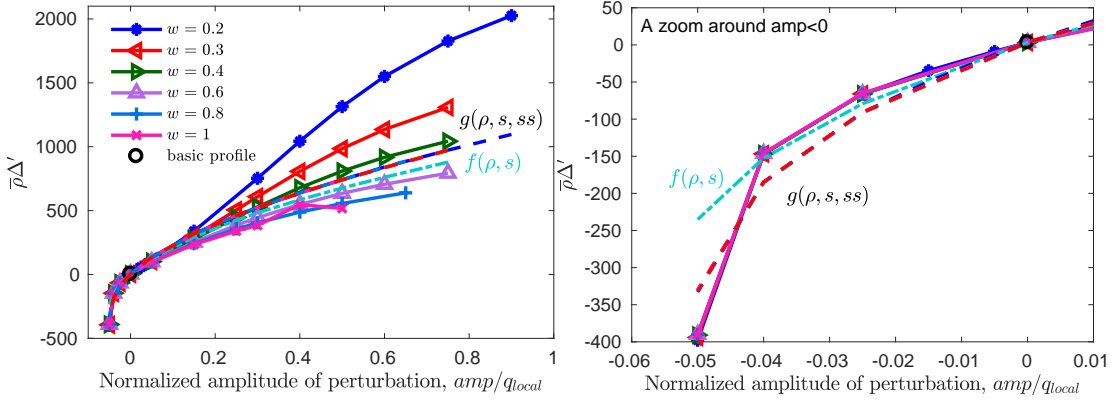


Figure A.14. $\bar{\rho}_{21}\Delta'$ (solid lines) of the amplitude and width scan of perturbations with $\rho_{center} = \rho_{mn}$ and cubic-like shape. Dash-dot cyan - estimation of $\bar{\rho}_{21}\Delta'$ based on function $f(\rho_{mn}, s_{mn})$ defined in equation (A.4) for the case with $w_{full} = 0.3$ (solid red curve with left-pointing triangles); dashed curves with corresponding colors with the solid curves: estimations of $\bar{\rho}_{21}\Delta'$ based on function $g(\rho_{mn}, s_{mn}, ss_{mn})$ defined in equation (A.5) for all the cases.

It can be seen from figure A.14 that with increasing $|amp|$ of the perturbations, there is an increasing variation of $\bar{\rho}_{21}\Delta'$ with respect to the reference value (open black circle), similar to the observations in the amplitude scan near the center or edge discussed before (figure A.9). The narrower the width of the perturbation, the stronger its effect on $\bar{\rho}_{21}\Delta'$ under the same amp . This is different from previous tests near the center or edge, where it is shown that the variation of $\bar{\rho}_{21}\Delta'$ is larger with wider width and fixed ρ_{center} (figure A.9). But as mentioned, that may be entangled with the distance from the $q = 2$ surface - the perturbation overall gets closer to the $q = 2$ surface with wider width in those cases. This will be further illustrated by perturbations with quadratic-like shapes (i.e. the same as used in the previous section) and $\rho_{center} = \rho_{21}$, as will be discussed in the next section.

To have an idea of the effects of local parameters on $\bar{\rho}_{21}\Delta'$, $f(\rho_{mn}, s_{mn})$ defined in equation

Appendix A. A sensitivity study of Δ'

(A.4) has been evaluated (with $\text{coeff} = 300$) for the cases with $w_{\text{full}} = 0.3$ (solid red curve with left-pointing triangles) and is shown by the dash-dotted cyan curve in figure A.14. The general monotonic trend of the resulting $f(\rho_{mn}, s_{mn})$ follows quite well that of $\bar{\rho}_{21}\Delta'$, though the exact values are not. Interestingly, $\bar{\rho}_{21}\Delta'$ curves in figure A.14 exhibit a sudden change of slope at $\text{amp} = 0$, being steeper with $\text{amp} < 0$. This is in accordance with the trend of ss_{21} shown in figure A.13 (b), indicating the possible role of ss_{21} on $\bar{\rho}_{21}\Delta'$. An additional term has thus been added to $f(\rho_{mn}, s_{mn})$ to include the effect of ss_{mn} and a new function $g(\rho_{mn}, s_{mn}, ss_{mn})$ is defined as

$$g(\rho_{mn}, s_{mn}, ss_{mn}) = \bar{\rho}_{mn}\Delta'_{ref} + \text{coeff} \cdot \left(\sqrt{\frac{\rho_{mn}}{\rho_{ref}} \cdot \frac{s_{mn}}{s_{ref}}} - 1 \right) - \text{coeff}_{ss} \left(\frac{ss_{mn}}{ss_{ref}} - 1 \right), \quad (\text{A.5})$$

where coeff_{ss} is a constant.

$g(\rho_{mn}, s_{mn}, ss_{mn})$ has been evaluated for all the cases (solid curves) shown in figure A.14, with corresponding local parameters as well as a fixed $\text{coeff} = 300$ and $\text{coeff}_{ss} = 15$, as depicted by the dashed lines with corresponding colors. It can be seen that $g(\rho_{mn}, s_{mn}, ss_{mn})$ curves of different w_{full} largely overlap and cannot explain the observed difference of $\bar{\rho}_{21}\Delta'$ at different w_{full} . This once again highlights the importance of the global change of q profiles on $\bar{\rho}_{21}\Delta'$, apart from the effects of local parameters. On the other hand, $g(\rho_{mn}, s_{mn}, ss_{mn})$ (dashed red curve) fits better the steep slope of $\bar{\rho}_{21}\Delta'$ at $\text{amp} < 0$ than $f(\rho_{mn}, s_{mn})$ (dash-dotted cyan), taking the case with $w_{\text{full}} = 0.3$ (solid red curve with left-pointing triangles) as an example.

To better understand the observed dependence of $\bar{\rho}_{21}\Delta'$ on amp and the change of slope at $\text{amp} = 0$, examples of ψ profiles for the case with $w_{\text{full}} = 0.2$ (solid blue trace with circles in figure A.14), where a refined amplitude scan around small amp has been performed, are shown in figure A.15. The corresponding q profiles used are shown in figure A.15 (a) and (b) with the same colors. Profiles for the reference case without any perturbations (i.e. based on the basic q profile) are marked by the dash-dotted black lines. Readers are reminded that $\text{amp} > 0$ for the cubic case means $\text{amp} > 0$ for $\rho > \rho_{\text{center}}$ (i.e. ρ_{21} in this case).

One can see that with $\text{amp} > 0$ (above the grey region in figure A.15 (d)), $\frac{\partial\psi}{\partial\rho}|_{\rho_{mn}+\epsilon} > 0$ (i.e. positive slope of the ψ profile) and tends to increase with increasing amp , whereas $\frac{\partial\psi}{\partial\rho}|_{\rho_{mn}-\epsilon} < 0$ and tends to decrease (i.e. more negative), leading to an increase of $\bar{\rho}_{21}\Delta'$ (equation (A.1)) with increasing amp observed in figure A.14; with $\text{amp} < 0$ (the grey region in figure A.15 (d)), $\frac{\partial\psi}{\partial\rho}|_{\rho_{mn}+\epsilon} < 0$ and tends to decrease (i.e. more negative) with increasing $|\text{amp}|$, whereas $\frac{\partial\psi}{\partial\rho}|_{\rho_{mn}-\epsilon} > 0$ and tends to increase, causing $\bar{\rho}_{21}\Delta' < 0$ for $\text{amp} < 0$ and an increase of the variation of $\bar{\rho}_{21}\Delta'$ with increasing $|\text{amp}|$ observed in figure A.14. With the same $|\text{amp}|$, the variation of $\frac{\partial\psi}{\partial\rho}$ is larger for $\text{amp} < 0$ than $\text{amp} > 0$, for example the cyan curve inside the grey region with respect to the purple curve outside, explaining the steeper slope of $\bar{\rho}_{21}\Delta'$ with $\text{amp} < 0$ observed in figure A.14. The corresponding j profiles are shown in figure A.15 (e) and (f) for completeness.

A.3. Scan of the amplitude and width of localized perturbations

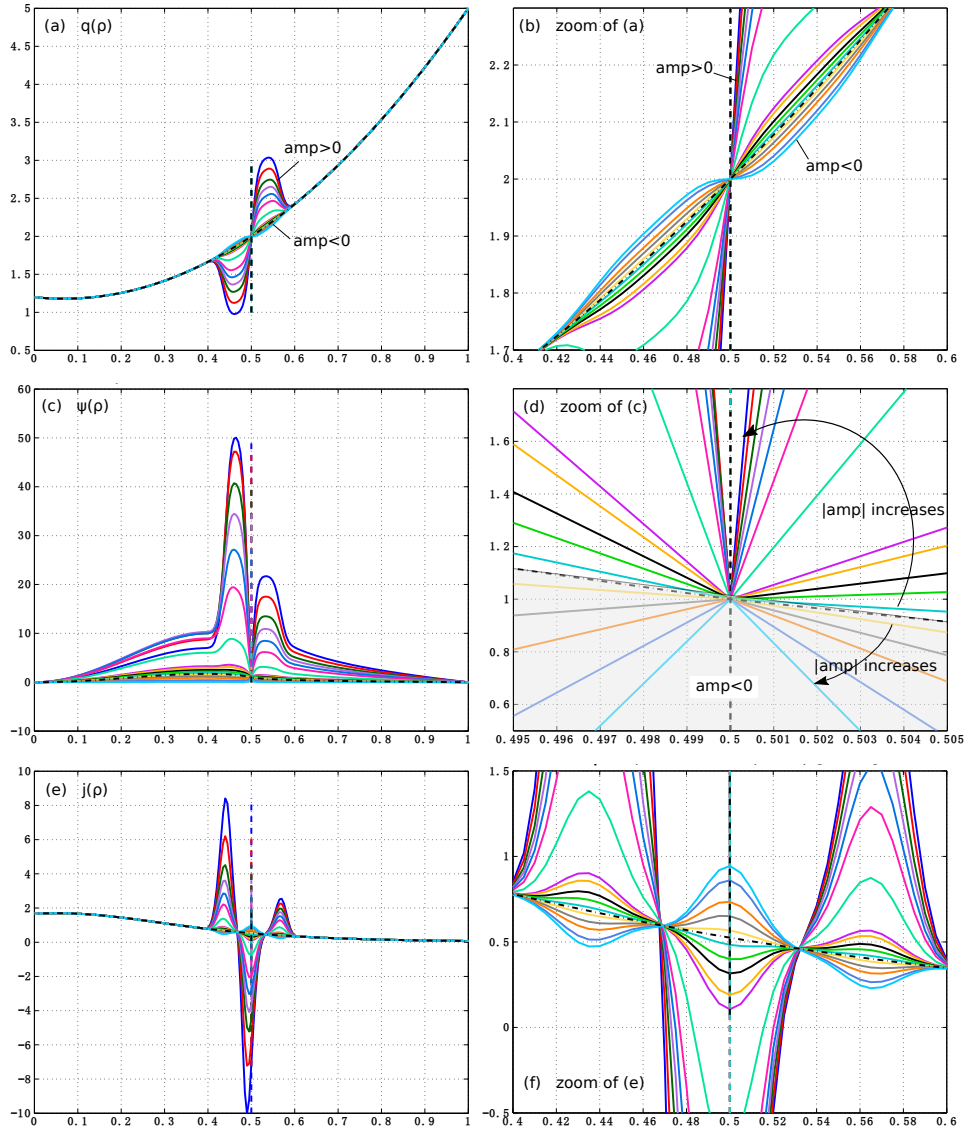


Figure A.15. Examples of the amplitude scan with $w_{\text{full}} = 0.2$: (a) q profiles used; (c) corresponding ψ profiles and (e) j profiles.

Similarly, ψ , j and j' profiles from the scan of w_{full} with fixed $\text{amp} = 0.6$ (i.e. $\text{amp}/q_{\text{local}} = 0.6/2 = 0.3$) shown in figure A.14 are depicted in figure A.16 to better understand the observed w_{full} -dependence of $\bar{\rho}_{21}\Delta'$. It can be seen that with the perturbations, ψ profiles become non-monotonic around ρ_{21} and there is a larger increase of $\frac{\partial\psi}{\partial\rho}|_{\rho_{mn}+\epsilon}$ as well as a large decrease (i.e. more negative) of $\frac{\partial\psi}{\partial\rho}|_{\rho_{mn}-\epsilon}$ with smaller w_{full} , explaining the larger $\bar{\rho}_{21}\Delta'$ with smaller widths observed in figure A.14.

Appendix A. A sensitivity study of Δ'

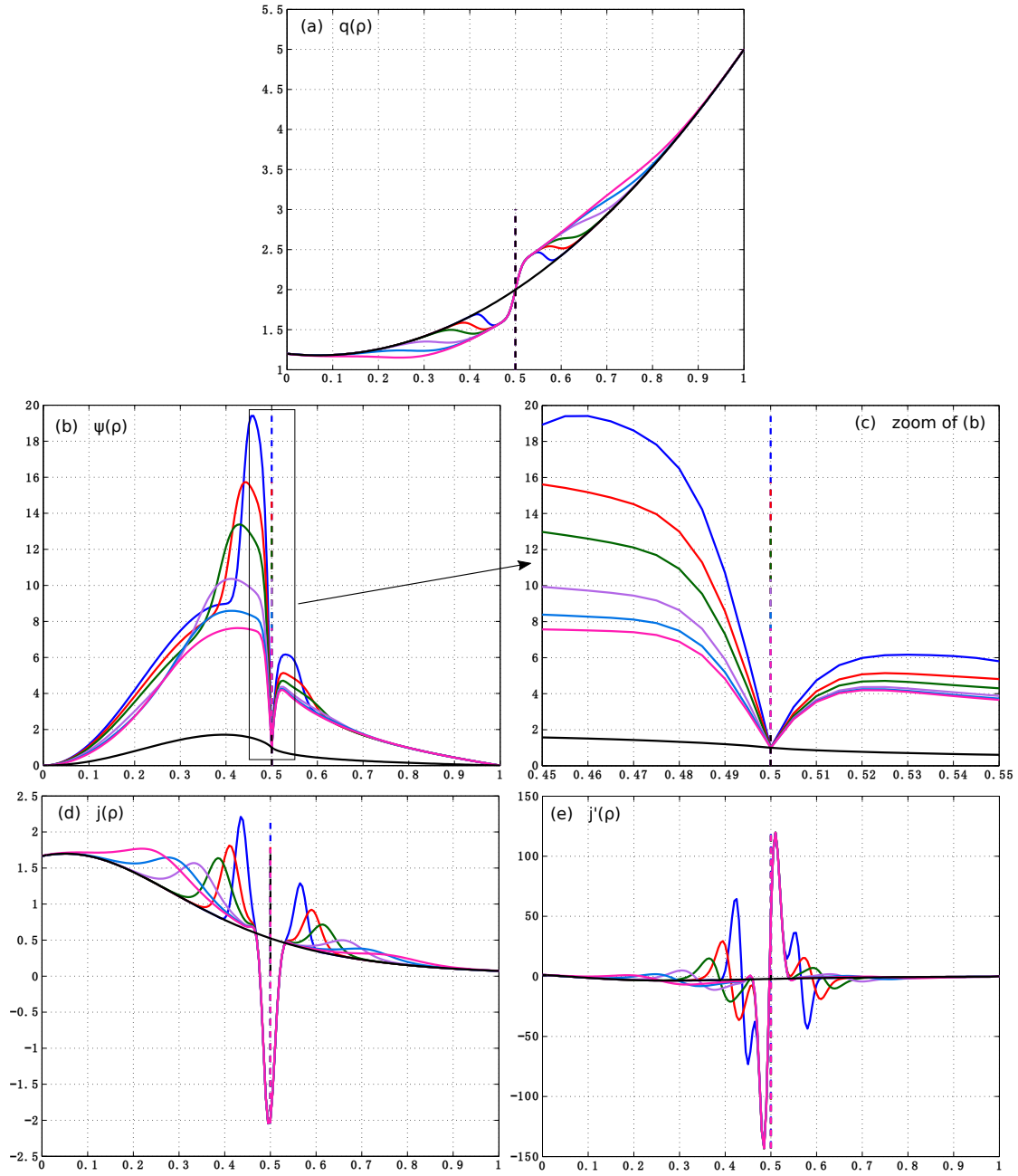


Figure A.16. Examples of the width scan with fixed $amp = 0.6$ (i.e. $amp/q_{local} = 0.3$): (a) q profiles used; (b) corresponding ψ profiles, (d) j profiles and (e) j' profiles.

With quadratic-like perturbations

Similar amplitude scan of perturbations centered at $\rho = 0.5$ has been performed for quadratic-like shapes, with $w_{full} = 0.1, 0.2$ and 0.4 , respectively. Shown in figure A.17 are some examples of the q profiles used.

A.3. Scan of the amplitude and width of localized perturbations

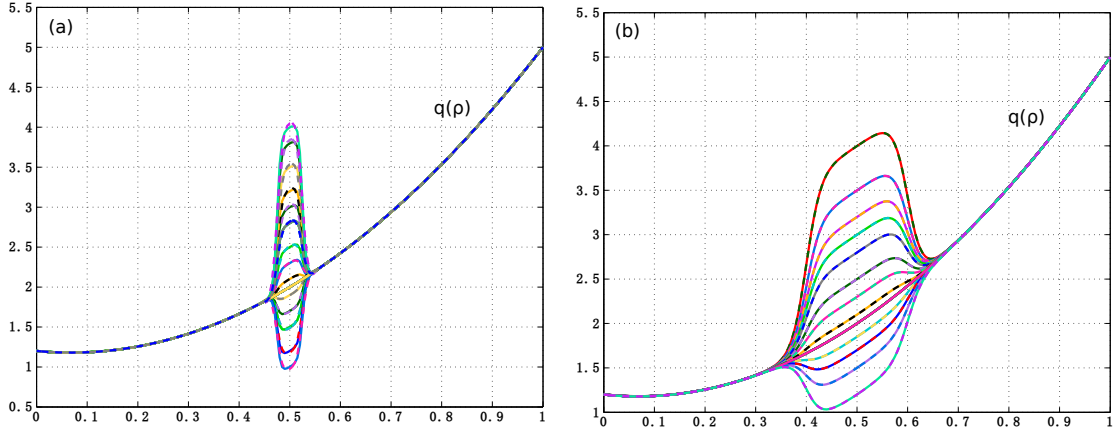


Figure A.17. Examples of the q profiles with quadratic-like perturbations centered at $\rho = 0.5$: (a) amplitude scan with $w_{\text{full}} = 0.1$; and (b) amplitude scan with $w_{\text{full}} = 0.4$.

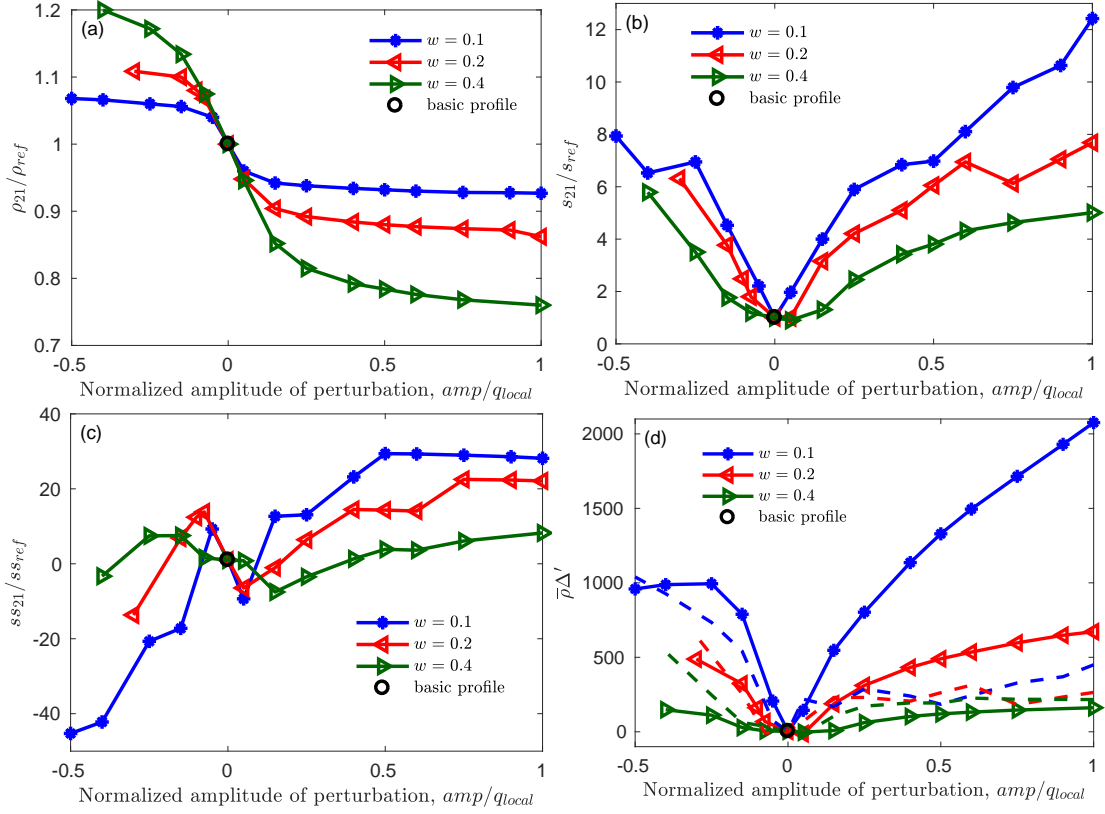


Figure A.18. Results of the scan with quadratic-like perturbations and $\rho_{\text{center}} = 0.5$ (figure A.17). Normalized local parameters at the $q = 2$ surface: (a) $\rho_{21}/\rho_{\text{ref}}$; (b) s_{21}/s_{ref} and (c) ss_{21}/ss_{ref} . Solid traces in (d) - computed $\bar{\rho}_{21}\Delta'$; dashed lines - corresponding $g(\rho_{mn}, s_{mn}, ss_{mn})$ (equation (A.5)) with the same color as the solid lines.

With these perturbations, local parameters such as ρ_{21} , s_{21} and ss_{21} are modified, as shown in figure A.18 (a) - (c). The resulting $\bar{\rho}_{21}\Delta'$ is summarized in (d), along with $g(\rho_{mn}, s_{mn}, ss_{mn})$

(dashed lines) evaluated based on equation (A.5) and corresponding local parameters. One can see that there is a dramatic increase of $\bar{\rho}_{21}\Delta'$ (i.e. more unstable) once there is perturbation exerted around the considered rational surface and the effects become larger with increasing $|amp|$, similar to previous observations with cubic-like perturbations (figure A.14); the narrower the perturbation width, the larger its effect on $\bar{\rho}_{21}\Delta'$, similar to the cubic-like cases as well and in contrast to the tests near the center or edge (figure A.9), where the effects of width may be entangled with the distance from the $q = 2$ surface, as discussed before.

A.4 Scan with global change of q profiles

Apart from the localized perturbations presented in section A.2 and A.3, effects of more global change of q profiles on $\bar{\rho}_{21}\Delta'$ have been investigated, through shifting the q profile rigidly (section A.4.1) or scanning q_a (i.e. $q(\rho = 1)$) with fixed $q_0 \equiv q(\rho = 0)$ (section A.4.2).

A.4.1 Rigid shifts of the q profile

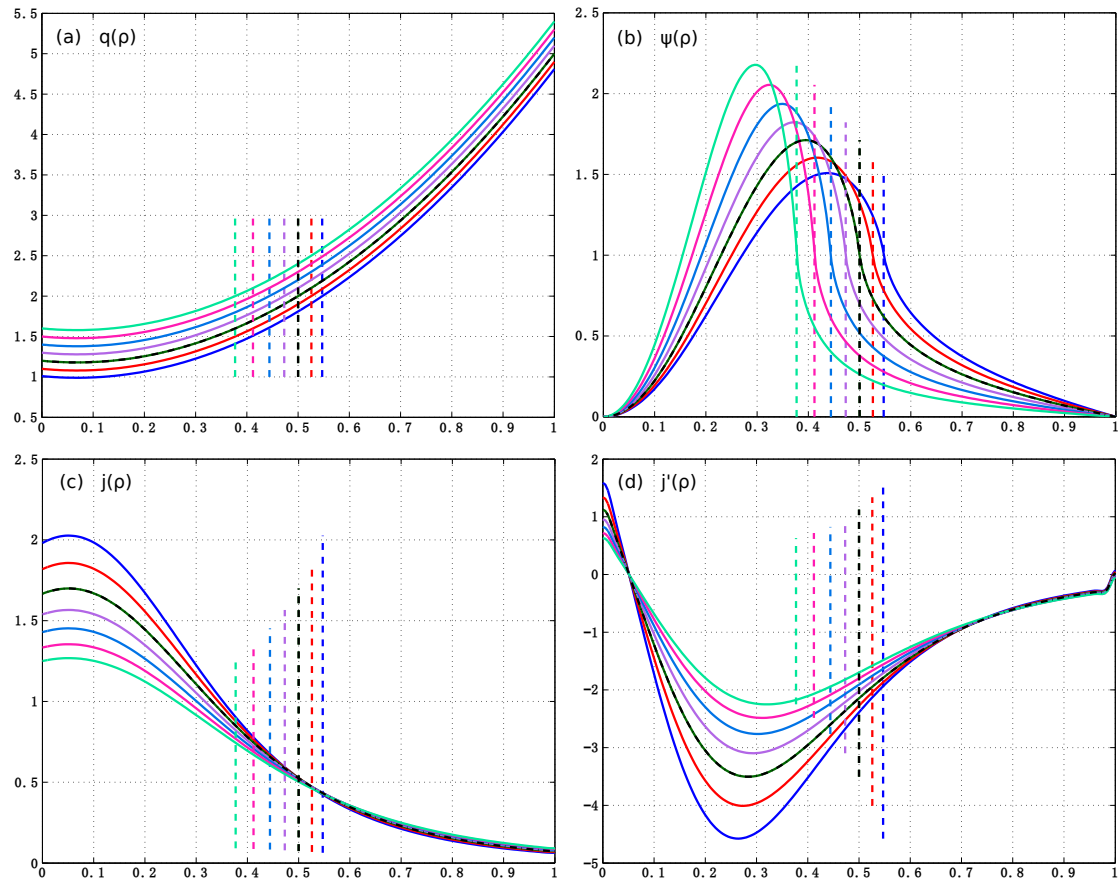


Figure A.19. Rigid shifts of q profile and corresponding ψ , j and j' profiles.

Examples of rigid shifts of the basic q profile are shown in figure A.19 (a), with corresponding ψ , j and j' profiles depicted in (b) - (d) with the same colors. Two “extreme” cases of the resulting q profiles, the steepest (with the lowest q_0 and highest q_a within the scanned range) and the flattest (with the highest q_0 and lowest q_a), are also analyzed, as illustrated in figure A.20 (green and purple, respectively). The black dash-dotted lines in the figures once again represent relevant profiles without perturbations, while ρ_{21} of each case is marked by a vertical dashed line with corresponding color.

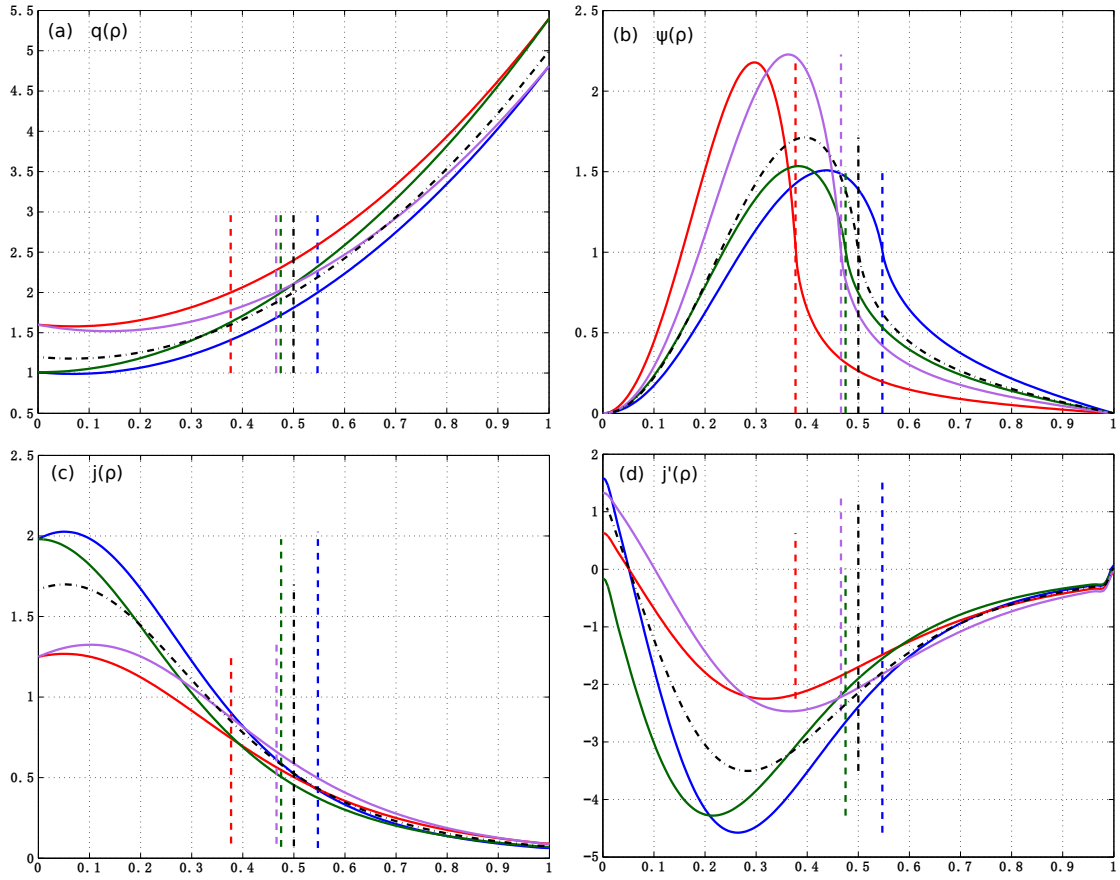


Figure A.20. Illustration of the two extreme cases (solid green and purple traces in (a)) of the rigid shifts of q profile; (b) - (c) corresponding ψ , j and j' profiles.

Local parameters, $\bar{\rho}_{21}\Delta'$ and corresponding $g(\rho_{mn}, s_{mn}, ss_{mn})$ of this series of tests are shown in figure A.21. Results of the two extreme q profiles (green and purple curves in figure A.20) are marked by two triangles with corresponding colors. It can be seen that with a large global change of the q profile, variation of local parameters (e.g. summarized by $g(\rho_{mn}, s_{mn}, ss_{mn})$ in figure A.21 (d)) itself cannot explain the trend of $\bar{\rho}_{21}\Delta'$ in the tests. The global effects are expected to play a more important role in these cases.

Appendix A. A sensitivity study of Δ'

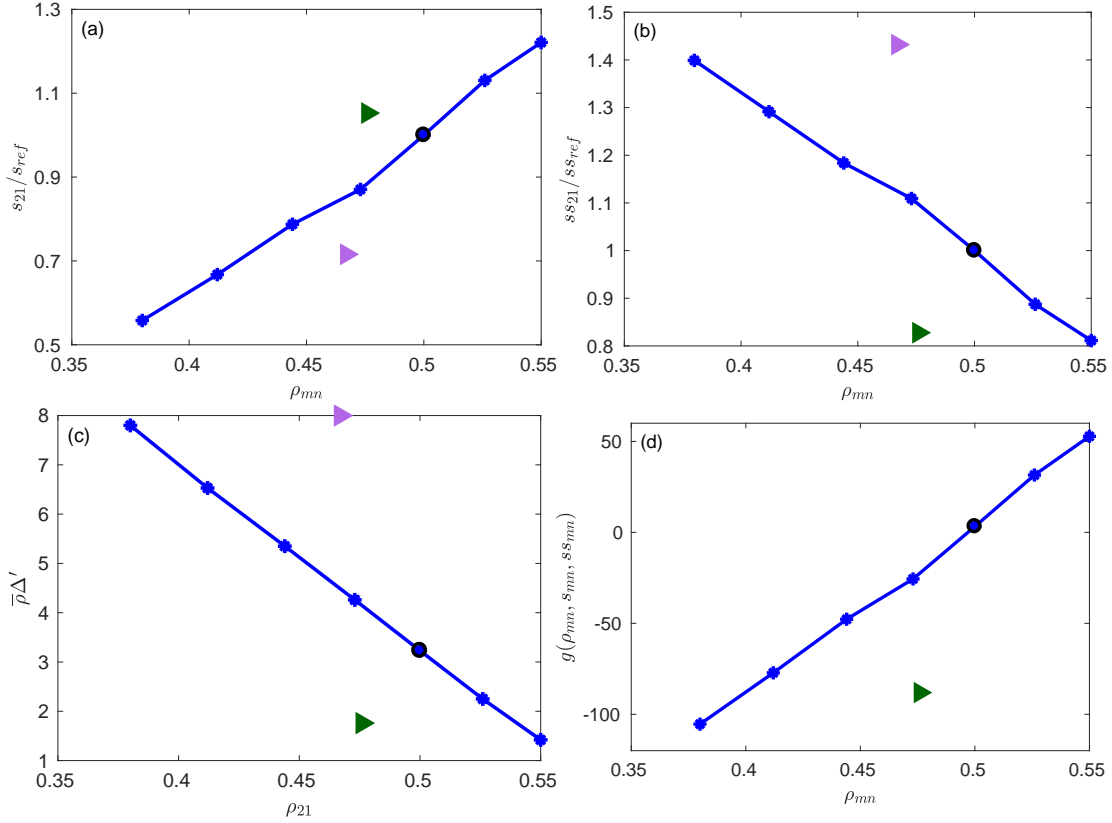


Figure A.21. Results from the rigid shifts of the basic q profile: (a) s_{21}/s_{ref} ; (b) ss_{21}/ss_{ref} ; (c) $\bar{\rho}_{21}\Delta'$ and (d) corresponding $g(\rho_{mn}, s_{mn}, ss_{mn})$. The green and purple triangles represent the results of the two extreme q profiles shown in figure A.20, with the same colors.

A.4.2 Scan of q_a with fixed q_0

The rigid shifts of q profile discussed in the previous section involve modifying both q_0 and q_a , to better isolate different effects, another set of q profiles with fixed q_0 and varying q_a have been investigated, as shown in figure A.22 (a). q_0 is fixed to 1.2 (as the basic q profile), whereas q_a varies from 2.1 to 10 in different tests. The inversion radius (ρ_{inv}) is set to increase from 0.1 to 0.8 with decreasing q_a , while ρ_{21} is chosen to be $\rho_{21} = \rho_{inv} + 0.18$ for each case. The black dash-dotted line represents the basic q profile. Corresponding ψ , j and j' profiles are depicted in figure A.22 (b) - (d) with corresponding colors.

The dependence of local parameters on q_a in this series of tests is illustrated in figure A.23. It can be seen that both s_{21} and ss_{21} decrease with increasing q_a , except for the $q_a = 2.1$ case (orange curves) that has quite different q and ψ profiles by construction (figure A.22). The computed $\bar{\rho}_{21}\Delta'$ and corresponding $g(\rho_{mn}, s_{mn}, ss_{mn})$ of this series of tests are shown in figure A.24, exhibiting similar trend as s_{21} and ss_{21} : $\bar{\rho}_{21}\Delta'$ decreases (i.e. more stabilizing) with increasing q_a . This seems to be in contrary to the experimental observations that lower plasma current (thus typically higher q_a) tends to be more unstable to tearing modes; however,

the change of plasma current involves more sophisticated modifications of the entire q profile that are out of the scope of these tests.

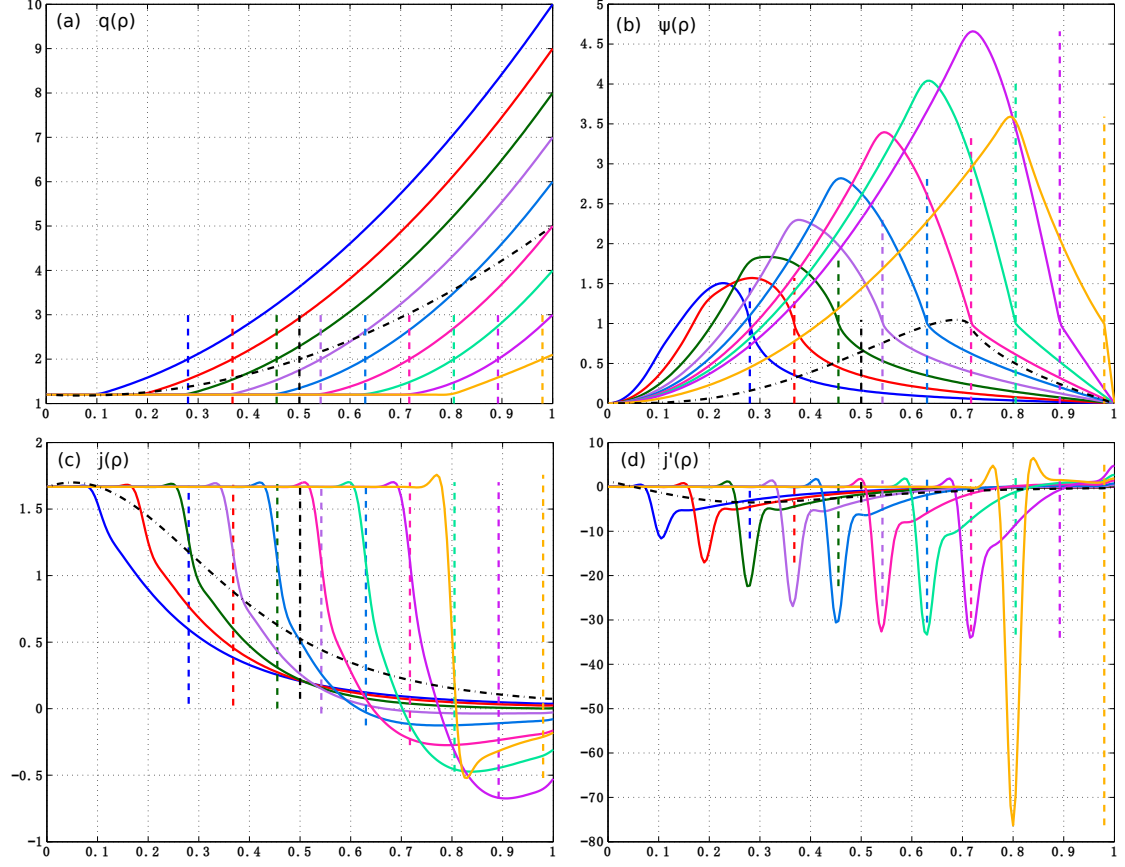


Figure A.22. Scan of q_a with constant q_0 : (a) q profiles used and (b) - (d) corresponding ψ , j and j' profiles.

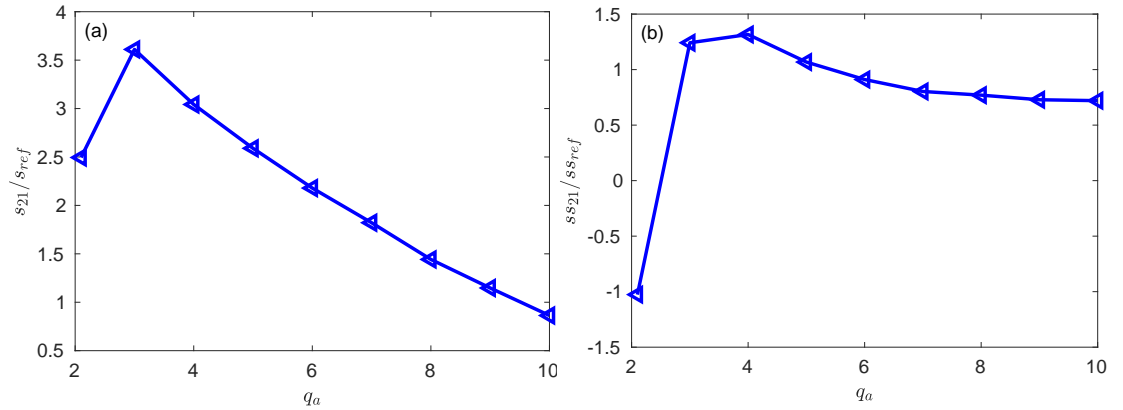


Figure A.23. Normalized local parameters at the $q = 2$ surface of the q_a scan shown in figure A.22: (a) s_{21}/s_{ref} and (b) ss_{21}/ss_{ref} .

Appendix A. A sensitivity study of Δ'

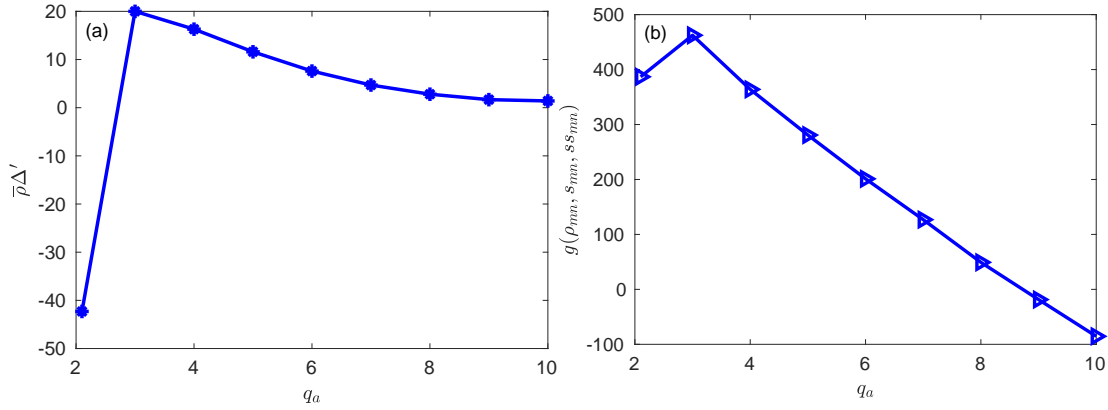


Figure A.24. (a) $\bar{\rho}_{21}\Delta'$ and (b) corresponding $g(\rho_{mn}, s_{mn}, ss_{mn})$ of the q_a scan shown in figure A.22.

A.5 Summary

A detailed sensitivity study of Δ' has been presented in this appendix, with artificial q profiles and perturbations. Both the effects from localized perturbations (with different location, amplitude and width) and from more global change of q profiles (e.g. rigid shifts, scan of q_a , etc.) have been studied. The main observations are summarized below.

- With localized perturbations and the same normalized perturbation amplitude (with respect to the local q value), the degree of effects on Δ' is ordered as: located around the considered rational surface ($q = 2$ in this study) > near the center > near the edge; for the latter two cases, the closer the perturbation to the $q = 2$ surface, the larger the effect
- Perturbations near the center or edge are shown to affect Δ' differently based on the sign of the perturbation: with $amp < 0$ near the center or $amp > 0$ near the edge, the q profile becomes more stable, whereas $amp > 0$ near the center or $amp < 0$ near the edge leaves the profile more unstable (figure A.8)
- With localized perturbations, the change of Δ' is found to be correlated with the change of local parameters such as ρ_{mn} , s_{mn} and ss_{mn} with an estimated dependence (equation (A.5))

$$g(\rho_{mn}, s_{mn}, ss_{mn}) = \bar{\rho}_{mn}\Delta'_{ref} + \text{coeff} \cdot \left(\sqrt{\frac{\rho_{mn}}{\rho_{ref}} \cdot \frac{s_{mn}}{s_{ref}}} - 1 \right) - \text{coeff}_{ss} \left(\frac{ss_{mn}}{ss_{ref}} - 1 \right),$$

where coeff and coeff_{ss} are constant positive coefficients

- Even with well-localized perturbations, global effects resulting from the overall modification of the q profile prove to play a role in Δ' ; the global effects are more evident when more global change of the q profile is exerted, e.g. rigid shifts, varying q_a values, etc.

B Locking/Acceleration of NTMs with tangential neutral beam injection (NBI)

B.1 Introduction

Tangential neutral beam injection (NBI) is able to alter plasma rotation and in turn affects the rotation of NTMs [Snipes et al. 1988, 1990; Rice 2016, and references therein]. Based on the studies of rotating NTMs presented in previous chapters, another series of experiments have been carried out in TCV with its tangential NBI, exhibiting evident modifications of mode rotation: locking/locked NTM or accelerated NTM depending on the relative injection direction with respect to the mode, as illustrated in figure B.1.

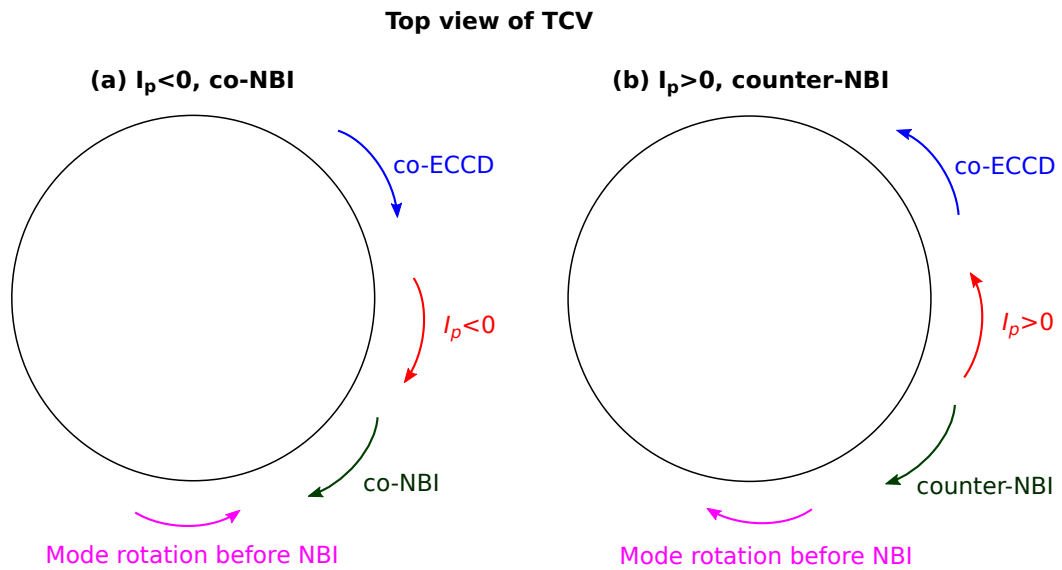


Figure B.1. Illustration of the effects of tangential NBI on the rotating of NTMs (from a top view of TCV): (a) with $I_p < 0$ and co-current NBI, locking/locked NTMs; (b) with $I_p > 0$ and counter-current NBI, accelerated NTMs.

In this series of experiments, co-ECCD is deposited near the plasma center for the onset of NTMs, similar to the setup in chapter 4 and 5; NTMs are triggered and typically rotate in the

electron diamagnetic drift direction; the tangential NBI is then switched on, modifying the rotation of existing NTMs. To better demonstrate the effects of NBI, different I_p direction, i.e. different relative direction of NBI with respect to the rotating mode has been tested in the experiments. As illustrated in figure B.1, with $I_p < 0$ (i.e. clockwise in TCV's convention), NBI is in a co-current manner (denoted as *co-NBI*) and is opposite to the rotation direction of NTMs, leading to locking and eventually locked NTMs; with $I_p > 0$, the resulting *counter-NBI* is in the same direction as the rotating NTMs, causing an acceleration of NTMs. These effects will be demonstrated through two series of experiments with different signs of I_p shown in section B.2 and B.3, respectively.

B.2 Locking/Locked NTMs with co-current NBI

The first example of locking/locked NTMs with co-NBI is TCV #62601 shown in figure B.2, with constant $I_p \approx -90$ kA and $B_0 = -1.42$ T, similar to the experiments in previous chapters. One EC launcher ($L1$) with a nominal power of 750 kW is applied to deposit co-ECCD near the plasma center to trigger NTMs. As shown in figure B.2 (b), a rotating 2/1 NTM is triggered along with the ramp-up of the EC power and saturates at a frequency of about 5 kHz, similar to the observations in chapter 4 and 5. NBI is switched on at $t = 1.1$ s, with its power increased from 90 kW to 480 kW step by step. Interesting behavior of mode rotation is observed: mode frequency drops from 5 kHz to about 2 kHz with 90 kW NBI and eventually to 0 (i.e. fully locked) when NBI power is increased to 160 kW; the mode stays locked with increasing NBI power and is directly “unlocked” when completely turning off NBI at $t = 1.9$ s, recovering 5 kHz from 0.

TCV's saddle flux loops introduced in chapter 2 are used to analyze the amplitude and phase of the locked mode. These saddle loops, located outside the vacuum vessel (i.e. with high frequency perturbations screened out) and with much larger detection areas than the in-vessel magnetic probes, are more sensitive to low frequency radial perturbations (given the orientation of these saddle loops) and are suitable for the detection of locked modes. Similar to the analyses of magnetic probe signals, saddle flux loops at different toroidal and poloidal locations can be used to infer the m and n number of a given mode. Shown in figure B.2 (c) and (d) are the amplitude and phase of the $n = 1$ component of the perturbed radial magnetic field (δB_r), respectively, based on a toroidal array of 8 saddle flux loops located on the equatorial plane of TCV.

As indicated by the vertical dash-dotted black lines in figure B.2 (c) and (d), there is a sudden increase of the amplitude of δB_r when the mode gets fully locked at about $t = 1.3$ s; the phase of the $n = 1$ component stays constant when the mode is fully locked - the small transient change at $t = 1.5$ s stems from the sudden increase of NBI power at that time, indicating a change of the toroidal location of the locked mode. Note that there is a larger perturbation on plasma equilibrium with higher NBI power (e.g. above 160 kW at $t \in [1.5, 1.9]$ s), as indicated by the plasma elongation κ (red curve in figure B.2 (a)), which can affect the amplitude of δB_r as well. The vertical position of the magnetic axis (z_{axis}) starts to vary since $t = 2$ s (as

pre-programmed), affecting the amplitude and phase of δB_r seen in (c) and (d).

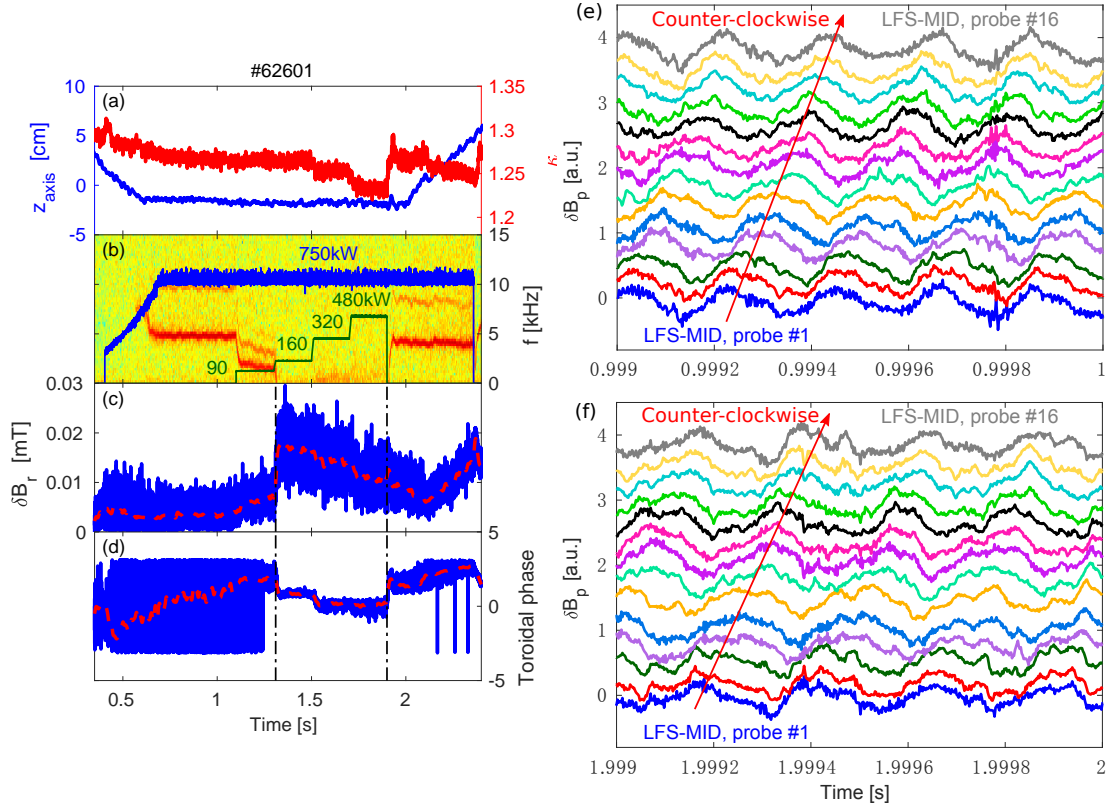


Figure B.2. Overview of TCV #62601 with co-NBI and locking/locked NTMs: (a) blue - vertical position of the magnetic axis; red - plasma elongation; (b) NTM spectrogram from magnetic probes; blue - scaled EC power trace; green - scaled NBI power trace; (c) amplitude of the $n = 1$ component of δB_r based on saddle flux loop measurements; (d) toroidal phase of the $n = 1$ component of δB_r ; (e) signals from a toroidal array of magnetic probes (LFS-MID) at around $t = 1$ s, indicating the direction of mode rotation; rigid shifts of the measured amplitudes have been made to avoid overlapping; and (f) similar to (e), but at around $t = 2$ s.

To have an idea of the rotation direction of NTMs, an equatorial toroidal array (*LFS-MID*) of TCV's magnetic probes introduced in chapter 2 are used, involving 14 magnetic probes (#1 to #16, except #4 and #8) in these experiments. These probes are labeled such that increasing probe index represents the counter-clockwise direction viewed from the top of TCV. Signals from the 14 probes at around $t = 1$ s and $t = 2$ s are shown in figure B.2 (e) and (f), respectively, with rigid shifts of the amplitude of perturbations to avoid overlapping (larger shifts with increasing probe index). It can be seen that the mode rotates in the same direction as increasing probe index, i.e. counter-clockwise, confirming the illustration in figure B.1 (a).

As depicted in figure B.3, a complementary experiment based on #62601 has been performed, with a slow ramp-up of NBI power around the power threshold for mode locking in this case (in between 90 and 160 kW as seen from figure B.2). Similar to #62601, a 2/1 NTM is triggered by central co-ECCD and rotates counter-clockwise with a frequency of about 5 kHz (figure

Appendix B. Locking/Acceleration of NTMs with tangential neutral beam injection (NBI)

B.3 (b) and (e)); the mode gradually slows down but is still in the counter-clockwise direction (figure B.3 (f)) along with the slow ramp-up of NBI power and gets fully locked at about $t = 1.5$ s when the NBI power reaches 135 kW, in accordance with the observations in figure B.2. A large increase of the amplitude of δB_r is observed at the same time, with relatively constant z_{axis} and κ , confirming the occurrence of a locked mode at $t \in [1.5, 1.6]$ s.

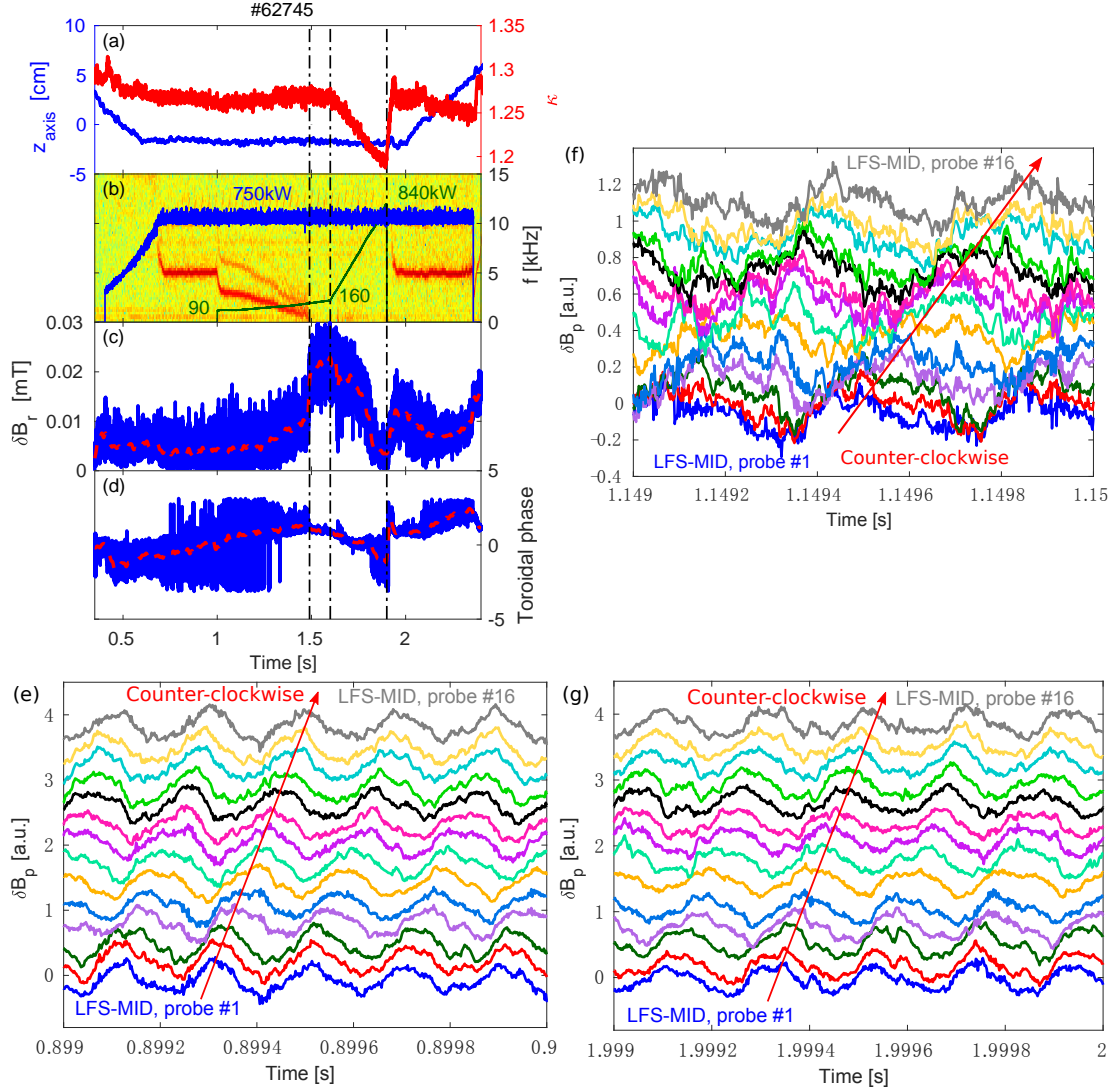


Figure B.3. Overview of #62745 with co-NBI and locking/locked NTMs: (a) blue - z_{axis} ; red - plasma elongation; (b) NTM spectrogram from magnetic probes; blue and green - scaled EC and NBI power traces, respectively; (c) amplitude of the $n = 1$ component of δB_r based on saddle flux loops; (d) toroidal phase of the $n = 1$ component of δB_r ; (e) signals from a toroidal array of magnetic probes (with rigid shifts to avoid overlapping) at around $t = 0.9$ s, indicating the direction of mode rotation; (f) magnetic probe signals at around $t = 1.15$ s and (g) $t = 2$ s.

The NBI power is ramped up sharply since $t = 1.6$ s and reaches a maximum of about 840 kW before completely turning off at $t = 1.9$ s. A large drop of the amplitude of δB_r is observed

along with the rapid increase of NBI power, resulting mainly from the variation of plasma equilibrium itself, as indicated by plasma κ (red curve in figure B.3 (a)). It is thus difficult to determine the existence of locked modes at $t \in (1.6, 1.9)$ s based on the saddle loop signals. In fact, the 20 ms delay in the re-appearance of rotating mode after switching off NBI and the initial decrease of mode frequency from about 10 to 5 kHz (instead of increasing from 0 to 5 kHz as in figure B.2 (b)) seem to suggest that the locked mode is self-stabilized during the large ramp-up of NBI power, probably through a large change of Δ' , and is re-triggered again by co-ECCD after turning off NBI. Simulations with TORAY-GA show that the deposition location of $L1$ moves off-axis (from $\rho_\psi \approx 0.2$ to 0.35, still far from the $q = 2$ surface at $\rho_\psi \approx 0.7$) and its driven current decreases during the fast ramp-up of NBI power and the large change of κ at $t \in [1.6, 1.9]$ s. These are expected to affect Δ' (e.g. equation (4.2)) and the dynamics of NTMs. No clear local flattening of the electron temperature profile can be observed at $t \in (1.6, 1.9)$ s either. The rotating mode after turning off NBI is in the counter-clockwise direction (figure B.3 (g)), similar to the observations in #62601 (figure B.2).

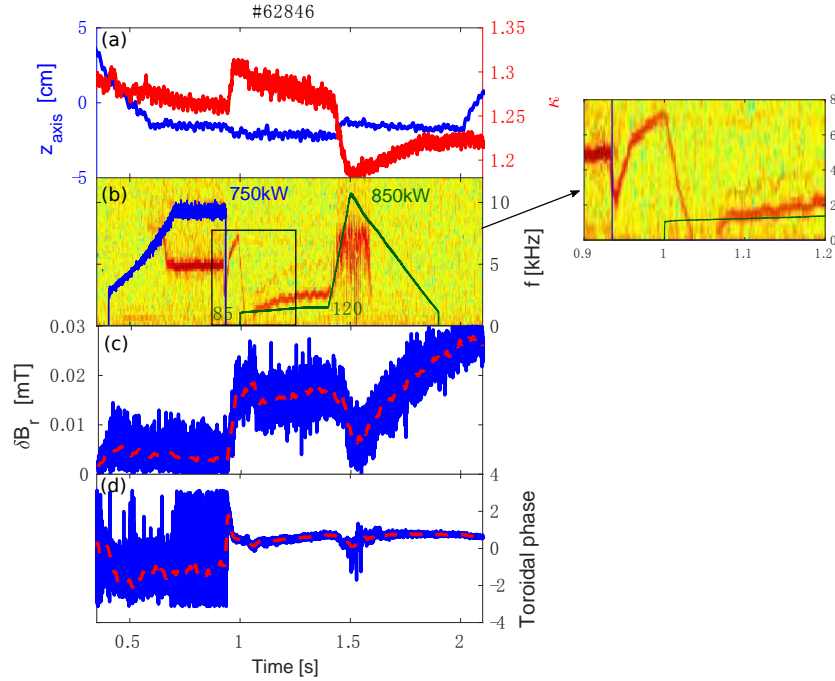


Figure B.4. Overview of TCV #62846 with co-NBI, locking/locked NTMs and flipped mode rotation: (a) blue - z_{axis} ; red - plasma elongation; (b) NTM spectrogram from magnetic probes; blue and green - scaled EC and NBI power traces, respectively; (c) amplitude of the $n = 1$ component of δB_r and (d) toroidal phase of the $n = 1$ component of δB_r .

In the third example shown in figure B.4, an interesting “flip” of mode rotation is observed: the initial 2/1 NTM rotates counter-clockwise (figure B.5 (a)) at about 5 kHz before turning off EC power at $t = 0.935$ s; the mode then weakens and rotates faster without EC, in the counter-clockwise direction as before (figure B.5 (b)); before reaching the full self-stabilization of the mode, co-NBI is switched on at $t = 1$ s, which sustains the mode and slows down mode

Appendix B. Locking/Acceleration of NTMs with tangential neutral beam injection (NBI)

rotation along with a very slow ramp-up of NBI power; the mode is eventually fully locked at $t = 1.035$ s and stays locked until $t = 1.066$ s when the ramp-up of NBI power “unlocks” the mode (figure B.4 (b)); the mode then rotates in the clockwise direction (figure B.5 (c) and (d)), i.e. the same as I_p and the injection direction of the co-NBI.

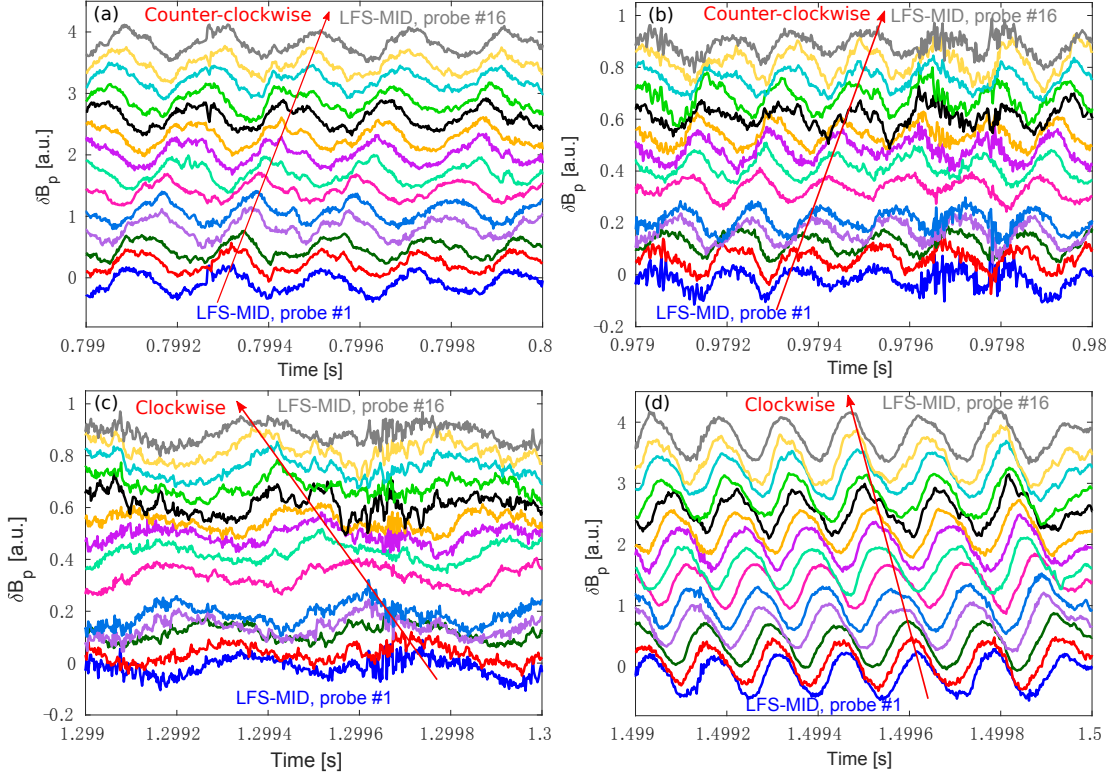


Figure B.5. Signals from a toroidal array of magnetic probes at around $t = 0.8$, 0.98 , 1.3 and 1.5 s, respectively, indicating the “flip” of mode rotation after switching on co-NBI at $t = 1$ s. Rigid shifts of the measured amplitudes from different probes have been made to avoid overlapping.

As seen in figure B.4 (b), there is a rapid increase of NBI power during $t \in [1.4, 1.5]$ s, causing a faster rotation of the mode. Interestingly, mode frequency seems to “saturate” at about 7 kHz and does not increase any more with higher NBI power, possibly through the electromagnetic drag due to the eddy currents in the wall and viscous drag from the bulk plasma [Ramponi et al. 1999; La Haye et al. 2006], as will be further discussed in section B.4. The NBI power is ramped down from $t = 1.5$ s to 1.9 s, during which the mode disappears from the spectrogram at around $t = 1.6$ s. It is conjectured that the mode self-stabilizes during the dramatic decrease of NBI power (and β_p). Note that there is a large variation of plasma equilibrium during the fast ramp-down of NBI power, as indicated by the red curve in figure B.4 (a), which affects the measurements of saddle flux loops shown in (c) and (d). It is thus difficult to determine the existence of a locked mode from these measurements. Instead, averaged T_e profiles at different time intervals have been compared, as illustrated in figure B.6. The numbers in the legend represent the time intervals considered. Local flattening of T_e profile around $q = 2$ can

be observed for the cases in which 2/1 NTMs clearly exist (i.e. $t \in [1.25, 1.3]$ s and $t \in [1.45, 1.5]$ s as seen in figure B.4 (b)), whereas no clear flattening can be seen during the ramp-down of NBI power, suggesting that there is no (locked) 2/1 mode, at least after $t = 1.7$ s. The vertical dashed lines refer to the radial location of the $q = 2$ surface taken from LIUQE.

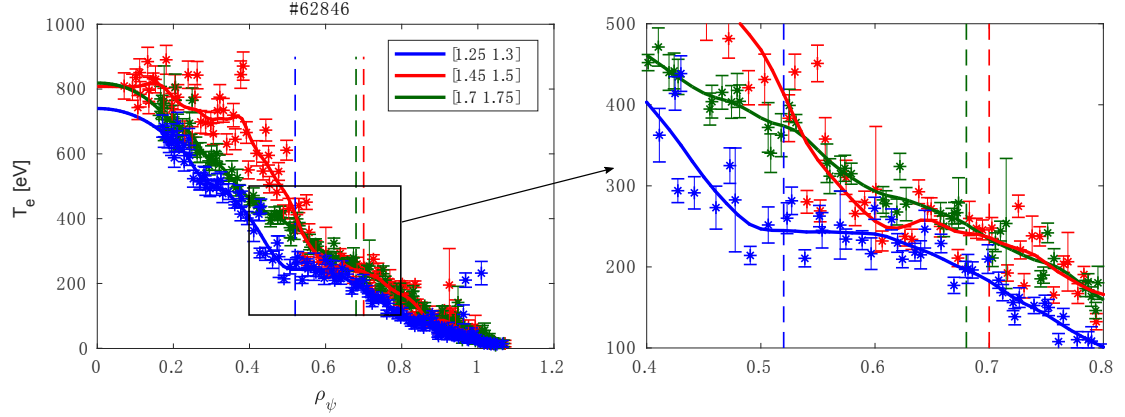


Figure B.6. Averaged T_e profiles based on Thomson scattering measurements. Time intervals during which the profiles are averaged are listed by the numbers in the legend. Vertical dashed lines refer to the radial location of the $q = 2$ surface from LIUQE.

B.3 Acceleration of NTMs with counter-current NBI

In the series of experiments presented in this section, positive I_p (i.e. in the counter-clockwise direction) is used so that NBI injects counter- I_p , accelerating the clockwise rotation of NTMs, as illustrated in figure B.1 (b). Shown in figure B.7 (TCV #62602) is an example of these counter-NBI experiments, with the same EC and NBI power traces as used in #62601 (figure B.2). However, central counter-ECCD (instead of the typical co-ECCD) is used in this discharge and a 3/1 NTM is triggered when the EC power reaches 750 kW, through a modification of Δ' (e.g. heating effects on NTM onset as discussed in section 4.5.2, chapter 4). The 3/1 mode rotates at about 8 kHz in the clockwise direction (figure B.7 (d)) and is “accelerated” to about 9 kHz when adding 90 kW NBI at $t = 1.1$ s; mode frequency increases gradually with increasing NBI power (figure B.7 (c) and (e)) and drops to about 7.5 kHz after switching off NBI at $t = 1.9$ s. The 3/1 mode keeps rotating in the clockwise direction (figure B.7 (f)) until turning off EC power at $t = 2.35$ s, shortly after which the mode self-stabilizes.

As indicated by the n_{el} and κ traces in figure B.7 (a) and (b), plasma conditions are different before and after the NBI phase (e.g. $t = 1$ s versus 2 s), explaining the slight difference in mode frequency (i.e. 8 kHz versus 7.5 kHz) at the two phases. Note that higher-frequency modes (40 ~ 60 kHz) with both odd n and even n components are triggered when NBI power reaches 320 kW and beyond (figure B.7 (c)), possibly through mode coupling and/or the effects of fast ions from NBI. More investigations are desired to better understand the origin of these high-frequency modes.

Appendix B. Locking/Acceleration of NTMs with tangential neutral beam injection (NBI)

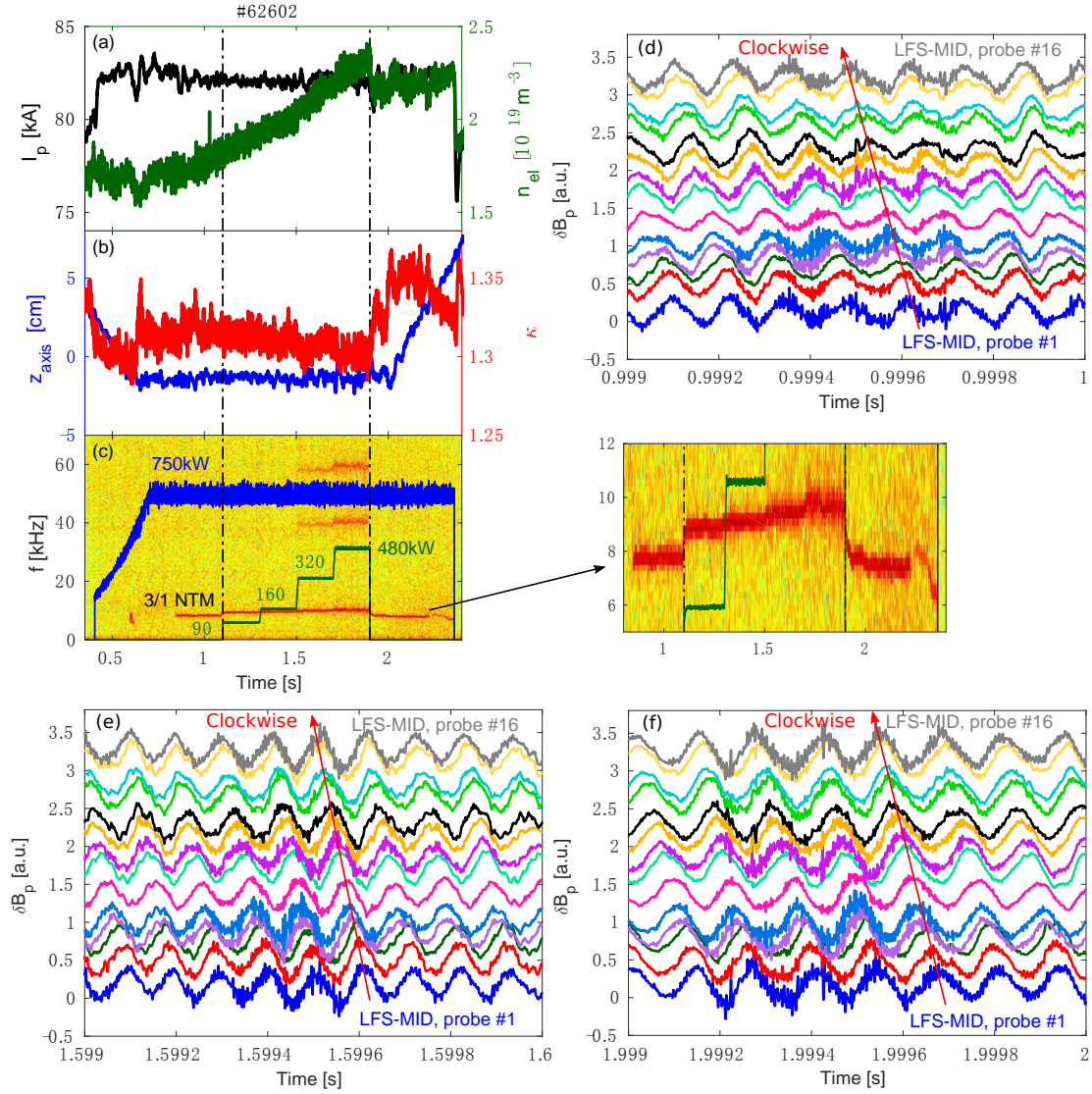


Figure B.7. Overview of TCV #62602 with counter-NBI and accelerated 3/1 NTMs: (a) black - plasma current; green - central line-averaged density; (b) blue - z_{axis} ; red - plasma elongation; (c) NTM spectrogram from magnetic probes; blue and green - scaled EC and NBI power traces, respectively; (d) - (f) signals from a toroidal array of magnetic probes at around $t = 1, 1.6$ and 2 s, respectively, indicating the direction of mode rotation.

Another two examples of mode acceleration with counter-NBI are illustrated in figure B.8 and B.9, respectively, where higher NBI power and different ratio of NBI to EC power are involved. Standard central co-ECCD was applied in these two discharges, triggering 2/1 NTMs in both cases. In #62735 (figure B.8), the 2/1 mode is triggered when EC power reaches 750kW and rotates in the clockwise direction at about 5kHz; similar to #62602 (figure B.7), mode frequency increases along with the ramp-up of NBI power and “saturates” at about 8kHz; high frequency modes (above 40kHz) are triggered when NBI power reaches about 820kW and 2/1 mode frequency reaches above 10kHz at $t = 1.68$ s, leading to plasma disruption at around

$t = 1.8$ s. The time-evolution of the island width in #62735 is shown in figure B.11, together with the simulations based on the MRE, as will be discussed in the next section.

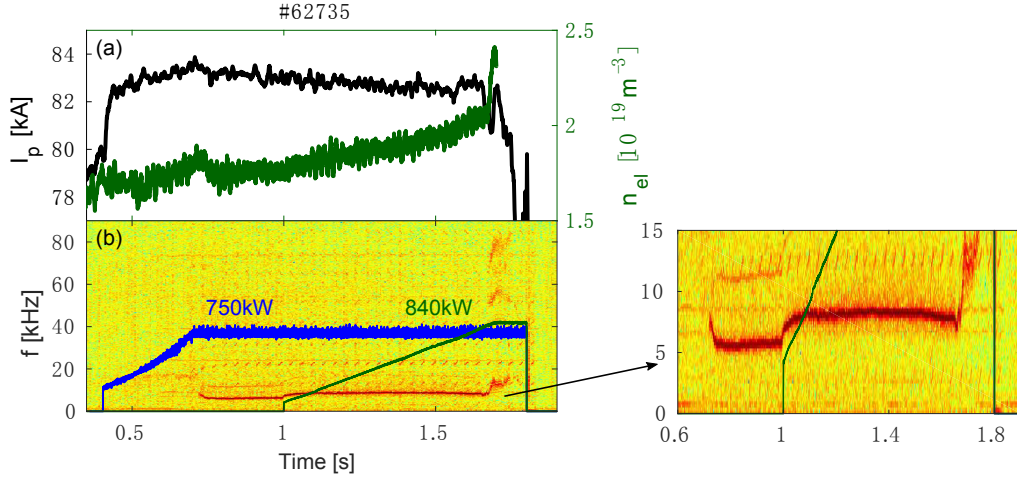


Figure B.8. Overview of #62735 with counter-NBI and accelerated 2/1 NTM: (a) black - plasma current; green - central line-averaged density; (b) Spectrogram from magnetic probes; blue and green - scaled EC and NBI power traces, respectively.

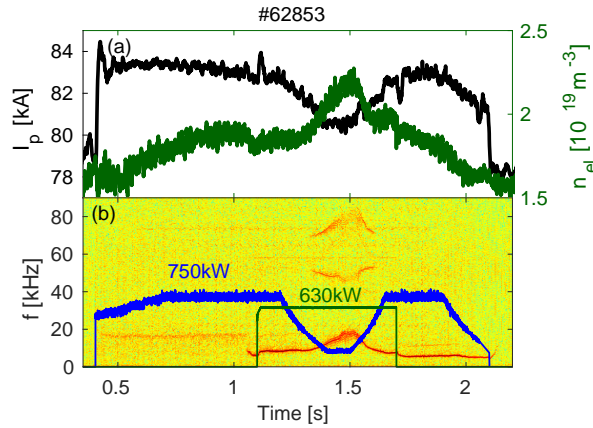


Figure B.9. Overview of #62853 with counter-NBI and accelerated 2/1 NTM: (a) black - plasma current; green - central line-averaged density; (b) Spectrogram from magnetic probes; blue and green - scaled EC and NBI power traces, respectively.

In #62853 (figure B.9), a 2/1 NTM is triggered by co-ECCD, shortly before switching on NBI at $t = 1.1$ s. As seen in figure B.9 (b), constant NBI power is maintained until $t = 1.9$ s, whereas the EC power is varied in this case, causing interesting variations of mode frequency. Similar to previous two examples, high frequency modes are triggered when the 2/1 mode is accelerated to about 10 kHz and self-stabilize when the 2/1 mode frequency decreases. This seems to suggest that the rapid rotation of NTMs plays an important role in the onset of these high frequency modes, the underlying mechanisms of which require further investigations and are out of the scope of this thesis.

B.4 Discussions and outlook

The experimental results presented in previous sections, involving both locking/locked NTMs and accelerated NTMs, can serve as a data set for validating the theoretical model concerning the toroidal angular frequency (ω) of NTMs [Smolyakov et al. 1995; Ramponi et al. 1999; Nowak et al. 2014; Basiuk et al. 2017]:

$$\frac{d\omega}{dt} = \frac{1}{I_\Phi} [-n(T_{\Phi EM} + T_{\Phi visc}) - (\omega - \omega_T) \frac{dI_\Phi}{dt}], \quad (B.1)$$

where $I_\Phi \propto R^3 \bar{\rho}_{mn} \rho_i w$ is the effective moment of inertia of the plasma associated with the island (with width w), ρ_i being the ion mass density; $T_{\Phi EM} \propto [(2\pi^2 R)/\mu_0] \bar{\rho}_{mn} \text{Im}(\Delta'_w) w^4$ refers to the electromagnetic torque due to the eddy currents in the resistive wall, with

$$\bar{\rho}_{mn} \Delta'_w = 2m \left(\frac{\bar{\rho}_{mn}}{d} \right)^{2m} \frac{(\omega \tau_w)^2 + i(\omega \tau_w)}{1 + (\omega \tau_w)^2} \quad (B.2)$$

the effects of the resistive wall (with time constant τ_w) on NTM width (through its real part) and frequency (imaginary part), d being the radial distance of the island separatrix to the wall; $T_{\Phi visc} \propto \rho_i \bar{\rho}_{mn}^2 R(\omega - \omega_T)/(w \tau_M)$ is the viscous torque, with ω_T the equilibrium toroidal rotation frequency and τ_M the momentum confinement time.

Considering the effects of the resistive wall on island width evolution, the original MRE (equation (3.3)) can be updated as

$$\frac{\tau_R}{\bar{\rho}_{mn}} \frac{dw}{dt} = \bar{\rho}_{mn} \Delta' + \bar{\rho}_{mn} \Delta'_{BS} + \bar{\rho}_{mn} \Delta'_{GGJ} + \bar{\rho}_{mn} \Delta'_{CD} + \bar{\rho}_{mn} \Delta'_H + \bar{\rho}_{mn} \Delta'_{WALL}, \quad (B.3)$$

where $\bar{\rho}_{mn} \Delta'_{WALL} \equiv -a_w \text{Re}(\bar{\rho}_{mn} \Delta'_w)$ is the additional term considering the wall effect. Future work can be done to solve the coupled w equation (B.3) and ω equation (B.1) to quantify the contribution of various terms, whereas this section presents preliminary simulations solving only equation (B.3), with prescribed $\omega = 2\pi f$ taken from experiments (f is the measured mode frequency in Hertz).

For the case of locking/locked NTM with co-NBI, TCV #62601 illustrated in figure B.2 is taken as an example. NBI is switched on at $t = 1.1$ s and the 2/1 mode is completely locked during $t \in [1.3, 1.9]$ s with higher NBI power. As depicted by the solid red curve in figure B.10 (a), a simulation has been performed with the original MRE without including explicitly the wall term (i.e. equation (3.3)), following the same procedures as used in chapter 4 and 5. Note that this is relevant for cases with relatively constant mode rotation, where $\bar{\rho}_{mn} \Delta'_w$ (equation (B.2)) thus $\bar{\rho}_{mn} \Delta'_{WALL}$ is almost constant and neglecting the wall term does not affect much the dynamics of island width, as indicated by the comparison between the solid red and dashed cyan curves in figure B.10 (a) (at the time intervals without NBI). This also explains why the wall term has been neglected in the simulations in previous chapters, where only relatively constant mode rotations are involved.

The blue traces in figure B.10 (a) are based on magnetic probe measurements, which are only relevant for rotating NTMs. During the time window when the mode is fully locked (i.e. $t \in [1.3, 1.9]$ s), its amplitude can in principle be inferred from saddle flux loop signals, however, the measurement (including its trend) can be “polluted” by the variations of plasma equilibrium (e.g. κ shown in figure B.2 (a)) and may not be accurate enough to reflect (the trend of) w . Therefore, the amplitude of the locked mode is only “predicted” by simulations.

Based on equation (B.3), another simulation has been performed to include the effects of the resistive wall, with $\tau_w = 0.5$ ms in equation (B.2), as shown by the dashed cyan trace in figure B.10 (a). $a_w = 0.1$ has been taken in *ad-hoc* and $a_2 = 1.9$ (instead of 1.5 in the simulation without the wall term, solid red) is used to fit the experimental w_{sat} marked by the blue triangle at $t = 1$ s. The stabilizing effect from the wall term, as shown in figure B.10 (b), drops to 0 when the mode is fully locked, causing a larger simulated w than the case without explicit wall term (i.e. effectively constant wall effect, solid red in (a)).

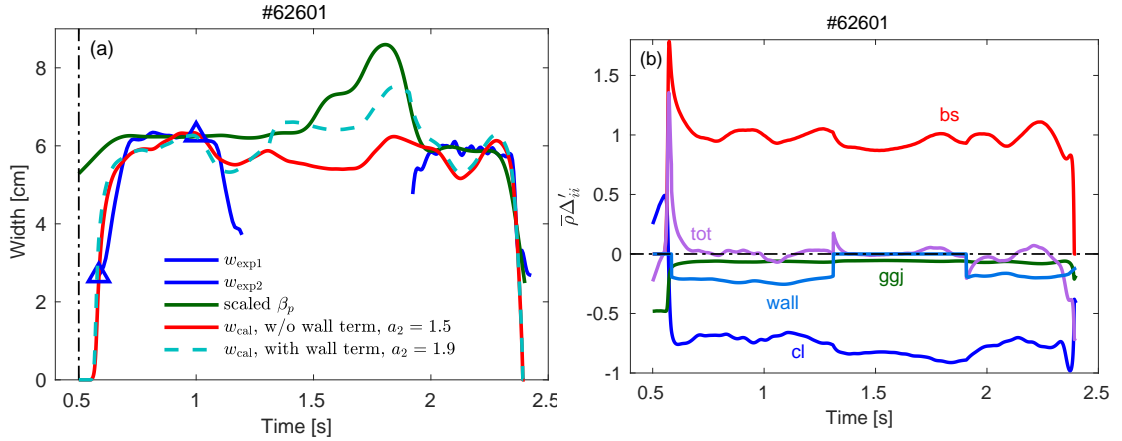


Figure B.10. Simulation results of #62601 (figure B.2). (a) Island width evolution: blue - experimental w based on magnetic probe measurements; red - simulation with the MRE without considering the wall effect (equation (3.3)); dashed cyan - simulation with the updated MRE including the wall term (equation (B.3)). (b) Time-evolution of various MRE terms of the simulation including wall effect (i.e. dashed cyan curve in (a)).

For the case of accelerated NTM with counter-NBI, simulations have been performed for TCV #62735 (figure B.8), as shown in figure B.11 (a). Simulation without including explicitly the wall term is depicted by the solid red trace, following the same procedures as used in previous chapters. The dashed cyan curve represents the simulation based on equation (B.3), with corresponding MRE terms illustrated in figure B.11 (b). It can be seen that the decrease of island width after turning on NBI at $t = 1$ s mainly results from a more stabilizing $\bar{\rho}_{mn} \Delta'$ shown by the blue trace in figure B.11 (b), similar to the simulation without the wall term (solid red curve in B.11 (a)). The more negative $\bar{\rho}_{mn} \Delta'$ stems from a decrease of the driven current from ECCD (based on TORAY-GA) during the ramp-up of NBI power, which leads to a smaller $\bar{\rho}_{mn} \Delta'_0$ based on equation (4.2) and thus decreased $\bar{\rho}_{mn} \Delta'$ (equation (3.25)).

Appendix B. Locking/Acceleration of NTMs with tangential neutral beam injection (NBI)

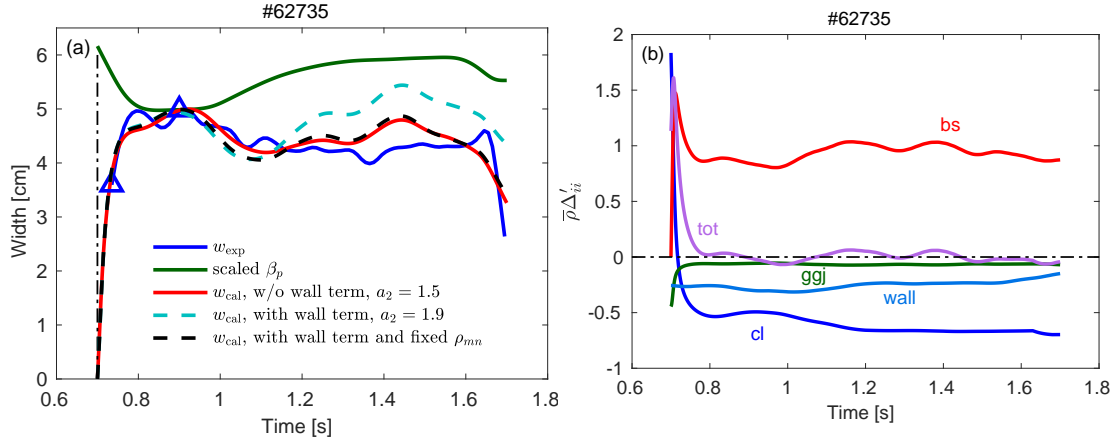


Figure B.11. Simulation results of #62735 (figure B.8). (a) Island width evolution: blue - experimental w based on magnetic probe measurements; red - simulation with the MRE without considering the wall effect (equation (3.3)); dashed cyan - simulation with the updated MRE including the wall term (equation (B.3)); dashed black - simulation including the wall term and with a fixed $\bar{\rho}_{mn}$. (b) Time-evolution of various MRE terms of the simulation including the wall effect (dashed cyan curve in (a)).

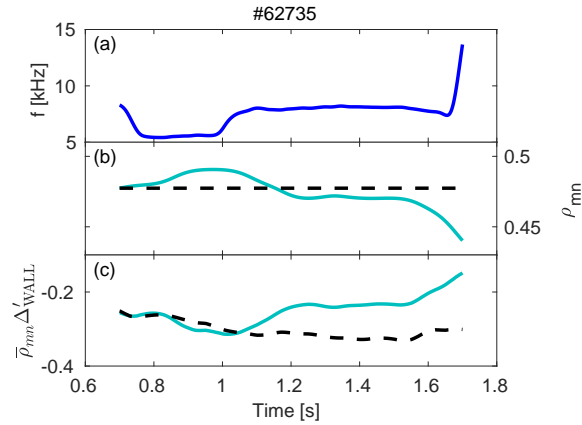


Figure B.12. Comparison of the simulated wall effect of the simulations shown in figure B.11 (a) (dashed cyan and black). (a) Rotation frequency of 2/1 NTM, taken from experimental measurements (figure B.8); (b) cyan - normalized radial location (with respect to a) of $q = 2$ surface, taken from ASTRA outputs; dashed black - a fixed ρ_{mn} used in the simulation shown by the dashed black curve in figure B.11 (a); (c) $\bar{\rho}_{mn} \Delta'_{\text{WALL}}$ of the simulations shown in figure B.11 (a), with the same color.

The simulated wall term, as shown in figure B.11 (b) or the cyan curve in figure B.12 (c), actually becomes less stabilizing with increasing mode frequency, leading to the increase of simulated w shown in figure B.11 (a) (dashed cyan). To better understand this phenomenon, the radial location of $q = 2$ surface taken from ASTRA outputs, another parameter in the definition of the wall effect (equation (B.2)), is shown as the cyan curve in figure B.12 (b). It can be seen that the computed $\bar{\rho}_{mn} \Delta'_{\text{WALL}}$ (figure B.12 (c)) is dominated by the evolution of ρ_{mn} in this case, given the relatively small change of mode frequency with NBI. Another simulation with

the wall term but a fixed $\bar{\rho}_{mn}$ (dashed black curve in figure B.12 (b)) for the computation of $\bar{\rho}_{mn}\Delta'_{\text{WALL}}$ is shown as the dashed black trace in figure B.11 (a) to better illustrate the effects of $\bar{\rho}_{mn}$ on $\bar{\rho}_{mn}\Delta'_{\text{WALL}}$ and w .

Similar simulations can be performed for more experiments presented in this appendix and future work can be carried out to solve the coupled equations (B.3) and (B.1). This will not only help to quantify the effects of various terms on NTM evolution, but also contribute to the validation of theoretical model and the determination of free coefficients involved, similar to the discussions in chapters 4 and 5. The validated model, especially the frequency equation, can then be used for real-time purposes, for example predicting the proximity of a given NTM to mode locking. This will further extend the capabilities of the RT-MRE discussed in chapter 6, facilitating the reliable control of NTMs and efficient integrated multi-actuator control of tokamak plasmas.

Bibliography

- S. Alberti, G. Arnoux, L. Porte, J. P. Hogge, B. Marletaz, P. Marmillod, Y. Martin, and S. Nowak. Third-harmonic, top-launch, ECRH experiments on TCV tokamak. *Nucl. Fusion*, 45(11): 1224–1231, 2005. ISSN 00295515. doi: 10.1088/0029-5515/45/11/002.
- S. Alberti, J. Genoud, T. Goodman, J.P. Hogge, L. Porte, M. Silva, T. M Tran, M. Q Tran, K. Avramidis, I. Pagonakis, J. Jin, S. Illy, G. Gantenbein, J. Jelonnek, M. Thumm, W. Bin, A. Bruschi, S. Garavaglia, A. Moro, W. Kasperek, F. Legrand, E. Perial, Y. Rozier, F. Cismondi, and N. Doelman. Recent progress in the upgrade of the TCV EC-system with two 1MW/2s dual-frequency (84/126GHz) gyrotrons. *EPJ Web Conf.*, 157:95–98, 2017. ISSN 2100014X. doi: 10.1051/epjconf/201715703001.
- H. Anand, C. Galperti, S. Coda, B.P. Duval, F. Felici, T. Blanken, E. Maljaars, J.-M. Moret, O. Sauter, T.P. Goodman, and D. Kim. Distributed digital real-time control system for the TCV tokamak and its applications. *Nucl. Fusion*, 57(5):056005, 2017. ISSN 0029-5515. doi: 10.1088/1741-4326/aa6120.
- C. Angioni, T. P. Goodman, M. A. Henderson, and O. Sauter. Effects of localized electron heating and current drive on the sawtooth period. *Nucl. Fusion*, 43(6):455–468, 2003. ISSN 00295515. doi: 10.1088/0029-5515/43/6/308.
- M. Anton, H. Weisen, M. J. Dutch, W. Von Der Linden, and F. Buhlmann. X-ray tomography on the TCV tokamak. *Plasma Phys. Control. Fusion*, 38(11):1849–1878, 1996. doi: 10.1088/0741-3335/38/11/001.
- H. Arnichand, Y. Andrebe, P. Blanchard, S. Antonioni, S. Couturier, J. Decker, B.P. Duval, F. Felici, C. Galperti, P.-F. Isoz, P. Lavanchy, X. Llobet, B. Marlétaz, P. Marmillod, and J. Masur. New capabilities of the incoherent Thomson scattering diagnostics in the TCV tokamak: divertor and real-time measurements. *J. Instrum.*, 14(09):C09013–C09013, 2019. ISSN 1748-0221. doi: 10.1088/1748-0221/14/09/c09013.
- L. A. Artsimovich. Tokamak devices. *Nucl. Fusion*, 12(2):215–252, 1972. ISSN 17414326. doi: 10.1088/0029-5515/12/2/012.
- S. Barry. *The extension of the FIR interferometer of TCV to a polarimeter and measurements of the Faraday rotation caused by the poloidal magnetic field*. PhD thesis, National University of Ireland, 1999.

Bibliography

- V. Basiuk, P. Huynh, A. Merle, S. Nowak, and O. Sauter. Towards self-consistent plasma modelisation in presence of neoclassical tearing mode and sawteeth: Effects on transport coefficients. *Plasma Phys. Control. Fusion*, 59(12):125012, 2017. ISSN 13616587. doi: 10.1088/1361-6587/aa8c8c.
- N. Bertelli, D. De Lazzari, and E. Westerhof. Requirements on localized current drive for the suppression of neoclassical tearing modes. *Nucl. Fusion*, 51(10), 2011. ISSN 00295515. doi: 10.1088/0029-5515/51/10/103007.
- P. Blanchard. Thomson scattering measurements in the divertor region of the TCV Tokamak plasmas. *J. Instrum.*, 14(09):C10038, 2019. doi: 10.1088/1748-0221/14/10/C10038.
- T. C. Blanken, F. Felici, C. J. Rapson, M. R. de Baar, and W. P.M.H. Heemels. Control-oriented modeling of the plasma particle density in tokamaks and application to real-time density profile reconstruction. *Fusion Eng. Des.*, 126:87–103, 2018. ISSN 09203796. doi: 10.1016/j.fusengdes.2017.11.006.
- T.C. Blanken, F. Felici, C. Galperti, N.M.T. Vu, M. Kong, O. Sauter, and M.R. de Baar. Real-time plasma state monitoring and supervisory control on TCV. *Nucl. Fusion*, 59(2):026017, 2019. ISSN 0029-5515. doi: 10.1088/1741-4326/aaf451.
- A. Bortolon, B. P. Duval, A. Pochelon, and A. Scarabosio. Observation of spontaneous toroidal rotation inversion in ohmically heated tokamak plasmas. *Phys. Rev. Lett.*, 97(23):1–4, 2006. ISSN 10797114. doi: 10.1103/PhysRevLett.97.235003.
- D. P. Brennan, R. J. La Haye, A. D. Turnbull, M. S. Chu, T. H. Jensen, L. L. Lao, T. C. Luce, P. A. Politzer, E. J. Strait, S. E. Kruger, and D. D. Schnack. A mechanism for tearing onset near ideal stability boundaries. *Phys. Plasmas*, 10(5):1643–1652, 2003. ISSN 1070-664X. doi: 10.1063/1.1555830.
- D. P. Brennan, A. D. Turnbull, M. S. Chu, R. J. La Haye, L. L. Lao, T. H. Osborne, and S. A. Galkin. Resistive stability of 2/1 modes near 1/1 resonance. *Phys. Plasmas*, 14(5), 2007. ISSN 1070664X. doi: 10.1063/1.2515224.
- R. J. Buttery, O. Sauter, R. Akers, M. Gryaznevich, R. Martin, C. D. Warrick, and H. R. Wilson. Neoclassical tearing physics in the spherical tokamak MAST. *Phys. Rev. Lett.*, 88(12):1250051–1250054, 2002. ISSN 00319007. doi: 10.1103/PhysRevLett.88.125005.
- R. J. Buttery, R. J. La Haye, P. Gohil, G. L. Jackson, H. Reimerdes, and E. J. Strait. The influence of rotation on the β_N threshold for the 2/1 neoclassical tearing mode in DIII-D. *Phys. Plasmas*, 15(5), 2008. ISSN 1070664X. doi: 10.1063/1.2894215.
- G. P. Canal, B. P. Duval, F. Felici, T. P. Goodman, J. P. Graves, A. Pochelon, H. Reimerdes, O. Sauter, and D. Testa. Fast seeding of NTMs by sawtooth crashes in TCV and their preemption using ECRH. *Nucl. Fusion*, 53(11), 2013. ISSN 00295515. doi: 10.1088/0029-5515/53/11/113026.

- Z. Chang and J. D. Callen. Global energy confinement degradation due to macroscopic phenomena in tokamaks. *Nucl. Fusion*, 30(2):219–233, 1990. doi: 10.1088/0029-5515/30/2/003.
- I. T. Chapman. Controlling sawtooth oscillations in tokamak plasmas. *Plasma Phys. Control. Fusion*, 53(1), 2011. ISSN 07413335. doi: 10.1088/0741-3335/53/1/013001.
- O. Chellaï, S. Alberti, M. Baquero-Ruiz, I. Furno, T. Goodman, B. Labit, O. Maj, P. Ricci, F. Riva, L. Guidi, and E. Poli. Millimeter-wave beam scattering by edge-plasma density fluctuations in TCV. *Plasma Phys. Control. Fusion*, 61(1):014001, 2019. ISSN 13616587. doi: 10.1088/1361-6587/aae7bf.
- Francis F. Chen. *Introduction to plasma physics and controlled fusion*. Springer, 2 edition, 2007. ISBN 978-8181288028.
- S. Coda, M. Agostini, R. Albanese, and Others. Physics research on the TCV tokamak facility : from conventional to alternative scenarios and beyond. *Nucl. Fusion*, 59(11):112023, 2019. doi: 10.1088/1741-4326/ab25cb.
- Ronald H. Cohen. Effect of trapped electrons on current drive. *Phys. Fluids*, 30(8):2442, 1987. ISSN 00319171. doi: 10.1063/1.866136.
- J. W. Connor, F. L. Waelbroeck, and H. R. Wilson. The role of polarization current in magnetic island evolution. *Phys. Plasmas*, 8(6):2835–2848, 2001. ISSN 1070664X. doi: 10.1063/1.1370062.
- D. De Lazzari and E. Westerhof. On the merits of heating and current drive for tearing mode stabilization. *Nucl. Fusion*, 49(7):075002, 2009. ISSN 00295515. doi: 10.1088/0029-5515/49/7/075002.
- D. De Lazzari and E. Westerhof. On the merits of heating and current drive for tearing mode stabilization. *Nucl. Fusion*, 50(7):079801, 2010. doi: 10.1088/0029-5515/50/7/079801.
- N. Den Harder, D. Rittich, G. Orozco, and C. Hopf. Neutral beam injection at ASDEX Upgrade: Transmission and beamline losses. *44th EPS Conf. Plasma Physics, EPS 2017*, pages 1–4, 2017. URL <http://ocs.ciemat.es/EPS2017PAP/pdf/P5.147.pdf>.
- S. S. Denk, R. Fischer, H. M. Smith, P. Helander, O. Maj, E. Poli, J. Stober, U. Stroth, W. Suttrop, E. Westerhof, and M. Willensdorfer. Analysis of electron cyclotron emission with extended electron cyclotron forward modeling. *Plasma Phys. Control. Fusion*, 60(10), 2018. ISSN 13616587. doi: 10.1088/1361-6587/aadb2f.
- T. P. Donaldson. Theory of foil-absorption techniques for plasma x-ray continuum measurements. *Plasma Phys.*, 20(12):1279–1289, 1978. ISSN 00321028. doi: 10.1088/0032-1028/20/12/005.

Bibliography

- B. Dudley. BP Statistical Review of World Energy Statistical Review of World. Technical report, 2019. URL <https://www.bp.com/content/dam/bp/business-sites/en/global/corporate/pdfs/energy-economics/statistical-review/bp-stats-review-2019-full-report.pdf>.
- N. W. Eidietis, W. Choi, S. H. Hahn, D. A. Humphreys, B. S. Sammulu, and M. L. Walker. Implementing a finite-state off-normal and fault response system for disruption avoidance in tokamaks. *Nucl. Fusion*, 58(5), 2018. ISSN 17414326. doi: 10.1088/1741-4326/aab62c.
- U. Fantz, P. Franzen, W. Kraus, M. Berger, S. Christ-Koch, M. Fröschle, R. Gutser, B. Heinemann, C. Martens, P. McNeely, R. Riedl, E. Speth, and D. Wunderlich. Negative ion RF sources for ITER NBI: Status of the development and recent achievements. *Plasma Phys. Control. Fusion*, 49(12 B), 2007. ISSN 07413335. doi: 10.1088/0741-3335/49/12B/S53.
- A. Fasoli, H. Reimerdes, S. Alberti, M. Baquero-Ruiz, B.P. Duval, E. Havlikova, A. Karpushov, J.-M. Moret, M. Toussaint, H. Elaian, M. Silva, C. Theiler, and D. Vaccaro. TCV heating and divertor upgrades. *Nucl. Fusion*, 60(1):016019, 2020. doi: 10.1088/1741-4326/ab4c56.
- H. Faugel, P. Angene, W. Becker, F. Braun, V. V. Bobkov, B. Eckert, F. Fischer, D. A. Hartmann, G. Heilmair, J. Kneidl, J. M. Noterdaeme, G. Siegl, and E. Würsching. The ASDEX upgrade ICRF system: Operational experience and developments. *Fusion Eng. Des.*, 74(1-4):319–324, 2005. ISSN 09203796. doi: 10.1016/j.fusengdes.2005.06.268.
- H. Faugel, V. Bobkov, H. Eixenberger, Y. Podoba, and I. Stepanov. Upgrading the ICRF data acquisition system at ASDEX Upgrade. *AIP Conf. Proc.*, 1580(February 2015):378–381, 2014. ISSN 15517616. doi: 10.1063/1.4864567.
- G. Federici, C. Bachmann, L. Barucca, W. Biel, L. Boccaccini, R. Brown, C. Bustreo, S. Ciattaglia, F. Cismondi, M. Coleman, V. Corato, C. Day, E. Diegele, U. Fischer, T. Franke, C. Gliss, A. Ibarra, R. Kembleton, A. Loving, F. Maviglia, B. Meszaros, G. Pintsuk, N. Taylor, M. Q. Tran, C. Vorpahl, R. Wenninger, and J. H. You. DEMO design activity in Europe: Progress and updates. *Fusion Eng. Des.*, 136(April):729–741, 2018. ISSN 09203796. doi: 10.1016/j.fusengdes.2018.04.001. URL <https://doi.org/10.1016/j.fusengdes.2018.04.001>.
- F. Felici, O. Sauter, T. P. Goodman, B. Labit, and C. Zucca. Self-consistent simulation of tearing modes during ECCD experiments on TCV. In *36th EPS Conf. Plasma Phys.*, 2009. ISBN 9781622763368. URL <https://infoscience.epfl.ch/record/142671>.
- F. Felici, O. Sauter, S. Coda, B. P. Duval, T. P. Goodman, J. M. Moret, and J. I. Paley. Real-time physics-model-based simulation of the current density profile in tokamak plasmas. *Nucl. Fusion*, 51(8), 2011. ISSN 00295515. doi: 10.1088/0029-5515/51/8/083052.
- F. Felici, T. P. Goodman, O. Sauter, G. Canal, S. Coda, B. P. Duval, and J. X. Rossel. Integrated real-time control of MHD instabilities using multi-beam ECRH/ECCD systems on TCV. *Nucl. Fusion*, 52(7), 2012. ISSN 00295515. doi: 10.1088/0029-5515/52/7/074001.
- F. Felici, T. Blanken, E. Maljaars, H. van den Brand, J. Citrin, D. Hogewei, M. Scheffer, M.R. de Baar, M. Steinbuch, S. Coda, and Others. Real-time model-based plasma state estimation,

- monitoring and integrated control in TCV, ASDEX-Upgrade and ITER. *26th IAEA Fusion Energy Conf.*, (633053):Poster-223469, 2016. URL <https://conferences.iaea.org/indico/event/98/session/32/contribution/519/material/paper/0.pdf>.
- Federico Felici. *Real-Time Control of Tokamak Plasmas: from Control of Physics to Physics-Based Control*. PhD thesis, École polytechnique fédérale de Lausanne, 2011. URL <http://dx.doi.org/10.5075/epfl-thesis-5203>.
- J. R. Ferron, M. L. Walker, L. L. Lao, H. E.S.T. John, D. A. Humphreys, and J. A. Leuer. Real time equilibrium reconstruction for tokamak discharge control. *Nucl. Fusion*, 38(7):1055–1066, 1998. ISSN 00295515. doi: 10.1088/0029-5515/38/7/308.
- O. Février, P. Maget, H. Lütjens, J. F. Luciani, J. Decker, G. Giruzzi, M. Reich, P. Beyer, E. Lazzaro, and S. Nowak. First principles fluid modelling of magnetic island stabilization by electron cyclotron current drive (ECCD). *Plasma Phys. Control. Fusion*, 58(4):45015, 2016. ISSN 13616587. doi: 10.1088/0741-3335/58/4/045015.
- O. Février, P. Maget, H. Lütjens, and P. Beyer. Comparison of magnetic island stabilization strategies from magneto-hydrodynamic simulations. *Plasma Phys. Control. Fusion*, 59(4): 1–14, 2017. ISSN 13616587. doi: 10.1088/1361-6587/aa5861.
- R. Fitzpatrick. Helical temperature perturbations associated with tearing modes in tokamak plasmas. *Phys. Plasmas*, 2(3):825–838, 1995. ISSN 1070664X. doi: 10.1063/1.871434.
- O. P. Ford, J. Howard, and R. C. Wolf. The prototype imaging motional Stark effect diagnostic for ASDEX upgrade. *Rev. Sci. Instrum.*, 86(9), 2015. ISSN 10897623. doi: 10.1063/1.4929873. URL <http://dx.doi.org/10.1063/1.4929873>.
- E. D. Fredrickson. Observation of spontaneous neoclassical tearing modes. *Phys. Plasmas*, 9(2):548, 2002. ISSN 1070664X. doi: 10.1063/1.1435003.
- Jeffery Freidberg. *Plasma physics and fusion energy*. Cambridge University Press, New York, 2007.
- C. Galperti, C. Marchetto, E. Alessi, D. Minelli, M. Mosconi, F. Belli, L. Boncagni, A. Botrugno, P. Buratti, G. Calabro', B. Esposito, S. Garavaglia, G. Granucci, A. Grosso, V. Meller, A. Moro, V. Piergotti, G. Pucella, G. Ramogida, W. Bin, and C. Sozzi. Development of real-time MHD markers based on biorthogonal decomposition of signals from Mirnov coils. *Plasma Phys. Control. Fusion*, 56(11), 2014. ISSN 13616587. doi: 10.1088/0741-3335/56/11/114012.
- C. Galperti, S. Coda, B. P. Duval, X. Llobet, P. Milne, O. Sauter, J. M. Moret, and D. Testa. Integration of a Real-Time Node for Magnetic Perturbations Signal Analysis in the Distributed Digital Control System of the TCV Tokamak. *IEEE Trans. Nucl. Sci.*, 64(6):1446–1454, 2017. ISSN 00189499. doi: 10.1109/TNS.2017.2711625.
- G. Gantenbein, H. Zohm, G. Giruzzi, and S. Günter. Complete Suppression of Neoclassical Tearing Modes with Current Drive at the Electron-Cyclotron-Resonance Frequency in ASDEX Upgrade Tokamak. *Phys. Rev. Lett.*, 85(6):1242–1245, 2000. doi: 10.1103/PhysRevLett.85.1242.

Bibliography

- J. Genoud, S. Alberti, T. M. Tran, G. Le Bars, P. Kaminski, J. Ph Hogge, K. A. Avramidis, and M. Q. Tran. Parasitic Oscillations in Smooth-Wall Circular Symmetric Gyrotron Beam Ducts. *J. Infrared, Millimeter, Terahertz Waves*, 40(2):131–149, 2019. ISSN 18666906. doi: 10.1007/s10762-018-0548-5.
- S. P. Gerhardt, D. P. Brennan, R. Buttery, R. J. La Haye, S. Sabbagh, E. Strait, M. Bell, R. Bell, E. Fredrickson, D. Gates, B. Leblanc, J. Menard, D. Stutman, K. Tritz, and H. Yuh. Relationship between onset thresholds, trigger types and rotation shear for the $m/n = 2/1$ neoclassical tearing mode in a high- β spherical torus. *Nucl. Fusion*, 49(3):032003, 2009. ISSN 00295515. doi: 10.1088/0029-5515/49/3/032003.
- A. H. Glasser, Z. R. Wang, and J. K. Park. Computation of resistive instabilities by matched asymptotic expansions. *Phys. Plasmas*, 23(11), 2016. ISSN 10897674. doi: 10.1063/1.4967862.
- A. S. Glasser and E. Kolemen. A robust solution for the resistive MHD toroidal deltap matrix in near real-time. *Phys. Plasmas*, 25(8), 2018. ISSN 10897674. doi: 10.1063/1.5029477.
- T. P. Goodman. Experience in integrated control of the multi-megawatt electron cyclotron heating system on the TCV tokamak: The first decade. *Nucl. Fusion*, 48(5), 2008. doi: 10.1088/0029-5515/48/5/054011.
- T. P. Goodman, F. Felici, O. Sauter, and J. P. Graves. Sawtooth pacing by real-time auxiliary power control in a tokamak plasma. *Phys. Rev. Lett.*, 106(24):15–18, 2011. ISSN 00319007. doi: 10.1103/PhysRevLett.106.245002.
- J. P. Graves, I. Chapman, S. Coda, L. G. Eriksson, and T. Johnson. Sawtooth-control mechanism using toroidally propagating ion-cyclotron-resonance waves in tokamaks. *Phys. Rev. Lett.*, 102(6):1–4, 2009. ISSN 10797114. doi: 10.1103/PhysRevLett.102.065005.
- A. Gude, S. Günter, and S. Sesnic. Seed island of neoclassical tearing modes at ASDEX Upgrade. *Nucl. Fusion*, 39(1-4):127–131, 1999. ISSN 00295515. doi: 10.1088/0029-5515/39/1/308.
- J. Hawke, Y. Andrebe, R. Bertizzolo, P. Blanchard, R. Chavan, J. Decker, B. Duval, P. Lavanchy, X. Llobet, B. Marlétaz, P. Marmillod, G. Pochon, and M. Toussaint. Improving spatial and spectral resolution of TCV Thomson scattering. *J. Instrum.*, 12(12), 2017. ISSN 17480221. doi: 10.1088/1748-0221/12/12/C12005.
- C. C. Hegna and J. D. Callen. On the stabilization of neoclassical magnetohydrodynamic tearing modes using localized current drive or heating. *Phys. Plasmas*, 4(8):2940–2946, 1997. ISSN 1070664X. doi: 10.1063/1.872426.
- R. S. Hemsworth, A. Tanga, and V. Antoni. Status of the ITER neutral beam injection system (invited). *Rev. Sci. Instrum.*, 79(2), 2008. ISSN 00346748. doi: 10.1063/1.2814248.
- T. C. Hender, J. C. Wesley, J. Bialek, A. Bondeson, A. H. Boozer, R. J. Buttery, A. Garofalo, T. P. Goodman, R. S. Granetz, Y. Gribov, O. Gruber, M. Gryaznevich, G. Giruzzi, S. Günter, N. Hayashi, P. Helander, C. C. Hegna, D. F. Howell, D. A. Humphreys, G. T.A. Huysmans, A. W.

- Hyatt, A. Isayama, S. C. Jardin, Y. Kawano, A. Kellman, C. Kessel, H. R. Koslowski, R. J. La Haye, E. Lazzaro, Y. Q. Liu, V. Lukash, J. Manickam, S. Medvedev, V. Mertens, S. V. Mirnov, Y. Nakamura, G. Navratil, M. Okabayashi, T. Ozeki, R. Paccagnella, G. Pautasso, F. Porcelli, V. D. Pustovitov, V. Riccardo, M. Sato, O. Sauter, M. J. Schaffer, M. Shimada, P. Sonato, E. J. Strait, M. Sugihara, M. Takechi, A. D. Turnbull, E. Westerhof, D. G. Whyte, R. Yoshino, and H. Zohm. Chapter 3: MHD stability, operational limits and disruptions. *Nucl. Fusion*, 47(6), 2007. ISSN 00295515. doi: 10.1088/0029-5515/47/6/S03.
- M. Henderson, G. Saibene, C. Darbos, D. Farina, L. Figini, M. Gagliardi, F. Gandini, T. Gassmann, G. Hanson, A. Loarte, T. Omori, E. Poli, D. Purohit, and K. Takahashi. The targeted heating and current drive applications for the ITER electron cyclotron system. *Phys. Plasmas*, 22(2), 2015. ISSN 10897674. doi: 10.1063/1.4908598.
- B. A. Hennen, E. Westerhof, P. W.J.M. Nuij, J. W. Oosterbeek, M. R. De Baar, W. A. Bongers, A. Bürger, D. J. Thoen, and M. Steinbuch. Real-time control of tearing modes using a line-of-sight electron cyclotron emission diagnostic. *Plasma Phys. Control. Fusion*, 52(10), 2010. ISSN 07413335. doi: 10.1088/0741-3335/52/10/104006.
- F. Hofmann, J. B. Lister, W. Anton, S. Barry, R. Behn, S. Bernel, G. Besson, F. Buhlmann, R. Chavan, M. Corboz, M. J. Dutch, B. P. Duval, D. Fasel, A. Favre, S. Franke, A. Heym, A. Hirt, C. Hollenstein, P. Isoz, B. Joye, X. Llobet, J. C. Magnin, B. Marletaz, P. Marmillod, Y. Martin, J. M. Mayor, J. M. Moret, C. Nieswand, P. J. Paris, A. Perez, Z. A. Pietrzyk, R. A. Pitts, A. Pochelon, R. Rage, O. Sauter, G. Tonetti, M. Q. Tran, F. Troyon, D. J. Ward, and H. Weisen. Creation and control of variably shaped plasmas in TCV. *Plasma Phys. Control. Fusion*, 36(12):B277, 1994. doi: 10.1088/0741-3335/36/12B/023.
- C. Hopf, D. Rittich, J. Schäffler, and J. Thalhammer. Helium neutral beam injection into ASDEX Upgrade. *Fusion Eng. Des.*, 123:281–284, 2017. ISSN 09203796. doi: 10.1016/j.fusengdes.2017.05.052.
- D. Humphreys, G. Ambrosino, P. De Vries, F. Felici, S. H. Kim, G. Jackson, A. Kallenbach, E. Kolemen, J. Lister, D. Moreau, A. Pironti, G. Raupp, O. Sauter, E. Schuster, J. Snipes, W. Treutterer, M. Walker, A. Welander, A. Winter, and L. Zabeo. Novel aspects of plasma control in ITER. *Phys. Plasmas*, 22(2), 2015. ISSN 10897674. doi: 10.1063/1.4907901.
- D. A. Humphreys, J. R. Ferron, R. J. La Haye, T. C. Luce, C. C. Petty, R. Prater, and A. S. Welander. Active control for stabilization of neoclassical tearing modes. *Phys. Plasmas*, 13(5), 2006. ISSN 1070664X. doi: 10.1063/1.2173606.
- K. Imada, H. R. Wilson, J. W. Connor, A. V. Dudkovskaia, and P. Hill. Finite ion orbit width effect on the neoclassical tearing mode threshold in a tokamak plasma. *Nucl. Fusion*, 59(4): ab00ba, 2019. ISSN 17414326. doi: 10.1088/1741-4326/ab00ba.
- A. Isayama. Steady-state sustainment of high- β plasmas through stability control in Japan Atomic Energy Research Institute Tokamak-60 Upgrade. *Phys. Plasmas*, 12(5):1–10, 2005. ISSN 1070664X. doi: 10.1063/1.1883669.

Bibliography

- A. Isayama, Y. Kamada, S. Ide, K. Hamamatsu, T. Oikawa, T. Suzuki, Y. Neyatani, T. Ozeki, Y. Ikeda, and K. Kajiwara. Complete stabilization of a tearing mode in steady state high- β p H-mode discharges by the first harmonic electron cyclotron heating/current drive on JT-60U. *Plasma Phys. Control. Fusion*, 42(12):L37–L45, 2000. ISSN 0741-3335. doi: 10.1088/0741-3335/42/12/102.
- A. Isayama, Y. Kamada, N. Hayashi, T. Suzuki, T. Oikawa, T. Fujita, T. Fukuda, S. Ide, H. Takenaga, K. Ushigusa, T. Ozeki, Y. Ikeda, N. Umeda, H. Yamada, M. Isobe, Y. Narushima, K. Ikeda, S. Sakakibara, K. Yamazaki, and K. Nagasaki. Achievement of high fusion triple product, steady-state sustainment and real-time NTM stabilization in high- β p ELMy H-mode discharges in JT-60U. *Nucl. Fusion*, 43(10):1272–1278, 2003. ISSN 00295515. doi: 10.1088/0029-5515/43/10/031.
- A. Isayama, G. Matsunaga, T. Kobayashi, S. Moriyama, N. Oyama, Y. Sakamoto, T. Suzuki, H. Urano, N. Hayashi, Y. Kamada, T. Ozeki, Y. Hirano, L. Urso, H. Zohm, M. Maraschek, J. Hobirk, and K. Nagasaki. Neoclassical tearing mode control using electron cyclotron current drive and magnetic island evolution in JT-60U. *Nucl. Fusion*, 49(5), 2009. ISSN 00295515. doi: 10.1088/0029-5515/49/5/055006.
- X. Q. Ji, Y. Xu, C. Hidalgo, P. H. Diamond, Yi Liu, O. Pan, Z. B. Shi, and D. L. Yu. On the interplay between neoclassical tearing modes and nonlocal transport in toroidal plasmas. *Sci. Rep.*, 6 (September):1–8, 2016. ISSN 20452322. doi: 10.1038/srep32697.
- A. N. Karpushov, R. Chavan, S. Coda, V.I. Davydenko, F. Dolizy, A.N. Dranitchnikov, B. P. Duval, A. A. Ivanov, D. Fasel, A. Fasoli, V. V. Kolmogorov, P. Lavanchy, X. Llobet, B. Marlétaz, P. Marmillod, Y. Martin, A. Merle, A. Perez, O. Sauter, U. Siravo, I. V. Shikhovtsev, A. V. Sorokin, and M. Toussaint. Neutral beam heating on the TCV tokamak. *Fusion Eng. Des.*, 123:468–472, 2017. doi: 10.1016/j.fusengdes.2017.02.076.
- M. Keilhacker, A. Gibson, C. Gormezano, P. J. Lomas, P. R. Thomas, M. L. Watkins, P. Andrew, B. Balet, D. Borba, C. D. Challis, I. Coffey, G. A. Cottrell, H. P.L. De Esch, N. Deliyanakis, A. Fasoli, C. W. Gowers, H. Y. Guo, G. T.A. Huysmans, T. T.C. Jones, W. Kerner, R. W.T. König, M. J. Loughlin, A. Maas, F. B. Marcus, M. F.F. Nave, F. G. Rimini, G. J. Sadler, S. E. Sharapov, G. Sips, P. Smeulders, F. X. Söldner, A. Taroni, B. J.D. Tubbing, M. G. Von Hellermann, and D. J. Ward. High fusion performance from deuterium-tritium plasmas in JET. *Nucl. Fusion*, 39(2):209–234, 1999. ISSN 00295515. doi: 10.1088/0029-5515/39/2/306.
- Doohyun Kim. *Real-Time Control of Sawteeth and NTMs in TCV and ITER*. PhD thesis, École polytechnique fédérale de Lausanne, 2015. URL <http://dx.doi.org/10.5075/epfl-thesis-5203>.
- M. Kim, Kyungjin Kim, M. G. Yoo, D. H. Na, T. S. Hahm, Y. S. Hwang, and Yong Su Na. Numerical study on neoclassical tearing mode stabilization via minimum seeking method for the island width growth rate. *Nucl. Fusion*, 55(2):023006, 2015. ISSN 17414326. doi: 10.1088/0029-5515/55/2/023006.

- N. A. Kirneva, R. Behn, G. P. Canal, S. Coda, B. P. Duval, T. P. Goodman, B. Labit, N. A. Mustafin, A. N. Karpushov, A. Pochelon, L. Porte, O. Sauter, M. Silva, B. Tal, and V. Vuille. High density experiments in TCV ohmically heated and L-mode plasmas. *Plasma Phys. Control. Fusion*, 57(2), 2015. ISSN 13616587. doi: 10.1088/0741-3335/57/2/025002.
- R. Koch. The ion cyclotron, lower hybrid and alfvén wave heating methods. *Fusion Sci. Technol.*, 49(2T):187–194, 2006. doi: 10.13182/FST06-A1118.
- E. Kolemen, A. S. Welander, R. J. La Haye, N. W. Eidietis, D. A. Humphreys, J. Lohr, V. Noraky, B. G. Penaflor, R. Prater, and F. Turco. State-of-the-art neoclassical tearing mode control in DIII-D using real-time steerable electron cyclotron current drive launchers. *Nucl. Fusion*, 54(7), 2014. ISSN 17414326. doi: 10.1088/0029-5515/54/7/073020.
- M. Kong, O. Sauter, T. C. Blanken, F. Felici, C. Galperti, T. P. Goodman, G. M.D. Hogeweij, D. Kim, S. H. Kim, E. Maljaars, B. Mavkov, A. Merle, M. Reich, and T. Vu. Real-time control of neoclassical tearing modes and its integration with multiple controllers in the TCV Tokamak. In *44th EPS Conf. Plasma Physics, EPS 2017*, pages 3–6, 2017. ISBN 9781510849303. URL <http://ocs.ciemat.es/EPS2017PAP/pdf/P4.152.pdf>.
- M. Kong, T.C. Blanken, F. Felici, C. Galperti, E. Maljaars, O. Sauter, T. Vu, F. Carpanese, A. Merle, J.-M. Moret, F. Pesamosca, E. Poli, M. Reich, and A.A. Teplukhina. Control of neoclassical tearing modes and integrated multi-actuator plasma control on TCV. *Nucl. Fusion*, 59(7): 076035, 2019. doi: 10.1088/1741-4326/ab1e1e.
- M. Kong, O. Sauter, F. Felici, A. Merle, and S. Nowak. On the triggerless onset of 2 / 1 neoclassical tearing modes in TCV. *Nucl. Fusion*, 60(2):026002, 2020. doi: 10.1088/1741-4326/ab56c5.
- H. R. Koslowski, M. F. F. Nave, B. Alper, C. Perez von Thun, S. D. Pinches, O. Sauter, and S. E. Sharapov. MHD studies in radiating mantle plasmas on JET. In *21st EPS Conf. Plasma Physics, Funchal (PT), 18-22 June*, volume 23, page 1999, 2001.
- M. Kovari, M. Coleman, I. Cristescu, and R. Smith. Tritium resources available for fusion reactors. *Nucl. Fusion*, 58(2), 2018. ISSN 17414326. doi: 10.1088/1741-4326/aa9d25.
- R. J. La Haye. Neoclassical tearing modes and their control. *Phys. Plasmas*, 13(5), 2006. ISSN 1070664X. doi: 10.1063/1.2180747.
- R. J. La Haye and O. Sauter. Threshold for metastable tearing modes in DIII-D. *Nucl. Fusion*, 38(7):987–999, 1998. ISSN 00295515. doi: 10.1088/0029-5515/38/7/303.
- R. J. La Haye, B. W. Rice, and E. J. Strait. Increasing the beta limit due to neoclassical tearing modes by raising the axial safety factor $q(0) > 1$. *Nucl. Fusion*, 40(1):53–58, 2000. ISSN 00295515. doi: 10.1088/0029-5515/40/1/304.
- R. J. La Haye, S. Günter, D. A. Humphreys, J. Lohr, T. C. Luce, M. E. Maraschek, C. C. Petty, R. Prater, J. T. Scoville, and E. J. Strait. Control of neoclassical tearing modes in DIII-D. *Phys. Plasmas*, 9(5):2051–2060, 2002. ISSN 1070664X. doi: 10.1063/1.1456066. URL <https://doi.org/10.1063/1.1456066>.

Bibliography

- R. J. La Haye, D. A. Humphreys, J. R. Ferron, T. C. Luce, F. W. Perkins, C. C. Petty, R. Prater, E. J. Strait, and A. S. Welander. Higher stable beta by use of pre-emptive electron cyclotron current drive on DIII-D. *Nucl. Fusion*, 45(11):11–16, 2005. ISSN 00295515. doi: 10.1088/0029-5515/45/11/L02.
- R. J. La Haye, R. Prater, R. J. Buttery, N. Hayashi, A. Isayama, M. E. Maraschek, L. Urso, and H. Zohm. Cross-machine benchmarking for ITER of neoclassical tearing mode stabilization by electron cyclotron current drive. *Nucl. Fusion*, 46(4):451–461, 2006. ISSN 00295515. doi: 10.1088/0029-5515/46/4/006.
- R.J. La Haye, A. Isayama, and M. Maraschek. Prospects for stabilization of neoclassical tearing modes by electron cyclotron current drive in ITER. *Nucl. Fusion*, 49:1–8, 2009. doi: 10.1088/0029-5515/49/4/045005.
- B. Labit, G. P. Canal, N. Christen, B. P. Duval, B. Lipschultz, T. Lunt, F. Nespoli, H. Reimerdes, U. Sheikh, C. Theiler, C. K. Tsui, K. Verhaegh, and W. A.J. Vijvers. Experimental studies of the snowflake divertor in TCV. *Nucl. Mater. Energy*, 12:1015–1019, 2017. ISSN 23521791. doi: 10.1016/j.nme.2017.03.013.
- M. Lauret, F. Felici, G. Witvoet, T. P. Goodman, G. Vandersteen, O. Sauter, and M. R. De Baar. Demonstration of sawtooth period locking with power modulation in TCV plasmas. *Nucl. Fusion*, 52(6), 2012. ISSN 00295515. doi: 10.1088/0029-5515/52/6/062002.
- E. Lazzaro, S. Nowak, O. Sauter, G. Canal, B. Duval, L. Federspiel, A. N. Karpushov, D. Kim, H. Reimerdes, J. Rossel, D. Testa, and D. Wagner. Effects of central electron cyclotron power on plasma rotation and on triggerless onset of NTMs in the TCV tokamak. *Nucl. Fusion*, 55(9):93031, 2015. ISSN 17414326. doi: 10.1088/0029-5515/55/9/093031.
- H. B. Le, F. Felici, J. I. Paley, B. P. Duval, J. M. Moret, S. Coda, O. Sauter, D. Fasel, and P. Marmillod. Distributed digital real-time control system for TCV tokamak. *Fusion Eng. Des.*, 89(3):155–164, 2014. ISSN 09203796. doi: 10.1016/j.fusengdes.2013.11.001.
- M. Lennholm, T. Blackman, I. T. Chapman, L. G. Eriksson, J. P. Graves, D. F. Howell, M. De Baar, G. Calabro, R. Dumont, M. Graham, S. Jachmich, M. L. Mayoral, C. Sozzi, M. Stamp, M. Tsalas, and P. De Vries. Feedback control of the sawtooth period through real time control of the ion cyclotron resonance frequency. *Nucl. Fusion*, 51(7), 2011. ISSN 00295515. doi: 10.1088/0029-5515/51/7/073032.
- Y. R. Lin-Liu, V. S. Chan, and R. Prater. Electron cyclotron current drive efficiency in general tokamak geometry. *Phys. Plasmas*, 10(10):4064–4071, 2003. ISSN 1070-664X. doi: 10.1063/1.1610472.
- J. B. Lister, F. Hofmann, J.-M. Moret, F. Bühlmann, M. J. Dutch, D. Fasel, A. Favre, P. F. Isoz, B. Marletaz, P. Marmillod, Y. Martin, A. Perez, and D. J. Ward. The control of tokamak configuration variable plasmas. *Fusion Technol.*, 32(3):321–373, 1997. ISSN 07481896. doi: 10.13182/FST97-A1.

- F. K. Liu, B. J. Ding, J. G. Li, B. N. Wan, J. F. Shan, M. Wang, L. Liu, L. M. Zhao, M. H. Li, Y. C. Li, Y. Yang, Z. G. Wu, J. Q. Feng, H. C. Hu, H. Jia, Y. Y. Huang, W. Wei, M. Cheng, L. Xu, Q. Zang, B. Lyu, S. Y. Lin, Y. M. Duan, J. H. Wu, Y. Peysson, J. Decker, J. Hillairet, A. Ekedahl, Z. P. Luo, J. P. Qian, B. Shen, X. Z. Gong, and L. Q. Hu. First results of LHCD experiments with 4.6 GHz system toward steady-state plasma in EAST. *Nucl. Fusion*, 55(12), 2015. ISSN 17414326. doi: 10.1088/0029-5515/55/12/123022.
- N. J. Lopes Cardozo, A. G.G. Lange, and G. J. Kramer. Fusion: Expensive and Taking Forever? *J. Fusion Energy*, 35(1):94–101, 2016. ISSN 01640313. doi: 10.1007/s10894-015-0012-7.
- E. Maljaars and F. Felici. Actuator allocation for integrated control in tokamaks: architectural design and a mixed-integer programming algorithm. *Fusion Eng. Des.*, 122(August):94–112, 2017. ISSN 09203796. doi: 10.1016/j.fusengdes.2017.09.004.
- E. Maljaars, F. Felici, T. C. Blanken, C. Galperti, O. Sauter, M. R. De Baar, F. Carpanese, T. P. Goodman, D. Kim, S. H. Kim, M. Kong, B. Mavkov, A. Merle, J. M. Moret, R. Nouailletas, M. Scheffer, A. A. Teplukhina, and N. M.T. Vu. Profile control simulations and experiments on TCV: A controller test environment and results using a model-based predictive controller. *Nucl. Fusion*, 57(12), 2017. ISSN 17414326. doi: 10.1088/1741-4326/aa8c48.
- M. Maraschek. Control of neoclassical tearing modes. *Nucl. Fusion*, 52(7), 2012. ISSN 00295515. doi: 10.1088/0029-5515/52/7/074007.
- M. Maraschek, G. Gantenbein, T. P. Goodman, S. Günter, D. F. Howell, F. Leuterer, A. Mück, O. Sauter, and H. Zohm. Active control of MHD instabilities by ECCD in ASDEX Upgrade. *Nucl. Fusion*, 45(11):1369–1376, 2005. ISSN 17414326. doi: 10.1088/0029-5515/45/11/018.
- M. Maraschek, G. Gantenbein, Q. Yu, H. Zohm, S. Günter, F. Leuterer, and A. Manini. Enhancement of the stabilization efficiency of a neoclassical magnetic island by modulated electron cyclotron current drive in the ASDEX upgrade Tokamak. *Phys. Rev. Lett.*, 98(2):13–16, 2007. ISSN 00319007. doi: 10.1103/PhysRevLett.98.025005.
- Claudio Marini. *Poloidal CX visible light plasma rotation diagnostics in TCV*. PhD thesis, École polytechnique fédérale de Lausanne, 2017. URL <http://dx.doi.org/10.5075/epfl-thesis-8031>.
- K. Matsuda. Ray Tracing Study of the Electron Cyclotron Current Drive In DIII-D Using 60 GHz. *IEEE Trans. Plasma Sci.*, 17(1):6–11, 1989. ISSN 19399375. doi: 10.1109/27.21664.
- B. Mavkov, E. Witrant, C. Prieur, and D. Moreau. Multi-experiment state-space identification of coupled magnetic and kinetic parameters in tokamak plasmas. *Control Eng. Pract.*, 60 (July 2016):28–38, 2017. ISSN 09670661. doi: 10.1016/j.conengprac.2016.12.006.
- J. P. Meskat, H. Zohm, G. Gantenbein, and And Others. Analysis of the structure of neoclassical tearing modes in ASDEX Upgrade Analysis of the structure of neoclassical tearing modes in ASDEX Upgrade. *Nucl. Fusion*, 43:1325–1332, 2001.

Bibliography

- H. Meyer. Overview of physics studies on ASDEX Upgrade. *Nucl. Fusion*, 59(11):112014, 2019. doi: 10.1088/1741-4326/ab18b8.
- J. M. Moret, F. Buhlmann, D. Fasel, F. Hofmann, and G. Tonetti. Magnetic measurements on the TCV Tokamak. *Rev. Sci. Instrum.*, 69(6):2333–2348, 1998. ISSN 00346748. doi: 10.1063/1.1148940.
- J. M. Moret, B. P. Duval, H. B. Le, S. Coda, F. Felici, and H. Reimerdes. Tokamak equilibrium reconstruction code LIUQE and its real time implementation. *Fusion Eng. Des.*, 91:1–15, 2015. ISSN 09203796. doi: 10.1016/j.fusengdes.2014.09.019.
- K. Nagasaki, A. Isayama, and S. Ide. Stabilization effect of early ECCD on a neoclassical tearing mode in the JT-60U tokamak. *Nucl. Fusion*, 43(10), 2003. ISSN 00295515. doi: 10.1088/0029-5515/43/10/L01.
- K. Nagasaki, A. Isayama, N. Hayashi, T. Ozeki, M. Takechi, N. Oyama, S. Ide, and S. Yamamoto. Stabilization of neoclassical tearing mode by ECCD and its evolution simulation on JT-60U tokamak. *Nucl. Fusion*, 45(12):1608–1617, 2005. ISSN 00295515. doi: 10.1088/0029-5515/45/12/016.
- R. Neu, M. Balden, and V. Bobkov. Plasma wall interaction and its implication in an all tungsten divertor tokamak. *Plasma Phys. Control. Fusion*, 49(12 B), 2007. ISSN 13616587. doi: 10.1088/0741-3335/49/12B/S04.
- P. Nikkola, O. Sauter, R. Behn, S. Coda, I. Condrea, T. P. Goodman, M. A. Henderson, and R. W. Harvey. Modelling of the electron cyclotron current drive experiments in the TCV tokamak. *Nucl. Fusion*, 43(11):1343–1352, 2003. ISSN 00295515. doi: 10.1088/0029-5515/43/11/006.
- S. Nowak, E. Lazzaro, O. Sauter, G. Canal, B. Duval, L. Federspiel, A. N. Karpushov, D. Kim, D. Raju, H. Reimerders, J. Rossel, D. Testa, and D. Wagner. Plasma rotation and NTM onset driven by central EC deposition in TCV tokamak. *AIP Conf. Proc.*, 1580(February):502–505, 2014. ISSN 15517616. doi: 10.1063/1.4864598.
- T. Omori, F. Albajar, T. Bonicelli, G. Carannante, M. Cavinato, F. Cismondi, C. Darbos, G. Denisov, Daniela Farina, Mario Gagliardi, F. Gandini, T. Gassmann, T. Goodman, G. Hanson, M. A. Henderson, K. Kajiwara, K. McElhaney, R. Nousiainen, Y. Oda, A. Oustinov, D. Parmar, V. L. Popov, D. Purohit, S.L. Rao, D. Rasmussen, V. Rathod, D.M.S. Ronden, G. Saibene, K. Sakamoto, F. Sartori, T. Scherer, N. P. Singh, D. Strauß, and K. Takahashi. Progress in the ITER electron cyclotron heating and current drive system design. *Fusion Eng. Des.*, 96-97:547–552, 2015. ISSN 09203796. doi: 10.1016/j.fusengdes.2014.12.023.
- J. W. Oosterbeek, A. Bürger, E. Westerhof, M. R. De Baar, M. A. Van Den Berg, W. A. Bongers, M. F. Graswinckel, B. A. Hennen, O. G. Kruijt, J. Thoen, R. Heidinger, S. B. Korsholm, F. Leipold, and S. K. Nielsen. A line-of-sight electron cyclotron emission receiver for electron cyclotron resonance heating feedback control of tearing modes. *Rev. Sci. Instrum.*, 79(9), 2008. ISSN 00346748. doi: 10.1063/1.2976665.

- J. I. Paley, S. Coda, B. Duval, F. Felici, and J. M. Moret. Architecture and commissioning of the TCV distributed feedback control system. *Conf. Rec. - 2010 17th IEEE-NPSS Real Time Conf. RT10*, 2010. doi: 10.1109/RTC.2010.5750487.
- Y. S. Park and A. S. Welanders. Real-time determination of magnetic island location for neoclassical tearing mode control in DIII-D. *Plasma Phys. Control. Fusion*, 48(9):1447–1454, 2006. ISSN 07413335. doi: 10.1088/0741-3335/48/9/013.
- R. J. Pearson, A. B. Antoniazzi, and W. J. Nuttall. Tritium supply and use: a key issue for the development of nuclear fusion energy. *Fusion Eng. Des.*, 136(November 2017):1140–1148, 2018. ISSN 09203796. doi: 10.1016/j.fusengdes.2018.04.090.
- A. G. Peeters. The bootstrap current and its consequences. *Plasma Phys. Control. Fusion*, 42: B231–B242, 2000.
- G. V. Pereverzev and P. N. Yushmanov. ASTRA: Automated System for Transport Analysis. Technical Report February, IPP, 2002.
- F. Piras, J. M. Moret, and J. X. Rossel. Measurement of the magnetic field errors on TCV. *Fusion Eng. Des.*, 85(5):739–744, 2010. doi: 10.1016/j.fusengdes.2010.04.049.
- A. Pletzer and F. W. Perkins. Stabilization of neoclassical tearing modes using a continuous localized current drive. *Phys. Plasmas*, 6(5):1589–1600, 1999. ISSN 1070-664X. doi: 10.1063/1.873412.
- E. Poli, A. Bergmann, and A. G. Peeters. Role of kinetic effects on the polarization current around a magnetic Island. *Phys. Rev. Lett.*, 94(20):1–4, 2005. ISSN 00319007. doi: 10.1103/PhysRevLett.94.205001.
- E. Poli, E. Fable, G. Tardini, H. Zohm, D. Farina, L. Figini, N. B. Marushchenko, and L. Porte. Epj-conf_Ec2012_01005.Pdf. *EPJ Web Conf.*, 32:01005, 2012. doi: 10.1051/epjconf/20123201005.
- E. Poli, C. Angioni, F. J. Casson, D. Farina, L. Figini, T. P. Goodman, O. Maj, O. Sauter, H. Weber, H. Zohm, G. Saibene, and M. A. Henderson. On recent results in the modelling of neoclassical-tearing-mode stabilization via electron cyclotron current drive and their impact on the design of the upper EC launcher for ITER. *Nucl. Fusion*, 55(1):13023, 2015. ISSN 17414326. doi: 10.1088/0029-5515/55/1/013023.
- E. Poli, A. Bock, M. Lochbrunner, O. Maj, M. Reich, A. Snicker, A. Stegmeir, F. Volpe, N. Bertelli, R. Bilato, G. D. Conway, D. Farina, F. Felici, L. Figini, R. Fischer, C. Galperti, T. Happel, Y. R. Lin-Liu, N. B. Marushchenko, U. Mszanowski, F. M. Poli, J. Stober, E. Westerhof, R. Zille, A. G. Peeters, and G. V. Pereverzev. TORBEAM 2.0, a paraxial beam tracing code for electron-cyclotron beams in fusion plasmas for extended physics applications. *Comput. Phys. Commun.*, 225:36–46, 2018a. ISSN 00104655. doi: 10.1016/j.cpc.2017.12.018.
- F. M. Poli, E. D. Fredrickson, M. A. Henderson, S. H. Kim, N. Bertelli, E. Poli, D. Farina, and L. Figini. Electron cyclotron power management for control of neoclassical tearing modes

Bibliography

- in the ITER baseline scenario. *Nucl. Fusion*, 58(1):aa8e0b, 2018b. ISSN 17414326. doi: 10.1088/1741-4326/aa8e0b.
- R. Prater. Heating and current drive by electron cyclotron waves. *Phys. Plasmas*, 11(5):2349, 2004. doi: 10.1063/1.1690762.
- R. Prater, R. J. La Haye, J. Lohr, T. C. Luce, C. C. Petty, J. R. Ferron, D. A. Humphreys, E. J. Strait, F. W. Perkins, and R. W. Harvey. Discharge improvement through control of neoclassical tearing modes by localized ECCD in DIII-D. *Nucl. Fusion*, 43(10):1128, 2003. doi: 10.1088/0029-5515/43/10/014.
- R. Prater, R. J. La Haye, T. C. Luce, C. C. Petty, E. J. Strait, J. R. Ferron, D. A. Humphreys, A. Isayama, J. Lohr, K. Nagasaki, P. A. Politzer, M. R. Wade, and A. S. Welander. Stabilization and prevention of the 2/1 neoclassical tearing mode for improved performance in DIII-D. *Nucl. Fusion*, 47(5), 2007. ISSN 00295515. doi: 10.1088/0029-5515/47/5/001.
- D. Rafalskyi and A. Aanesland. Brief review on plasma propulsion with neutralizer-free systems. *Plasma Sources Sci. Technol.*, 25(4), 2016. ISSN 13616595. doi: 10.1088/0963-0252/25/4/043001.
- G. Ramponi, E. Lazzaro, and S. Nowak. On the stabilization of neoclassical tearing modes by electron cyclotron waves. *Phys. Plasmas*, 6(9):3561–3570, 1999. ISSN 1070664X. doi: 10.1063/1.873633.
- C. Rapson, L. Giannone, M. Maraschek, M. Reich, J. Stober, and W. Treutterer. Amplitude based feedback control for NTM stabilisation at ASDEX Upgrade. *Fusion Eng. Des.*, 89(5): 568–571, 2014. ISSN 09203796. doi: 10.1016/j.fusengdes.2014.01.007.
- C. J. Rapson, M. Reich, J. Stober, and W. Treutterer. Actuator management for ECRH at ASDEX Upgrade. *Fusion Eng. Des.*, 96-97:694–697, 2015. ISSN 09203796. doi: 10.1016/j.fusengdes.2015.01.007.
- C. J. Rapson, F. Felici, C. Galperti, P. T. Lang, M. Lennholm, E. Maljaars, M. Maraschek, B. Plockl, M. Reich, O. Sauter, J. Stober, and W. Treutterer. Experiments on actuator management and integrated control at ASDEX Upgrade. *Fusion Eng. Des.*, 123:603–606, 2017a. ISSN 09203796. doi: 10.1016/j.fusengdes.2017.03.014.
- C.J. Rapson, D.A. Humphreys, M. Maraschek, and W. Treutterer. Comment on ‘Numerical study on neoclassical tearing mode stabilization via minimum seeking method for the island width growth rate’. *Nucl. Fusion*, 56:038001, 2016. ISSN 17414326. doi: 10.1088/0029-5515/55/2/023006.
- C.J. Rapson, R. Fischer, L. Giannone, M. Maraschek, M. Reich, and W. Treutterer. Improved localisation of neoclassical tearing modes by combining multiple diagnostic estimates. *Nucl. Fusion*, 57(7):076023, 2017b. ISSN 0029-5515. doi: 10.1088/1741-4326/aa6e0f.

- S. K. Rathgeber, L. Barrera, T. Eich, R. Fischer, B. Nold, W. Suttrop, M. Willensdorfer, and E. Wolfrum. Estimation of edge electron temperature profiles via forward modelling of the electron cyclotron radiation transport at ASDEX Upgrade. *Plasma Phys. Control. Fusion*, 55 (2), 2013. ISSN 07413335. doi: 10.1088/0741-3335/55/2/025004.
- M. Reich, A. Bock, M. Maraschek, and Team Asdex Upgrade. NTM Localization by Correlation of Te and dB/dt. *Fusion Sci. Technol.*, 61(4):309–313, 2012.
- M. Reich, L. Barrera, K. Behler, A. Buhler, A. Bock, H. Eixenberger, S. Fietz, L. Giannone, K. Lackner, M. Lochbrunner, M. Maraschek, P. McCarthy, A. Mlynek, E. Poli, R. Preuss, C. J. Rapson, O. Sauter, M. Schubert, J. Stober, W. Treutterer, F. Volpe, D. Wagner, and H. Zohm. Real-time Control of NTMs Using ECCD at ASDEX Upgrade. In *25th Fusion Energy Conf. (FEC 2014)*, pages PPC/P1–26, Saint Petersburg, Russia, 2014. URL <http://www-naweb.iaea.org/naweb/physics/FEC/FEC2014/fec2014-preprints/430{ }PPCP126.pdf>.
- M. Reich, R. Bilato, U. Mszanowski, E. Poli, C. Rapson, J. Stober, F. Volpe, and R. Zille. Real-time beam tracing for control of the deposition location of electron cyclotron waves. *Fusion Eng. Des.*, 100:73–80, 2015. ISSN 09203796. doi: 10.1016/j.fusengdes.2015.04.024.
- H Reimerdes. *MHD stability limits in the TCV tokamak*. PhD thesis, École polytechnique fédérale de Lausanne, 2001. URL <http://dx.doi.org/10.5075/epfl-thesis-2399>.
- H. Reimerdes, O. Sauter, T. Goodman, and A. Pochelon. From Current-Driven to Neoclassically Driven Tearing Modes. *Phys. Rev. Lett.*, 88(10):4, 2002. ISSN 10797114. doi: 10.1103/PhysRevLett.88.105005.
- H. Reimerdes, S. Alberti, P. Blanchard, P. Bruzzone, R. Chavan, S. Coda, B. P. Duval, A. Fasoli, B. Labit, B. Lipschultz, T. Lunt, Y. Martin, J. M. Moret, U. Sheikh, B. Sudki, D. Testa, C. Theiler, M. Toussaint, D. Uglietti, N. Vianello, and M. Wischmeier. TCV divertor upgrade for alternative magnetic configurations. *Nucl. Mater. Energy*, 12:1106–1111, 2017. ISSN 23521791. doi: 10.1016/j.nme.2017.02.013.
- J. E. Rice. Experimental observations of driven and intrinsic rotation in tokamak plasmas. *Plasma Phys. Control. Fusion*, 58(8), 2016. ISSN 13616587. doi: 10.1088/0741-3335/58/8/083001.
- N. Rispoli, C. Sozzi, L. Figini, D. Micheletti, C. Galperti, M. Fontana, E. Alessi, S. Coda, S. Garavaglia, T. Goodman, M. Kong, M. Maraschek, A. Moro, L. Porte, O. Sauter, U. Sheikh, and D. Testa. Tracking of neoclassical tearing modes in TCV using the electron cyclotron emission diagnostics in quasi-in-line configuration. *Fusion Eng. Des.*, 146(December 2018): 666–670, 2019. ISSN 09203796. doi: 10.1016/j.fusengdes.2019.01.051.
- P. H. Rutherford. Nonlinear growth of the tearing mode. *Phys. Fluids*, 16(11):1903–1908, 1973. ISSN 10706631. doi: 10.1063/1.1694232.
- O. Sauter. On the contribution of local current density to neoclassical tearing mode stabilization. *Phys. Plasmas*, 11(10):4808–4813, 2004. ISSN 1070664X. doi: 10.1063/1.1787791.

Bibliography

- O. Sauter, R. J. La Haye, Z. Chang, D. A. Gates, Y. Kamada, H. Zohm, A. Bondeson, D. Bouchers, J. D. Callen, M. S. Chu, T. A. Gianakon, O. Gruber, R. W. Harvey, C. C. Hegna, L. L. Lao, D. A. Monticello, F. Perkins, A. Pletzer, A. H. Reiman, M. Rosenbluth, E. J. Strait, T. S. Taylor, A. D. Turnbull, F. Waelbroeck, J. C. Wesley, H. R. Wilson, and R. Yoshino. Beta limits in long-pulse tokamak discharges. *Phys. Plasmas*, 4(5):1654–1664, 1997. ISSN 1070664X. doi: 10.1063/1.872270.
- O Sauter, C Angioni, and Y. R. Lin-Liu. Neoclassical conductivity and bootstrap current formulas for general axisymmetric equilibria and arbitrary collisionality regime. *Phys. Plasmas*, 6(7):2834–2839, 1999.
- O. Sauter, C. Angioni, and Y. R. Lin-Liu. Erratum: Neoclassical conductivity and bootstrap current formulas for general axisymmetric equilibria and arbitrary collisionality regime (Physics of Plasmas (1999) 6 (2834)). *Phys. Plasmas*, 9(12):5140, 2002a. ISSN 1070664X. doi: 10.1063/1.1517052.
- O. Sauter, R. J. Buttery, R. Felton, T. C. Hender, and D. F. Howell. Marginal β -limit for neoclassical tearing modes in JET H-mode discharges. *Plasma Phys. Control. Fusion*, 44(9): 1999–2019, 2002b. ISSN 07413335. doi: 10.1088/0741-3335/44/9/315.
- O. Sauter, E. Westerhof, M. L. Mayoral, B. Alper, P. A. Belo, R. J. Buttery, A. Gondhalekar, T. Hellsten, T. C. Hender, D. F. Howell, T. Johnson, P. Lamalle, M. J. Mantsinen, F. Milani, M. F.F. Nave, F. Nguyen, A. L. Pecquet, S. D. Pinches, S. Podda, and J. Rapp. Control of Neoclassical Tearing Modes by Sawtooth Control. *Phys. Rev. Lett.*, 88(10):4, 2002c. ISSN 10797114. doi: 10.1103/PhysRevLett.88.105001.
- O. Sauter, M. A. Henderson, G. Ramponi, H. Zohm, and C. Zucca. On the requirements to control neoclassical tearing modes in burning plasmas. *Plasma Phys. Control. Fusion*, 52(2): 025002, 2010. ISSN 07413335. doi: 10.1088/0741-3335/52/2/025002.
- M. Schittenhelm and H. Zohm. Analysis of coupled MHD modes with mirnov probes in asdex upgrade. *Nucl. Fusion*, 37(9):1255–1270, 1997. ISSN 00295515. doi: 10.1088/0029-5515/37/9/I06.
- U. A. Sheikh, B. P. Duval, C. Galperti, M. Maraschek, O. Sauter, C. Sozzi, G. Granucci, M. Kong, B. Labit, A. Merle, and N. Rispoli. Disruption avoidance through the prevention of NTM destabilization in TCV. *Nucl. Fusion*, 58(10), 2018. ISSN 17414326. doi: 10.1088/1741-4326/aad924.
- M. Shimada, D. J. Campbell, V. Mukhovatov, M. Fujiwara, N. Kirneva, K. Lackner, M. Nagami, V. D. Pustovitov, N. Uckan, J. Wesley, N. Asakura, A. E. Costley, A. J.H. Donné, E. J. Doyle, A. Fasoli, C. Gormezano, Y. Gribov, O. Gruber, T. C. Hender, W. Houlberg, S. Ide, Y. Kamada, A. Leonard, B. Lipschultz, A. Loarte, K. Miyamoto, V. Mukhovatov, T. H. Osborne, A. Polevoi, and A. C.C. Sips. Chapter 1: Overview and summary. *Nucl. Fusion*, 47(6), 2007. ISSN 00295515. doi: 10.1088/0029-5515/47/6/S01.

- M. Siccinio, G. Federici, R. Kembleton, H. Lux, F. Maviglia, and J. Morris. Figure of merit for divertor protection in the preliminary design of the EU-DEMO reactor. *Nucl. Fusion*, 59(10): 106026, 2019. ISSN 0029-5515. doi: 10.1088/1741-4326/ab3153.
- A. I. Smolyakov, A. Hirose, E. Lazzaro, G. B. Re, and J. D. Callen. Rotating nonlinear magnetic islands in a tokamak plasma. *Phys. Plasmas*, 2(5):1581–1598, 1995. ISSN 1070664X. doi: 10.1063/1.871308.
- J. A. Snipes, D. J. Campbell, M. Hugon, P. J. Lomas, M. F. Nave, P. S. Haynes, T. C. Hender, N. J. Lopes Cardozo, and F. C. Schüller. Large amplitude quasi-stationary MHD modes in JET. *Nucl. Fusion*, 28(6):1085–1097, 1988. ISSN 17414326. doi: 10.1088/0029-5515/28/6/010.
- J. A. Snipes, D. J. Campbell, T. C. Hender, M. Von Hellermann, and H. Weisen. Plasma stored energy and momentum losses during large MHD activity in JET. *Nucl. Fusion*, 30(2):205–218, 1990. ISSN 17414326. doi: 10.1088/0029-5515/30/2/002.
- J. A. Snipes, S. Bremond, D. J. Campbell, T. Casper, D. Douai, Y. Gribov, D. Humphreys, J. Lister, A. Loarte, R. Pitts, M. Sugihara, A. Winter, and L. Zabeo. Physics of the conceptual design of the ITER plasma control system. *Fusion Eng. Des.*, 89(5):507–511, 2014. ISSN 09203796. doi: 10.1016/j.fusengdes.2014.01.063.
- E. J. Strait. Stability of high beta tokamak plasmas. *Phys. Plasmas*, 1(5):1415–1431, 1994. ISSN 1070664X. doi: 10.1063/1.870691.
- A. Sushkov, V. Andreev, Y. Camenen, A. Pochelon, I. Klimanov, A. Scarabosio, and H. Weisen. High-resolution multiwire proportional soft x-ray diagnostic measurements on TCV. *Rev. Sci. Instrum.*, 79(2), 2008. ISSN 00346748. doi: 10.1063/1.2833822.
- K. Takahashi, K. Kajiwara, Y. Oda, K. Sakamoto, T. Omori, and M. Henderson. Development of ITER Equatorial EC Launcher Components Toward the Final Design. *Fusion Sci. Technol.*, 67(4):718–731, 2015. ISSN 1536-1055. doi: 10.13182/fst14-830.
- Anna Teplukhina. *Realistic multi-machine tokamak profile simulations and numerical ramp-down optimization using the RAPTOR code*. PhD thesis, École polytechnique fédérale de Lausanne, 2018.
- M. Teschke, N. Arden, H. Eixenberger, M. Rott, M. Schandrul, and W. Suttrop. Optimizing BUSSARD: The new 16-phase inverter system of ASDEX upgrade. *Fusion Eng. Des.*, 124: 141–146, 2017. ISSN 09203796. doi: 10.1016/j.fusengdes.2017.02.056.
- V. Toigo, R. Piovan, and S. Dal Bello. The PRIMA Test Facility: SPIDER and MITICA test-beds for ITER neutral beam injectors. *New J. Phys.*, 19(8), 2017. ISSN 13672630. doi: 10.1088/1367-2630/aa78e8.
- W. Treutterer, R. Cole, K. Lüddecke, G. Neu, C. Rapson, G. Raupp, D. Zasche, and T. Zehetbauer. ASDEX upgrade discharge control system - A real-time plasma control framework. *Fusion Eng. Des.*, 89(3):146–154, 2014. ISSN 09203796. doi: 10.1016/j.fusengdes.2014.01.001.

Bibliography

- F. Troyon, R. Gruber, H. Saurenmann, S. Semenzato, and S. Succi. MHD-limits to plasma confinement. *Plasma Phys. Control. Fusion*, 26(1A):209, 1984. doi: 10.1088/0741-3335/26/1A/319.
- F. Turco, C. T. Holcomb, J. R. Ferron, T. C. Luce, P. A. Politzer, J. M. Park, A. E. White, D. P. Brennan, A. D. Turnbull, J. M. Hanson, M. Okabayashi, and Y. In. Sensitivity of transport and stability to the current profile in steady-state scenario plasmas in DIII-D. *Phys. Plasmas*, 19(12), 2012. ISSN 1070664X. doi: 10.1063/1.4772765.
- F. Turco, C. C. Petty, T. C. Luce, T. N. Carlstrom, M. A. Van Zeeland, W. Heidbrink, F. Carpanese, W. Solomon, C. T. Holcomb, and J. R. Ferron. The high- β_N hybrid scenario for ITER and FNSF steady-state missions. *Phys. Plasmas*, 22(5), 2015. ISSN 10897674. doi: 10.1063/1.4921161.
- F. Turco, T. C. Luce, W. Solomon, G. Jackson, G. A. Navratil, and J. M. Hanson. The causes of the disruptive tearing instabilities of the ITER Baseline Scenario in DIII-D. *Nucl. Fusion*, 58(10):106043, 2018. ISSN 17414326. doi: 10.1088/1741-4326/aadbb5.
- M. Vallar, A. N. Karpushov, M. Agostini, T. Bolzonella, S. Coda, B. P. Duval, A. Fasoli, C. Galperti, J. Garcia, B. Geiger, T. P. Goodman, R. Jacquier, B. Labit, R. Maurizio, A. Pimazzoni, C. Piron, G. Serianni, D. Testa, M. Valisa, P. Veltri, and N. Vianello. Status, scientific results and technical improvements of the NBH on TCV tokamak. *Fusion Eng. Des.*, 146(January): 773–777, 2019. doi: 10.1016/j.fusengdes.2019.01.077.
- H. Van Den Brand, M. R. De Baar, N. J. Lopes Cardozo, and E. Westerhof. Integrated modelling of island growth, stabilization and mode locking: Consequences for NTM control on ITER. *Plasma Phys. Control. Fusion*, 54(9), 2012. ISSN 07413335. doi: 10.1088/0741-3335/54/9/094003.
- H. Van Den Brand, W. A. Bongers, J. K. Stober, W. Kasperek, D. Wagner, N. Doelman, W. Klop, L. Giannone, M. Reich, E. Westerhof, and M. R. De Baar. Inline ECE measurements for NTM control on ASDEX Upgrade. *Nucl. Fusion*, 59(1):a4eea9, 2019. ISSN 17414326. doi: 10.1088/1741-4326/a4eea9. URL <https://doi.org/10.1088/1741-4326/a4eea9>.
- F. A. G. Volpe, M. E. Austin, R. J. La Haye, J. Lohr, R. Prater, E. J. Strait, and A. S. Welanders. Advanced techniques for neoclassical tearing mode control in DIII-D. *Phys. Plasmas*, 16(10), 2009. ISSN 1070664X. doi: 10.1063/1.3232325.
- Th von Woedtke, S. Reuter, K. Masur, and K. D. Weltmann. Plasmas for medicine. *Phys. Rep.*, 530(4):291–320, 2013. ISSN 03701573. doi: 10.1016/j.physrep.2013.05.005.
- N. M. T. Vu, R. Nouailletas, L. Lefèvre, and F. Felici. Plasma q-profile control in tokamaks using a damping assignment passivity-based approach. *Control Eng. Pract.*, 54:34–45, 2016. ISSN 09670661. doi: 10.1016/j.conengprac.2016.05.003.
- N. M. Trang Vu, T. C. Blanken, F. Felici, C. Galperti, M. Kong, E. Maljaars, and O. Sauter. Tokamak-agnostic actuator management for multi-task integrated control with application to TCV and

- ITER. *Fusion Eng. Des.*, 147(May):111260, 2019. ISSN 09203796. doi: 10.1016/j.fusengdes.2019.111260.
- F. L. Waelbroeck, J. W. Connor, and H. R. Wilson. Finite larmor-radius theory of magnetic island evolution. *Phys. Rev. Lett.*, 87(21):215003–1–215003–4, 2001. ISSN 10797114. doi: 10.1103/PhysRevLett.87.215003.
- D. Wagner, J. Stober, M. Kircher, F. Leuterer, M. Münich, and M. Schubert. Extension of the multi-frequency ECRH system at ASDEX upgrade. *EPJ Web Conf.*, 149:03004, 2017.
- Yuanxi. Wan, J. Li, Y. Liu, X. Wang, V. Chan, C. Chen, X. Duan, P. Fu, X. Gao, K. Feng, S. Liu, Y. Song, P. Weng, B. Wan, F. Wan, H. Wang, S. Wu, M. Ye, Q. Yang, G. Zheng, G. Zhuang, and Q. Li. Overview of the present progress and activities on the CFETR. *Nucl. Fusion*, 57(10), 2017. ISSN 17414326. doi: 10.1088/1741-4326/aa686a.
- D. J. Ward. The physics of DEMO. *Plasma Phys. Control. Fusion*, 52(12):0–12, 2010. ISSN 07413335. doi: 10.1088/0741-3335/52/12/124033.
- C. D. Warrick, R. J. Buttery, G. Cunningham, S. J. Fielding, T. C. Render, B. Lloyd, A. W. Morris, M. R. O’Brien, T. Pinfold, K. Stammers, M. Valovic, M. Walsh, and H. R. Wilson. Complete stabilization of neoclassical tearing modes with lower hybrid current drive on COMPASS-D. *Phys. Rev. Lett.*, 85(3):574–577, 2000. ISSN 00319007. doi: 10.1103/PhysRevLett.85.574.
- W. Wehner and E. Schuster. Control-oriented modelling for neoclassical tearing mode stabilization via minimum-seeking techniques. *Nucl. Fusion*, 52(7), 2012. ISSN 00295515. doi: 10.1088/0029-5515/52/7/074003.
- John Wesson. *Tokamaks*. Oxford University Press, Oxford, 3 edition, 2004.
- E. Westerhof. Letters: Tearing mode stabilization by local current density perturbations. *Nucl. Fusion*, 30(6):1143–1147, 1990. ISSN 17414326. doi: 10.1088/0029-5515/30/6/017.
- E. Westerhof, H. J. De Blank, and J. Pratt. New insights into the generalized Rutherford equation for nonlinear neoclassical tearing mode growth from 2D reduced MHD simulations. *Nucl. Fusion*, 56(3):36016, 2016. ISSN 17414326. doi: 10.1088/0029-5515/56/3/036016.
- R. B. White, D. A. Monticello, Marshall N. Rosenbluth, and B. V. Waddell. Saturation of the tearing mode. *Phys. Fluids*, 20(5):800–805, 1977. ISSN 10706631. doi: 10.1063/1.861939.
- J. R. Wilson and P. T. Bonoli. Progress on ion cyclotron range of frequencies heating physics and technology in support of the International Tokamak Experimental Reactor. *Phys. Plasmas*, 22(2), 2015. ISSN 10897674. doi: 10.1063/1.4901090.
- Q. Yu, X. D. Zhang, and S. Günter. Numerical studies on the stabilization of neoclassical tearing modes by radio frequency current drive. *Phys. Plasmas*, 11(5):1960–1968, 2004. ISSN 1070-664X. doi: 10.1063/1.1710521.

Bibliography

- G. Zhuang, G.Q. Li, J. Li, Y.X. Wan, Y. Liu, X.L. Wang, Y.T. Song, V. Chan, Q.W. Yang, B.N. Wan, X.R. Duan, P. Fu, and B.J. Xiao. Progress of the CFETR design. *Nucl. Fusion*, 59(11):112010, 2019. ISSN 0029-5515. doi: 10.1088/1741-4326/ab0e27.
- H. Zohm, G. Gantenbein, S. Günter, F. Leuterer, M. Maraschek, J. Meskat, A. G. Peeters, W. Suttrop, D. Wagner, ASDEX Upgrade Team, and ECRH Group. Experiments on neoclassical tearing mode stabilization by ECCD in ASDEX Upgrade. *Nucl. Fusion*, 39(5):480–483, 1999. doi: 10.1088/0029-5515/39/5/101.
- H. Zohm, G. Gantenbein, F. Leuterer, M. Maraschek, E. Poli, and L. Urso. Control of NTMs by ECCD on ASDEX Upgrade in view of ITER application. *Plasma Phys. Control. Fusion*, 49(12B):B341–B347, 2007. ISSN 0741-3335. doi: 10.1088/0741-3335/49/12b/s31.

Acknowledgements

My story with Switzerland began with a beautiful coincidence: during a casual chat with a Swiss student Mark about my plans of applying for a PhD position overseas in a summer school held in Beijing on July 2014, I was introduced to EPFL for the first time. So I would like to thank Mark first for opening the doors for me to this beautiful country. I still remember the joyfulness I had on my first train from Zurich Airport to Lausanne on October 2015 - the breath-taking scenery immediately wiped out all my fatigue from the long journey. At that moment I was already sure that it would be a wonderful experience in Switzerland and now I can reconfirm that I was right. These great four years, of course, could not have been possible without all the lovely people I met here.

My deepest gratitude goes to my thesis supervisor, Olivier. It must not have been an easy task to guide a PhD student who barely knew anything about plasma physics or fusion. I can never thank you enough for your endless patience, your tremendous optimism and your continuous encouragement. The thesis would not have been possible without your efforts and guidance. Thank you for making me a better researcher as well: the scientific insights and ways of thinking I have learned from you (even though only a tiny portion of yours) will continue helping me in the long run. I also would like to thank you for your willingness to help whenever I ask - I would not have adapted to this new country quickly without your kindness.

I am also very grateful to Federico E., who guided me into the world of control. I have greatly benefited from close collaborations with you and always been amazed by your brilliant ideas and high efficiency. Being a genius does not make you a dull person - thank you for being so open-minded and humorous, which made it even easier to learn from you. Thank you sincerely for being in my thesis committee - your questions during the oral exam and your comments of the draft thesis have greatly improved the quality of this work.

I also appreciate the efforts of the other members in my thesis committee: Prof. R. Houdré for organizing and hosting my private defense; Dr. T. Hender and Prof. H. Zohm for the careful reading of this thesis, the useful suggestions and the journey to Switzerland for my defense.

I was very lucky to study and work at the Swiss Plasma Center (SPC), where intelligent minds and lovely people gather. I would like to thank Prof. Fasoli and Prof. Ricci for giving me the chance to enter this big SPC family. Special thanks to Basil and Holger, who interviewed me at

Acknowledgements

the lounge of a hotel near Beijing Capital International Airport before rushing to their flights; your kindness has facilitated my final decision of coming to EPFL. I also owe John and Stephan a big thank you, for your precious help in all the courses I have taken with you and for taking me as a teaching assistant in your mathematics course. I also enjoyed working with Christian T. and Justin for maintaining the online MOOC course and would like to thank you both for sharing your experience and knowledge with me. I am grateful to the SPC secretaries as well, in particular Edith and Roxane, who have provided warm support in my daily work; interactions with you have always been a pleasure.

The experimental work in this thesis could not have been achieved without the support and hard work of the entire TCV team. I am very grateful to Stefano C. for giving me tremendous trust and freedom of performing the experiments; thanks a lot for your support for my various proposals and papers as well. I would like to thank all the pilots (in particular Alexdander, Yanis and PF), PdJs (in particular Benoît, Antoine and Laurie), GdJs (especially Miguel), DDJs, Gristian G., Xavier, Joan, and all the engineers and technicians for their support.

Just like fusion research itself, these four years have witnessed close teamwork everywhere. I was very lucky to have been a member of various groups, from the TCV team to the EUROfusion MST1 team, from the OS group to the RAPTOR group. I would like to thank all the team/group members for the inspiring discussions, the willingness to help, and of course, the happy moments at restaurants and bars after work. A big thanks to Anna, Trang, Francesco, Simon, Alessandro, Bert and Thomas - it has been a great pleasure to work with you all. I also would like to thank our collaborators in IPP Garching, in particular Matthias and Marc who helped me a lot in getting familiar with AUG facilities and data; Giovanni Tardini, Emiliano Fable and Emanuele Poli who helped me in running TORBEAM and ASTRA in IPP; Ondrej (and Xenia) who invited me to warm parties at home; and Filip, who showed me the way to the team room.

Life would not have been this colorful without the accompany of my friends, fellow PhD students and post-docs. Thank you Dahye, Sam and Jérémy for all the happy memory on campus, at home, on the lake and in the mountains, and thank you for helping me moving all my treasure to the new apartment! Thank you Trang for your accompany in exploring the many hiking routes in Switzerland and your optimism and encouragement. Thank you, my dear office mates Federico N., Joyeeta, Oulfa, Pedro, Fabien, Francesco, Mirko, Lorenzo and Jean (guess in what order?) - I was extremely lucky to share the office with you guys. Thank you Carrie, Claudia, Sophie, Ajay, Aylwin, Claudio, Hugo, Kevin, Madhu, Maurizio, Noé, Roberto, Zhouji and all my fellow PhDs. Thank you also the “older” scientist and post-doc group, including Umar, Justin, Olivier F. and Cristian S.

Finally, my sincere gratitude to my family, who are always ready to share my happiness and sorrow, support me and make me feel warm though thousands of miles away from home.

Lausanne, 12 February 2020

Mengdi

Mengdi Kong

Email: kongmengdi@hotmail.com

Nationality: Chinese

Date of Birth: 11 November 1990



EDUCATION

Nov. 2015 – Feb. 2020 École polytechnique fédérale de Lausanne (EPFL), Lausanne, Switzerland

Ph.D. in Physics

Supervisor: Dr. Olivier Sauter

Thesis topic: Towards integrated control of tokamak plasmas: physics-based control of neoclassical tearing modes in the TCV tokamak

2012 – 2015 Beihang University, Beijing, China

M.Sc. in Aerospace Engineering

Supervisor: Prof. Haibin Tang

Thesis topic: Study on the working mechanisms and performance of applied-field magnetoplasma dynamic thrusters (in Chinese)

2008 – 2012 Nanjing University of Science and Technology, Nanjing, China

B.Sc. in Engineering, School of Mechanical Engineering

RESEARCH EXPERIENCES

Nov. 2015 – Feb. 2020 Ph.D. Student, Swiss Plasma Center (SPC), EPFL, Lausanne

- Performed experimental and numerical studies on neoclassical tearing modes (NTMs)
- Developed a model for the classical stability index, which provides a comprehensive modified Rutherford equation (MRE) for simulating consistently NTMs and TMs, including both NTM stabilization and prevention cases
- Developed a novel real-time (RT) module based on the MRE, able to estimate the electron cyclotron power needed to control NTMs and to predict NTM evolutions, in RT
- Contributed to integrated control studies in TCV - participated in the development of a new generic plasma control system framework and in RT integrated control experiments
- Participated in medium size tokamak (MST1) campaigns in TCV and ASDEX Upgrade

2012 – 2015 Master Project, Beihang University, Beijing, China

- Performed numerical studies on the acceleration mechanisms of applied-field magnetoplasma dynamic (AF-MPD) thrusters with the particle-in-cell (PIC) method
- Conducted experimental studies on the effects of applied magnetic field, discharge current and propellant type on the ignition and steady operation of AF-MPD thrusters

SELECTED JOURNAL PUBLICATIONS

- **M. Kong**, O. Sauter, F. Felici et al. (2020). *On the triggerless onset of 2/1 neoclassical tearing modes in TCV*, Nucl. Fusion 60, 026002, <https://doi.org/10.1088/1741-4326/ab56c5>
- **M. Kong**, T.C. Blanken, F. Felici et al. (2019). *Control of NTMs and integrated multi-actuator plasma control on TCV*, Nucl. Fusion 59, 076035, <https://doi.org/10.1088/1741-4326/ab1e1e>
- N.M.T. Vu, et al. incl. **M. Kong** (2019). *Tokamak-agnostic actuator management for multi-task integrated control with application to TCV and ITER*, Fusion Eng. Design 147, 111260
- N. Rispoli, et al. incl. **M. Kong** (2019). *Tracking of neoclassical tearing modes in TCV using the electron cyclotron emission diagnostics in quasi-in-line configuration*, Fusion Eng. Design 146, 666

- T.C. Blanken, et al. incl. **M. Kong** (2019). *Real-time plasma state monitoring and supervisory control on TCV*, Nucl. Fusion 59, 026017
- U.A. Sheikh, et al. incl. **M. Kong** (2018). *Disruption avoidance through the prevention of NTM destabilization in TCV*, Nucl. Fusion 58, 106026
- Z. Zhang, H. Tang, **M. Kong**, et al. (2018). *Temporal Evolution and Spatial Distribution of the Plume Plasma from an MPD Arc Generator*, IEEE Trans. Plasma Sci.46, 2901
- E. Maljaars, et al. incl. **M. Kong** (2017). *Profile control simulations and experiments on TCV: a controller test environment and results using a model-based predictive controller*, Nucl. Fusion 57, 126063
- Z. Zhang, H. Tang, **M. Kong**, et al. (2015). *Electron temperature measurement in Maxwellian non-isothermal beam plasma of an ion thruster*, Rev. Sci. Instrum 86, 023506

SELECTED CONFERENCE PRESENTATIONS & PROCEEDINGS

- **M. Kong**, O. Sauter, et al. (2019). *Inclusion of predictive modeling in NTM control algorithms towards advanced integrated control of long-pulse tokamaks*. 61st Annual Meeting of APS-DPP, 21 - 25 Oct., Fort Lauderdale, Florida, USA (poster, PP10.00091)
- **M. Kong**, T.C. Blanken, et al. (2018). *Integrated control on TCV including real-time monitoring, supervision and actuator management*. 2nd Asia-Pacific Conference on Plasma Physics, 12-17 Nov., Kanazawa, Japan (invited talk, MF-I46)
- **M. Kong**, T.C. Blanken, et al. (2018). *Control of NTMs and integrated multi-actuator control on TCV*. 27th IAEA Fusion Energy Conference, 22-27 Oct., Gandhinagar, India (poster, EX/P1-25)
- **M. Kong**, O. Sauter, et al. (2017). *Real-time control of neoclassical tearing modes and its integration with multiple controllers in the TCV tokamak*. 44th European Physical Society Conference on Plasma Physics, 26-30 Jun., Belfast, the UK (poster, P4.152)
- **M. Kong**, T. P. Goodman, et al. (2016). *Stabilization and preemption of NTMs with ECCD/ECRH in TCV*. Swiss Physics Society Annual Meeting, 23-25 Aug., Lugano, Switzerland (oral presentation)
- **M. Kong**, H. Tang, et al. (2015). *Analyses of Ignition Processes of an Applied-Field Magnetoplasmdynamic Thruster*, AIAA Sci. and Tech. Forum, 5-9 Jan., Kissimmee, USA
- **M. Kong** and H. Tang (2013). *Geometric Effects on the Acceleration Mechanisms in Applied-Field Magnetoplasmdynamic Thrusters*, 33rd International Electric Propulsion Conference, 6-10 Oct., Washington, D.C., USA (oral presentation, IEPC-2013-115)

SELECTED HONORS & AWARDS

- National Scholarship for Postgraduates (top 1%), Ministry of Education of P. R. China, 2013
- National Scholarship for Undergraduates (top 1%) , Ministry of Education of P. R. China, 2009-2011

TEACHING EXPERIENCES

Teaching assistant for several courses at EPFL

2019, 2016	Massive Open Online Courses (MOOC) on Plasma Physics
2018	Mathematical Methods for Physicists (2nd year bachelor)
2017	“Mise à niveau” of General Physics I (1st year bachelor)

SKILLS

Operating System & Programming: Linux, Windows, MATLAB, C, Visual Basic, FORTRAN

Scientific tools: Simulink, LaTeX, Word, Power Point, Excel, ANSYS, AutoCAD, SolidWorks

LANGUAGES

Chinese (native), English (fluent), French (basic, A2/B1)